Improving TB diagnostics for use in low-resource settings

By

Stephanie Irene Pearlman

Dissertation

Submitted to the Faculty of the

Graduate School of Vanderbilt University

in partial fulfillment of the requirements

for the degree of

DOCTOR OF PHILOSOPHY

in

Biomedical Engineering

May 13, 2022

Nashville, TN

Approved:

Frederick R. Haselton, Ph.D.

Todd Giorgio, Ph.D.

Anita Mahadevan-Jansen, Ph.D.

Raymond L. Mernaugh, Ph.D.

April C. Pettit, M.D., MPH

DEDICATION

To my parents.

And to Dr. Immel.

I did it.

"Do it for all of us. May I be the first? Dr. Stephanie Pearlman."

-Dr. Joseph H. Immel, Jr. (1952 − 2016)

ACKNOWLEDGEMENTS

I start by thanking my dissertation advisor, Dr. Frederick Haselton, for agreeing to serve as my PI for the last five and a half years. While we may have disagreed more than we agreed, your guidance was important for my degree completion, especially early on. I would also like to thank my dissertation committee members, Dr. Todd Giorgio, Dr. Mahadevan-Jansen, Dr. Raymond Mernaugh, and Dr. April Pettit. Your experience and direction were invaluable for completing my dissertation, and I could not have finished without you.

I thank all the members of the Haselton Lab that have been here during my tenure, namely Dr. Megan Pask, Dr. Mindy Leelawong, Dr. Nick Adams, and Dr. Patricia Russ, for their guidance and support. Often you provided an alternate perspective that helped me with both the personal and professional struggles of being a Ph.D. student. Thanks to my fellow grad students Dr. Zack Zimmers, Mike Jacobs, Emily Kight, Dalton Nelson, David Evans, Nick Spurlock, and Nicole Malofsky for creating a warm and welcoming environment and for not just being great coworkers but also great friends.

Kelly Richardson, Christian Warren, Eric Tang, Dr. Megan van der Horst, Dr. Kenny Tao, Dr. Raymond Mernaugh, and Lejla Pasic at VU or VUMC, and Dr. Johnathan Blackburn and Dr. Leshern Karamchand from the University of Cape Town were all critical to collaborations that resulted in the completion of this dissertation. This would not have been possible without their expertise, and I thank them for their contributions.

To the research mentors I had before coming to Vanderbilt, Dr. Scott Oakes at UCSF, Dr. Jered Haun at UC Irvine, and Dr. Emil Bogenmann with the NIDDK STEP-UP Program − my experiences with you all led me to attend graduate school, and without your guidance and mentorship, I would not have chosen this path. Thank you.

To my teachers from Tech High – namely Dr. Joe Immel, Mr. Greg Weaver, Mr. Ken Torre, and Mrs. Heather Brown – you were instrumental in helping me become the scientist I am today, even before my official academic journey started. Thank you, Mrs. Nancy Hyde, for making me do my homework in kindergarten. Who knows what I would have become without that fundamental lesson, and I hypothesize that becoming Dr. Pearlman would not be on that list.

I thank my friends, both inside and outside the university, for their friendship throughout this process. My cohort members Dr. Laura Masson and Dr. Katie Ozgun, fellow graduate students Kelly Richardson, John Albert Rector IV, Ben Perlin, collaborator, and, more importantly, friend Lejla Pasic. I sincerely hope we remain friends long after we have all left Vanderbilt.

Thank you to the friends I made outside of Vanderbilt during my time here, for creating a space that was important in maintaining my sanity, and for being kind, genuine people. To The Crag Crew, everyone in Swing Dance Nashville, Hunter Tomsett, Rhea Evelyn Darling Walton, and Morgan Mosher, thank you for helping me remember that there is life outside of academia, helping me grow as a person beyond my career aspirations, and serving as both physical and emotional support. Thank you to Drs. Jonathan and Donna Perlin for adopting me into your family during my last year of graduate school, as this was more beneficial to my wellbeing both inside and outside of school than I realized.

To the friends that have been with me long before my graduate school journey, Nathaniel Carreon, Hayly Peacock, Lena Eiger, Maya Mejia, Nav Gill, and Cory Mortimer, and I sincerely thank you for your continued support, all our text messages, and video calls, and for listening to me complain about how terrible grad school was at times. You continue to help keep me lucid, and I am so grateful for our continued friendship. You are my chosen family and always will be.

Everyone that knows me knows how much I love my cats and how important they are to me, so I must of course thank Sierra and Miss Caddy. These sassy ladies were both instrumental in helping maintain my physical and mental health throughout grad school.

Last, I want to thank my family for supporting me through this journey. While I cannot name everyone, my parents, Carl and Patti Pearlman, grandmother Helen Pearlman, and sister Virginia Pearlman were the most important in helping me finish my Ph.D. There is no acknowledgment that I can give for the support they have given and continue to give me every day. Thank you to everyone in my family for cheering me on and reminding me I was capable when I doubted myself. And, thanks to Uncle Sam for saying that I could not do it, that I would not finish, that I would drop out and would not complete my Bachelor's degree, let alone my doctorate. When things got hard, sometimes it was the spite of knowing I was proving you wrong that drove me. From now on, it's Dr. Pearlman.

TABLE OF CONTENTS

LIST OF TABLES

LIST OF FIGURES

LIST OF VIDEOS

Video A1. Paramagnetic bead separation from a flowing fluid stream using high-gradient magnetic separation. An external magnet is applied next to the ferromagnetic matrix to magnetize it. When the magnetic force is sufficiently great, the magnetic force draws beads to the surface of the wire, capturing them in the matrix. After all of the bead suspension has passed, all of the particles are retained in the ferromagnetic matrix, and no beads remain in the flow through.

Video A2. Paramagnetic bead separation from a flowing fluid stream using a stationary magnet. An external magnet is applied alongside the flowing fluid stream to separate particles from suspension. After all of the bead suspension has passed, only some of the beads are retained in the flow channel, and many still remain in the flow through. This is because the viscous drag forces applied by the liquid medium overcome the magnetic forces applied to the beads.

Video B1. Sequential OCT images of evaporating 1 μL droplet containing 10^6 polystyrene particles/uL, which are 1 μm in diameter. A total of 800 repeated frames were taken at the same position for a total acquisition time of 36 s per measurement in order to monitor the changes in particle flow and the droplet evaporation. For each droplet, measurements were taken at two minute intervals beginning at one minute following droplet placement until complete evaporation.

Video B2. Sequential fluorescence microscopy images at 100x total magnification of evaporating 5 μL droplet containing 10^4 polystyrene particles/uL, which are 1 μm in diameter. A total of 40 frames at 100 ms exposure were taken at the same position near the solvent-substrate for a total acquisition time of 40 seconds per measurement in order to monitor the changes in particle flow and the droplet evaporation. In focus particles move inward along the substrate. Once particles reach the center of the droplet, they become out of focus, and begin moving in the opposite direction. This is consistent with the particles moving upward towards the top of the droplet, then moving outward along the outer surface of the droplet. Combined, the particle movement is consistent with the Marangoni flow pattern shown in **Figure 4.1**.

LIST OF ABBREVIATIONS

A

ABTS – 2,2'-azino-bis(3-ethylbenzothiazoline-6-sulfonic acid

AF405 – Alexa Fluor™ 405

AFB – acid-fast bacilli

AIDS – Acquired Immunodeficiency Syndrome

AlereLAM – Alere™ Determine™ TB LAM Ag Test

AM – arabinomannan

AmpCan – 100 µg/mL ampicillin + 34 µg/mL chloramphenicol

anti-Flag-650 – DyLight® 650 Anti-DDDDDK (FLAG® tag) antibody

anti-His_6-650 – DyLight® 650 Anti-6x His tag® antibody

AO – auramine O

APC – Allophycocyanin

AR – auramine-rhodamine stain

AraLAM – lipoarabinomannan with no terminal carbohydrate cap

ATB – active tuberculosis

B

BCG – *Mycobacterium (M.) bovis* Bacillus Calmette–Guérin

BEI – Biodefense and Emerging Infections

bp – base pair

BSA – bovine serum albumin

C

CDC – Centers for Disease Control

CFU – colony forming units

CV – column volumes

D

DMN-tre - 4-N,N-dimethylamino-1,8-naphthalimide conjugated to trehalose

DNA – deoxyribonucleic acid

DOT – directly observed therapy

DTNB – 5,5'-dithiobis-(2-nitrobenzoic acid)

DTT – dithiothreitol

E

E. coli - *Escherichia coli*

EDTA – ethylenediaminetetracetic acid

ELISA – enzyme-linked immunosorbent assay

EMB – ethambutol

F

FACS – fluorescence-activated cell-sorting

FAM – isomer derivative of fluorescein

FIND – Foundation for Innovative New Diagnostics

FISH – fluorescence in situ hybridization

FITC – fluorescein isothiocyanate

FM – fluorescence microscopy

FMO – Fluorescence Minus One

FSC – forward scatter; measures particle size

FujiLAM – Fujifilm SILVAMP TB LAM

G

GFP – green fluorescent protein

GMean – geometric mean

H

HEX - hexachlorinated fluorescein

HGMS – high-gradient magnetic separation

HIV – Human Immunodeficiency Virus

HRP – Horseradish peroxidase

I

IABkFQ – Iowa Black® Dark FQ fluorophore quencher

IFN-γ – interferon gamma

IGRA – interferon-gamma release assay

IMAC – immobilized metal affinity chromatography

INH – isoniazid

IPTG – isopropyl β-D-1-thiogalactopyranoside

ITO – indium tin oxide

L

LAM – lipoarabinomannan

LAMP – loop-mediated isothermal amplification

LB – Lysogeny Broth

LED – light emitting diode

LM - lipomannan

LOD – limit-of-detection

LTBI – TB infection, also known as latent tuberculosis infection

M

MACS® – magnetic-activated cell sorting (by Miltenyi)

ManLAM – mannose-capped lipoarabinomannan

MDR-TB – multi drug-resistant tuberculosis

X-mer – oligonucleotide X bases in length

MES – (N-morpholino)ethanesulfonic acid

min – minute

M. smeg – *Mycobacterium* (*M.*) *smegmatis*

M.tb – *Mycobacterium* (*M.*) *tuberculosis*

MTBC – *Mycobacterium tuberculosis* complex species (*M. tuberculosis*, *M. bovis*, *M. bovis* BCG, *M. africanum*, *M. microti*, *M. canetti*, among others)

MTX – 5-methylthio-D-xylofuranose

MVN – microvirin-N

MWCO – molecular weight cut-off

N

NA – numerical aperture

NAE – nucleic acid extraction

NEM – N-ethylmaleimide

Ni(II)NTA - nickel (II) nitrilotriacetic acid

NIAID – National Institute of Allergy and Infectious Diseases

NIH – National Institutes of Health

NP – nanoparticle

NTM – non-tuberculous mycobacteria

O

OD600 – Optical density/absorbance at 600 nm

P

PAGE – polyacrylamide gel electrophoresis

PBS – Phosphate-buffered saline (1x PBS – 137 mM NaCl, 2.7 mM KCl, 10 mM Na_2HPO_4, 1.8 mM KH_2PO_4, pH = 7.4)

PBS-T – Phosphate-buffered saline + Tween-20

PBS-T-BSA – Phosphate-buffered saline + Tween-20 + Bovine serum albumin

PCR – polymerase chain reaction

PDMS – polydimethylsiloxane

PEG_X – polyethylene glycol polymer, X repeating units in length

PE-TexasRed – R-phcoerthrin/Texas Red® tandem fluorophore

*pf*HRP-II – *Plasmodium falciparum* histidine-rich protein two (2)

PG – peptidoglycan

PILAM – phosphatidyl-*myo*-inositol capped lipoarabinomannan

PIM – phosphatidylinositol mannosides

PLL – poly-L-lysine

POC – point-of-care

ppb – parts per billion

ppm − parts per million

PS – polystyrene

PTFE – polytetrafluoroethylene

PZA – pyrazinamide

Q

qPCR – real-time polymerase chain reaction

R

Rb – rabbit

rcf – relative centrifugal force, or g-force

rSD – robust standard deviation

Re – Reynolds Number

Req. - Requirement

RIF – rifampin

RNA – ribonucleic acid

rpm – revolutions per minute

RPT – rifapentine

RR-TB – rifampin-resistant TB

S

s.d. – standard deviation

SDS – sodium dodecyl sulfate

SEC – size exclusion chromatography

SEM – standard error of the mean

SSC – size scatter; measures particle granularity/complexity

T

TB – tuberculosis

TBS – Tris-buffered saline

TCEP HCl – Tris(2-carboxyethyl)phosphine hydrochloride

TE – 10 mM Tris-HCl, 1 mM EDTA, pH = 8

TIFF – tagged image file format

TNB – 2-nitro-5-thiobenzoic acid

TNF-α – tumor necrosis factor alpha

TST – tuberculin skin test (Mantoux test)

V

v/v – volume per volume

W

WHO – World Health Organization

w/v – weight per volume

X

XDR-TB – extensively drug-resistant tuberculosis

Z

ZN – Ziehl-Nielsen

LIST OF SYMBOLS

Base Units

° – Degrees (arc length)

°C – Degrees Centigrade

Da – Dalton (unit)

G – Gauss (unit)

g – gram

h – hour

L – liter

m – meter

P – poise (unit of viscosity)

s – seconds

W – watt (unit of power)

Binding Kinetics

k_{on} – association constant

k_{off} – dissociation constant

K_D – equilibrium dissociation constant

Chemical Symbols

Ag – gold

Ca^{2+} – calcium ion with +2 charge

$CaCl_2$ – calcium chloride

Fe^{X+} – iron ion with +X charge

$FeSO_4 \cdot 7H_2O$ – iron(II)sulfate heptahydrate

HCl – hydrochloric acid

H_2O_2 – hydrogen peroxide

H_2SO_4 – sulfuric acid

KCl – potassium chloride

K_2HPO_4 – potassium phosphate dibasic

KH_2PO_4 – potassium phosphate monobasic

M – molar concentration (moles/L)

N – equivalent concentration (solution normality)

NaCl – sodium chloride

$NaHCO_3$ – sodium bicarbonate

Na_2HPO_4 – sodium phosphate dibasic

Miscellaneous

~ – Approximately

% – Percentage (fraction of 100)

χ – magnetic susceptibility

Υ – surface tension

Υ_L – surface tension of liquid (droplet solvent)

C_t – qPCR cycle threshold

Hz – Hertz (s^{-1})

k – thermal conductivity

k_L – thermal conductivity of liquid (droplet solvent)

k_s – thermal conductivity of solid substrate

T, t – Relative temperature

Unit Prefixes

k – kilo (10^3)

c – centi (10^{-2})

m – milli (10^{-3})

μ – micro (10^{-6})

n – nano (10^{-9})

p – pico (10^{-12})

DISSERTATION ABSTRACT

Tuberculosis (TB) remains a major cause of infectious disease death worldwide, particularly in developing countries. One major barrier to TB elimination is a lack of effective diagnostic tools available for use at the point-of-care (POC). Despite its poor diagnostic sensitivity, century-old microscopic examination of sputum smears remains the most common diagnostic method. Furthermore, increases in multi-drug resistant TB cases highlight the urgent need for improved diagnostic tools available at the POC.

To begin addressing the lack of molecular diagnostics available at the POC, a magnetic bead-based nucleic acid extraction (NAE) assay enabled by high-gradient magnetic separation was developed, performing comparably to two commercial NAE kits for detection of cell-free TB DNA from urine and sputum. This method also worked with large-volume samples, which is universally a limiting factor of commercial kits. Additionally, this technique was featured in a total NAE challenge using pathogen-spiked blood, sputum, and stool with the Gates Foundation, demonstrating applicability with other infectious diseases.

To address the poor diagnostic sensitivity of sputum smear microscopy, I designed an assay using microfluidic flows in evaporating droplets to spatially concentrate *M. bovis* BCG following volumetric magnetic enrichment, concentrating samples over 100-fold. Optical coherence tomography confirmed that inward-oriented Marangoni flows were responsible for spatial enrichment. This combined enrichment method improved the limit-of-detection for sputum smear microscopy by 10-fold compared to direct smear while using inexpensive reagents already available at the POC.

Diagnostic development begins with creating artificial samples derived from pathogens grown in vitro. Currently there is no information on the impact these required preparation methods have on surface marker accessibility of *M.tb* before use in assay development. To address this, novel molecular recognition elements that bind different structural features of *M.tb.* surface antigen lipoarabinomannan (LAM) were characterized and then used to investigate the impact of mechanical or enzymatic processing on LAM accessibility. Mechanical dissociation recovered more *M.tb* bacilli from clumps formed during bacterial culture, and yielded greater LAM accessibility than unprocessed or enzymatically digested bacilli.

While there is still significant work to be done, the advancements made here for POC TB diagnosis in low-resource settings are an important step towards global TB elimination.

CHAPTER 1 : BACKGROUND AND CLINICAL MOTIVATION

Public Health Burden of Tuberculosis

While the number of deaths globally due to infectious diseases has been declining, they remain a significant challenge for low-income countries[1, 2] The causative agent of TB, *Mycobacterium tuberculosis (M.tb)*, has caused more human deaths than any other infectious disease in human history. Of note, the global burden of TB disease today stands at 10 million cases per annum worldwide (**Figure 1.1**). *M.tb* infection is also the most common opportunistic infection in individuals with human immunodeficiency virus (HIV), with HIV/TB co-infection rates in some countries as high as 60%. Across Africa, 86% of individuals with TB also have documented HIV. Thirty-two percent (32%) of HIV deaths globally have TB co-infection. It is estimated that 30% of TB disease cases are never diagnosed.[2]

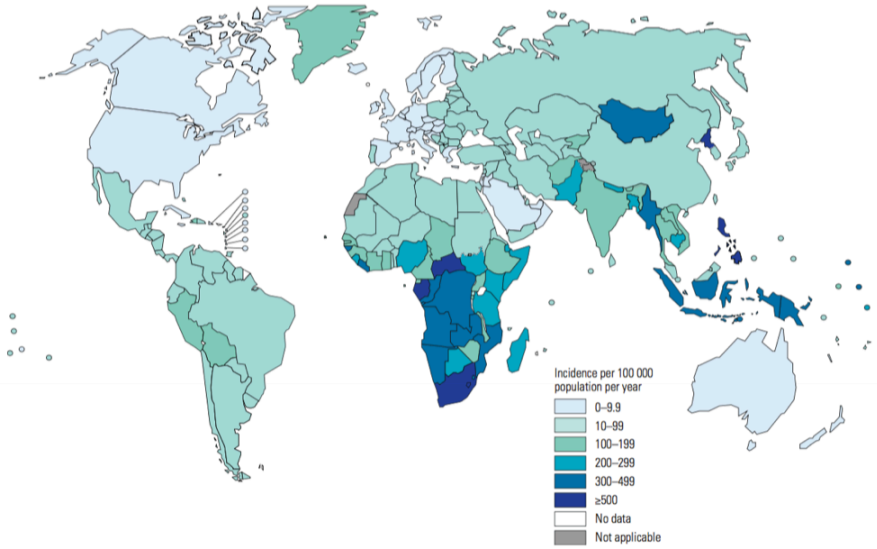

Figure 1.1. Estimated global TB incidence rates by country for 2019. Figure from cited reference.[2]

The emergence of antibiotic-resistant infections compounds these issues.[3] In 2019, approximately half a million cases of rifampin-resistant TB (RR-TB) and multi-drug resistant TB (MDR-TB) were reported,[2] and only one-third of patients with RR-TB and MDR-TB globally had access to appropriate treatment. Furthermore, World Health Organization (WHO) estimates that the treatment success rate for MDR-TB is only 56% for those with access to proper treatment.[2] The fraction of diagnosed patients who do not return to commence treatment are

considered "lost to follow-up," and these patients can make up to 38% of diagnosed patients in low-resource countries.[4]

The WHO estimates that approximately one-third of the world's population has latent *M.tb* infection (LTBI, or TB infection) and has a 10% per lifetime risk of developing active TB (ATB) disease from infection reactivation. This risk rises to 10% per year in HIV-positive individuals, representing a massive reservoir of potential new TB cases. Moreover, recent longitudinal tuberculin skin testing studies in high-burdened suburbs of Cape Town, South Africa, have shown no evidence of any decline in annual risks of TB infection over the past few decades.[5] The Stop TB Partnership's Global Plan to Stop TB thus states that *"…the central target for TB control is to cut disease transmission from person to person through early and efficient [diagnosis and] treatment of infectious TB cases."*[6] Essentially, these programs call for active TB case identification and drug resistance typing in both urban and rural communities. Yet, we currently lack effective point-of-care (POC) diagnostic tools to do this in low-resource settings.

TB Pathogenesis and Pathophysiology

TB bacteria spread through respiratory droplets expelled in the air by infected patients breathing or coughing, though it can also be transmitted during aerosol-producing medical procedures. The aerosols (1-5 μm in diameter) are inhaled by another individual and settle in the lungs' alveoli. Transmission success is dependent on proximity, duration of contact, the infectious potential of the primary host, and the immune status of the newly infected individual. There are four possible outcomes following exposure to TB bacteria: (**1**) individuals may never develop an infection, or (**2**) may become infected and clear the infection without additional intervention. Out of the 30-40% of individuals that become chronically infected, (**3**) approximately 90% of those individuals will develop LTBI. The other 10% of chronically infected individuals will (4) develop ATB disease at some point in their lives, with an increased risk of development associated with specific comorbidities.[7] In some individuals with TB disease, the TB bacteria can cause infection in other parts of the body beyond the lungs, known as disseminated disease. The outcome of exposure is multi-factorial and dependent on environmental, host, and pathogen factors.

Once in the alveoli, *M.tb* multiply over two to eight weeks in phagocytic cells; macrophages are the first immune cell to encounter *M.tb* and are the primary replicative host for *M.tb*, while dendritic cells are involved in

connecting adaptive and innate immune responses through antigen-presenting cells. There are multiple pathogenesis modes following TB infection, each dependent on the innate and adaptive immune response (**Figure 1.2**).

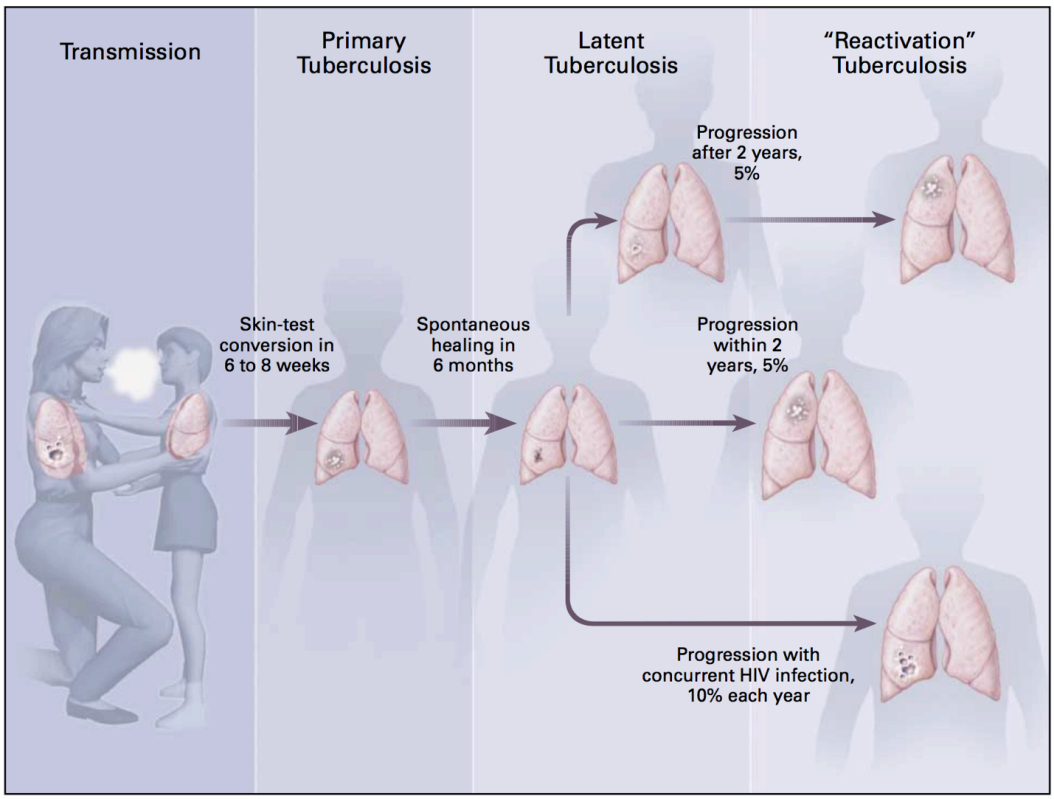

Figure 1.2. Transmission and disease progression of tuberculosis. TB bacteria are spread from person to person through aerosolized respiratory droplets, such as those produced from coughing. Of individuals infected with TB bacteria, ~10% of individuals will develop active disease throughout their lifetime. Immunocompromised individuals, such as those co-infected with HIV, are more likely to develop ATB disease, both upon initial infection and reactivation of latent TB infection. Figure from cited reference.[8]

When individuals are initially infected with *M.tb*, the innate immune system responds with phagocytic cells, which accumulate in the lungs.[9] This stage of the innate immune response recognizes mycobacterial structures, which lead to the release of pro-inflammatory cytokines. *M.tb* grows uninhibited during this initial innate immune response; specifically, *M.tb* has evolved multiple environmental manipulation mechanisms (e.g., constitutive expression of stress-adaptive genes, changing the environment for its benefit), which allow for this rapid growth.[9] Avoiding these mechanisms of lysosomal damage and degradation (e.g., oxidation, acidification, hypoxia, nitrosative stress, and poor nutrition) aid in the formation of phagosomes, an environmental niche *M.tb* has adapted

to survive in. Because the macrophage-mediated innate immune response can result in cell necrosis, apoptosis, and survival of the infected macrophages, *M.tb* uses its virulence factors to optimize spread between host cells. By hijacking mechanisms controlling necrotic cell death, which results in cell lysis, *M.tb* can spread into other macrophages or immune cells. The immune system uses cell apoptosis as a mechanism to contain *M.tb* bacteria, since it does not lyse infected cells. Therefore, by preventing host cell apoptosis, *M.tb* can shift host cells towards non-apoptotic death pathways that allow greater bacterial spread. When enough dendritic cells are infected throughout this process, the adaptive immune response can be initiated.[9, 10]

TB infection (LTBI)

The 90% of individuals infected with *M. tuberculosis* that never develop an active infection have LTBI, or TB infection, though these carriers of remain *M.tb* reservoirs for reactivation of *M.tb* and progression if not treated (**Figure 1.2**). These individuals cannot spread TB bacteria and are not an active contributor to disease spread unless their infection is reactivated[11]

Current information about TB infection was primarily obtained from animal studies, though some human studies provide insight into the complex immune response to *M.tb* infection.[10] The onset and efficacy of the adaptive immune system determine if an individual develops LTBI. Infected dendritic cells are responsible for presenting live mycobacteria to naïve T-cells after migration to the lymph nodes; this process is delayed compared to the immune response in other infections.[9, 12] Antigen-specific CD4+ T-cell responses take an average of 11-14 days longer than expected in mice.[13, 14] It is hypothesized that TB infection inhibits the dendritic cell migration necessary for T-cell activation.[13-15] This delay is also measurable in humans, with a first measurable immune response through tuberculin skin testing (TST) averaging 42 days post-infection.[10]

Once this adaptive immune response begins, bacterial growth is inhibited. During this time, some patients experience temporary symptoms of TB disease, including fever and erythema nodosum.[7, 10] The adaptive immune response arrests bacterial growth through the accumulation of effector CD4+ and CD8+ T-cells in the lungs. Release of interferon-gamma (IFN-γ) from activated T-cells plays a crucial role in protection against TB. Tumor necrosis factor-alpha (TNF-α) produced during macrophage, dendritic cell, and T-cell activation is also essential in TB protection.[9, 10, 16] Studies in mice show that although there is a plateau in *M.tb* cell growth during this time, the T-cell responses are not enough to clear the infection completely.[17] In addition, studies in nonhuman primates demonstrate

the accumulation of genetic mutations in *M.tb* during latency.[18] Together, these data provide evidence that LTBI is not a state of stasis but a dynamic equilibrium between the host immune system and *M.tb*.

Pulmonary TB

Around 5% of individuals infected with *M.tb* will have inadequate T-cell responses, failing to establish latency as described. IFN-γ and TNF-α are critical immune factors that play a role in ATB development, and having an insufficient inflammatory response is known to increase the risk of ATB development. It is well established that susceptibility to TB infection is inversely associated with CD4+ T-cell counts, with low cell counts often seen in individuals with untreated HIV.[9] Patients on TNF-α inhibitors are also at increased risk of infection due to insufficient immune response. In addition, a significant amount of pathology, such as bulk tissue necrosis, seen in ATB disease is a result of collateral damage from the host immune system's attempt to control infection through the release of TNF-α, reactive oxygen species, nitrogen intermediates, granzymes, perforin, and other cytotoxic species.[7, 10, 16, 19]

Approximately 5% of individuals with LTBI will transition to ATB disease within their lifetime following the period of latent infection, known as reactivation.[12] While the exact process is unknown, two known immune mechanisms can explain some, but not most, cases of *M.tb* reactivation, which parallel the same immunodeficiencies that increase the risk of ATB development; these are changes in both quantity and quality of T-cell responses, most often due to old age, cancer, or HIV infection, or changes in TNF-α responses, most often due to old age or individuals using TNF-α inhibitors for other medical conditions.[10]

With primary infection, where individuals develop ATB in the weeks following exposure, infections are often located in the middle and lower portion of the lungs, exhibiting opacities and enlargement of the lymph nodes in the chest upon imaging. Patients with reactivation after years of latency often have lesions in the upper lungs that show cavities, fibrotic scar tissue, or opacities and are more likely to have localized disease.[7, 20]

The formation of granulomas or tuberculomas in the lungs is characteristic of patients with active pulmonary disease, though there is little information on the exact mechanisms through which they develop. Three types of granulomas form in pulmonary TB patients: (**1**) non-necrotic, (**2**) caseous or necrotic, or (**3**) cavitary, which is considered part of end-stage TB.[7, 16] These granulomas can be solid or liquid, and the degree of liquefaction may impact disease progression. The caesium inside the granulomas consists of a mixture of immune cells and debris,

with macrophages phagocytizing *M.tb* and creating necrotic cores; *M.tb* grows most densely at the periphery of the necrotic core.[16] Solid granulomas are thought to more efficiently contain the infection and yield decreased viability for *M.tb* growth and survival. Liquid granulomas can potentially burst and aspirate into other parts of the lungs, which transmits to new hosts once coughed up.[20] Though *M.tb* can influence the formation of granulomas, there are clear benefits to granuloma formation for both the host and *M.tb*.[7, 16, 21] If enough tissue damage occurs from granuloma formation, cavities can form, creating an environment where bacteria can multiply uncontrollably.[22]

Up to 70% of pulmonary TB patients will transition to cavitary disease due to the spread of liquid caesium from granulomas. With the exponential growth of *M.tb* in the formed cavities, bacteria counts can be as high as 10^{11} bacilli/g, making these patients highly infectious.[10, 22] Patients with cavitating disease are also at higher risk for disease relapse following treatment because of difficulty delivering antibiotics to the center of the TB-filled cavity.[22]

Extrapulmonary TB

Some individuals (10-42%) will develop TB disease in other parts of their body, known as disseminated disease or extrapulmonary TB. Extrapulmonary TB can form in any body organ but is most common in the lymph nodes, followed by pleural infection.[23] The exact mechanism through which disseminated disease occurs is unknown. However, it is known to spread hematogenously.[24] It is hypothesized that an inadequate effector T-cell response fails to contain *M.tb* bacteria.[25] Knowing that dendritic cells transport live *M.tb* to lymph nodes for T-cell activation, it has been hypothesized that this translocation is additionally beneficial for *M.tb* and is at least partially responsible for the development of some cases of extrapulmonary TB[26] Disseminated disease can also present as miliary disease, which consists of innumerable lesions 1-3 mm in diameter throughout the body. Without treatment, 50-80% of patients with extrapulmonary TB do not survive.[25, 27]

Signs and Symptoms of TB Infection

Patients with LTBI display no symptoms of infection. Patients with active pulmonary TB display symptoms consistent with other chronic respiratory diseases, including persistent cough (>3 weeks), fever, fatigue, dyspnea, chills, or night sweats. Patients with active disease may also present with unintentional weight loss, loss of appetite, and coughing up blood or bloody mucus.[8]

In individuals with disseminated disease, patients display clinical features specific to the infected organ system. For example, patients can present with anemia, including leukopenia and pancytopenia, high erythrocyte sedimentation rate, abnormal liver function tests, ascites, hepatomegaly, jaundice, splenomegaly, delirium or psychosis, convulsions, meningism or encephalitis, skin infection or other signs of dermatologic disease, diarrhea, vomiting, pleural effusion, lymphedema, or regional pain in addition to pulmonary TB symptoms.[16, 23, 27]

Individuals with specific comorbidities are at increased risk for developing or reactivating TB disease beyond living in countries with high TB caseloads. HIV infection is the single most significant risk factor for the development of TB,[9] and relevant comorbidities are:

- Primary (e.g., cystic fibrosis, autoimmune disease) or secondary (e.g., HIV/AIDS, immunosuppressive therapy) immunodeficiency. [28]
- Chronic lung disease, exposure to significant pollution, or use of tobacco products.[29]
- Have chronic diseases such as diabetes mellitus,[29] kidney disease, or hepatitis. [28]
- Individuals living in close quarters or communal living situations – prison inmates, homeless or living in homeless shelters, nursing home residents.[30]
- Alcohol (> 40 g/day)[29] and intravenous drug users.[30]
- Malnutrition.[31]
- Health care workers.
- Close contact with an individual with ATB disease.

TB Treatment and Prevention

Antibiotic chemotherapy

Treatment for TB varies based on the kind of infection but is known for taking months or years to treat completely. Life-altering side effects from treatment (e.g., orange discoloration of body fluids, gastrointestinal symptoms, hepatotoxicity, liver failure, peripheral neuropathy, central nervous system effects, polyarthralgia, gout)[30] and extensive treatment time (at least six months) result in patients stopping antibiotic treatment before completing therapy; this is the primary cause of antibiotic-resistant TB.[32] For this reason, it is recommended that these patients use directly observed therapy (DOT) as part of treatment. DOT uses trained healthcare workers or other designated

individuals outside of the patient's family to provide TB antibiotics and observe the patient taking the drug(s). Compared to self-observed therapy, DOT can increase treatment completion from 61% to ~88%.[33] With smartphones and cellular phone and data services available globally, smartphone-enabled video-observed therapy is more effective than DOT,[34] and is recommended by WHO as an alternative to DOT.[35]

For LTBI, there are four CDC-recommended treatment regimens for LTBI, which use isoniazid (INH), rifapentine (RPT), and rifampin (RIF). Studies by CDC and the National Tuberculosis Controllers Association recommend short-course (3-4 months) treatments using multiple antibiotics in place of INH monotherapy (6-9 months) when possible, though many parts of the world still use INH monotherapy for LTBI treatment. The four treatment regimens recommended by CDC are listed in **Table 1.1**.[11]

Table 1.1. CDC Recommended LTBI Treatment Regimens.[11*]

Drug(s)	Duration[†]	Dose	Frequency	Total Doses
INH and RPT	3 months	> 12 years: INH: 15 mg/kg rounded up to the nearest 50 or 100 mg; 900 mg maximum RPT: 10-14 kg: 300 mg 14.1-25 kg: 450 mg 25.1-32 kg: 600 mg 32.1-49.9 mg: 750 mg >49.9 kg: 900 mg maximum	Once Weekly	12
		Aged 2-11 years: INH: 25 mg/kg RPT: as above		
RIF	4 months	Adults: 10 mg/kg Children: 15-20 mg/kg Maximum dose: 600 mg	Daily	120
INH and RIF	3 months	Adults: INH: 5 mg/kg; 300 mg maximum RIF: 10 mg/kg; 600 mg maximum	Daily	90
		Children: INH: 10-20 mg/kg; 300 mg maximum RIF: 15-20 mg/kg; 600 mg maximum		
INH	6 months **9 months**	Adults: 5 mg/kg Children: 10-20 mg/kg[‡] Maximum dose: 300 mg	Daily	180 **270**
		Adults: 15 mg/kg Children: 20-40 mg/kg[‡] Maximum dose: 900 mg	Twice weekly	52 **76**

Individuals with drug-susceptible TB are treated with a combination therapy consisting of INH, RIF, ethambutol (EMB), and pyrazinamide (PZA). Treatment of drug-susceptible TB has some of the same challenges as LTBI treatment, namely that the treatment is lengthy (at least 6-9 months), and some patients experience significant side effects that make treatment difficult. There have been clinical trials to try and reduce the treatment time[36, 37]

[*] *Table adapted from cited reference.*

[†] *Minimum interval/duration.*

[‡] *American Academy of Pediatrics recommends INH at 10-15 mg/kg for the daily regimen and 20-30 mg/kg for the twice-weekly regimen.*

though it extended regimens are more successful and have lower recurrence rates.[30] Patients with HIV or cavitary disease are not eligible for shorter dosing regimens due to high failure rates and increased acquired drug resistance rates. The four treatment regimens recommended by CDC are listed in **Table 1.2**. Drug-susceptible regimens are listed in order of most to least effectual, with Regimens 3 and 4 not advised for use in patients with HIV or cavitary disease.[30]

Table 1.2. CDC Recommended Antibiotic Regimens for Drug-Susceptible TB Disease.[30*]

	Intensive Phase			Continuous Phase			
Regimen	Drugs	Dose (mg/kg)	Interval[†]	Drugs	Dose (mg/kg)	Interval	Total Doses
1	INH	Adult: 5 Child: 10-15	7 doses/week x 8 weeks[§]	INH	Adult: 5 Child: 10-15	7 doses/week x 18 weeks[§]	182
	RIF	Adult: 10 Child: 10-20		RIF	Adult: 10 Child: 10-20		
	PZA	Adult: 25 Child: 35					
	EMB	Adult: 15-20 Child: 15-25					
2	INH	Adult: 5 Child: 10-15	7 doses/week x 8 weeks[§]	INH	Adult: 15 Child: NE[**]	3 doses/week x 18 weeks	110
	RIF	Adult: 10 Child: 10-20		RIF	Adult: 10 Child: NE[**]		
	PZA	Adult: 20-30 Child: 30-40					
	EMB	Adult: 15-20 Child: 15-25					
3	INH	Adult: 15 Child: NE[**]	3 doses/week x 8 weeks	INH	Adult: 15 Child: NE[**]	3 doses/week x 18 weeks	78
	RIF	Adult: 10 Child: NE[**]		RIF	Adult: 10 Child: NE[**]		
	PZA	Adult: 30-40 Child: NE[**]					
	EMB	Adult: 25 Child: 15-25					
4	INH	Adult: 5/15 Child: 10-15/25	7 doses/week x 2 weeks followed by 2 doses/week x 6 weeks	INH	Adult: 15 Child: 25	2 doses/week x 18 weeks	62
	RIF	Adult: 10 Child: 10-20		RIF	Adult: 10 Child: 10-20		
	PZA	Adult: 25/50 Child: 35/50					
	EMB	Adult: 15-20/25 Child: 50					

There are multiple forms of antibiotic-resistant TB, and classification is essential for determining the most effective treatment. Antibiotic resistance is classified as:

- Monodrug-resistant TB - resistance to a single anti-TB drug, which includes:[29, 38]
- Rifampin-resistant TB (RR-TB).

[§] *In cases where DOT is used, five dosages/week may be substituted.*

[**] *NE = Not established. Some experts use the adult dosage for older children, and the same dose as twice-weekly therapy for younger children.*

- Isoniazid-resistant.
- Polydrug-resistant - resistant to more than one anti-TB drug, but not both RIF and INH.[29, 38]
- Multi-drug resistant TB (MDR-TB) - resistant to both RIF and INH.[29, 38]
- Pre-extensively drug-resistant (pre-XDR-TB) - MDR-TB plus resistance to one fluoroquinolone or a second-line injectable.[29, 38]
- Extensively-drug resistant TB (XDR-TB) MDR-TB plus resistance to at least one fluoroquinolone and a second-line injectable agent.[29, 38]
- Incurable strains of TB.[39]

Culture on selective media and drug susceptibility assays are used to determine antibiotic resistance. There are numerous possible combinations of drug resistance, making exact treatment regimens highly personal and complicated. In cases of MDR-TB, it is not uncommon for treatment to last longer than 18 months.[29, 38]WHO provides drug groups in order of priority for use in treating MDR-TB and XDR-TB and gives recommendations on when shorter courses of treatment are appropriate, such as during pregnancy. Of the groups of drugs, WHO recommends treatment starts with all three Group A drugs (levofloxacin or moxifloxacin, bedaquiline, linezolid) and at least one Group B drug (clofazimine, cycloserine, or terizidone). If fewer Group A drugs are used, both Group B drugs can be used. Suppose there are not enough medications between Group A and B for treatment. In that case, doctors may move to Group C drugs (EMB, delamanid, PZA, imipenem-cilastatin or meropenem, amikacin or streptomycin, ethionamide or prothionamide, *p*-aminosalicylic acid).[40]

WHO also provides a list of recommendations for treatment approaches to antibiotic-resistant strains of TB in addition to the guidelines for selecting antibiotics to begin treatment. Though not exhaustive, key recommendations include:[29]

- Regimens should generally include at least four drugs likely to be effective in the first six months, followed by three drugs after that, with oral medications preferable to injectable medications.[29, 40]
- Fluoroquinolones are strongly recommended for treatment times longer than six months.[29, 40]
- MDR-TB and XDR-TB regimens should be monitored monthly using cultures, rather than just sputum smear microscopy.[29, 40]

Additional therapeutic considerations

Treatment of TB can be multifaceted, and there are considerations beyond the antibiotic regimen that should be considered throughout treatment. For individuals with TB that are HIV-negative, it is routine to test for HIV since it is the most significant contributing factor to ATB disease development.[8] For those with confirmed HIV, patients must be on antiretroviral therapy for HIV to reduce the impact of immunosuppression due to infection. For other comorbidities, patients must be adequately treated for these conditions to ensure the best chance at treating *M.tb* infections.[30, 31]

It is also well established that rifamycins can significantly impact the concentrations of other drugs, and medications used for these conditions may need to be adjusted or completely changed for the duration of TB treatment. A significant number of antiretroviral drugs used in the treatment of HIV are significantly reduced in concentration when administered concurrently with rifamycins, and dosages may require increasing to account for the impact the TB treatment has on HIV management. Other drugs negatively impacted by co-administration of rifamycins include:[30]

- Anti-effectives, including azole antifungal agents, some macrolide antibiotics, and mefloquine.
- Hormone therapy, such as birth control, tamoxifen, and levothyroxine.
- Methadone.
- Warfarin.
- Immunosuppressive agents, including cyclosporine and corticosteroids.
- Anticonvulsants phenytoin and lamotrigine.
- Cardiovascular agents, including anti-hypertensive drugs, Angiotensin-converting enzyme inhibitors, antiarrhythmics.
- Sulfonylurea hypoglycemics.
- Hypolipidemics.
- Psychotropic drugs, including nortriptyline, haloperidol, and benzodiazepines.

For treatment of TB, additional medications may be beneficial or help patients continue treatment long-term. For example, in patients that experience or are at risk for peripheral neuropathy, vitamin B6 is administered with INH.[41] Corticosteroids have shown mortality and morbidity benefits is recommended that they be administered

concurrently in patients with high levels of inflammation in the pericardial fluid of patients with large effusions or signs of pericardial restriction.[30]

TB vaccine

In countries with high TB caseloads, newborns are inoculated with the TB vaccine, known as the BCG vaccine. This vaccine is an injection of *M. bovis* Bacillus Calmette–Guérin (BCG), an attenuated strain of *M. bovis*. This vaccine is the only licensed TB vaccine.[42] The protective efficacy is variable, with studies showing anywhere from no effectiveness to 80% efficacy against pulmonary TB.[43] The vaccine's efficacy varies between studies based on genetics, geographic location, exposure to other environmental bacteria,[44] and laboratory conditions used to grow BCG for the vaccine.[45] BCG does significantly protect children from developing TB meningitis and miliary disease[46] and is therefore administered to approximately 100 million newborns per year across the world in countries with high case rates of TB.[46] It is also administered prophylactically in select individuals living where TB case rates are low, such as healthcare workers.[47]

Diagnostic Strategies Not Recommended for POC Use in Low-resource Settings

Chest X-ray

Mass screening for TB by chest X-ray has previously proved an effective tool in the developed world and can still triage potential ATB patients by visualizing potential cavities, fibrosis, and calcifications in the lungs. However, accuracy is highly variable because it requires experienced interpreters to read the images, individuals that are difficult to come by across most of the globe.[2] As a result, some countries, such as the high-burden country South Africa, have discontinued it due to costs and the low diagnostic yield. Because in a generalized TB epidemic where repeat infection is common, the inability of chest X-rays to distinguish previous from current episodes of TB is problematic and complicates radiographic interpretation. This, together with the vast reservoir of latent TB infection and the recognized radiation dose problems associated with repeat testing by X-ray, has led WHO to specifically call for the development of new mass screening tools for TB to replace radiography.[48]

Measurement of host immune response

Two main biomarker-based tests are available in countries with advanced healthcare and low TB caseloads, and these tests measure the immune response in patients to determine if a patient has TB. Tuberculin skin testing (TST, or Mantoux test) is the most common TB screening tool used in the United States. The test consists of an intradermal injection of tuberculin purified protein derivative in the forearm, and the immune system's reaction to the antigen mixture is monitored and recorded. Unfortunately, individuals that have previously received the TB vaccine can have false-positive test results. Furthermore, in individuals that have received the TB vaccine, the size of the TST reaction is not a factor in determining if an individual has LTBI or if the response is due to prior vaccination. This complicates treatment decisions, especially when other tests are unavailable, so TB is often diagnosed empirically and based primarily on symptomology alone. TSTs also require patients to return to the physician's office 48-72 hours after the initial injection for the test reading, making this test not implementable at the POC, where patients are routinely lost to follow-up and never return.

Within the last decade, interferon-gamma (IFN-γ) release assays (IGRA) have been available as a diagnostic tool in high-resource countries, with examples including the QuantiFERON® TB-Gold In-Tube test and T-SPOT®.*TB*.[49] These whole-blood assays measure the white blood cell response to TB-specific antigens. In patients infected with *M.tb*, white blood cells will release IFN-γ when mixed with the antigens derived from *M.tb*. Unlike the TST, prior BCG vaccination will not cause a false-positive result.[50] Often, blood for IGRA tests is collected only in the morning since the assay itself has a 24 hour incubation time, followed by the final assay protocol and readout. With a minimum time to completion of two days, this method is incompatible with POC diagnosis.

Both TST and IGRA tests are beneficial in helping diagnose both LTBI and ATB disease. However, these tests are unavailable in low-resource countries or are incompatible with some patient histories due to independent infection treatment and prevention factors. Therefore, individuals living in parts of the world with limited healthcare infrastructure have no method to diagnose LTBI.

Bacterial culture

In the absence of reliable biomarker-based POC diagnostic tests for TB, the gold standards for accurate TB diagnosis and drug sensitivity testing continue to rely on microscopic pathogen detection in sputum smears with

diagnostic confirmation and drug sensitivity testing using bacterial culture methods. However, the extensive time and infrastructure barriers required to implement culture are too slow for use at point-of-care, as time-to-result is at least three to four weeks, but up to eight weeks. In addition, it is well established that difficulties in replicating growth conditions in vitro result in the estimate that 99% of all bacteria cannot be cultured using standard culture protocols, *M.tb* included. This likely leads to gross under-estimations of bacillary loads from culture analysis, especially in drug-treated TB patients.

The Current State of Low-resource POC TB Diagnostics and Why They Fail Patients

Problem 1: Currently implemented nucleic acid-based tests are inefficient for rapid POC TB diagnosis.

WHO has endorsed the polymerase chain reaction (PCR)-based GeneXpert MTB/RIF assay as a frontline diagnostic and drug resistance test for TB in endemic settings.[51] The Xpert MTB/RIF assay consists of a self-contained cartridge that performs automated sputum extraction and nucleic acid amplification following insertion into the specialized Xpert Instrument System.[52] Unfortunately, Xpert possesses significant limitations that hinder its capacity to serve as a comprehensive screening tool. First, its claimed detection limit at ~130 *M.tb* bacilli/mL[53] is closer to ~800 *M.tb* bacilli/mL in practice as determined through external validation.[54] Additionally, Xpert cannot quantify bacillary load or monitor early bactericidal activity, which is critical for monitoring patient treatment response.[55] It is also ineffective for monitoring or diagnosis in drug-treated patients.[56] These factors combined with its relative expense (~$15/test, even with subsidies) have resulted in a low global implementation rate, even though it was designed for low-resource POC use. Most importantly, case detection has not significantly improved with the rollout of Xpert.[57] The true benefit of the Xpert MTB/RIF assay, therefore, appears to lie in its more rapid, albeit limited, rifampicin resistance testing capabilities than culture.

Despite these limitations, the South African Department of Health has implemented 325 Xpert devices nationwide to diagnose TB using the MTB/RIF assay, making it the largest procurer of such devices worldwide. Unfortunately, these devices are predominantly located in 203 centralized testing labs or tertiary health care facilities in densely-populated urban areas (**Figure 1.3**).[57] In contrast, most of the South African population still lives in rural, sparsely-populated regions.[58] Inaccessibility of Xpert for rural TB suspects requires that patient sputum specimens be shipped from remote clinics to testing centers, imposing a lengthy turnaround time (days to

weeks) for a diagnostic test that should only take two hours. This exacerbates pre-treatment loss to follow-up rates. Therefore, empiric treatment without molecular diagnosis or bacteriologic confirmation remains commonplace.[2, 4]

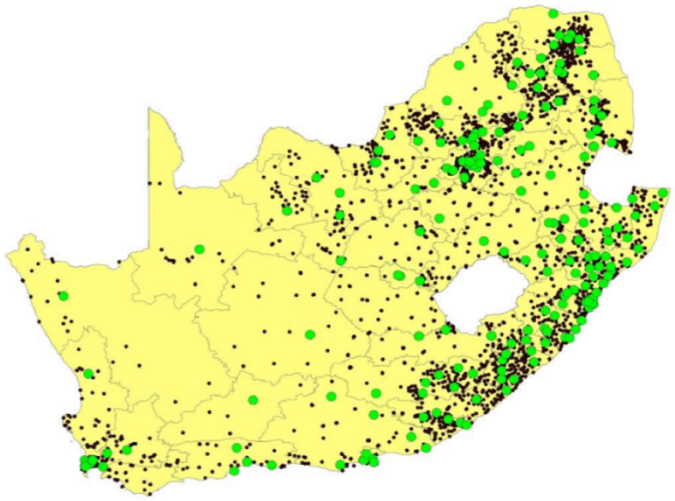

Figure 1.3. GeneXpert MTB/RIF testing center locations, indicated by large green dots, and Department of Health Facilities, indicated by small black dots, in South Africa in 2019. Figure adapted from cited reference.[59]

The inability to rapidly and accurately diagnose TB disease and evaluate resistance with high sensitivity and specificity at the POC continues to be a confounder in disease transmission, patient mortality and morbidity, and time to treatment initiation in the developing world; this is a significant barrier to effective medicine for TB.

Problem 2: Microscopy limits TB diagnosis.

With the advent of nucleic acid amplification tests, the century-old microscopic examination of a sputum smear is in danger of being forgotten. Still, it remains the most commonly used method for TB diagnosis outside of a laboratory environment in the developing world. Sputum smear staining for microscopy has the advantage of having high clinical specificity (>99%) while being inexpensive and easy to perform. Unfortunately, these advantages do not overcome the poor clinical sensitivity (~50%), subjectivity, and laboriousness. Manual inspection of stained sputum smear slides can take 15 minutes to three hours, depending on the degree of infection and the microscopist experience.[60] Understaffed and busy clinics that still rely on smear inspection are particularly prone to false negatives resulting from the improper examination of smears.[61]

There has been substantial effort to develop fluorescence microscopy and sample concentration-based methods to overcome the limitations of bright-field microscopy.[62-66] In both protocols, bacteria are isolated from large-volume sputum samples using polymer-coated beads or centrifugation and paired with fluorescence microscopy as the readout (**Figure 1.4**). While promising, and even though literature supports that increasing the sputum sample volume can increase diagnostic sensitivity,[67] both concentration methods have failed to yield the hoped-for improvements in clinical performance because of their lack of molecular specificity. However, the minimal adoption of these protocols extends beyond their lack of specificity, as they use more complex and time-intensive procedures than conventional microscopy with ZN staining. Furthermore, these concentration protocols are followed by staining with dyes known to bind to Actinomycetes, bacteria that inhabit the mouth and commonly contaminate sputum samples through saliva, not just *M.tb*. As a consequence, these methods show only mild improvements in clinical sensitivity (e.g., ~65% for magnetic bead FM; ~59% for centrifugation with direct FM),[68] but reduced specificity (e.g., ~89% for magnetic bead FM; ~99.4% for centrifugation with direct FM)[68, 69] In addition, these methods' reliance on fluorescence microscopy, a technology that is generally unavailable in primary clinics in countries with limited healthcare infrastructure, creates another barrier to adoption and implementation.[61]

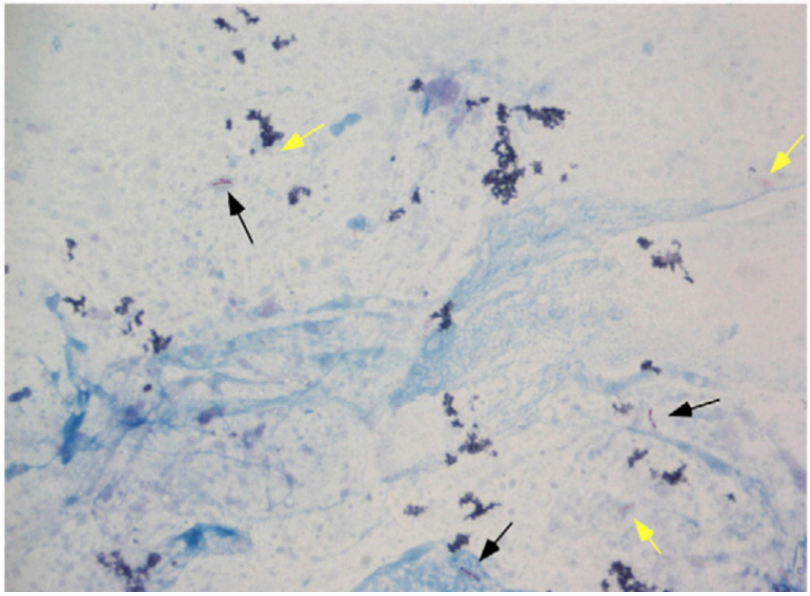

Figure 1.4. Image of a sputum smear for TB diagnosis. Black arrows indicate confirmed TB bacilli. Yellow arrows indicate TB bacilli that cannot be accurately detected with bright-field smear inspection and instead require fluorescent stain/imaging for accurate observation. Figure from cited reference.[70]

Problem 3: There is no method to determine if an infection is caused by tuberculous or non-tuberculous mycobacteria.

Acid-fast staining works by taking advantage of the almost impenetrable mycobacterial cell wall. As shown in **Figure 1.5**, it continues to be performed just as it was at the turn of the 20th century.[71] Specifically, the thick and waxy cell wall is primarily comprised of long-chain fatty acids known as mycolic acids. This mycolic acid makes the walls challenging to open, so they are physically melted using heat.[71, 72] Therefore, to stain mycobacteria, the primary carbol fuschin dye is applied to the sample and heated over a flame until steaming. Once cool, acid-alcohol removes primary pigment from inside cells that can be readily penetrated with chemicals. This rinse decolorizes everything except for mycobacteria. These easily penetrated cells are then counterstained with methylene blue, turning everything that is not mycobacteria (or acid-fast) blue.[71]

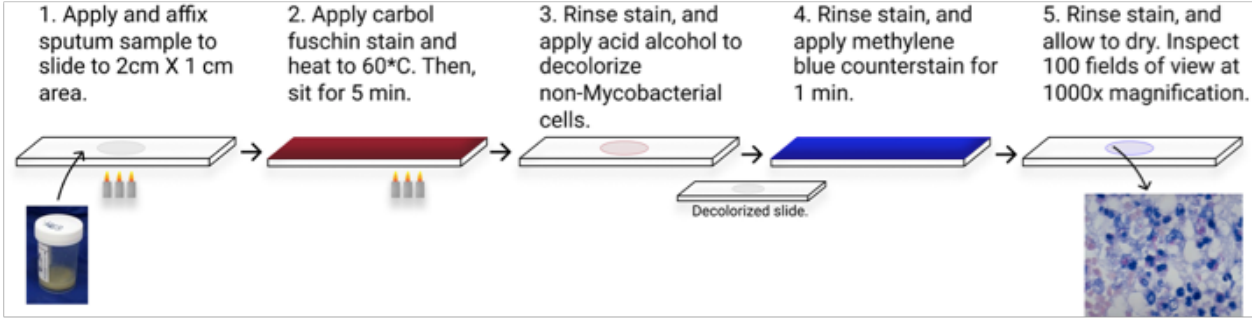

Figure 1.5. Acid-fast staining protocol for clinical identification of *M.tb* in sputum using the Ziehl-Neelsen method.

While acid-fast staining is generally quite specific for identifying if a patient has a mycobacterial infection, it cannot tell the microscopist what species of mycobacteria is causing the infection.[73] This well-documented observation has been known for over a century.[74] Because the staining process relies only on if cells are decolorized with acid-alcohol, which occurs for all mycobacterial species, it means that there is no way to discern which mycobacterial species are causing an infection. Tuberculous mycobacteria (species that cause TB disease) and non-tuberculous mycobacteria (NTM; species that do not cause TB disease or leprosy but may cause other clinically significant infections) both cause pulmonary infections and both present independent clinical challenges for patients.

NTM infections present significant morbidity and mortality across the globe.[75] Infections caused by tuberculous mycobacteria and NTM present with similar symptomology,[76, 77] are both opportunistic infections

common in TB-endemic countries and target similar populations: immunocompromised, elderly, impoverished, and those with abnormal lung pathologies, among others.[75] However, NTM pulmonary infections are seen in previously healthy individuals and are on the rise in developed nations.[78] In the United States in 2010, the number of NTM infections outnumbered the number of TB cases.[79] The two diseases have different antibiotic treatment regimens, making it imperative that patients start on the correct treatment as soon as possible.[75]

Because NTM infections are not as well studied or characterized as infections caused by TB disease-causing *M.tb* complex species (*M. tuberculosis*, *M. bovis*, *M. bovis* BCG, *M. africanum*, *M. microti*, *M. canetti*, among others), determining the difference between TB disease and an NTM infection relies on culture protocols. Widely used molecular TB diagnosis techniques, such as Xpert, cannot determine if a patient has an NTM infection.[80] However, for the same reasons that culture does not work well for TB diagnosis, it also does not work well for NTM diagnosis. Therefore, particularly in developing nations with high TB case rates, NTM infection is more likely to remain unidentified due to (**1**) a higher probability of TB infection and (**2**) a lack of diagnostic resources. As discussed, these patients are diagnosed and treated based on symptoms alone without bacteriologic confirmation.[2, 4] This delay in NTM infection treatment averages two years,[81] and often results in permanent lung damage, loss of lung function, and death.[82] These issues result in care gaps, where patients often have poor treatment success, especially compared to TB disease.[83] Immunocompromised individuals are more likely to be negatively impacted by these care gaps. Creating a POC tool to discriminate between tuberculous and NTM infections simultaneously is critical for improved patient care and outcomes for both types of infection.

Design Requirements for an Improved TB Diagnostic

In 2000, the WHO published a set of criteria for an ideal POC test designed for use in healthcare-limited settings to help drive disease diagnosis and treatment. They are known as the ASSURED criteria, which is an acronym for **A**ffordable (for those who need it, generally no more than £1-5), **S**ensitive, **S**pecific, **U**ser-friendly (simple to perform, requiring minimal training), **R**apid and/or **R**obust (delivers results in 15-60 minutes), **E**quipment-free, and **D**eliverable to those who need them.

Based on the ASSURED criteria, in the context of this dissertation, the required design criteria for developing sensitive and specific POC assay for *M.tb* diagnosis are:

- Requirement 1: **S**pecificity for tuberculous mycobacteria and ability to discriminate between NTM and TB infections without loss of **S**ensitivity.
- Requirement 2: **U**ser-friendly and **R**apid and **R**obust *M.tb* biomarker collection and concentration protocol.
- Requirement 3: **U**ser-friendly *M.tb* assay readout with minimal background interference and easy to interpret results.
- Requirement 4: Detection strategies that are **E**quipment-free or implement existing technology and methods already **D**elivered and performed as part of the current diagnostic workflow.

This dissertation aimed to design and test new tools for a next-generation, point-of-care diagnostic test for TB that technically performs as well as the Xpert MTB/RIF assay (~85% sensitivity, ~95% specificity). Unlike the Xpert assay, the approaches discussed in this dissertation require minimal resources and utilize only widely available or easily acquired equipment (e.g., magnets). Improving the current methodology will enable active case finding where the population lives, decreasing the time to diagnosis and treatment relative to disease onset. Though the assays developed here would ideally meet the criteria for **A**ffordability, the total cost per test is often higher during small-scale development, and cost reduction occurs with further technical refinement and mass production. For this reason, the price per test was not explicitly included as a design requirement but is discussed in the broader context of the assay design and future potential.

Proposed Solutions

Proposed Solution 1: Nucleic acid extraction towards a POC solution for molecular diagnosis.

Rapid isolation of genomic material from patient samples can provide sensitive and specific semi-quantitative testing for *M.tb* and detection of drug-resistant strains. Using a chaotropic binding solution, nucleic acids are preferentially adsorbed to the surface of silica magnetic beads while leaving behind non-genomic material (**Req. 1**). These magnetic particles are then quickly concentrated volumetrically using magnetic separation (**Req. 2**) and eluted into small volumes (**Req. 3**), which are ideal for quantitative analysis using established molecular techniques (**Req. 4**).

Magnetic separation for biomarker recovery is not a new concept, and kits are commercially available. However, the most commonly used format for magnetic beads separation has drawbacks that limit its application. This approach uses stationary magnets to create a low-gradient magnetic field across an entire sample volume to separate beads. Since magnetic fields decay from the magnet surface at a rate of $1/L^3$, the magnet must be sufficiently strong to quickly concentrate beads in the low-gradient field. Sub-micron scale particles used in these applications increase the biomarker capture area. However, without further tuning of the magnetic field and nanoparticle chemical properties, the stationary application of a magnet for separation is slow and not amenable for use in time-sensitive assays.[84] Using this method in low-resource settings is also labor-intensive. It requires the manual removal and application of reagents throughout the extraction process, only allowing for low-throughput sample processing.[85] These challenges preclude application issues for large and dilute volume samples (e.g., urine), which require processing with parallel aliquots or in series.

To solve the issues associated with manual extraction protocols using traditional magnetic separation, in Chapter 3, I developed and applied an alternative form of magnetic separation known as high-gradient magnetic separation (HGMS). HGMS is rapid and not limited by sample volume, extracting and concentrating the naturally dilute quantities of nucleic acids from large volumes into useable test samples. This nucleic acid extraction protocol enabled by HGMS does not require user training and is not reliant on laboratory equipment with limited accessibility (e.g., GeneXpert, refrigeration, centrifugation). Developing the HGMS extraction device is a step towards molecular testing at the POC, which will reduce time barriers that currently exist. While the HGMS device is applied for nucleic acid extraction, the system is versatile and can be modified for specific isolation and detection of other biomarkers, including proteins or whole cells (**Req. 1**).

Proposed Solution 2: Combined volumetric and spatial concentration of M.tb *bacilli using induced Marangoni flows for improved sputum smear detection of TB disease.*

Isolation of *M.tb* from patient sputum would provide a method to create a more sensitive and specific microscopic inspection strategy. Various methods nonspecifically concentrate TB bacteria, trying to improve the sensitivity of sputum smear microscopy, but it has only led to mild improvements while also reducing the specificity.[62-66] To solve issues with microscopic inspection, in Chapter 4, I used nanoparticles to magnetically separate *M.tb* bacilli from large-volume samples and volumetrically concentrate them. The nanoparticle-bacilli

complexes were then deposited in a 50 μL droplet onto a substrate-coated glass microscope slide and visualized using bright-field microscopy (**Req. 3**). This substrate was explicitly designed to induce spatially concentrating Marangoni flows during droplet evaporation through concentration in the center of the drop, dramatically reducing the inspection area and, therefore, time for microscopic inspection. (**Req. 4**) Using nanoparticles smaller in diameter than the diffraction limit of light yields a capture medium that does not significantly interfere with bright-field microscopic visualization.

Proposed Solution 3: Screening of M.tb-*specific surface antigen recognition elements.*

Using biolayer interferometry, in Chapter 5, I screened newly available mycobacterial biomarker lipoarabinomannan (LAM) recognition elements (**Req. 1**), including antibodies and novel lectin microvirin-N (MVN). Specifically, *M.tb* complex and NTM species have different sugar caps on this cell surface marker, LAM, with slow-growing *M.tb* complex (MTBC) species expressing LAM with a terminal mannose cap (ManLAM), and fast-growing NTM species express LAM with a terminal phosphatidylinositol cap (PILAM). MVN is known to bind specifically to the mannose linkages on ManLAM.[86] In addition, LAM makes up 15% of the total mycobacterial cell surface mass,[87] making it an abundant biomarker for use in TB detection assays.

Once characterized for ManLAM/PILAM specificity, I used these LAM recognition elements to measure changes in the surface accessibility of LAM from different mechanical and enzymatic processing methods. Though mundane, the well-known clumping of mycobacteria in suspension culture continues to create problems for TB researchers, requiring the use of mechanical force,[88, 89] chemical,[90] or enzymatic[89] digestion methods to dissociate these clumps. The impact of processing on antibiotic susceptibility has been established, but detailed investigations about changes in the accessibility of surface structures are not available in the literature. I expect that this key information will interest many TB investigators seeking precise preparation methods that preserve as many surface-accessible biomarkers as possible.

Proposed Solution 4: Development of an M.tb-*specific nanoparticle for whole-cell capture and differentiation between MTBC and NTM infections at the POC.*

Chapter 6 detailed work towards designing and developing an *M.tb*-specific magnetic capture particle (**Req. 4**) surface-functionalized with novel lectin MVN (**Req. 1**). This chapter outlines the design optimization of

individual fluorescent components for flow cytometry readout, used to visualize individual binding interactions between different mycobacterial species, MVN, and nanoparticles using the size, granularity, and co-localization of fluorophores. However, significant challenges encountered throughout this design process created barriers to completion, all discussed. The research performed in Chapter 5 identified solutions to the primary problem encountered, and the issues and solutions are examined in tandem. Future work required for completion of the particle design is also outlined.

CHAPTER 2 : INTRODUCTION TO SCIENTIFIC PRINCIPLES AND PRIOR ART

The scientific principles and techniques that make up this dissertation's scientific focus are explained in this chapter, and prior art is discussed.

High-gradient Magnetic Separation

In the past few decades, magnetic separation techniques have been commonly applied for liquid sample processing in low-resource biomarker extraction assays.[91-94] Magnetic forces function independently of the sample's chemical and biological properties; this makes it an ideal phenomenon for analytical applications. Surface-functionalized paramagnetic beads have the additional advantages of remote handling and manipulation within a sample that, when combined with the high surface area, provide a method for chemical capture, purification, and concentration of biomarkers of interest.

HGMS is a technique that utilizes a ferromagnetic matrix that is converted into an induced magnet when exposed to an external magnetic field. This matrix creates strong field gradients near the matrix surface upon magnetic field application. When fluid containing paramagnetic particles flows through the matrix, magnetophoresis draws and magnetically captures beads on the matrix's surface via the high-gradient field (**Figure 2.1**). The matrix is demagnetized upon removing the external field, allowing for particle removal and recovery. Without the presence of the ferromagnetic matrix, using magnetic application alone, particle recovery is very poor. HGMS has multiple benefits over traditional magnetic separation using a stationary magnet; the most prominent is its capacity to separate sub-micron-sized magnetic particles from large sample volumes rapidly.

Clay processing.

The earliest description of a high-gradient magnetic separator dates to the 1930s, separating materials based on their magnetic susceptibilities. The patent highlights the potential importance of high gradient magnetic separation – at the time, magnetic separators were most commonly limited to a pulley, belt, and rotor-driven separators that failed to isolate magnetic material from fine dry powders, yielding inefficient separations. With the advent of an HGMS system, fine particles could now be efficiently separated from both dry mixtures and liquid suspensions.[95]

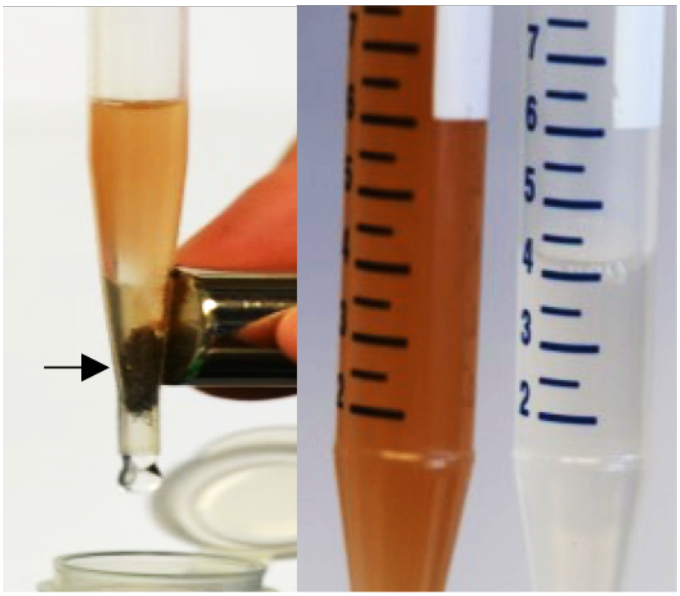

Figure 2.1. Example of high-gradient magnetic separation of one micron magnetic beads from a flow using a small steel wool plug (black arrow) and an external magnet (left panel); change in the appearance of a magnetic bead suspension after separation (right panel). Photo credit: Cassandra Wessely.

Use of the first commercial of HGMS began in 1969 with the beneficiation of kaolin clays used in paper coatings.[96] At the time, there was a desire to extend high-quality kaolin reserves. The use of crude or low-quality kaolin, followed by removal of impurities that cause darkening of the clay, would allow for this extension while also reducing the utilization of leeching chemicals used to brighten clays at the time.[97] It would also yield an increased monetary value for the clay due to improved brightness.[98]

The separators used for kaolin clay processing were capable of processing 4,000 liters (L) of kaolin slurry per minute, or 60 dry tons per hour, achieving a high-speed processing operation. The separators used a stainless-steel wool matrix magnetized by a 20-kiloGauss (kG) electromagnet. Processing the clay removed iron and associated contaminants, such as potassium and aluminum; removing just 1-2% of contaminants could increase the brightness by two to four brightness units, demonstrating how efficiently reducing clay contaminants can significantly improve the clay's quality.[97, 98] This advance combined five variables that made the use of large-scale high-gradient magnetic separation feasible: retention time, extreme gradients, high-intensity magnetic fields, electro-kinetic dispersion, and efficient magnet design. The most critical discovery was that very slow flow rates are necessary to increase the retention time and separation efficiency; this provided micro and nanoscale paramagnetic

particles with a lower magnetic susceptibility maximal time to be captured within the ferromagnetic matrix.[99] This led to the development of commercial HGMS systems by Sala Magnetics.[100, 101]

Coal liquefaction.

The progress made in HGMS development with kaolin clay beneficiation allowed other industries to implement HGMS processing, mainly for removing contaminants. By 1981, at least five companies, including Sala Magnetics, made commercially available HGMS systems for various applications.[101] Coal liquefaction is a process that has the potential benefit of yielding low sulfur coal compared to unprocessed coal,[102] allowing for the use of coal to meet energy demands while meeting air quality mandates for sulfur oxide in the 1970s. It also reduces the number of ash particulates released during burning. However, liquefaction is problematic because particulates remain even after organic components have dissolved into the solution. While traditional filtration can remove micron-scale particulate matter and sulfur from the coal, it requires extreme temperature and pressure conditions; it also needs a slow filtration rate to be performed efficiently, with the flow as low as 0.6 gallons/min/feet^2 of filter area. Due to these requirements, filtration of liquefied coal had severe technical and economic limitations that were not feasible.[103] In addition to filtration, magnetic separation was attempted on coal slurries as early as the 1950s, using heating to convert the weakly magnetic material pyrite to the ferromagnetic pyrrhotite, which has a higher magnetic susceptibility.[104, 105] This method, however, required temperatures up to 300°C and an inert gas atmosphere to prevent the ignition of the coal, which created significant barriers to practical implementation. This conversion did allow for improved separation of sulfur from the coal but was never efficient enough to warrant further development.[105]

The first attempt to use HGMS for coal liquefaction was performed by Trindade, though others have used it experimentally for the same application.[102, 106-108] Trindade created and experimentally confirmed a model for removing coal particulates, specifically those containing paramagnetic pyrite, from coal slurry; the undertaking did not require any conversion of pyrite, as was previously mentioned deemed necessary for magnetic separation.[105] This model focused on using a force balance to predict the forces acting on single particles near a magnetized strand in the ferromagnetic capture matrix. These forces helped predict the effects of coal particle size distribution, packing density of the magnetic matrix, magnetic field strength, and slurry velocity through the separator, some of which were already known factors important for efficient kaolin clay brightening. Using coal-water slurry with known

characteristics – amount of coal, particle size distribution, packing density of column, and quantity of dispersant added to prevent agglomeration of the smallest hydrophobic particles – particles were separated using HGMS by measuring the magnetization of remaining minerals after low-temperature ashing; a process which removes hydrocarbons without damaging the minerals in the coal. This procedure measured the sulfur in the original input slurry, the number of captured particulates, and the flow-through. Optimal capture was achieved with particle sizes of approximately 50 μm, with capture efficiencies dropping significantly for smaller particles. Decreased viscosity yielded high removal efficiencies than more viscous slurries, and increasing the magnetic field strength improved product purity due to higher percent ash and sulfur removal.[106] Ideally, this method would have also allowed for ash reduction, but this only yielded a slight improvement in ash content.[105] The work performed here allowed for further development and pilot testing of HGMS for coal desulfurization.

Further development allowed for multiple improvements or variations of Trindade's original work. Rather than use water to create slurries, small-scale experimentation showed methanol was a beneficial alternative and provided better separation than water. Specifically, particles failed to aggregate due to increased particle hydrophilicity in the presence of methanol, even in solutions as low as 10% methanol. However, 100% methanol provided the best separation of sulfur and ash from the liquefied coal. In contrast, methanol-water mixtures improved particle separation over water alone, with separation efficiency falling between pure methanol and pure water.[108] The use of methanol also had the benefit of already being a by-product of coal gasification, and some coal processing methods had the final goal of methanol production. By allowing the coal to settle out of the methanol following HGMS processing, the methanol can be recycled, and the coal would not need to be dried before burning as is required when water is used.[105] The recycling process through the HGMS system three times reduced inorganic sulfur content by 76.1% and ash by 64% from coal-water slurry without dispersant in a 20 kiloØrested magnetic field at a residence time of 18.3 s with a packing density of the matrix at 6%.[107] Another variation of separation is the use of dry coal feeds, though this process required more investigation and development before it could be used on a larger scale.[108]

Soil processing.

High-gradient magnetic separation was also applied to soil decontamination since soils containing radioactive substances, such as uranium and plutonium, cost between approximately $2,200 and $6,700 per cubic

meter to dispose of safely (in 2022s dollar value); removing contaminants in 90% of the processed soil could decrease disposal costs 10-fold while allowing recycling and reuse of the soil upon decontamination. Methods at the time, such as soil washing and gravimetric separation, could not remove particulates smaller than 50 μm, with a majority of the contaminants being less than 50 μm in size.[109]

Wastewater treatment.

Many industrial processes create wastewater that can potentially contaminate water sources. Using HGMS, multiple individuals have demonstrated the feasibility of removing pollutants from water streams using flocculation of magnetic particles to non-magnetic contaminants in the water. Using magnetite particles and flocculent, and fields as low as 3,000 G, Petrakis and Ahner demonstrated a reduction in the concentrations of oil, solid particulates, and phenol to concentrations as low as five ppm, one ppm, and 260 ppb respectively from refinery water effluent at the American Petroleum Institute following the standard reduction of particulates through an air flotation unit.[110] Sala Magnetics would go on to use their separator to demonstrate the removal of iron oxide scale from steel mill wastewater streams in Sweden, reducing the concentration of particulates from 133 mg/L to less than ten mg/L at a flow rate of 200 m/h and under a magnetic flux of 1,900 G. Oil contained in the wastewater was reduce by 60-80%.[100]

Besides industrial water sources, raw sewage and farming practices can contaminate natural bodies of water. Using HGMS, de Latour demonstrated that biological and chemical contaminants found in water sampled from the Charles River Basin and contaminants found in raw sewage from Deer Island Wastewater Treatment Facility in Boston, Massachusetts, could be significantly reduced or eliminated. This process also reduced water turbidity and color; HGMS processing also increased the water-processing rate by magnitude. Aluminum ions, which underwent metal ion hydrolysis once in solution, were used as a flocculent rather than polymer. Following, the metal ion coordinated an olation reaction to produce an aluminum ion joined to hydroxide groups, yielding strong adsorption to solid surfaces; this aided in the flocculation process. At concentrations of aluminum lower than two ppm, the complete association between bacterial cells and magnetic seed did not occur, with cells remaining in the water as a result.[111] He demonstrated the same principle with other metal ions, stressing that the pH of the solution was essential to the particle charge, so the pH of the solution is crucial for choosing a metal flocculent. If

the charge of the particle is positive or negative, it is possible for little to no flocculation to occur due to charge repulsions, resulting in a failed separation.[112]

The principles for seeding and high-gradient magnetic separation developed by de Latour and others[113, 114] for water decontamination allowed further development and use for removing biologics from water. It was shown that while a pH change should result in reversal of maghemite seed binding to yeast, allowing for reuse of seeds as shown previously with magnetite,[115] the yeast surface chemisorbed the seeds. Even after boiling in a 2 M caustic solution, the authors could not remove the seed from the yeast.[116] In another example, the authors were able to remove T_7 *Escherichia coli* (*E. coli*) bacteriophage from water using HGMS by first coagulating magnetite seeds to *E. coli* using calcium chloride, though this procedure varied for flocculation of viruses due to biological variation between different species.[117]

Biologic applications.

While there are many industrial applications for HGMS, its use goes beyond separating contaminants. High-gradient magnetic separation has also been implemented for various biological uses outside of contaminant removal and had demonstrated feasibility as early as the 1970s. Early use of HGMS for biological applications focused on separating erythrocytes from whole blood. Melville *et al.* showed that reducing oxyhemoglobin to deoxyhemoglobin using sodium dithionite converts the iron contained in hemoglobin from a diamagnetic (Fe^{2+}, with paired electrons) to paramagnetic (Fe^{3+}, with an unpaired electron) state, influencing it using a magnetic field. The device used a 40 mL volume filter with a 2% packing density of stainless-steel wire with a 25 μm diameter was subsequently exposed to a 1.75 Torr (17.5 kG) magnetic field. They estimated that the gradient field next to wires was approximately 8×10^3 Torr/m. By analyzing the effluent's hemoglobin content, approximately 70% of erythrocytes put into the column were captured. The authors stressed the importance of capture optimization and filter performance by investigating the effects of input flow rate and applied magnetic field.[118] High-gradient separation was again used by Owen *et al.*, instead of oxidizing hemoglobin to methemoglobin with 20 mM sodium nitrite. He further varied the paramagnetic state of the methemoglobin by adding potassium cyanide to the buffer used to pass the cells into the device. Omission of potassium cyanide yielded a higher spin state and higher magnetic susceptibility, as evidenced by his data. He also investigated the effect of flow rate and field strength on capture, demonstrating the hypothesized dependence that capture efficiencies are proportional to the magnetic moment of the

cells divided by the flow rate through the magnetic column.[119] Use of the inherent magnetic properties of the cell were revisited and used decades later for improved malaria diagnosis. Specifically, the authors used the paramagnetic properties of hemozoin; a metabolic by-product found in red blood cells infected with the malaria parasite species *Plasmodium falciparum.* With the hemozoin displaying paramagnetic properties, infected cells were concentrated and separated from non-infected red cells containing only the diamagnetic iron in hemoglobin. These cells could then be removed from the HGMS device with flushing and observed using thin smears.[120]

Following magnetic isolation of red cells using their inherent magnetic properties, red cells were magnetically separated via immunospecific labeling of red cells with 30-40 nm iron-dextran nanoparticles and a 500 G magnet.[121] The addition of the magnetic particle increased the magnetic susceptibility of the cell, separating with a fixed magnet only. Taking this a step further, after stabilizing the iron in heme in a diamagnetic state using carbon dioxide, Molday and Molday used these particles to retain ~96% of red cells in a high-gradient column containing 30 mg of stainless-steel wool and 0.75 Torr applied field; without these particles, the diamagnetic properties of the cells only captured only 3% of the cells in the column. The addition of magnetic nanoparticles was a clear improvement from previous red cell work.[122] This idea of using immunospecific beads for cell capture was not lost, with multiple applications following.

With a minimum of 204,000 published papers referencing or using the system (as determined via Google Scholar search) at the time of dissertation submission, the most prevalent HGMS system for biological use is a high-gradient system first published in 1990; termed "magnetic-activated cell sorting" (MACS), the system labels and isolates cells of interest using antibodies and magnetic nanoparticles.[123] By tagging cells of interest, these cells can either be removed from a population for enrichment or depletion.[124] The original system developed by Miltenyi *et al.* began staining cells of interest with an antibody and then loaded the tagged cells with a fluorescein-biotin complex; this fluorescent tag ultimately allowed for further analysis or sorting using fluorescence-activated cell sorting or flow cytometry techniques. Last, the cells were onto approximately 100 nm superparamagnetic particles functionalized with biotin. The cells were then magnetically separated using a column packed at a 4% packing density of Grade 0 stainless steel wool (100 mg), coated in a plastic polymer to prevent cell damage and degradation of the ferromagnetic matrix. In depletion experiments, the authors of this study demonstrated that cells were removed from a population of interest. Depending on the cell population, the MACS system could deplete T-lymphocytes from a population of murine spleen cells by up to 3,500-fold. However, some nonspecific capture of

unlabeled cells was observed in these experiments. The enrichment process required elution of the initially bound beads from the column, followed by the reapplication of the eluted cells and a second elution. A B-lymphocyte population from the murine spleen was enriched 124-fold. However, the enrichment process could not totally isolate rare cell populations, though the use of fluorescence-activated cell sorting would allow for total enrichment following MACS.[123-126]

Since the original development of MACS, there have been changes to the ferromagnetic matrix based on the intended application. A shared design theme across HGMS separators before this point had been the use of steel wool for ferromagnetic matrix since the sharp edges help create high field gradients.[127] However, other paramagnetic materials in different forms can also serve as the matrix, such as rods/pins, beads/balls, grooved plates, screens, or metal filters with any variety of pore shapes and sizes, though it is important to note that size and geometry can significantly affect the capture of particles.[128] In addition to still offering columns made with coated ferromagnetic wire and proprietary matrices, Miltenyi Biotech offers columns made with coated ferromagnetic spheres that can amplify the applied field by 10,000x.[129] The beads in the column are packed in a lattice structure, creating channels of identical size and flow patterns for the sample to pass through during separation. The size of the spheres may be varied to improve the isolation of cells of different sizes. An example given in Patent US005705059A filed by Miltenyi describes the average diameter of spheres for large-diameter cell isolation as being 0.2 mm to 1.5 mm in diameter, and 0.05 mm to 0.2 mm in diameter for isolation of lysed cell components. The diameter of the flow channel between the spheres is equivalent to the largest diameter sphere that would fit between the gaps in the sphere matrix lattice.[130] The staining and isolation protocols are similar to those initially developed by Miltenyi *et al.*[129-131]

Microfluidic Flows in Evaporating Sessile Droplets

There are two types of radial flows that can form in an evaporating sessile droplet. Under specific conditions, one radial flow can dominate and be the primary driver of fluid and particle movement during evaporation. Significant research has determined the physical parameters that drive or suppress these microfluidic flows and the resulting particle deposition patterns, including edge pinning,[132-134] solvent type, particle size and shape,[135-137] surfactant effects,[138-140] evaporation flux,[141] contact angle,[142, 143] material thermal conductivity,[142] among

others. The Haselton Research Group has previously developed diagnostic tools based on the physics of a sessile evaporating droplet on a solid surface.[135, 144-146] The benefits and limitations of these technologies are discussed.

Coffee ring phenomenon.

When coffee is spilled and allowed to dry, an increased density of coffee particles is observed at the edge of the drop relative to its center, lending the microfluidic phenomenon to its name. More specifically, the evaporative flux of the water in the coffee is higher at the edge of the spilled drop than at its middle. Because water's surface tension pins the coffee drop's edge, the evaporated fluid must constantly be replenished to maintain this edge pinning. This edge pinning is irregular and caused by surface irregularities and is stronger and more stable with solutes (e.g., particles) than without; precisely, the solutes deposited at the edge further augments the surface imperfections initially responsible for the edge pinning. As a result, radial capillary flows move from the drop's center to the pinned edges (**Figure 2.2**). This flow pulls suspended particles with it, depositing them at the edge as the water continues to evaporate. A well-defined ring structure forms throughout evaporation, which is easily visible to the naked eye.[132, 134] Droplets with a smaller contact angle are also more likely to result in coffee ring formation than a large contact angle, as has the initial fraction volume of suspended colloids in the droplet.[143]

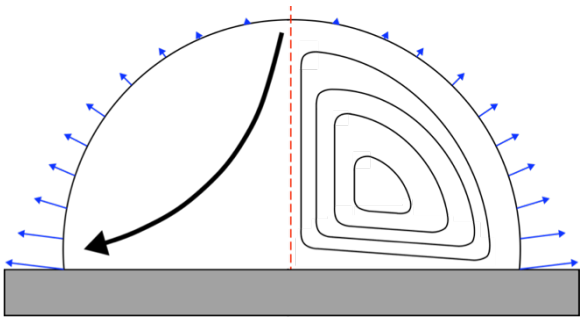

Figure 2.2. Capillary flows (internal black lines) consistent with fluid streams formed during evaporation for the coffee ring phenomenon (left) and recirculating Marangoni flows (right). Depending on material properties, Marangoni flows can circulate inward or outward along the substrate.

The starting point for coffee ring flows was performed by Deegan *et al.*, who first identified the evaporation-driven capillary flow as the ring formation mechanism.[147] Successful efforts to exploit the visual appeal of this effect for disease detection were first described when the Haselton Research Group successfully

demonstrated that the presence of poly-L-histidine, a peptide mimic of the malaria biomarker *pf*HRP-II, induces a visible color change in a drying drop containing functionalized probe and control fluorescent beads (**Figure 2.3**).[146] In these preliminary studies, Trantum *et al.,* identified features that control droplet edge pinning, intradrop microfluidics, and evaporation rate. The initial design capitalized on the naturally occurring outward radial flows in an evaporating drop, combined with a solution-phase enzyme-linked immunosorbent assay (ELISA)-like reaction. This design selectively modified one of the two-colored microbeads to produce a colorimetric signal, indicating the presence of the malarial target biomarker. The biomarker concentration could also be measured using RGB values at the droplet edge and center with this colorimetric change.[146]

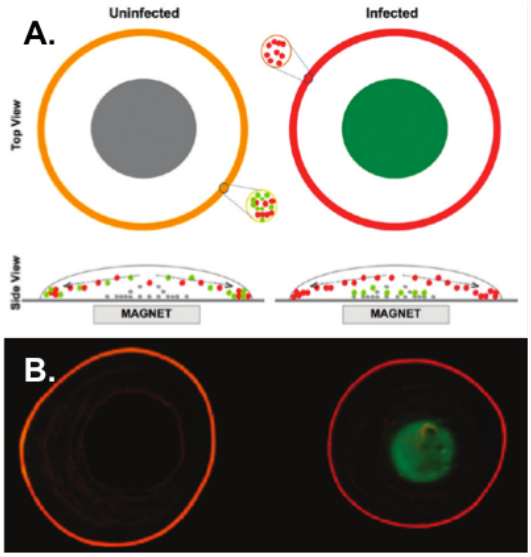

Figure 2.3. The original concept for coffee ring color modulated by infection (**A.**). Application of coffee ring phenomenon for malaria diagnosis through detection of *pf*HRP-II mimic, poly-L-histidine (**B.**). The negative control is shown on the left column for both figures, and the sample positive for poly-L-histidine is shown in the right column. Positive signal, defined as a green center and red ring color, shifted to a single yellow-orange outer ring with decreasing biomarker concentration. Images adapted from cited publication.[146]

Although the assay generated an easily interpretable pattern that microscopy could visualize, there were several fundamental limitations. Most importantly, because the microfluidics only works with pure water, significant cleanup of samples was required; this can be difficult to achieve with low-resource sample prep methods, even with multiple rigorous wash steps. This limitation makes the coffee ring effect challenging to implement with authentic clinical specimens, making it unlikely to be successfully implemented in a low-resource clinical setting for

diagnostic use. The assay also failed to achieve a LOD equivalent to malaria diagnostics available at the time of publication (0.08-20 nM), as the calculated LOD was at least one order of magnitude higher (~250 nM) than these other technologies.

Further work was performed in collaboration between the Haselton and Wright Research Groups to improve the LOD and implementation of the coffee ring assay for the detection of malaria. In the new design, recombinant *pf*HRP-II was captured from solution on nickel (II) nitrilotriacetic acid (Ni(II)NTA) gold polystyrene microparticles via immobilized metal affinity chromatography (IMAC). IMAC is a technique that separates proteins by their affinity for transition metal ions immobilized by chelation on an insoluble matrix.[148] In the context of malaria, 85% of *pf*HRP-II amino acids are in repeat sequences containing multiple histidines flanked by alanine residues. Histidine repeats are known to preferentially form coordinate covalent bonds to the metals chelated on IMAC resins,[94] making this technique an easy method for specific protein isolation without requiring antibody-functionalized particles, as Trantum *et al.* used. When combined with recombinant *pf*HRP-II, Ni(II)NTA gold microparticles cross-linked as multiple particles interacted with single peptides. After incubating and facilitating this cross-linking, a droplet of the bead-sample solution was placed onto a glass slide also coated with Ni(II)NTA and left to evaporate. During evaporation, particles were transported to the edge of the droplet using the coffee ring effect. Once dry, the slide was washed with water to remove unbound particles. Because the captured protein interacts with both the particles and slide surface via IMAC chemistry, when the particles are deposited on the slide surface, the cross-linked particles are also cross-linked with the microscope slide surface. By anchoring the particles to the glass substrate, the deposited particles remained bound during washing instead of rinsing from the surface. Therefore, the presence of a ring would indicate detection of recombinant *pf*HRP-II, and the absence indicated no biomarker was present.[148] In addition, the signal intensity at the ring edge theoretically could be used to quantify the biomarker concentration. Ultimately, not only did this method of detection successfully detect recombinant *pf*HRP-II in the operational range of malaria diagnostics, but the LOD viewable by eye at 10 pM is one order of magnitude lower than the WHO's lower recommendation threshold for malarial diagnostics. However, the ring edge intensity rapidly saturated at concentrations ≥100 pM, making this technique more amenable to qualitative diagnosis than quantitative.[148] Even with the significant improvement in LOD and user-friendly reading, similar sample preparation barriers continue to prevent clinical use of these evaporating droplet-based diagnostics.

Marangoni flows.

The secondary radial flow that forms in evaporating droplets is known as Marangoni flows. These flows are usually suppressed in pure water, so the coffee ring effect dominates in pure water; this effect is not seen in organic solvents. The addition of salts and surfactants to aqueous solvents also suppresses the outward radial flow that forms a coffee ring, so Marangoni flows dominate.[149] Marangoni flows are driven by the surface tension gradient created by the drop edge, just as seen with the coffee ring effect. They are also driven by a thermal gradient resulting from the relationship between the substrate and solvent thermal conductivities and uneven cooling from the non-uniform evaporation rate along the air-liquid interface.[142, 149] These Marangoni flows are circulatory (**Figure 2.2**), and they can move inward along the substrate or outward along the substrate. Combined with the impact of particle size and shape, a wide variety of deposition patterns can be observed, including but not limited to edge deposition, central deposition, or uniform deposition upon droplet drying.

With the limitations of the coffee ring phenomenon noted, Trantum focused on harnessing the secondary radial flows in evaporating sessile droplets as an alternative to the coffee ring phenomenon for visual detection of disease. In his 2014 publication, Trantum *et al.* effectively created a reverse coffee ring by driving particle deposition to the center of the droplet instead of the edges using re-circulatory Marangoni flows (**Figure 2.4**). Using a similar ELISA-like reaction to his previous work, immunospecific beads cross-linked in the presence of the model biomarker, M13K07 bacteriophage. These particle aggregations prevented particle transport to the droplet edge during evaporation and were deposited in the center of the droplet instead—the concentration of M13K07 directly correlated with the diameter of the centrally deposited particle aggregates. The authors also confirmed that re-circulatory radial flows were responsible for the deposition pattern observed using optical coherence tomography (OCT). They also observed by OCT that using a mixed-solvent system for the evaporating droplet, composed of aqueous buffer containing salt, 8% glycerol, and trace detergent, enhanced these flows. Removal of glycerol resulted in weaker Marangoni flows, though they were still present.

One benefit to using Marangoni flows instead of the radial flows responsible for coffee ring formation is the impact salt, or other contaminants can have on the flows. Specifically, contaminating salts or trace detergents (less than 0.01%) do not significantly impact the microfluidics of the droplet, reducing the barrier to implementation by changing the sample purity requirement. However, it is known that higher concentrations of detergents (greater than 0.01%) or salts can impact fluid flow patterns, so there is still a minimum sample cleanup barrier required for

use as a diagnostic assay readout.[150] In addition, the Marangoni flow-based readout eliminated the need for fluorescence detection instruments, which helps lower the barrier for POC implementation.

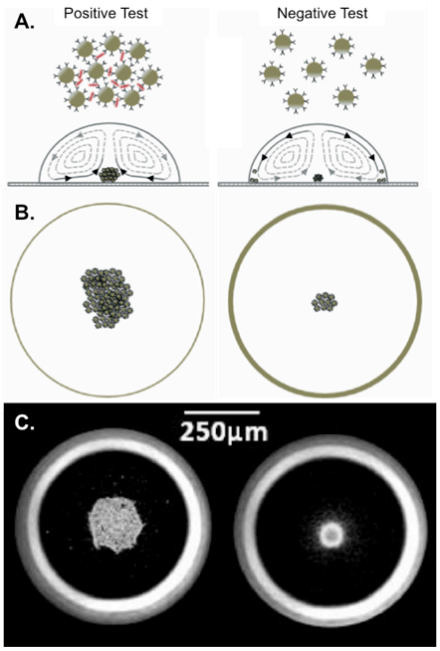

Figure 2.4. Original concept for Marangoni flow-based detection of model organism M13K07 bacteriophage (**A.** and **B.**) Marangoni flow accumulation in the center of an evaporating drop for biomarker detection (**B.** and **C.**). Assay signal observed as a large collection of beads in the center of the drop, as shown in the left column, with the diameter of the central spot corresponding to the amount of biomarker in the sample. Negative control is seen in the right column. Image adapted from cited publication.[145]

Microscopy-based TB Diagnosis

Identification of TB using microscopy is primarily performed with conventional bright-field microscopy because it implements more straightforward laboratory facilities and is inexpensive compared to culture or other diagnostic methods. Fluorescence staining and microscopy can sometimes make imaging less laborious but requires much more complex and expensive microscopy equipment. Regardless of the staining and visualization method used, staff must follow standard operating procedures after training to ensure samples meet minimum quality standards.[151]

For traditional staining methods, such as Ziehl-Neelsen (ZN) or auramine O (AO) staining, sputum smears are prepared on a clean, plain glass microscope slide. A small volume of the purulent portion of a sample, where

bacilli are most likely to be found, is collected using a sterile flame loop or sampling stick. Saliva commonly contaminates samples, and incorrect sampling can produce false-negative test results. The sample is smeared in a thin layer across a 2 cm^2 area on the slide, allowed to air dry, and then heat-fixed by quickly passing the slide through an open flame. Unless otherwise stated, when discussing available staining methods, it is assumed that samples are prepared in this way before staining. Applying too much sputum or over-fixing the sample can make quality staining difficult or destroy a sample. For these methods, applying a stain or decolorizer for too short or too long or allowing stains to dry on the sample before staining is complete will make imaging problematic and can yield an inaccurate diagnosis.[151]

Mycobacteria are "acid-fast" because they resist de-colorization with acid solution after initial staining, which forms the basis of most traditional *M.tb* staining methods. The *M.tb* cell wall consists primarily of mycolic acids, which are notoriously difficult to penetrate. Mycolic acids melt when heated with a flame, and the initial dye penetrates the cell wall, with the phenol acting as a mordant to carry the fuschin stain into the waxy cell wall. Once cool, the mycolic acids return to a solid upon cooling, and the dye impregnates the cell wall; at this point, the de-colorizing agent cannot penetrate *M.tb* to remove the dye. Most cells, such as contaminating epithelial cells, are not acid-fast, making this an effective method for determination between *Mycobacterium* spp. and other species.[151]

In addition to the extensive work performed to try and improve conventional sputum smear microscopy, there are three main areas where scientific efforts have focused on improving sputum smear microscopy. The first aims to design new fluorescent dyes to improve diagnostic sensitivity. The second area of research has focused on reducing barriers to equipment access, often through the design of inexpensive instrumentation. The third focuses on reducing labor requirements and human subjectivity when inspecting and interpreting a smear by creating bacilli counting algorithms. Discussed below are examples for each of these areas.

Conventional bright-field staining methods.

The ZN method is the most common method of staining *M.tb* bacilli before microscopic inspection (**Figure 1.5**). Having been the most accessible diagnostic method for over 100 years, the simple colorimetric differentiation of conventional staining and inspection makes this a more straightforward method for individuals to learn compared to fluorescence inspection. *M.tb* cells are first stained red using a solution of 1% carbol fuschin and 5% phenol in 10% ethanol, which is introduced to the cell interior by heating the smear and stain solution over a flame for one to

two minutes until steaming; the phenol carries the fuschin dye into the waxy cell wall and acts as a mordant to hold the dye in the cell wall. After, the stain cools for at least three minutes, but ideally, ten minutes, provided the stain does not dry on the slide. The smear is then rinsed with water and decolorized with acid (25% H_2SO_4 or 6% HCl) or acid-alcohol (3% HCl, 95% ethanol) for three minutes. After rinsing with water, the sample is counterstained with 0.1% methylene blue or 3% malachite green no more than one minute, which re-colorizes the decolorized sample areas and turns the background blue or green. Excess stain is rinsed from the slide, and the sample air-dried before microscopic examination.[151]

Bright-field sample inspection uses a basic tabletop white light microscope. Samples are inspected at high-power magnification under oil immersion because *M.tb* bacilli are only a few microns in length and are difficult to visualize otherwise accurately. At 200x total magnification, purulent or mucoid material is first identified to locate where bacilli are most likely to be observed. Once the viewing area is selected, the magnification power is increased to 1,000x total magnification, and at least 100 fields of view are inspected; this area is equivalent to one length across the two-centimeter axis of the smear. The number of acid-fast bacilli (AFB) is counted using the semi-quantitative method listed in **Table 2.1**.[151] Examples of ZN smears can be found in **Figure 1.4** and **Figure 2.5**. Two samples per patient need to be stained and inspected, with the caveat that they must be collected on two different days, with one collected in the morning. As previously discussed, the diagnostic specificity of conventional sputum smear microscopy is >99%, but it suffers from poor sensitivity, averaging 50%. The sensitivity can vary widely (30-90%) among locations and individuals performing the protocol.[152]

Table 2.1. Semi-quantitative Grading of Sputum Smears for ZN and AO Staining Methods[151*]

What is observed			What to report
ZN at 1000x	AO at 200x	AO at 400x	
No AFB in 100 fields	No AFB in one length[††]	No AFB in one length	No AFB observed
-	1-4 AFB in one length	1-2 AFB in one length	Confirmation required[‡‡]
1-9 AFB in 100 fields	5-49 AFB in one length	3-24 AFB in one length	Scanty - record exact number of bacilli
10-99 AFB in 100 fields	3-24 AFB in one field	1-6 AFB in one field	1+
1-10 AFB per field, check 50 fields	25-250 AFB in one field	7-60 AFB in one field	2+
>10 AFB per field, check 20 fields	>250 AFB in one field	>60 AFB in one field	3+

[††] One length = across the entire length of the two centimeter axis of the smear, equivalent to 100 fields-of-view at 1,000x total magnification.

[‡‡] Confirmation can be achieved by viewing additional fields, having another technician check the AFB morphology, or by collecting and staining another sputum sample.

Variations to the ZN method exist, and while most are no longer used, other adaptations have their advantages and disadvantages compared to ZN staining. Cold acid-fast staining, known as Kinyoun staining, performs the same protocol as traditional ZN staining but increases the concentration of carbol fuschin and phenol in the primary stain to 4% and 8%, respectively.[153] These increased concentrations aid in the chemical penetration and staining of the waxy cell wall without requiring heat, simplifying the staining protocol. For the initial staining step, the Kinyoun stain is applied to the smear and left to stain for at least two minutes before rinsing and decolorizing.[153] Inspection occurs as outlined for ZN staining. Kinyoun staining slightly underperforms the ZN method for diagnostic sensitivity in comparison studies.[154-156] It also has lower diagnostic sensitivity when applied in the field.[157]

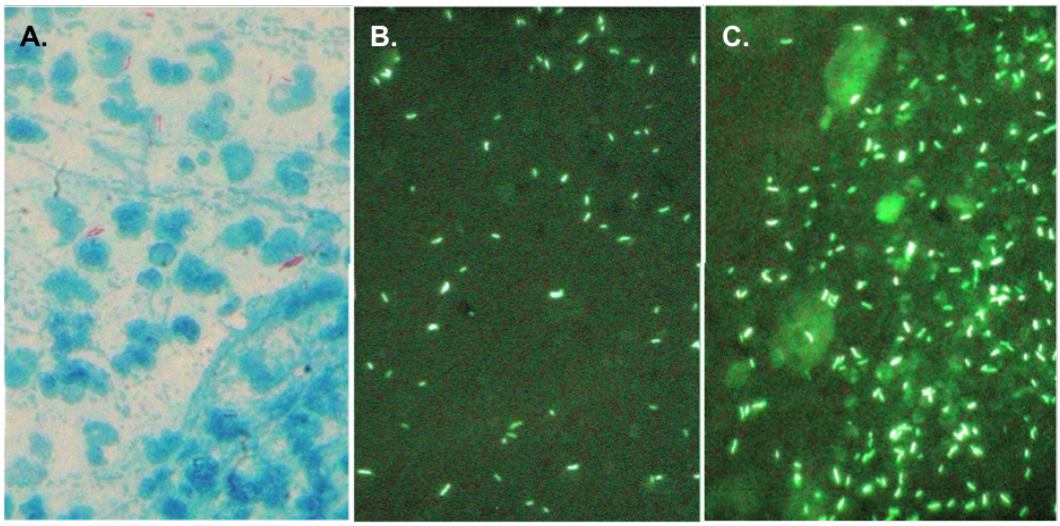

Figure 2.5. Photographic comparison of different sputum smear staining and imaging methods. All images have sputum grading of 3+ (see **Table 2.1**). **A.** ZN staining at 1,000x magnification. **B.** AO staining at 200x magnification using conventional FM. **C.** AO staining at 200x magnification with light-emitting diode (LED) FM. Figure adapted from cited reference.[158]

Gabbet's method is an alternative form of cold staining, which starts by air-drying without additional heat fixation of the sample to the slide. Initial staining applies ZN carbol fuschin stain to the sample for ten minutes without heat. After rinsing with water, the sample is decolorized and counterstained simultaneously for two minutes using a solution of 2% methylene blue, 20% H_2SO_4, 30% methanol.[159] Three studies agree that bacilli morphology appeared subtler and were less intense in color when stained using Gabbet's method than with ZN, and Gabbet's has

a lower sensitivity when compared to ZN.[160-162] Lahiri *et al.* does argue, however, that the simplicity of Gabbet's cold staining method still makes it valuable in situations where trained personnel are unavailable.[162]

Tan Thiam Hok's cold staining method combines Kinyoun and Gabbet's modifications, stating that the method was superior to traditional ZN. Hok performed a quadruple-paired comparison of ZN, Kinyoun, Gabbet, and Hok on 1,210 smears. For 100% of samples positive for AFB after culturing, each method detected 60.1%, 60.0%, 61.5%, and 65.6%, respectively. The Hok method also detected an average of 961 bacilli/100 fields compared to 524 bacilli/100 fields for ZN.[163]

Fluorescent stains.

Though not as common as conventional, auramine O (AO) staining is the most commonly available fluorescent stain used for acid-fast bacteria. AO binds the mycolic acids of the cell wall and intercalates DNA and RNA inside the cell during staining,[164] fluorescing green upon excitation (excitation maximum at 432 nm, emission maximum at 499 nm). AO is prepared as a 1% concentrated solution in alcohol and then diluted to 0.1% in a final concentration of 3% phenol upon use. The primary AO stain application is applied just as cold ZN for a minimum of 20 minutes. De-colorizing is performed for one to two minutes using 0.5% acid alcohol, followed by counterstaining with 0.3% methylene blue for a maximum of one minute. A solution of 0.5% potassium permanganate can be used as an alternative, acting as a quenching agent, though methylene blue is recommended.[151]

A variation of AO is Truant staining, also known as auramine-rhodamine (AR) staining; this process uses a mixture of 1.1% auramine O and 0.56% rhodamine B in 7.4% phenol and 56% glycerol to stain acid-fast bacteria for 15 min. AR also recommends potassium permanganate over methylene blue to quench background fluorescence.[165]

While the staining protocol for AO is longer than ZN and requires that the smear be inspected soon after staining due to fluorescence loss, the fluorescence is easier to visualize at lower magnification, performed using 200x or 400x total magnification. This phenomenon may result from AO binding nucleic acids and that this intracellular staining pattern is consistent with non-uniform nucleic acid distribution.[166] Because this staining patter is distinctive at 400x total magnification, it is unnecessary to perform secondary ZN staining for confirmation.[152, 166, 167] Consequently, the semi-quantitative reporting of AFB for fluorescence microscopy differs from conventional. However, both methods inspect one full length of the smear. Sputum smear grading for AO at both 200x and 400x total magnification levels are listed in **Table 2.1**,[151] with an example photograph available in **Figure 2.5**.[158] In a

systematic review comparing auramine staining methods to ZN, AO generally had a diagnostic sensitivity 10% greater than ZN, with a reported range of 52% to 97% across studies.[152] Additionally, auramine staining has a more straightforward protocol. The diagnostic specificity was similar for both ZN and AO and, when averaged across all studies, was 0% different.[152]

Shapiro *et al.* interestingly first attempted to use ZN staining reagents with FM in 2008 and found that upon excitation with 546 nm light and use of a 590 nm long-pass filter, orange-red emission from fuschin was observed.[70] Before this point, scientists believed that FM was more sensitive than ZN because the AO-stained mycolic acid was more resistant to de-colorization from acid alcohol than ZN-stained mycolic acid. This hypothesis was based on findings by Richards *et al.*[168] Up until this point, a direct comparison between FM and bright-field imaging was not possible because ZN staining could not be repeated on AO previously stained slides, and AO is not visible with transmitted light. However, because Shapiro *et al.* knew (**1**) the primary source of AO signal was the result of binding to nucleic acids, (**2**) they observed a similar staining pattern between AO and fuschin in a prior study,[164] and (**3**) they knew fuschin also binds nucleic acids,[164] they hypothesized that they could perform paired fluorescence imaging because fuschin could bind nucleic acids within the bacilli similar to AO. Though their study was limited in scope, they imaged ZN-stained bacilli using fluorescence and identified bacterial that were not visible using bright-field imaging.[70] This finding suggests that the findings by Richards *et al.*, performed on pure mycolic acid and not intact bacteria,[168] may be incorrect. More investigation is needed to determine why there is a difference in diagnostic sensitivity between bright-field and fluorescence imaging. Shapiro *et al.* also suggest the possibility of re-imaging ZN smear-negative slides using fluorescence, with the potential for identification of false-negative cases.[70]

With the difficulty of using culture to monitor treatment success or failure, the cell viability assay using fluorescein-diacetate with ethidium bromide[169] was reapplied to microscopy-based treatment monitoring.[170] This assay first exposes cells to fluorescein-diacetate for 30 minutes at 37°C, followed by ethidium bromide for ten minutes at room temperature. Fluorescein-diacetate is cleaved by esterases from viable cells, resulting in free fluorescein and green fluorescence. This green fluorescence is bright enough to overwhelm the signal from ethidium bromide binding to internal DNA. Dead cells do not cleave fluorescein-diacetate, and therefore only am orange signal from the ethidium bromide is observed. In addition, ZN can be performed on the sample following staining with fluorescein-diacetate and ethidium bromide, confirming if organisms are acid-fast. Though this method may

make treatment monitoring easier, the reagent does require freezer storage, introducing an additional barrier for implementation.[171]

More recent advancements for staining TB have focused on staining DNA inside cells. Ryan *et al*. developed an acid-fast stain employing SYBR™ Gold, a stain developed for sensitive and selective staining of nucleic acids.[172] This asymmetric cyanine dye exhibits over 1,000-fold fluorescence enhancement when bound to nucleic acids, is 25-100 times more sensitive than ethidium bromide, and has a high quantum yield of ~0.7. It also has very low background fluorescence compared to other nucleic acid stains. When bound to nucleic acids, SYBRTM Gold excites maximally at both 300 nm and 495 nm and has an emission maximum at 538 nm, creating a bright green fluorescent signal.[173] The dye itself consisted of a 1:1,000 dilution of the stock reagent in 8% phenol, 60% glycerol, and 14% isopropyl alcohol. The stain was applied by heating the sample to 65°C for five minutes, similar to ZN staining, and was then rinsed and decolorized with acid-alcohol for three minutes. No counterstaining was performed. SYBR™ Gold stained 99% of *M.tb* cells from log-phase culture, determined by comparing the number of fluorescently stained cells to the total number of cells observed under phase-contrast imaging. It outperformed ZN, AR, and AO staining methods, which stained 66%, 54%, and 67%, respectively. When *M.tb* was grown under hypoxic conditions for seven days, SYBR™ Gold maintained 99% sensitivity, followed by ZN at ~85%, AO at ~80%, and AR at ~73%. In addition, when five other Gram-positive and Gram-negative bacteria species were stained with SYBR™ Gold, no nonspecific staining from SYBR™ Gold was observed, demonstrating acid-fast specificity. Given that SYBR™ Gold is also highly resistant to fading over 21 months, this technique significantly improves on other acid-fast stains, though high the cost and stability of the dye potentially limit its clinical applicability.[172]

Other traditional nucleic acid stains have been assessed for DNA binding in *M.tb*, followed by imaging on a microscope. Because 4', 6-diamidino-2-phenylindole, commonly known as DAPI, fluorescence relies on binding to adenine-thymine pairs, and the *M.tb* genome has a disproportionately high percentage of guanine-cytosine pairs, 4', 6-diamidino-2-phenylindole only produces a weak fluorescent signal. TO-PRO™-1 Iodide and SYTO™ RNASelect™ both produced sufficient fluorescent signal but required a high working concentration of dye and exhibited nonspecific background fluorescence.[172]

Staining the nucleic acids present within bacterial cells with DNA-sequence-specific probes makes it possible to determine if a specific species cause an infection. The well-known fluorescence in situ hybridization

(FISH) was used by Baliga *et al*. to detect and differentiate MTBC from NTM in sputum in clinical samples.[174] Though this is not the first application of FISH with mycobacteria,[175-178] these methods applied the technology to assays not using sputum samples,[175, 176, 178] or they have poor diagnostic sensitivity or specificity when used with sputum samples.[179, 180] In the one assay with both sensitivity and specificity >80%, there was no species differentiation between MTBC and NTM.[177]

In Balgia *et al.*, the authors applied the commercially available *Mycobacterium/Nocardia* Genus MTBC-FISH assay by ID-FISH Technology, Inc., which used two different DNA probes. The first probe hybridizes to the 16s rRNA sequence conserved across *Mycobacterium* spp. and *Nocardia* spp., fluorescing green upon hybridization. The second probe binds to the 23S rRNA sequence specific to MTBC, fluorescing orange upon hybridization. Assessing the binding of one or both probes using dual-color fluorescence provides information on if NTM causes the infection or MTBC.[181] The assay characterized 202 sputum samples and compared them to DNA sequencing and bacterial culture. The sensitivity and specificity for MTBC were 89.7% and 95.5%, respectively, and the limit-of-detection (LOD) was ~22,000 colony-forming units per milliliter of sputum.[174] This value is relatively consistent with a previous report, which used the same assay to determine the LOD from culture to be ~50,000 colony-forming units per milliliter.[181] While the assay requires at least double the bacteria per milliliter than the LOD for ZN staining, the added utility for species determination could make this useful alongside other confirmatory diagnostic methods. In addition, because FISH does not use enzymatic nucleic acid amplification methods, such as PCR, and is therefore not impacted by nucleic acid amplification inhibitors, the technique is more suitable for application in low-resource settings provided a fluorescence imaging system is available.

Aiming to develop an effective diagnostic tool that can assess *M.tb* viability, Kamariza *et al.* developed an extremely novel stain that is simple, rapid, and specific to mycobacteria.[182] Multiple sources of inspiration led to the development of this dye. The first inspiration comes from their observation that mycobacteria can incorporate trehalose analogs into their cell wall, enabled by a lack of substrate specificity in the antigen 85 complex responsible for the mycolylation of trehalose. They theorized that this active metabolic process might provide a method to distinguish between live and dead cells by incorporating a trehalose-conjugated dye into the cell wall. Interestingly, the environmentally-sensitive fluorogenic dye, 4-N, N-dimethylamino-1, 8-naphthalimide (DMN), undergoes a 700-fold fluorescence intensity enhancement when transitioned from an aqueous to a hydrophobic environment. With this, the authors hypothesized that conjugating DMN and trehalose (DMN-tre) would create a wash-free fluorescent

dye that only fluoresces when incorporated into *M.tb*'s hydrophobic cell wall. They showed that this was possible using cultured cells, and application of DMN-tre to mycobacteria dyed the cells green.[182] Specificity and robustness of DMN-tre against different bacterial species were tested. First, phylogenetic analysis confirmed the specificity of the antigen 85 complex to a few specific subsets of the phylogenetic order *Actinomycetales*, which includes mycobacteria. This complex was not identified in any common bacteria or humans. Applying DMN-tre to different species of bacteria for one to six hours demonstrated specificity to *Mycobacterium* spp. and *Corynebacterium* spp., but not Gram-positive or Gram-negative cells. In addition, no background fluorescence was observed from unincorporated DMN-tre, which remained on the sample during imaging. Kamariza *et al.* took their experiments one step further, performing DMN-tre staining on heat-killed *Mycobacterium smegmatis*, and performed staining on antibiotic-treated *M. smegmatis (M. smeg) M.tb*. They found that metabolically inactive cells did not fluoresce after DMN-tre staining and antibiotic treatments inhibited staining. In cells treated with antigen 85 inhibitors, the decrease of DMN-tre staining observed was dose-dependent, helping confirm that antigen 85 complex was responsible for the staining observed. Finally, the authors also showed that DMN-tre stained *M.tb* from patient sputum samples within one hour.[182] With this dye's high specificity and user-friendly nature, DMN-tre has significant potential for application to *M.tb* diagnosis and treatment monitoring anywhere with access to a fluorescent microscope.

Instrumentation.

Even with the development of new fluorescent dyes that have extreme promise in changing TB diagnosis and treatment monitoring, the inaccessibility to fluorescent microscopes remains the most significant barrier to adopting fluorescent staining methods in place of ZN staining. With the improvement of technology and design often comes affordability and improved manufacturing, so researchers have worked to create solutions to instrumentation access.

Traditional fluorescence microscopy (FM) uses mercury vapor bulbs for excitation, producing bright spectral bands within the visible light spectrum. Unfortunately, mercury vapor bulbs only last around 200 hours, and they can cost hundreds or thousands of dollars depending on the system. Assuming an eight-hour workday, each clinic using fluorescence microscopy would be spending a minimum of thousands of $2,500 to $5,000 a year for the maintenance cost of bulbs alone.[183] They also have high power consumption rates, which combined with the other

drawbacks, makes FM not suitable for most POC clinics. For these reasons, light-emitting diode (LED) fluorescence microscopy has become a significantly less expensive alternative for traditional FM.

LED fluorescence microscopy is a less expensive alternative to conventional FM. LEDs cost 10% of a standard mercury vapor bulb and have a useable life of 20,000 to 50,000 hours.[167, 183] Additionally, LEDs can run on battery packs, solar panels, or other low-voltage power sources, making LED adaptations significantly more accessible for resource-limited clinics. Various studies have compared conventional FM to LED FM and found that it performs as well as or better than conventional FM (**Figure 2.3**). Because of the LED's high power, they also eliminate the need for a darkroom and instead can be used in rooms with low light.[158, 167, 183-185]

There are a few commercial systems available for fluorescence microscopy specifically for use in low-resource clinics. The Zeiss Primo Star iLED is an epi-fluorescent microscope, developed in collaboration with FIND Diagnostics and the STOP TB Partnership, and provides an accessible alternative to conventional FM. It also has the instrumentation required for traditional bright-field imaging. Through this partnership, the microscope is available to countries most impacted by TB at a prorated cost of £1,250 at the time of dissertation publication.[186, 187] The CyScope® is another FM microscope commercially available for microscopic pathogen diagnosis, with four excitations LED wavelength options (365 nm, 470 nm, 528 nm, 624 nm).[188, 189] The CyScope® also includes a camera interface, allowing for elementary computer imaging, and includes rechargeable batteries that last for six hours of use. At the time of publication, the CyScope® had a listed market price starting at £990.[188] Both microscopes are comparable in cost to bright-field microscopes already used in resource-limited settings, such as the Olympus CX23 (W. Silva, personal communication, March 19, 2019).[184] However, the monocular version of the system may make it tiring for long periods of use.[190] Two studies have demonstrated that AO staining and imaging with both the Zeiss iLED and CyScope® outperform traditional ZN staining with bright-field imaging.[185, 191]

Academic groups have also focused on producing small-format FM for TB diagnosis in developing countries. The CellScope is a 3 kg, 20 cm by 20 cm by 10 cm, portable battery-powered digital fluorescence microscope. The system used a 20x 0.4-numerical aperture (NA) objective with a nominal resolution of 0.76 μm.[192] Excitation was provided by a 460 nm 1W LED and a 0.65 NA condenser. The system incorporated a light sensor similar to those used in commercial phone cameras, and it could be connected to a computer through USB 2.0 if necessary. With high-frequency image sampling, the images were viewed at an apparent total magnification of 3,500x using interpolation.[192] When tested in a paired analysis with AO staining, 39% of patient sputum samples

were culture positive, 32% of samples were positive using LED FM by experienced readers, and 34% of samples were positive using CellScope with inexperienced readers, demonstrating that CellScope performed as well as LED FM. LED FM and CellScope also had comparable sensitivity (70% vs. 63%, respectively) and specificity (92% vs. 85%, respectively) in a blinded analysis. The CellScope system also had significant inter-reader reliability. These combined results demonstrate that CellScope may be suitable for resource-limited settings, though more work is required to confirm this.[192]

Though not demonstrated for use with sputum smear microscopy, Lu *et al.*[193] designed an open-access combined bright-field and fluorescence microscope with a manufacturing cost of less than $500 at the time of publication in 2018. The microscope used off-the-shelf parts that require no customization prior to use, essentially creating a kit of parts for assembly. The system used a modern "4f" infinity-corrected microscope configuration and used a reverse board lens instead of a standard objective. Board lenses are short-length focal lenses, such as those found in smartphones. By placing the lens in reverse, instead of assuming objects are at an infinite length, the object of interest is placed where the sensor would reside, behaving like an objective lens. An additional CCTV lens acted as a tube lens and sent the image plane to a USB CMOS camera detector. The lens had a 4 mm focal length and an equivalent NA of 0.35. A blue-light LED provided fluorescence excitation and was filtered using a band-pass filter at 470 nm ± 10 nm.[193] In addition, an automated stage operating on open-loop stepper motors translated the entire optical system on the X-Y plane and physically moved the sample in the Z-plane for focusing. Auto-focus used the Brenner criterion. The entire system was controlled through a custom graphical interface in LabVIEW™, with final image mosaicking and stitching performed in Fiji. This automation enabled an application to whole-slide imaging, which tiles together images from the entire specimen and saves them for later analysis by a trained reader.[193] However, one drawback to the automation is that the user must place the sample in the upper-left corner and assist in sample location, and odd-shaped samples or samples with holes may not be adequately imaged. The travel only allows for 13 mm of total movement in the X-Y plane. Because the field-of-view of the microscope is equivalent to 8.5x magnification (680 μm x 510 μm), further development of the system is required for sputum smear TB diagnosis, though it still demonstrates applicability in other diagnostic needs, including fecal smears.[193]

In addition to the microscopes discussed, researchers have focused on adapting portable cell phones into low-cost microscopes. The Foldscope is the most widely known smartphone adaptation, both inside and outside clinical and academic communities. Designed to cost less than $1, the Foldscope is an origami paper microscope

meant initially to improve the accessibility of science. Folded from a piece of paper, the only other components of the Foldscope are a glass ball lens, a three-volt battery that powers the LED, and a switch and some copper tape to connect and control power to the LED.[194] Depending on the ball lens, the total magnification could be 1,450x or 2,180x, achieving submicron resolution. The pocket-sized microscope is also compatible with fluorescence microscopy since the LED can be changed to a narrow spectra width LED for the desired excitation range, with polymeric sheets inserted into the optical path for excitation and emission filtering.[194] Though it has not been used for sputum smear microscopy, the microscope has been used for diagnosis of urinary tract infections, *Schistosoma haematobium* and *S. mansoni*, *Loa loa* filariasis nematode infection, and Pap smear assessment, among other conditions.[194-197]

While many early works focused on using the digital imaging capabilities and the computational power of smartphones, creating a fully integrated microscope could provide the added benefit of a completely portable imaging system. Work using cell phone cameras started in the 2000s, once cell phones with cameras became common and sufficiently powerful. One early example of this used a Nokia N73 with a 3.2-megapixel CMOS camera and poor quality camera by current standards. Nonetheless, by creating an external system on optical rails using a 20x wide field eyepiece with a 60x objective (0.85 NA), the system's spatial resolution was estimated at 1.2 μm.[198] Ambient light generally provided sufficient illumination for bright-field imaging, and an optional white light LED could be used for darker conditions. A 455 nm LED provided excitation light for fluorescence, and excitation and emission polymer sheet filters were inserted in the optical path or removed, based on the microscopy method used. LEDs were oriented in trans-illumination geometry, reducing system cost and complexity compared to an epi-illumination configuration. The designed system could visualize stained erythrocytes infected with malaria and TB bacilli stained using AO. Because this system used only a 3.2-megapixel camera, the entire microscope slide field could not be imaged at maximum resolution by the camera, and the area in the field-of-view was limited to a 180 μm diameter.[198] However, modern smartphone cameras do not suffer from this limitation, and this system would likely perform significantly better with updated hardware. Modern smartphones also have significant data storage and processing capabilities that could automatically count bacilli.

While the advancement of cell phone cameras provided great technological benefits for many, manufacturer differences in camera hardware and automated and proprietary image processing software created a new barrier, specifically for image quantification. Using existing knowledge and basic design components from

prior work,[198] a new mobile phone microscope was designed and characterized on ten different smartphones from four different manufacturers. The optical design used an achromatic objective with a 20x wide-field eyepiece, which directed the optical signal into the CMOS smartphone cameras. By 3D printing acrylonitrile butadiene styrene plastic, each smartphone model had an accompanying adapter that simplified interfacing with the microscope. The optical housing, 2-axis sample stage, and plastic diffuser were also 3D printed. A threaded adapter focused on the sample image and made the system versatile enough for multiple imaging applications. Incorporation of a LED flashlight powered by a watch battery standardized illumination.[199] By testing smartphone models released over six years, the authors demonstrated that a five-megapixel camera performed as well as a low-cost microscope and scientific camera; cell phones with lower pixel density demonstrated relative performance limitations across both Apple and Android phones. However, the authors did note that the numerical aperture of the condenser (~0.4) ultimately limited the visual resolution of the device, even when higher numerical aperture objectives were used.[199] The authors also assessed the spatial dependence on magnification and found a spatial distortion of less than 8%, comparable to the 3-12% pincushion distortion observed on traditional microscopes. The feature size and overall magnification were controlled through the autofocus feature of each smartphone. Color balance issues between images and phones were balanced by disabling the automatic color and white balance adjustment through additional software. Unfortunately, the automatic sharpening that each manufacturer uses is different and non-uniform, requiring phone-specific proprietary methods to remove lost information.[199] While some imaging artifacts remain as a result of user-limited software control, at least among the most common manufacturers, the increased prevalence of smartphones and data plans worldwide demonstrates the strong potential for use with low-resource, point-of-care diagnostic assays.

Molecular TB Diagnosis

Molecular diagnosis detects the genetic material (DNA) or non-genetic material (TB-specific proteins, carbohydrates, and lipids) of TB. Alternatively, molecular detection can detect the host's immune response to TB antigens instead of TB itself. Most molecular detection assay development for TB has focused on the isolation and amplification of nucleic acids. Because of the breadth of this topic, the discussion focuses on the most common commercial methods for TB diagnosis and methods previously developed by the Haselton Research Group.

Nucleic acid isolation and genetic detection.

Many nucleic acid extraction technologies, and those developed in this dissertation, rely on the binding of nucleic acids to silica. How this occurs is not entirely understood, but it is generally accepted that an electrostatic interaction is partially responsible (**Figure 2.6**). Under most experimental conditions, nucleic acids and silica are both negatively charged and do not interact. Placing silica in acidic conditions decreases the density of negatively charged silanol groups on the surface via protonation, which reduces the electrostatic repulsion between nucleic acids and silica and improves binding. For this reason, the pH of the chaotropic binding buffer should be at the pKa of the silica surface used for solid-phase purification.[200] Layers of water molecules, which maintain solubility in aqueous solutions, typically surround both nucleic acids and silica. Chaotropic salts, such as guanidine thiocyanate, may help disrupt this hydrate layer by forming cationic salt bridges between nucleic acids and silica.[201] This disrupts the structure and charge of water, while organic solvents like isopropanol help dilute water molecules and dehydrate DNA.[202] Removal of the salt and addition of base reverses this electrostatic interaction and deprotonates the silanol surface, which results in nucleic acid elution into the low-salt solution (**Figure 2.6**).[200] The total amount of nucleic acids that can bind to a silica surface ultimately depend on the solution pH, ionic strength, type and valence of electrolyte(s), and nucleic acid confirmation (e.g., plasmid, linear, supercoiled) and length (e.g., fragmented DNA, intact genomic DNA).[200, 203]

The most widely implemented form of genetic detection for TB diagnosis is the GeneXpert MTB/RIF assay, endorsed by WHO in 2010. Intended to be an "on-demand, near-patient PCR assay," the Xpert system automatically performs most of the sample preparation and PCR detection in a contained cartridge. Before placing a sample in the cartridge, two parts of proprietary NaOH and isopropyl alcohol sample treatment are added to one part sputum, shaken to mix, and incubated for 15 minutes at room temperature; this helps reduce sample viscosity and decontaminates the sputum with a greater than eight log reduction in colony-forming units (CFU) of viable TB. Up to three milliliters of this digested sample containing a maximum of one milliliter of patient sputum is placed into the cartridge. TB DNA is extracted from the sample and then amplified using a hemi-nested PCR assay from lyophilized reagents in the cartridge, with the entire processing taking approximately two hours.[53]

Hemi-nested PCR works by amplifying the *rpoB* gene using five different sets of primers and fluorescent probes. This 81-base gene is specific to *M.tb* complex species and mutated in 95% to 98% of cases of RR-TB. Since RR-TB usually also displays isoniazid resistance, detection of mutations in the *rpoB* gene can find a large majority

of MDR-TB cases. For a positive TB diagnosis, two of the five molecular probes must meet the PCR cycle threshold (C_t) within two PCR cycles of one another. Failure of one or more *rpoB* fluorescent probes failing to hybridize to the amplified DNA determines rifampin resistance; quantitatively defined by a >3.5 cycle gap between the earliest and latest *rpoB* signals or complete failure of one or more probes to amplify. The assay also contains a known amount of *Bacillus globigii* spores, which serve as a positive control for extraction and amplification.[53]

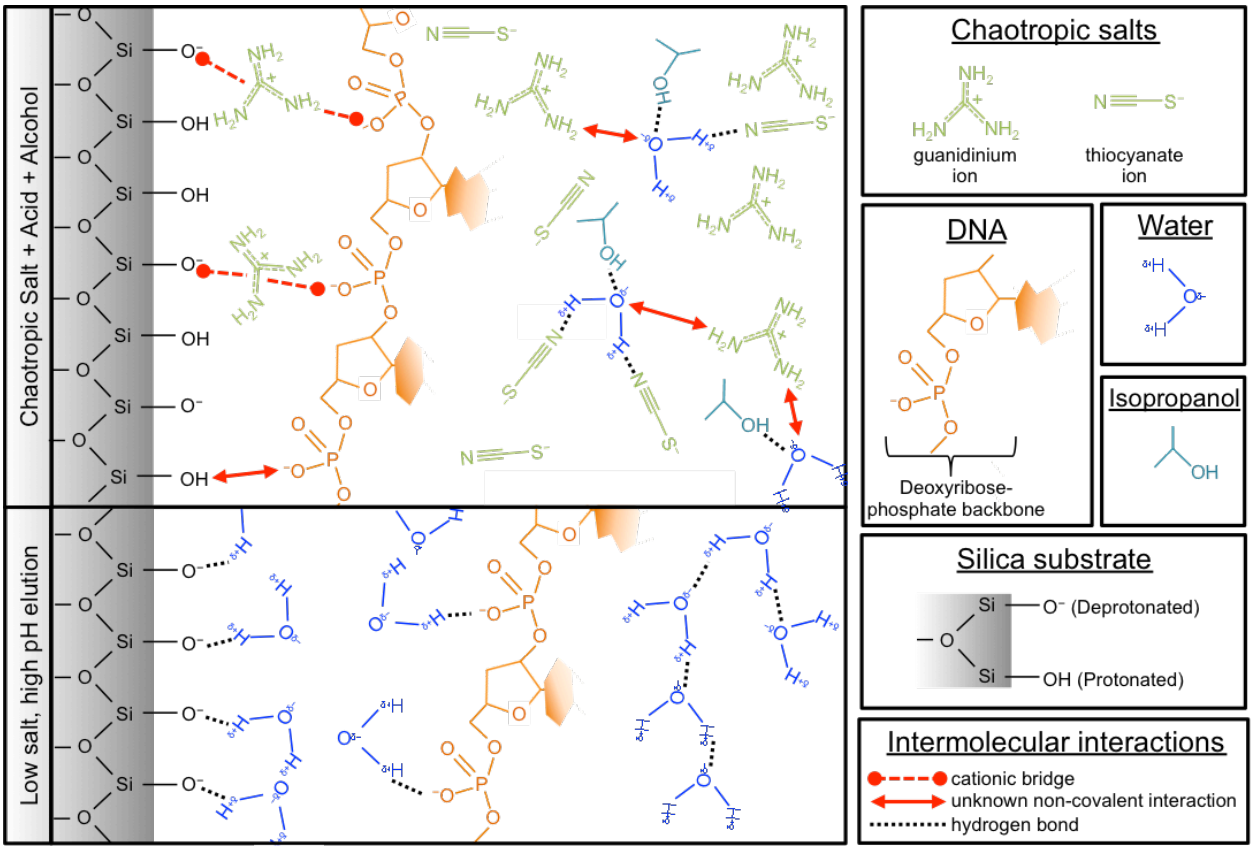

Figure 2.6. Hypothesized interactions between silica (black), DNA (orange), water (blue), chaotropic salt guanidine thiocyanate (green), and isopropanol (teal). It is thought that guanidine thiocyanate disrupts hydrate layers surrounding DNA and silica by creating cationic bridges (red dashed circle arrows) and generally disrupting hydrogen bonding. Using a binding buffer where the pH = pKa, the silanol groups can be protonated, reducing the surface density of negative charges, which can help improve DNA adsorption to silica (red dashed triangle arrows). Isopropanol aids in water dilution and interruption of the hydrate layers. The electrostatic changes reverse when placed in a low-salt solution, and DNA desorbs from the capture matrix.[200-202]

The initial study performed by Helb *et al.* demonstrated the specificity of the Xpert MTB/RIF for *M.tb* complex species, with 20 NTM species. *M. intracellular* 35790, *M. abcessus*, *M. thermoresistable*, and *M. xenopi* showed low amplification levels of at least one *rpoB* probe, but no NTM species met the less than two cycles threshold for diagnosis. The authors also demonstrated detection of low-levels of *M.tb* (200 CFU/mL) in high concentrations (10^6 CFU/mL) of NTM. Only under one condition (10^6 CFU of *M. malmoense*) produced two weakly positive *rpoB* molecular beacon signals with a cycle gap of 5.2, which, when added to mixed samples containing 200 CFU of drug-sensitive *M.tb*, produced false-positive results for rifampin resistance. Increasing the concentration of *M.tb* to 300 CFU resulted in an accurate diagnosis of rifampin-sensitive TB; this indicates the possibility of co-infection of the two species causing a false-positive result. The reported Xpert MTB/RIF assay sensitivity, specificity, and limit-of-detection are 98.6%, 100%, and 131 CFU/mL, respectively.[53] However, external validation has found that in practice, these values are 83%, 95%, and 786 CFU/mL, respectively.[54]

In 2017, Chakravorty *et al.* released a publication describing the development and testing of a new version of the Xpert TB assay, known as the Xpert MTB/RIF Ultra.[204] The study's goal was to improve assay performance and improve detection of *rpoB* point mutations falsely recognized by the original Xpert assay. In addition, Xpert was shown to have poor performance in smear-negative samples and HIV+ patients.[52] First, to improve the detection of *rpoB* mutations, a fourth *rpoB* molecular beacon was added to the assay. In addition, the Ultra assay substitutes two molecular probes for *M.tb* multi-copy genes IS*6110* and IS*1081* in place of the original *rpoB* probes originally used for *M.tb* specificity. Because the Xpert device is limited to six fluorescent channels, the IS*6110* and IS*1081* probes share the same fluorescent channel.[204] Comparisons of the original assay to the Ultra assay used a combination of clinical and simulated spiked samples, assessing sensitivity, specificity, and LOD. For Xpert, these values were 81.0%, 98.7%, and 112.6 CFU/mL, respectively. Ultra outperformed on sensitivity and LOD, with reported values of 87.5% and 15.6 CFU/mL, respectively. Though the original Xpert misidentified two clinical samples as false positives, the Ultra assay had comparable specificity and accuracy for rifampin resistance detection. The Ultra assay also detects rifampin hetero-resistance, which the original assay cannot detect.[204] External validation reported similar diagnostic sensitivity and specificity, and the Ultra outperformed Xpert in smear-negative samples. Unfortunately, the improved sensitivity achieved by Ultra was at the cost of diagnostic specificity, with the reported Ultra specificity being 96% versus 98% for the original Xpert assay.[37]

Before the development of Xpert, the Roche AMPLICOR MTB test was one of the only commercially available methods for TB diagnosis via genetic biomarker detection.[205] When first developed, nucleic acid detection was in its infancy, and assays generally took a minimum of two weeks for laboratory confirmation of TB infection. However, the AMPLICOR test produced results the same day as specimen collection, hoping to reduce the number of patients lost to follow-up. To perform the assay, patient sputum samples were decontaminated, and cells in the sample were washed via centrifugation before lysis. After neutralizing the lysed product, PCR was used to amplify a 584-base region of the 16s rRNA gene in mycobacteria. Uracil was included in the PCR mixture in place of thymine to prevent inter-sample contamination. Following amplification, samples could be cleaved using uracil-*N*-glycosylase, effectively degrading any contaminating amplicons from previous reactions; innovative for its time, improvements in nucleic acid amplification technology and understanding have reduced contamination errors and made the addition of uracil and uracil-*N*-glycosylase unnecessary for most assays. After 35 amplification cycles, the PCR product was bound to DNA probes specific for MTBC species. Hybridization of probes was measured using an avidin-Horseradish peroxidase conjugate-tetramethylbenzidine substrate system, which produces a colorimetric product quantified by absorbance spectrophotography at 450 nm. The reported sensitivity and specificity of the AMPLICOR MTB assay were 61.8% and 98.5%.[205] Though the diagnostic sensitivity is significantly lower than most current assays the ability to detect 6/10 TB cases on the same day patients sought care aimed to make a positive and reliable impact on TB case detection, with results that could be confirmed using traditional culture techniques. Because the sequence for 16s rRNA is genetically conserved across all mycobacterial species and because the reporter probe sequences are not reported, how the assay achieves specificity for TB remains unknown. It is likely that specific short-sequence or single point variations exist between MTBC and NTM species would allow for the species-specific differentiation from the amplified 16s rRNA sequence, but this is entirely speculative.

With time and improved technology and understanding, the AMPLICOR MTB assay performance also improved. In 2006, Ozkutuk *et al.* evaluated the efficacy of the improved Roche Cobas® Amplicor MTB test in both pulmonary and extrapulmonary samples. Though the technical aspects of the assay remained similar (e.g., amplification of 16s rRNA gene with uracil, ELISA-like colorimetric detection), the inclusion of an internal amplification control provided information on the presence of PCR inhibitors that may reduce the assay's clinical sensitivity.[206] With this addition, the clinical sensitivity for pulmonary TB samples rose to 76%, with a specificity of 100%, though the diagnostic sensitivity was 92% in smear-positive samples. For extrapulmonary samples, the

sensitivity and specificity were 42% and 100%, respectively.[206] Though these results are similar to those reported by other confirmatory studies, the sample type (e.g., bronchoalveolar lavage) and decontamination diluted the samples, resulting in samples too dilute to detect, particularly in cases of smear-negative TB accurately. In addition, the heterogeneity of samples and sample volume limitations are compounding factors to decontamination and dilution.[206]

Several other assays use genetic analysis after traditional diagnosis methods, such as culture or sputum smear microscopy, for antibiotic resistance determination. An example is the Hain Lifescience GenoType MTBDR*plus* assay.[207] This dissertation focuses on identifying TB cases through the development of new diagnostic assays and does not address antibiotic resistance detection. Therefore, these technologies were not explicitly included in the literature review since it is outside the scope of this work.

The Haselton Research Group has many publications extracting DNA and RNA from biological matrices using magnetic particles,[91, 203, 208-211] with multiple projects focusing on isolating TB DNA.[203, 210, 211] Hali Bordelon developed an automated magnetic bead extraction cassette for isolation of nucleic acids,[203, 208, 209, 211] and was used to isolate of cell-free TB DNA from clinical urine samples. The extraction cassette consisted of a single length of uniform diameter tubing containing volumes of extraction buffers separated by air gaps created due to surface tension of the liquids, known as surface tension valves (**Figure 2.7**).[203, 208] This tubing could be loaded onto an automated system driven by a gear and motor (**Figure 2.8**), manipulating the tubing up and down (**Figure 2.8B**) or around a circular cassette holder made to drive multiple extractions simultaneously and asynchronously (**Figure 2.8A**).[209, 211] The stationary magnets placed outside the tubing mixed and recollected silica-coated magnetic beads, which served as the nucleic acid capture matrix.[203] Alternatively, a magnet could be manually passed along the length of the tube, performing the same mixing and recollection actions without a need for external mechanical equipment (**Figure 2.7A**).[203, 208] Following recollection, the beads were passed through the surface tension valves from one extraction buffer to another, physically isolating each buffer in the same container. Once eluted, the nucleic acids could be collected and used in a downstream genetic analysis; PCR assessed extraction efficiency and performance. Bordelon *et al.* demonstrated reliable TB DNA extraction from urine, with an extraction efficiency of ~50% from a starting volume of one milliliter of urine. This efficiency was consistent across spiked DNA concentrations from 5×10^3 to 5×10^8 copies/mL.

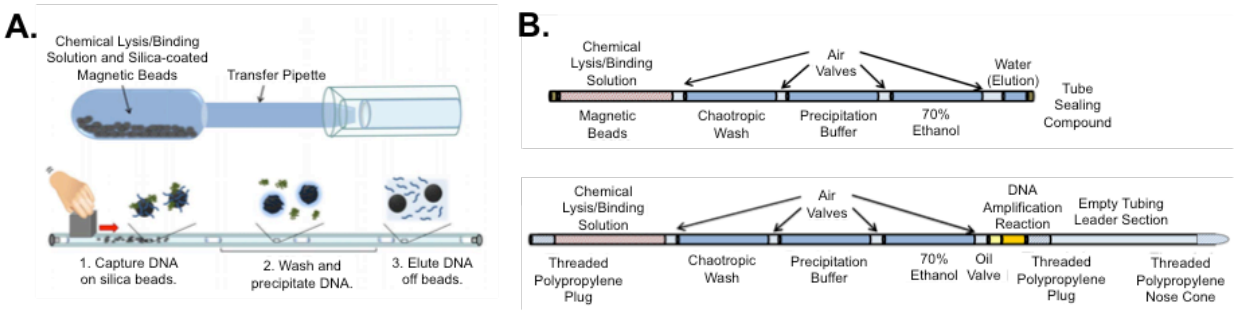

Figure 2.7. Design and implementation of extraction cassettes using surface tension valves. **A.** Sample was drawn into a transfer pipette containing lysis/binding reagents and silica magnetic beads. Once combined, this mixture was loaded into the cassette, where a magnet manually mixed, recollected, and transferred the magnetic beads between processing solutions. **B.** Design of extraction cassette for manual manipulation or use with a circular cassette holder (top) or a linear actuator driving both extraction and downstream amplification in the same cassette (bottom). Figure adapted from cited references.[203, 210]

Bordelon further adapted and tested this system with clinical samples, using lyophilized binding reagents (e.g., guanidine, silica-coated magnetic beads) in a transfer pipette, which rehydrated upon sample introduction. In addition, a total of 5×10^8 copies of a 120-base pair (bp) DNA target for mouse glyceraldehyde 3-phosphate dehydrogenase was included in the extraction reagents and used as a control to determine if the extraction and PCR reaction were successful.[211] The extraction efficiency was calculated for both spiked IS*6110* DNA (140-bp) and the mouse glyceraldehyde 3-phosphate dehydrogenase, with reported values of 46% and 36%, respectively;[211] the difference attributed to the 20-bp length difference in the two DNA strands, given longer DNA is more efficiently extracted than short DNA.[203] When detecting the extracted mouse control DNA from urine in patients, control mouse DNA was detected in 97.5% of one-milliliter samples from Peru and 97.7% of five-milliliter samples from South Africa. Across both patient cohorts, there was no statistical difference in C_t for TB IS*6110* trans-renal DNA or the mouse control DNA between the TB-infected and TB-uninfected patient populations. When assessing patient samples by their HIV status, there was a statistical increase in the C_t of detected trans-renal IS*6110* DNA between TB/HIV+ co-infected individuals and TB-uninfected/HIV+ individuals, but this statistical increase was not seen for the control mouse DNA, indicating an increase in the amount of trans-renal TB DNA in HIV+ patients.[211] It is known that malnourished or immunocompromised individuals can have renal barrier dysfunction, which may explain these results.[212, 213] Therefore, more research is needed to determine if the detection of trans-renal TB DNA is practical for clinical use beyond HIV+ patient populations.

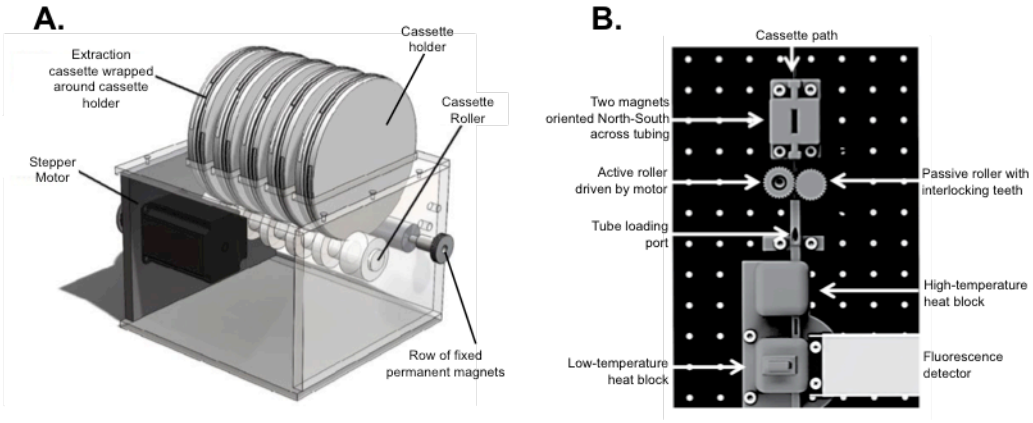

Figure 2.8. Automated extraction systems using surface tension valve extraction cassettes. **A.** Extraction cassette was wrapped around a circular holder, and a stepper motor drove the movement of the cassette past stationary magnets, which mixed, collected, and transferred the beads between each extraction buffer. The drive belt is not shown. **B.** Linear cassette orientation, using a gear and motor to manipulate the cassette directly. Magnets were placed along the cassette path. In this case, two temperature blocks were placed below the magnets, performing fixed-temperature PCR after extraction in the same cassette. Figure adapted from cited references.[91, 209]

The automation and use of surface tension valves in the extraction cassette were taken a step further by both Russ *et al.* and Creecy *et al.* Russ *et al.* developed a fixed temperature PCR machine for downstream nucleic acid detection.[91] Specifically, after extraction, magnetic beads were passed into a PCR reaction mix solution (containing polymerase, primers, and SYTO 82 DNA intercalating dye), which was surrounded by mineral oil to prevent evaporation (**Figure 2.7B**). The PCR reaction chamber was linearly cycled between two fixed-temperature heaters to cycle the temperature of the reaction (**Figure 2.8B**), similar to the original PCR method developed by Mullis in 1985.[214, 215] The low-temperature heat block had an open window where a fluorescence detector could quantify DNA amplification during each cycle. For extraction of 5×10^6 copies of IS*6110* from 100 µL of Tris-EDTA buffer, the average reported C_t value on the automated fixed-temperature PCR following automated in tube extraction was 25.5 ± 1.4 cycles, which was statistically higher than negative control samples, which had an average C_t value of 34.0 ± 2.6 cycles. PCR efficiency for the fixed-temperature, variable-position PCR reaction was similar to traditional PCR machine using a fixed-position with variable-temperature.[91] The two temperature set points minimized nonspecific primer bind interactions at lower temperatures while also limiting polymerase degradation or denaturation at higher temperatures. However, the inability to cycle temperature higher and lower than the desired

reaction temperature results in slower thermal diffusion, resulting in a longer cycle time and longer total time to complete amplification.[91]

Creecy *et al.* used the extraction cassette method described by Bordelon *et al.* to detect TB DNA using integrated loop-mediated isothermal amplification (LAMP) in the final chamber. TB DNA was extracted from simulated sputum samples containing chemically inactivated *M.tb.*[210] The exact chemical composition of the chaotropic and wash buffers differed slightly from prior publications to improve TB cell lysis, but the basic principles and steps for nucleic acid extraction in the cassette were the same. Instead of performing fixed temperature PCR in the final chamber as Russ *et al.* performed, LAMP was implemented instead for readout, with the amplification reaction chamber held at a constant 65°C, with SYTO 9 used for fluorescent amplification quantification. By using a faster polymerase, the time to amplification was reduced up to 4-fold, which significantly shortened the total assay performance time. The LAMP reaction itself performed as well as PCR, and the authors demonstrated efficient extraction of DNA from simulated samples containing 10^3 bacteria/mL, which is 10x lower than the LOD for sputum smear microscopy.[210]

While novel, the extraction cassette technology developed by the Haselton Research Group has significant limitations. A critical shortcoming of Bordelon *et al.*[211] was that the sample urine volume for extraction was limited to 5 mL; however, the average volume of micturition is ~162 mL,[216] signifying that a potential 97% of voided urine was not used in DNA extraction. These volume limits are typical in commercial extraction kits, accommodating less than 1 mL per extraction.[85] These results could improve by using larger sample volumes, as the added benefit of essentially unlimited sample volume allows for maximal nucleic acid recovery, something that is particularly important for detecting very dilute nucleic acids or other biomarkers.

In addition, prior automated extraction devices were difficult to load because they required precise length dimensions for both the surface tension valves and the wash/elution chambers within the tubing; without this, the extraction would fail. This necessitated pre-loading of the sample tubes for untrained users. Investigations also demonstrated that assay tubes were difficult to pre-load and then ship to rural clinic sites without the tension valves failing (unpublished data).

In addition to the extraction technologies developed, the Haselton Research Group has also worked to address PCR failures caused by inadequate sample prep and PCR inhibitors by developing a PCR system that can adapt to the presence of these contaminants in a reaction.[217] Known as Adaptive PCR, this adaptation of the Nobel

Prize-winning method relies on monitoring the molecular hybridization events occurring in a reaction instead of indirect measurements through temperature. It is well known that the exact conditions required for a successful PCR reaction are very narrow, and the introduction of contaminants remaining after sample preparation often results in PCR failures. These failures can cause false-negative diagnoses without appropriate controls while also limiting who can implement PCR for diagnostic purposes. To directly monitor hybridization events, synthetically made DNA that is a "mirror-image" to naturally occurring right-helical D-DNA, known as L-DNA. L-DNA does not interact or anneal with D-DNA is not enzymatically modified by naturally occurring enzymes, which interact with D-DNA. However, the basic physical properties of D-DNA apply to L-DNA (e.g., strand melting temperature, conformational changes in different salt conditions), making L-DNA a perfect reporter system for molecular changes in DNA throughout a PCR reaction.[217]

To use L-DNA as a reaction mechanism reporter, template strand L-DNA was functionalized with a fluorescent probe (HEX) on one strand and a quencher on the other strand. The primers were functionalized with a quencher or colored fluorophore (TexasRed), depending on which template strand the primer was complementary to. When the sample is heated and the template DNA melts, the fluorophore and quencher are physically separated as the hydrogen bonds melt, generating a HEX fluorescent signal, which indicates that the DNA has sufficiently melted. In addition, a TexasRed signal is observed because the primers cannot hybridize to DNA at high temperatures. Once detected, the temperature is cooled, and the reaction is monitored for primer annealing, which is seen through reduced TexasRed fluorescence resulting from co-localization of the fluorophore and quencher. Upon annealing, the temperature was turned up again and cycled up and down, with the switch point for temperature change controlled completely by fluorescence readings collected in real-time from the reaction tube and a control algorithm. In this case, SYTO 9 reported amplification of D-DNA alongside the HEX/TexasRed L-DNA melting and hybridization events, as is traditionally used in qPCR quantification.

Adams *et al.* demonstrated successful amplification of a 77-mer IS*6110* D-DNA template using the L-DNA adaptive PCR reporter system while also demonstrating through passive temperature measurements that the algorithm-determined switch points for melting and annealing occurred at the optimal melt/primer annealing temperatures determined using traditional melt analysis on a traditional PCR machine. In addition, this system was comparably amplified DNA at ambient temperatures that would typically exceed (35°C) the recommended operating temperatures for traditional PCR machines (18−30°C). The system compensated for the changed heating/cooling

kinetics by increasing the cooling time during each cycle. Standard PCR, however, which uses fixed heating/cooling periods, demonstrated delayed amplification, likely because inadequately cooling did not bring the reaction down to the necessary primer annealing temperature.[217] Adaptive PCR with L-DNA reporting also comparably amplified DNA in PCR reactions containing additional DNA stabilizer magnesium chloride, which should typically impact PCR success. In addition, the common contaminating nucleic acid extraction reagent ethanol was included in PCR reactions at up to 16%, and the adaptive monitoring method still successfully amplified DNA, albeit with some fluorescence reduction. For comparison, as measured through the maximum fluorescent signal achieved from D-DNA amplification, the fluorescent signal in traditional PCR decreased by ~90% at 5% ethanol. The reaction totally failed with 8% ethanol, whereas signal in adaptive PCR was reduced only 16% for reactions containing 8% ethanol, decreased ~65% containing 16% ethanol, and did not entirely fail until the PCR reaction contained 24% ethanol.[217] Combined, these data demonstrate that adaptive PCR overcomes sample contamination effects that may have otherwise resulted in failed DNA amplification by dynamically adapting to the chemical composition of the PCR reaction both temporally and thermally. Since the initial publication, the Haselton Research Group has demonstrated successful amplification of RNA targets using adaptive PCR and multiplexing RT-qPCR reactions for simultaneous amplification of different viral targets in the same tube.[218]

Non-genetic molecular detection.

Non-genetic molecular diagnosis TB aims to identify *M.tb*-specific proteins, carbohydrates, or lipids in patient samples. Because many of these markers are shared with *Mycobacterium* spp. or are not specific to just *M.tb* infection, some non-genetic molecular strategies also involve detecting an immune response to *M.tb*. Lipoarabinomannan (LAM) is a mycobacterial-specific glycolipid highly expressed in *Mycobacterium* spp.[219] The high expression and shedding of LAM from *M.tb*'s surface make it an excellent potential biomarker and a focus for molecular diagnostic assays. LAM is also known to pass into patient urine and is inefficiently filtered by the kidney,[220] making LAM detection in urine an optimal sample for TB detection. Using urine instead of sputum is beneficial in patients who cannot produce sputum or may have a low bacillary load. It is also useful for extrapulmonary TB diagnosis, particularly when a biopsy cannot be performed; this results in no diagnostic confirmation. Urine is produced in large volumes, and collection is very easy and inexpensive relative to most biological samples, further adding to the potential benefits of a urine-based LAM assay. However, most of the

structure is conserved across all *Mycobacterium* spp. the terminal carbohydrate cap of LAM is modified differently in NTM (phospho-*myo*-inositol cap) than it is MTBC (mannose cap), providing a very specific antigen target for immunoassay development.

In 2012, the first studies using the Alere™ Determine™ TB LAM Ag Test (AlereLAM)[221] were published before its release in 2013. The immunochromatographic strip test assay works similar to other lateral flow assays, such as pregnancy tests, to detect LAM. An anti-LAM polyclonal antibody conjugated to gold nanoparticles binds LAM in the sample. As the sample moves across the test strip, LAM binds a second polyclonal anti-LAM antibody on the test line, effectively creating an ELISA-like sandwich creating a red line to confirm LAM positivity. The AlereLAM lateral flow testing has undergone extensive external testing since its release, and it has suboptimal sensitivity and specificity in most patient populations. Unfortunately, the sensitivity and specificity were both reported at 66% in patients screened with only AlereLAM.[221] When the AlereLAM test was used in parallel with sputum smear microscopy for diagnosis, the reported sensitivity and specificity were 60% and 96%, respectively.[221] Smear microscopy performed similarly to the lateral flow test, but in cases of extrapulmonary TB, sensitivity for the AlereLAM increased to 41%, compared to 0% for microscopy. When investigating specific patient populations, the AlereLAM test most benefitted patients with a CD4 count ≤ 200/μL, with the assay detecting 50% of TB cases in sputum scarce or smear-negative TB-HIV co-infected individuals with a CD4 count ≤ 200/μL. The external validation also showed that a positive AlereLAM test was statistically associated with a CD4 count ≤ 200/μL, even after accounting for other potential clinical parameters (e.g., hydration status) that could have impacted these results.[221] Despite its poor performance, the AlereLAM lateral flow assay reduces patient mortality in immunocompromised inpatients with HIV.[222] Therefore, WHO endorsed the test for use in patients with CD4 counts ≤ 100/μL, or in patients that are defined as seriously ill based on symptomology (>39°C body temperature, heart rate >120 beats per min, >30 breaths per min respiration, or unable to walk without walking aid or assistance).[223]

Because of the poor sensitivity of the AlereLAM lateral flow test, researchers have tried developing an improved LAM-based assay for TB diagnosis. The Fujifilm SILVAMP TB LAM (FujiLAM)[213, 224] assay is also a lateral flow assay, which uses monoclonal LAM antibodies specific for *M.tb*-LAM, binding to the mannose-cap found on MTBC LAM, in addition to a silver amplification step.[224] The silver amplification step is similar to the chemical processes performed in photographic development, where silver halide crystals catalyze silver ions in the developer solution into metallic silver in the presence of light. For use in lateral flow assays, the antibody-bound

gold nanoparticles act as a catalyst for reducing silver ions into metallic silver in the presence of a reducing agent. The precipitation of metallic silver is rapid, occurring in as little as 30 seconds, forming silver clusters 5−10 μm in diameter on the test and control lines. This method can amplify the gold nanoparticle signal by up to 100-fold.[225] The hope with these design differences was that more specific antibodies could improve both the sensitivity and specificity of the assay, as the polyclonal antibodies used in the Alere™ test are nonspecific for MTBC. Sometimes the AlereLAM has detected NTM infections because the antibodies bind the conserved backbone structures of LAM instead of the MTBC-specific mannose cap.[86, 224, 226] This lack of specificity results in potential misdiagnoses, treatment delays, and possible permanent health complications as a result. In addition, the authors note that the use of silver amplification in the FujiLAM assay detects LAM concentrations 30x lower than the AlereLAM LOD,[224] which theoretically should also help improve diagnostic sensitivity.

FujiLAM and AlereLAM tests were used in a paired urine analysis in patients with HIV and severe immunosuppression (average CD4 count of 86 cells/μL), with microbiological confirmation of TB disease as the diagnostic standard. Overall, across 968 patients, the FujiLAM detected 70.4% of cases compared to 42.3% for the AlereLAM, achieving a significantly higher diagnostic sensitivity. Surprisingly, the FujiLAM had a slightly lower diagnostic sensitivity (90.8%) than the AlereLAM (95.0%). Similar to the trend observed with the AlereLAM, the FujiLAM test had a higher sensitivity (84.2%) in patients with CD4 counts <100 cells/μL, compared to 57.6% for the AlereLAM. When patients had a CD4 count >200 cells/μL, the diagnostic sensitivity of each assay reduced to 44% and 12.2%, respectively.[224] When a LAM lateral flow test and smear microscopy were used together for a diagnosis, the diagnostic specificity of FujiLAM and AlereLAM improved to 95.7% and 98.2%, respectively. However, both assays had lower diagnostic sensitivity in the composite analysis, with 64.9% for FujiLAM and 38.2% for AlereLAM.[224] Nonetheless, the improved diagnostic sensitivity of the FujiLAM could potentially to further reduce mortality in severely immunocompromised patients with HIV.

The FujiLAM and AlereLAM were also assessed in parallel for pulmonary TB diagnosis in children since children often cannot produce sputum samples and are disproportionately impacted by the lack of non-sputum TB diagnostics. A total of 204 children were assessed in a similar paired manner as described previously, using both LAM assays and microbiological confirmation. The diagnostic sensitivity for FujiLAM and AlereLAM were similar, reported at 42% and 50%, respectively. Both of these values were lower than Xpert sputum confirmation at 74%. As expected, the sensitivity was higher in children with HIV (60%) and malnourished children (62%).[213] The

diagnostic specificity in the pediatric population for each assay was 92% for FujiLAM and 66% for AlereLAM, with children two years or older exhibiting higher diagnostic specificities of 96% and 72%, respectively.[213] The low specificity of AlereLAM is consistent with prior studies and hypothesized to be due to fecal contamination of the urine samples, which is known to reduce AlereLAM's specificity.[221, 227] The urine collection method was not recorded, however, so this could not be confirmed.[213] If this were the case, then the use of monoclonal antibodies in the FujiLAM test would suggest the lateral flow has greater robustness to sample contamination from NTM or other environmental/biological contaminants that cross-react with the AlereLAM. Though the small sample size makes the conclusions of this study very limited, this study suggests that FujiLAM could be useful as a rapid "rule-in" diagnosis for TB diagnosis in children with a high probability of infection, with secondary confirmation using microbiological analysis.[213] Further studies also need to be performed to determine how both assays perform in children with extrapulmonary TB.

There are only two methods that can definitively diagnose latent TB in addition to active TB disease, and those tests look at the immune response of the patient to TB antigens instead of looking for the presence of TB itself. This technique is novel compared to the other assays described, given the amount of TB in a patient's system when they have latent TB is too low for even the most sensitive of assays to detect. The first method, developed over a century ago, is the tuberculin skin test (TST) or Mantoux test is most commonly used to screen individuals for TB, particularly in healthcare workers in low-caseload countries. The test has had a few iterations, and the version used today contains a purified protein derivative from *M.tb* culture. To perform the test, a healthcare worker intradermally injects 100 µL containing 5 tuberculin units in the forearm. After 48 h to 72 h, a healthcare worker reads the test. If the patient has TB, a visible reaction to the injected material occurs, and the size of the raised welt is associated with TB infection and the long-term risk of developing TB infection in patients without symptoms.[228, 229] Generally, a TST is considered positive if the size of the welt is 10-mm in diameter, though this recommendation can change based on patient geography and immune status.[229] Because the TST contains a variety of *M.tb* proteins, some of which are conserved across *Mycobacterium* spp., having received the TB vaccine (BCG) or previously having TB infection means the size of the reaction is not a factor in determining if a patient has LTBI. Patients with NTM infections also cross-react with the purified proteins in the injection. On the other hand, some patients can have a delayed hypersensitivity, where they do not react initially to the test but, upon repeat testing, overreact to the tuberculin injection.[230] For these patient populations, if they do not have access to other diagnostic methods, a false-

positive diagnosis and unnecessary treatment are possible. Because patients have to return to have the test read by their healthcare provider, a significant percentage (≤39%) of patients never return to have their test interpreted.[231] The reported sensitivity of the TST is widely variable based on the population tested and cut-off point used, varying from 59% to 100%. Specificity is generally higher and narrow, ranging from 95% to 100%.[230] In areas with high rates of NTM infections, the test's positive predictive value is significantly lower (100% vs. 32%).[230]

Because of the TST's limitations and our significantly advanced understanding of biology, science, and medicine, alternative methods for measuring the patient immune response have finally become available in the last two decades. Specifically, interferon-gamma (IFN-γ) release assays (IGRA) are excellent alternatives to the TST, with examples including the QuantiFERON® TB-Gold In-Tube test (and the newer QuantiFERON®-TB Gold Plus) and T-SPOT®.*TB*.[49] These tests collect patient blood into tubes containing TB-specific antigens (ESAT-6, CFP-10, and TB 7.7, or some combination thereof). These antigens are not conserved across *Mycobacterium* spp. and are found only in *M.tb*, providing assay specificity. When the patient's blood and antigens are mixed in the test tube, white blood cells recognize the antigens, and ultimately T-cells generate IFN-γ as part of the immune cascade. The amount of IFN-γ produced after 24 hours of TB antigen exposure is measured and compared to positive and negative controls, measured simultaneously using ELISA. IGRA tests significantly improved diagnostic specificity since prior BCG vaccination or NTM infection does not produce a false-positive result.[50] When initially released, there was a high number of false-positive results with the QuantiFERON® TB-Gold, so it was recommended that the cutoff value be increased to eliminate these results and improve assay specificity.[232] External analysis of the three IGRA assays mentioned here reported diagnostic sensitivities via external analysis of 98.9%, 97.9%, and 96.9% for the QuantiFERON® Gold Plus and Gold In-Tube, and T-SPOT® tests, respectively.[233] The manufacturer-reported sensitivity for each assay was ≤92%,[234] ~97%,[235] and ≥97%,[236, 237] respectively. Diagnostic specificity was comparable across all three tests in external validation, at around 98%.[233, 235, 237] The specificity values reported by the manufacturer's were >98%,[234] ~98%,[235] and >98%,[236, 237] respectively.

A systematic review compared TST to IGRAs looked at TB risk and assay positivity in individuals emigrating from high- and low-caseload countries to low caseload countries, encompassing results from 51 studies.[231] The 10 mm cut-off for TST was used as part of the study selection criteria. Using results from these studies, the pooled sensitivity and specificity for the TST were reported as 88% and 42% for detection of active TB, whereas the IGRA test had pooled values of 88.9% and 70.8%, respectively, for active TB case detection; active TB

case detection was higher in IGRA tested individuals. When assessing LTBI cases, the prevalence of positive IGRA tests was statistically lower than TST cases compared to immigrants from low-incidence and high-incidence countries, which correlated with the number of patients recommended for LTBI treatment. Individuals with a positive IGRA were more likely to develop active TB in long-term studies than those who tested positive with TST.[231] These results combined suggest that expanding IGRA testing could be beneficial for LTBI case detection, particularly in individuals arriving from TB-endemic countries, due to its increased accuracy. However, this is conditional given the similar case detection rates of active TB between the two tests. While this study provided fundamental analyses and aimed to minimize heterogeneity, the wide variance in study variables limits the applicability of these results, mainly since most of the studies did not report the confounding factor of BCG vaccination status.[231] More studies are needed to truly determine the accurate efficacy of TST vs. IGRA for TB case detection, particularly in populations with endemic TB and high BCG vaccination rates.

CHAPTER 3 : LOW-RESOURCE NUCLEIC ACID EXTRACTION METHOD ENABLED BY HIGH-GRADIENT MAGNETIC SEPARATION

Adapted from: Pearlman, S. I.; Leelawong, M.; Richardson, K. A.; Adams, N. M.; Russ, P. K.; Pask, M. E.; Wolfe, A. E.; Wessely, C.; Haselton, F. R., Low-resource Nucleic Acid Extraction Method Enabled by High-Gradient Magnetic Separation. *ACS Appl Mater Interfaces* **2020,** *12* (11), 12457-12467. with permission from coauthors and the American Chemical Society ©.[238]

Abstract

Nucleic acid-based diagnostic tests often require isolation and concentration of nucleic acids from biological samples. Commercial purification kits are difficult to use in low-resource settings because of their cost and insufficient laboratory infrastructure. Several recent approaches based on the use of magnetic beads offer a potential solution but remain limited to small volume samples. We have developed a simple and low-cost nucleic acid extraction method suitable for isolation and concentration of nucleic acids from small or large sample volumes. The method uses magnetic beads, a transfer pipette, steel wool, and an external magnet to implement high-gradient magnetic separation (HGMS) to retain nucleic acid-magnetic bead complexes within the device's steel wool matrix for subsequent processing steps. We demonstrate the method's utility by extracting tuberculosis DNA from both sputum and urine, two typical large volume sample matrices (5-200 mL), using guanidine-based extraction chemistry. Our HGMS-enabled extraction method is statistically indistinguishable from commercial extraction kits when detecting a spiked 123-base DNA sequence. For our HGMS-enabled extraction method, we obtained extraction efficiencies for sputum and urine of approximately 10% and 90%, whereas commercial kits obtained 10-17% and 70-96%, respectively. We also used this method previously in a blinded sample preparation comparison study published by Beall *et al.*, 2019. Our manual extraction method is insensitive to high flow rates and sample viscosity, with capture of ~100% for flow rates up to 45 mL/min and viscosities up to 55 cP, possibly making it suitable for a wide variety of sample volumes and types and point-of-care users. This HGMS-enabled extraction method provides a robust instrument-free method for magnetic bead-based nucleic acid extraction, potentially suitable for field implementation of nucleic acid testing.

Introduction

Tuberculosis (TB) remains a global challenge with an estimated 10 million infections and 1.3 million deaths per annum worldwide.[239] Diagnosis of active, transmissible infections remains a significant public health challenge particularly in low-resource settings.[61, 240] Sputum is the standard patient sample used in both traditional microscopic inspection,[240] and nucleic acid-based tests such as GeneXpert.[51] However, some patient populations, including children and HIV-positive individuals,[241] have difficulty producing sputum. Therefore, there is interest in assessing other potential sample types. Urine, in particular, is easily and noninvasively obtained. Unfortunately, the highly dilute number of targeted biomarkers available for detection and the presence of inhibitors of downstream detection methods limit its utility in nucleic acid-based testing. One fundamental limitation to improved diagnostic sensitivity remains the development of sample extraction and concentration methods, which convert dilute biomarkers into pure, inhibitor-free samples appropriate for downstream detection.

Magnetic beads have become a valuable tool in laboratory separations because of their low cost, tunable surface chemistries, and the use of magnets for isolation using simple processing steps. Because of this, magnetic bead biomarker isolation assays have been applied to liquid sample handling and processing in point-of-care biomarker detection assays.[91, 92, 208, 242] Furthermore, magnetic beads are easily added to a variety of liquid samples, providing a high surface area for specific chemical capture of biomarkers, which can then be recollected to purify and concentrate biomarkers of interest.[243]

One of the critical features in magnetic bead-based extraction methods is efficient transfer of magnetic beads from one processing solution to the next. The most common approach for magnetic bead processing is difficult to implement in low-resource settings. This approach uses stationary magnets to apply a magnetic field across a sample volume to physically separate magnetic beads and bound analyte(s) from solution. After separation, the fluid phase is removed, subsequent processing solutions are added, and after removing the magnetic field and mixing beads into the new solution, the separation process repeated. While this method can be automated using robotics, without robotics, sample processing using this method is labor-intensive, requires careful removal of solutions by pipetting, and is inefficient for processing large volume samples.

Alternatively, magnetic beads can be moved between different processing solutions while the liquid solutions remain stationary. The advantage of this approach is that it decreases the number of manual steps, eliminates the requirement of liquid handling, and allows for simple automation of bead manipulation.[211, 242, 244, 245]

The challenge with this approach, however, is maximizing the applied magnetic force on the beads, which is needed to efficiently transfer magnetic beads across fluid interfaces between processing solutions while minimizing bead loss. Despite this shortcoming, at least one sample-to-answerstem based on this approach is commercially available, the Cobas® Liat® Polymerase Chain Reaction System (Roche Molecular Diagnostics, Pleasanton, CA).

The third potential handling method for magnetic bead processing is based on a flow-through design. In this approach, a moving suspension of magnetic beads flows through a magnetic field, and beads are collected on the inside wall of the tube. Successive processing solutions are then applied by flowing through the tube. However, unless the fluid is moved at a very low flow rate, the drag forces of the fluid flow dominate over the magnetic forces on the beads, resulting in low bead capture and retention. While this has the potential for processing large sample volumes, there is a trade-off between processing speed and bead retention. Implementing this approach requires the incorporation of a highly robust magnetic bead capture and retention method beyond that achievable with just an external magnet.

In a previous nucleic acid extraction study, we used a transfer pipette as a way to efficiently contain and mix lyophilized DNA binding reagents and magnetic beads with patient urine samples before automated extraction of TB DNA.[211] Wanting to further expand the use of the transfer pipette for simple and contained sample handling, we sought to develop a flow-through magnetic bead separation platform by incorporating a highly efficient method to retain the paramagnetic beads and their surface-bound nucleic acids within the transfer pipette. This report describes the incorporation of a ferromagnetic matrix, such as steel wool, into the flow path of the magnetic bead suspension, and the use of an external magnet to capture paramagnetic beads on the surface of the matrix (**Figure 3.1**). Once the magnetic bead-biomarker complex is magnetically separated from the fluid suspension, subsequent processing steps are performed using the transfer pipette squeeze bulb to expose pre-aliquotted processing liquids to the bead surface by flow-through fluid exchange, ultimately yielding a purified and concentrated biomarker.

Described as early as the 1930s,[95] the use of a ferromagnetic matrix for paramagnetic particle capture from a flowing fluid stream is described in early literature as high-gradient magnetic separation or HGMS.[246] This process and theory were implemented in the 1970s for mining and sewage applications as a means to capture weakly paramagnetic materials, such as CuO, from a flowing mine slurry, or to remove paramagnetic contaminants from flowing sewage or water supplies.[246-250] Previous reports using HGMS for biological applications focused on direct separation of erythrocytes from whole blood by chemically converting the hemoglobin in the cell from a

diamagnetic to paramagnetic state.[118, 119] Using columns of loosely packed steel wool, the paramagnetic cells were efficiently captured in the matrix in the presence of an externally applied magnetic field. Miltenyi *et al.* then went on to modify the steel wool/immunospecific magnetic particle separation system[122] to develop magnetic activated cell sorting (MACS®) in the 1990s.[123] These reusable columns were first composed of steel wool,[123, 126] which was then followed by stacked magnetic spheres, with samples passing between them.[131] Miltenyi's MACS® is the most prevalent use of HGMS in biological systems.

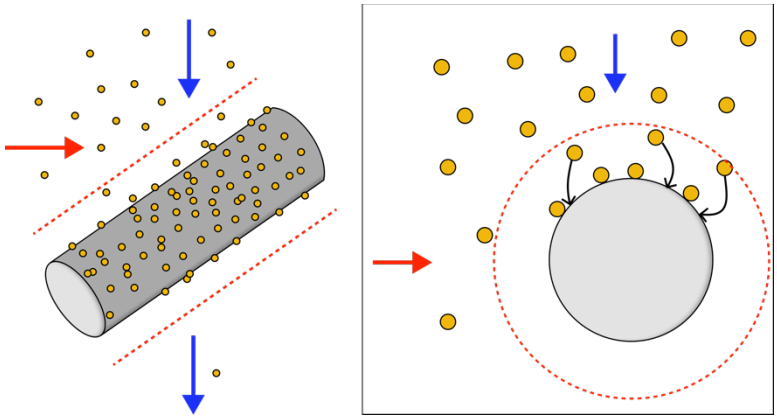

Figure 3.1. Simplified schematic showing capture of paramagnetic beads using high-gradient magnetic separation by a single matrix wire. An external magnetic field is applied (red horizontal arrow) to magnetize a ferromagnetic matrix. When a paramagnetic bead suspension flows through a magnetized matrix (blue vertical arrow), the high-gradient magnetic field around the wire strands in the matrix (red dashed line) creates a magnetic force on the beads that dominate over the viscous drag force in the region near the matrix, favoring bead capture on the wire surface

The method described in this paper was used previously and applied in a blinded sample preparation study sponsored by the Bill and Melinda Gates Foundation. In that study Beall *et al.*[251] compared our HGMS-enabled method to five other commercial extraction methods for total nucleic acid purification from sputum, whole blood, and stool. However, because the methods were not reported due to conflicts with commercial proprietary interests of the commercial participants, we describe here the details of the methods we used in this comparison study.

As described in this report, the HGMS phenomenon is robust, and for a variety of flows produced, the capture of paramagnetic beads in the steel wool matrix is consistently near 100%. The approach also offers the advantage of magnetic purification of biomarkers with minimal external contamination during processing. Device

performance and low cost of materials suggest that the HGMS phenomenon may be a promising approach for efficiently extracting nucleic acids from patient samples in low-resource settings.

Materials and Methods

Preparation of synthetic biological samples.

Synthetic sputum was prepared using a protocol generously provided by the nonprofit global health organization PATH (Seattle, WA): 114 mM NaCl, 33 mg/mL bovine serum albumin (BSA), 3.6 mg/mL phosphatidylcholine (MilliporeSigma, P3556), 4.7 mM $CaCl_2$, 47 mg/mL mucin from porcine stomach (MilliporeSigma, M2378), 6 mg/mL salmon sperm DNA (MilliporeSigma, D1626), and 2 mM sodium azide. These concentrations are based on sputum component concentrations as determined by Sanders *et al.*[252] The ingredients were mixed with a stir bar at 4°C overnight and then stored at 4°C. De-identified, disease-negative, residual urine samples were obtained from the Vanderbilt University Molecular Infectious Disease Laboratory. An exemption from IRB oversight was granted from the Vanderbilt University Institutional Review Board for use of these samples. Fifteen milliliters (15 mL) of each sample were pooled, pipetted into 1 mL aliquots, and stored at −80°C. Urine samples were pooled to minimize variability of PCR inhibitors expected among individual urine samples. These samples were thawed and allowed to equilibrate to room temperature before spiking with DNA. Synthetic sputum was stored at 4°C and warmed to room temperature with gentle mixing before spiking with DNA. One hundred microliters (100 µL) of synthetic sputum or pooled urine was spiked with 5µL containing a total of 5 x 10^6 copies of a synthetic 123-base DNA oligomer of the IS*6110* gene found in *Mycobacterium tuberculosis* (Integrated DNA Technologies, Coralville, IA). IS*6110* is a variably repeating DNA insertion element found in *Mycobacterium* tuberculosis, and is used as a specific diagnostic marker for infection.[241] The 123-mer sequence of the IS*6110* insertion sequence was previously reported in Ogusku *et al.*[253]

Extraction chemistry for biological samples.

The steps of the extraction procedure are illustrated schematically in **Figure 3.2A**. A DNA spiked sample was combined with 300 µL of binding buffer (4 M guanidine thiocyanate, 10 mM Tris HCl (pH 8), 1 mM EDTA (pH 8), 0.5% Triton X-100), 300 µL isopropanol, and 3 µL ß-mercaptoethanol in a 1.5 mL or 2 mL microcentrifuge

tube, and mixed through inversion. For urine samples only, 5.6 µg of poly-A carrier RNA (Qiagen, 1017647) was also added into the extraction mixture. Then, 2 mg (50 µL) of MyOne^{TM} Silane ^{TM} (ThermoFisher, 37002D) were added to the sputum or urine solution, mixed through inversion, and incubated at room temperature for three minutes, with inversions every minute to maintain bead suspension. A 200 µL pipette tip (Fisher Scientific, 02-707-505) containing 17 ± 1 mg of alloy 434 stainless steel wool (Lustersheen-online.com, SKU16162) was affixed to the end of a 3.2 mL transfer pipette (Fisher Scientific, 13-711-9D). The very bottom tip of the 200 µL tip was trimmed to remove void space located below the steel wool capture matrix (**Figure 3.2B** and **Figure 3.2C**). The solution was then drawn up and down using the squeeze bulb of the transfer pipette. Once well mixed and drawn into the pipette bulb, a magnet (K&J Magnetics, B666-N52) was applied to the steel wool matrix through the wall of the sample tube. As the bead solution was dispensed back into the original sample tube, the beads were captured in the magnetized matrix. Flow through was discarded, and magnet removed. Next, the beads were washed in the transfer pipette by passing 1.5 mL of a chaotropic wash (84% ethanol, 640 mM guanidine thiocyanate, 1.6 mM Tris HCl (pH 8), 160 µM EDTA (pH 8)) up and down through the pipette three times. The total volume was then drawn into the transfer pipette, and beads magnetically captured through the wall of a 2 mL microcentrifuge tube as previously described. Flow through was discarded, and the magnet removed. The previous step was repeated with 1.5 mL of a 70% ethanol wash, and flow through discarded. The pipettes were then allowed to sit in a clean microcentrifuge tube for one to two minutes to allow any residual rinse liquid to pool into the pipette tip, which was then expelled while maintaining bead capture in the steel wool matrix with the externally applied magnet. In addition, for sputum samples only, an additional rinse step was incorporated before eluting the nucleic acids off the beads. To perform this rinse, the magnet was applied to the matrix through the tube wall, and 100 µL of 10 Tris-HCl, 1 mM EDTA (TE) buffer, pH 8 was gently drawn up and then immediately expelled to rinse the beads without disturbing them. After rinsing, the magnet was removed, and 50 µL of TE, pH 8 was gently drawn up and down for approximately one minute to elute the nucleic acids, (approximately 20 times). The solution was then drawn into the pipette, and beads captured in the matrix using the magnet placed along the outside of a clean collection tube, into which the eluate was saved; qPCR was performed on the final sample eluate. Any beads that may have passed into the eluate were left in the sample and not removed. A single user processed triplicate samples in parallel in approximately 10-15 min. Triplicate samples with no spiked IS*6110* DNA were also performed, and no DNA was detected in these samples.

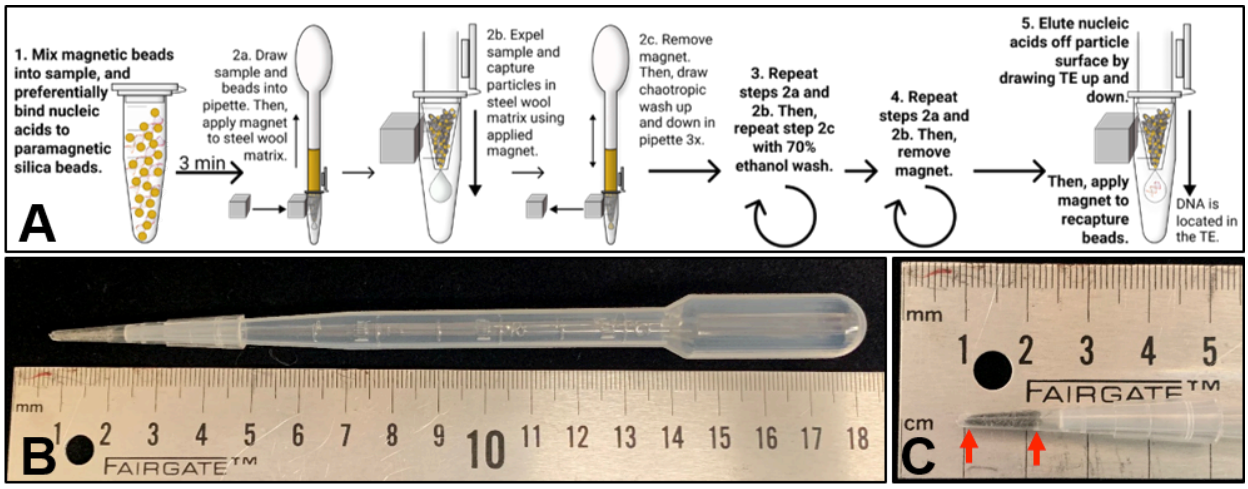

Figure 3.2. Design and detailed workflow of HGMS-enabled steel wool extraction device. **A.** The five processing steps of HGMS-enabled nucleic acid extraction. DNA is adsorbed to silca-coated paramagnetic beads using guanidine-based chemistry. Once bound, the solution is drawn into the transfer pipette, and an external magnet is applied to capture the magnetic beads in the steel wool matrix tip as the fluid flows through. The magnet is then removed to allow for release of the beads, which washes the bead surface and bound DNA. The magnet is then reapplied to recapture magnetic beads after each wash step. In the final step, the nucleic acids are eluted off the beads while the magnetic beads are retained in the steel wool. **B.** HGMS-enabled steel wool separator. **C.** Steel wool capture matrix. The matrix is placed between the two graduations on the pipette tip (indicated by red arrows), and the excess removed from the bottom.

Commercial extractions were also performed for comparison using the DNeasy Blood and Tissue Kit (Qiagen, 69504) for synthetic sputum, and the QIAamp Viral RNA Mini Kit for urine (Qiagen, 52904) according to the manufacturer's protocol. Both of these kits use guanidine-based chemistry to bind nucleic acids to the silica centrifuge columns. Qiagen recommends that the QIAamp Viral RNA Mini Kit be used for DNA extraction from urine because the included buffer, AVL, is optimized to inactivate the PCR inhibitors found in urine, unlike buffers found in their other commercially available kits. Extraction of both sputum and urine were also performed as per the manufacturer's protocol, with the Chargeswitch™ gDNA Mini Tissue Kit (ThermoFisher, CS11204), which is a magnetic bead-based extraction kit that uses guanidine-free extraction chemistry.

Determination of extraction efficiency using qPCR.

To determine the efficiency of the nucleic acid extractions, real-time PCR (qPCR) was performed using the Quanta UltraPlex 1-Step Toughmix (4X) (VWR, 10804-944) according to the manufacturer's protocol. We used this kit to most closely match the published methods performed in Beall *et al.*[251] The 123-base IS*6110* sequence from *M.*

tuberculosis was amplified using the forward primer 5'-CCTGCGAGCGTAGGCGT-3', reverse primer 5'CTCGTCCAGCGCCGCTT-3', and probe 5'-/56-FAM/CGACACATA/ZEN/GGTGAGGTCTGCTAC/3IABkFQ/-3'. All primers and probes were synthesized by Integrated DNA Technologies (Coralville, IA). The 20-mer primers in Ogusku *et al.*[253] were modified by trimming the 3'-ends to make 17-mers, which prevented the potential formation of primer dimers or hairpins.

The concentration of the primers and probes in the final PCR reaction were 600 nM of forward and reverse primers and 400 nM of probe. To the 1X master mix, 5 µL of the extracted sample was added for a total reaction volume of 20 µL. The samples were run according to the manufacturer's protocol; for the initial step, the samples were held at 50°C for 10 min, followed by a hold at 95°C for 3 min. The samples were then cycled from 95°C for 30 s to 60°C for 60 s for a total of 45 cycles in a Rotor-Gene Q thermal cycler (Qiagen, Germantown, MD). In addition to a no template negative control, an IS*6110* standard curve using 5 x 10^6 copies/reaction diluted 10-fold sequentially to 5 x 10^3 copies/reaction was included for conversion of C_t values to copies/reaction. Control samples containing 5 x 10^6 copies of DNA in a total of 50 µL TE were used to quantify the DNA eluate in a "perfect extraction" with 100% recovery and detection, which was used to calculate the percent extraction efficiency using post-extraction qPCR. Exact volumes of the final eluates were measured for accurate calculation of DNA recovery before performing PCR, because it was not uncommon for a few microliters of eluate to remain in the steel wool matrix after expulsion due to liquid surface tension. The PCR efficiencies of the standards, controls, and extracted samples were calculated using LinRegPCR software (available at http://linregpcr.nl), setting the fluorescence threshold above the fluorescence values of the negatives,[254, 255] and a statistical comparison was performed.

Baseline bead capture protocol for aqueous solutions.

A total of 800 µg (20 µL) of MyOne™ Silane ™ (ThermoFisher, 37002D) were mixed into 3 mL of 1x PBS (137 mM NaCl, 2.7 mM KCl, 10 mM Na_2HPO_4, and 1.8 mM KH_2PO_4, pH = 7.4) + 0.1% Tween-20 (final bead concentration of 267 µg/mL) and gently vortexed to combine. The solution was drawn into a 3.2 mL transfer pipette (Fisher Scientific, 13-711-9D), and 35 mg of Grade 000 steel wool (Global Material Technologies, Inc., Buffalo Grove, IL) was placed in a 200 µL pipette tip (Fisher Scientific, 02-707-505) at an approximate packing density of 0.91 g/mm^3. The very bottom tip of the 200 µL tip was trimmed to remove void space located below the steel wool matrix, and then the tip was affixed to the end of the transfer pipette. With a magnet (K&J Magnetics, DCX0) beside

the steel wool matrix, the bead solution was expelled (**Figure 2.1**, **Figure A1**, **Video A1**). Unless otherwise noted, flow rates less than 20 mL/min were used to process the samples.

To estimate the quantity of beads captured in the steel wool matrix, the beads in the flow through were concentrated using centrifugation at 3,086 x rcf for five minutes and re-suspended in an appropriate volume of PBS-T. This volume was variable, and was selected based on the quantity of beads in the sample. This was done to make certain the absorbance was within the linear range of the device and ensure accuracy of the measurement. Absorbance at 700 nm was measured in at least triplicate on a Nanodrop™ Spectrophotometer ND-1000, and the quantity of beads calculated using a standard curve (**Figure A2**). The quantity of beads captured was estimated by subtracting the quantity of beads located in the flow through from the quantity of starting beads.

Effect of steel wool matrix on paramagnetic bead capture.

The effect of steel wool quantity on capture was measured by including increasing quantities from 0 to 35 mg of Grade 000 steel wool placed in the pipette tip and performing the protocol for bead capture. Packing density was maintained as described across all steel wool masses. The effect of steel wool grade and alloy on capture was measured by incorporating different grades of 35 mg of steel wool of Grade 0000 (Lustersheen-online.com, SKU16246214), 000, 1, and 3 (Red Devil, Inc., 3332), steel wool alloys 434 (Lustersheen-online.com, SKU16162) and 316L (Lustersheen-online.com, SKU162751), or aluminum (Global Material Technologies, Inc., 166510-P) or copper (Rogue River Tools, 731847303978) wool in the pipette tip, or no matrix at all. Packing density was maintained across the different grades and materials.

Effect of magnet properties on paramagnetic bead capture.

The effect of magnet surface field on capture was investigated by measuring capture with cylinder magnets ¾" (1.91 cm) in diameter with surface fields increasing from 548 to 6180 Gauss (G) (K&J Magnetics, DC01, DCH1, DC2, DC3, DC4, DC8, DCX0) and performing the capture protocol outlined. The effect of magnet size on capture was also investigated by incorporating magnets increasing in size from 1/8" cube (0.32 cm) to 1" cube (2.54 cm), with a constant surface field of 6451 G (K&J Magnetics, B222-N52, B333-N52, B444-N52, B666-N52, B888-N52, BCCC-N52, BX0X0X0-N52) and performing the capture protocol outlined above.

Effect of flow rate and sample viscosity on paramagnetic bead capture.

The effect of flow rate on paramagnetic bead capture was measured using a stock solution of ™ at a concentration of 267 µg/mL in 1x PBS + 0.1% Tween-20. This solution was placed into a 60 mL syringe and loaded onto a syringe pump (RK TCI-II Syringe Pump). A 35 mg Grade 000 steel wool pellet was placed in the end of the pipette tip and trimmed as specified. This end was sealed onto a flexible tube affixed to the syringe. A total volume of 3 mL of the bead solution was passed through the steel wool with a magnet present (K&J Magnetics, DCX0). The uncaptured beads were centrifuged and measured as previously outlined. In between each trial, the solution in the syringe was mixed through inversion to maintain a well-distributed solution. For flows greater than 20 mL/min, the syringe was operated manually and the flow rate was estimated with a stopwatch.

Two types of viscous solutions were measured. First, glycerol solutions of 0 to 80% (v/v) in 1x PBS + 0.1% Tween-20 were prepared. Second, a diluent for sputum was also prepared as outlined in Creecy *et al:*[210] 4 M guanidine thiocyanate, 25 mM sodium citrate, 4.9% Triton X-100, 0.2% sodium dodecyl sulfate (SDS). Diluted sputum was prepared by mixing synthetic sputum in equal parts with the guanidine diluent on a Fisher Vortex Genie 2 at speed 4 for 10 minutes. The viscosities of these solutions were measured using a total volume of 500 µL of well-mixed, room temperature solution using a Brookfield DV-II+ Pro Viscometer (Middleboro, MD). Spindle 40Z was used for the measurement. Measurements were taken at a strain rate of 37.5 s^{-1} after increasing the strain rate from a minimum speed. This was important due to non-Newtonian, shear thinning rheology of sputum. The viscosity measurement was allowed to settle for a minimum of two to three full spindle rotations before a measurement was recorded. Measurements were performed in triplicate.

The effect of viscosity on capture was measured using 800 µg of MyOne™ Silane ™ placed into 2.5 mL of each of the viscous solutions and vortexed to thoroughly combine. The solution was drawn into the transfer pipette and 35 mg of Grade 000 steel wool was placed directly into the end of the transfer pipette. With the magnet beside the steel wool matrix, the bead containing solution was expelled through the pipette tip. To measure the concentration of uncaptured beads, the ™ contained in the flow through were centrifuged at 3,082 x rcf for a minimum of five minutes. More viscous solutions were diluted with PBS-T to reduce solution viscosity, and then centrifuged until the beads pelleted. The pelleted beads were washed in 1x PBS + 0.1% Tween-20, and then re-suspended in an appropriate volume of PBS-T as discussed to ensure accuracy of the spectrographic reading. Bead concentration was measured in triplicate using absorbance at 700 nm as previously outlined here.

Statistical analyses.

All statistical analyses were performed using MATLAB. One-way analysis of variance (ANOVA) was used to determine statistical significance for data containing three or more groups. Unpaired t-tests were performed for two group comparisons. Statistical significance was defined as $p < 0.05$. Tukey's range test was used to determine which data points were statistically significant relative to the rest of the data. Experimental variation was compared to the baseline method described above.

All samples and standards were analyzed in triplicate PCR reactions, except analysis of one QIAamp Viral RNA Mini Kit urine extraction; one of the PCR replicates was identified to be an outlier and removed. This value was greater than two standard deviations outside of the mean, which averaged all PCR values for each experimental condition (triplicate extractions with triplicate reactions for each sample, 9 reactions total). This criterion was applied to all samples, and this was the only identified outlier across all conditions in this study, and is likely due to a pipetting error.

Results

Mycobacterium tuberculosis *IS*6110 *DNA extraction from sputum and urine.*

For synthetic sputum samples, the HGMS-enabled extraction method recovered a total of 10.2% ± 4.03% of spiked DNA, the commercially available Qiagen DNeasy Blood and Tissue kit recovered 17.3% ± 4.65%, and the Chargeswitch™ gDNA Mini kit recovered 10.1% ± 1.12% (**Figure 3.3**). Extractions were more efficient for urine samples, with the HGMS-enabled extraction yielding 91.2% ± 7.46% of spiked DNA, the commercial Qiagen QIAamp Viral RNA Mini kit recovered 96.5% ± 10.46% of spiked DNA, and the commercial Chargeswitch™ gDNA Mini kit recovered 69.5% ± 15.4% (**Figure 3.3**). For all sample types and methods, there is some variation in the extraction efficiency, but the three methods were not statistically different. Using LinRegPCR for comparison of PCR efficiency, the HGMS-enabled extraction of sputum was approximately 10% lower than controls. A260/A280 readings for sample purity of the HGMS-enabled extraction measured at 1.86, suggesting that the PCR inhibitor(s) reducing reaction efficiency were not likely a contaminating protein (**Figure A3**).[256] Although not measured, likely inhibitor candidates are low concentrations of salts, metals, or alcohols introduced during processing.

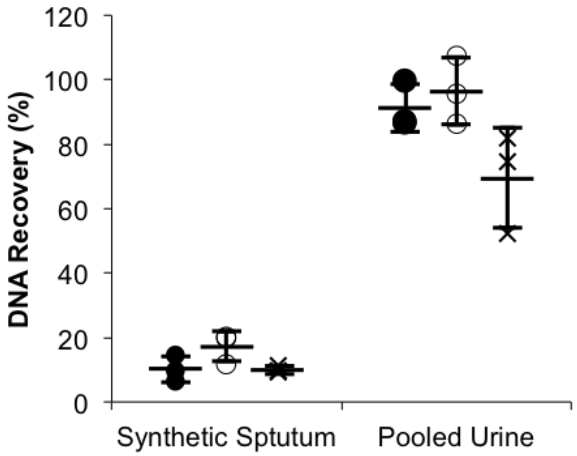

Figure 3.3. HGMS-enabled extraction performed similarly to commercial kits. Extraction of 5 x 10^6 copies of a 123-base IS*6110* TB DNA sequence using HGMS-enabled extraction (•), commercially available Qiagen kits (O), and Chargeswitch™ kit (×) are not statistically different from one another for both synthetic sputum and pooled urine. (mean ± s.d.), n ≥ 3.

Effect of physical properties of the steel wool matrix on paramagnetic bead capture.

The mass and the magnetic susceptibility of the separation matrix used in the pipette tip affected the capture of paramagnetic beads. As shown in **Figure 3.4A**, as the amount of steel wool was increased from 0 mg to 10 ± 1 mg, the capture efficiency of 1 μm ™ increased from 15.8% ± 5.27% to 99.2% ± 1.41%, with steel wool masses greater than 10 mg also capturing ~99% of beads. Tukey's range test identified 0 mg and 5 mg of steel wool as significantly less than the higher densities tested, suggesting that for this design, as long as the matrix is significantly magnetized and the packing density is maintained, the amount of matrix needed to capture a majority of the beads is quite small (**Video A2**).

Within the range of available materials, the diameter of the steel wool matrix had essentially no effect on bead capture. Steel wool Grades 0000, 000, 1, and 3, which correspond to strand diameters of approximately 25, 35, 60, and 90 μm, performed similarly and had capture efficiencies of at least 98% (**Figure 3.4B**).

Since the different alloy compositions of the matrix can have different magnetic properties, we also looked at the effect of alloy on capture (**Figure 3.5**). The magnetic susceptibility (χ) of the materials were varied, allowing for evaluation of their effect on capture − diamagnetic ($\chi<0$), paramagnetic ($\chi>0$), and ferromagnetic ($\chi>1$) materials were tested.[257] In the presence of an externally applied magnetic field, a weak magnetic dipole is induced in the opposite direction of the field for diamagnetic materials, and weakly in the same direction for paramagnetic

materials. For diamagnetic materials, copper and water (corresponding to no matrix), capture efficiencies are 41.8% ± 8.19% and 22.7% ± 8.44% respectively. For the paramagnetic materials aluminum and 316L stainless steel, paramagnetic bead capture was 51.7% ± 4.44% and 47.4% ± 8.38% respectively. In contrast, for ferromagnetic materials, which form a strong magnetic dipole parallel to the applied external field, the capture efficiencies for 434 stainless steel and low-carbon steel are 100.4% ± 0.082% and 99.9% ± 0. 071%. The capture in paramagnetic and diamagnetic matrices is statistically different from the ferromagnetic matrices. When no magnet is applied, the capture efficiencies of each matrix are ~10%, with the exception of no matrix and low carbon steel. The negative values are most likely due to measurement error, since the solutions measured were at the edge of the linear measurement range of the spectrophotometer. The capture values greater than 100% for 434 stainless steel are due to the concentration of beads in the centrifuged flow through being lower than the detection limit of the spectrophotometer.

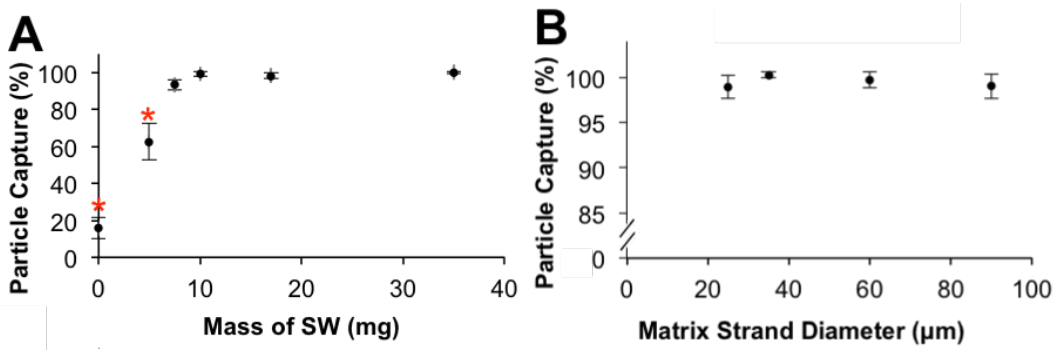

Figure 3.4. Effect of ferromagnetic matrix mass and strand diameter on capture of beads. **A.** Steel wool matrix mass ≤5 mg captured statistically fewer beads. **B.** Steel wool matrix strand diameter does not have an effect on paramagnetic bead capture efficiency. (mean ± s.d.), n ≥ 3. (*) Indicates statistical significance at $p < 0.05$.

Effect of magnet properties on paramagnetic bead capture.

As shown in **Figure 3.6A**, the capture efficiency increased with increasing surface field, with 548 G (Gauss) and 1701 G having capture efficiencies of 76.5% ± 13.1% and 88.6% ± 6.61%. Capture for the remaining magnets plateaued at ~99%. Only the smallest surface field examined, 548 G, exhibited statistically reduced capture efficiency. This suggests that as long as the magnetic surface field is greater than ~1700 G, capture efficiency will be nearly 100%. Close inspection reveals a minor decrease in bead capture efficiency from ~99% to ~94% when

using the 3309 G magnet, as theorized by Himmelblau,[127] the region of attractive magnetic force temporarily falls when the applied magnetic field is greater than the field needed to reach saturation. We hypothesize that this value is near the maximum saturation point of the ferromagnetic matrix. This effect is overcome when the applied field is sufficiently large. Further studies are needed to validate this hypothesis.

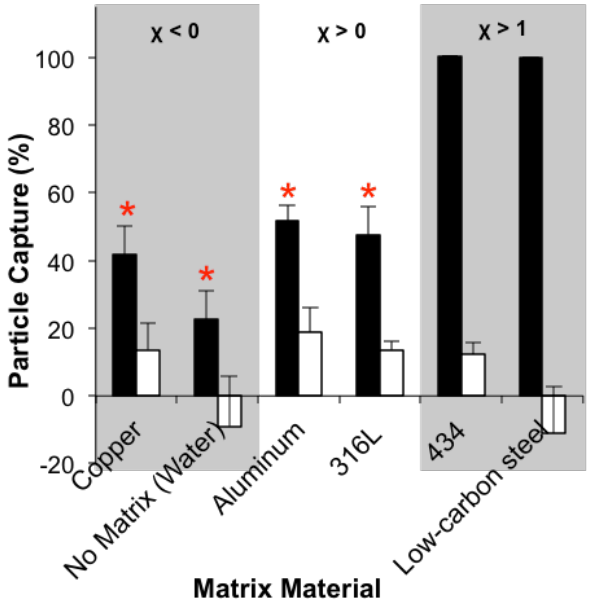

Figure 3.5. Effect of matrix magnetic susceptibility (χ) on capture. Ferromagnetic materials ($\chi>1$) captured more magnetic beads than paramagnetic ($\chi>0$) and diamagnetic ($\chi<0$) materials. Black bars – with applied magnetic field. White bars – no magnetic field present. (mean ± s.d.), $n \geq 3$. (*) Indicates statistical significance at $p < 0.05$.

The different cube magnets used **Figure 3.6B** had their surface field held constant, while a side length of the cube magnet varied. With increasing magnet size, capture efficiencies increased from 90.0% ± 1.03% for the smallest 0.32 cm magnet up to 99.9% ± 0.58% for the largest 2.54 cm magnet, with the smallest magnet of 0.32 cm capturing statistically fewer beads than the rest. This difference is likely due to the reduction in effective trapping length of the steel wool, since in this case the magnet dimension is smaller than the size of the steel wool matrix. However, it is important to note that capture efficiency only varies between highest and lowest capture efficiencies by 10%. While statistically significant, the difference may not be enough to warrant use of a larger and more expensive magnet, assuming a strong enough surface fields are applied.

Effect of sample viscosity and flow rate on paramagnetic bead capture.

We also assessed how the flow rate and sample viscosity influenced paramagnetic bead capture (**Figure 3.7**). Capture measurements were performed for samples passed through the HGMS-enabled separator with and without a steel wool matrix (**Figure A1**). Samples applied to the HGMS-enabled device with a steel wool capture matrix, at flow rates from 1 ± 0 mL/min to 46.5 ± 5.01 mL/min had capture efficiencies of at least 96%, and 60.1 ± 3.01 mL/min captured 89.2% ± 1.07%. Even though this is only a ~10% reduction, it is statistically significant. (**Figure 3.7A**). For samples passed through without a matrix, capture efficiencies were measured for flows only up to 20 mL/min, with capture efficiency rapidly declining with flow rate from ~100% bead capture at 1 mL/min to only ~25% capture at 20 mL/min. Capture efficiency was statistically reduced for flow rates of at least 10 mL/min.

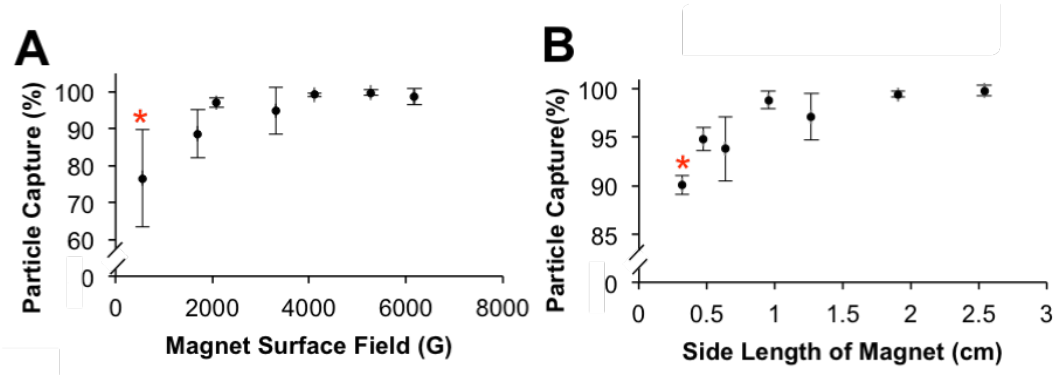

Figure 3.6. Effect of magnet surface field and magnet dimensions on bead capture. **A.** A smaller statistical percentage of paramagnetic beads were captured using a 548 G magnet. **B.** The smallest cube magnet with a side length of 0.32 cm captured statistically less beads due to decreased effective trapping length. (mean ± s.d.), $n \geq 3$. (*) Indicates statistical significance at $p < 0.05$.

Biological samples often differ in rheologic properties that may influence the capture performance of the HGMS-enabled system, since viscous drag forces on beads are much higher than the magnetic force, even when viscosity limits sample flow rates. As seen in **Figure 3.7B**, for the v/v% glycerol solutions prepared, the viscosities increased with increasing percentage of glycerol, measuring from 0.98 ± 0.06 cP to 54.7 ± 0.76 cP. The capture efficiency decreased by ~9% with increasing glycerol percentage from 100% ± 0.12% to 91.7% ± 6.78%, but this was not statistically different even though there is statistically significant difference in the sample viscosities. We also tested this using synthetic sputum with shear-thinning rheologic behavior. This was compared to bead capture from liquefied sputum in **Figure 3.7B**, since it is common for sputum samples to undergo liquefaction and

decontamination in protocols, such as those used for tuberculosis diagnosis. The measured viscosities of the synthetic and liquefied sputum were 20.0 ± 1.59 cP and 6.66 ± 0.22 cP. There was no statistically significant difference between the capture efficiencies, with both near 85% capture. Carrier RNA was not tested with the Chargeswitch™ kit.

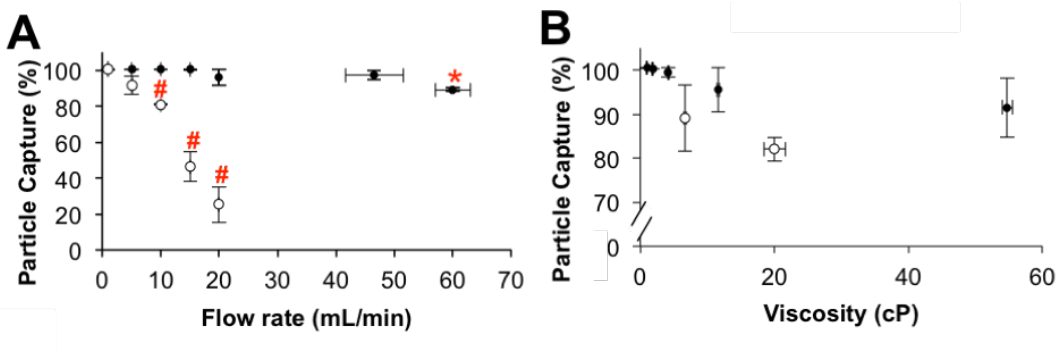

Figure 3.7. Effect of sample properties on bead capture. **A.** Increasing the flow rate did not statistically reduce bead capture in a 35 mg steel wool matrix (•) until reaching 60 mL/min, but was significantly decreased at 10 mL/min without any matrix present (O). **B.** Sample viscosity up to 55 cP did not reduce paramagnetic bead capture from either glycerol solutions (•) or synthetic sputum (O). (mean ± s.d.) $n \geq 3$. (*) And (#) indicate statistical significance at $p < 0.05$.

Discussion

The method reported here was used in a blinded sample preparation study sponsored by the Bill and Melinda Gates Foundation published in Beall *et al.*[251] That publication compared the sensitivity, specificity, and outcome features for stool, sputum, and whole blood for the HGMS-enabled method described in this report against five other commerical extraction methods. In parallel to this effort The Gates Foundation also commissioned a study comparing eight nucleic acid technologies suitable for low-resource settings.[258] In both of these studies, blinded samples were supplied to each of the study participants. For the extraction comparison, each sample matrix was spiked with a high, medium, or low amount of microbe appropriate to the matrix. In performing the experiments reported in **Figure 3.3,** we aimed to replicate the protocols and use the same processing reagents when possible as used in Beall *et al.* In Beall *et al.* we are coded as "Developer E" and ranked 3rd overall. The reported sensitivity and specificity for our extraction of chemically inactivated *M. tuberculosis* DNA from patient sputum were 76% and 100% respectively. Urine was not part of this comparison study. Other aspects of the six test systems, such as the

number of steps, time for extraction, and ASSUR criteria used for performance rankings are reported in Beall *et al.*[251]

In this report we focus on presenting the details of our HGMS-enabled method and a comparison to several commercially available manual kits. We found that in addition to performing well in comparison to automated systems reported in Beall *et al.*, our approach also performed well in comparison to other manual commercial kits. **Figure 3.3** shows the percent recovery of the HGMS-based method compared to both a silica column and another magnetic bead-based method, the recovery from sputum and urine for the three systems is similar.

We have also previously reported sputum and urine extraction results using a magnetic bead-based system both manually and semi-automatically. In these previous reports, the extraction processing was performed using a system of pre-arrayed solutions held stationary in a small diameter tube by surface tension forces, and biomarkers bound to magnetic beads were passed through consecutive solutions to perform the processing steps. With respect to sputum, this automated method was used to extract TB DNA from chemically inactivated *M. tuberculosis* in synthetic sputum in Creecy *et al.,* and extracted TB DNA was amplified by both PCR and isothermal amplification.[209, 210] In both studies, clinically relevant concentrations of TB mycobacteria were detectable by DNA amplification but extraction efficiencies were not calculable.

In previous urine extraction studies described in Bordelon *et al.*, using the tube extraction system manually, we extracted approximately 46% of DNA from urine, which is less than the 91.2% found in this report.[203] While here we report results from smaller volumes, our prior work used shorter binding times, fewer beads, and did not incorporate the addition of carrier RNA.[259] When carrier RNA was removed from the extraction protocols for both the HGMS-enabled extraction and Qiagen kit in this report, extraction efficiencies were reduced to 59.5% ± 7.59% and 88.2% ± 7.45% respectively. This was a statistically significant reduction for the HGMS-enabled extraction method, while the difference of the Qiagen extracts was not statistically significant (**Figure A4**). This is consistent with previous reports.[260]

A key difference between the Beall *et al.* study and the extraction studies reported here is the length of the DNA extraction targets. The Beall *et al.* studies were performed with whole pathogens, and the manual studies reported here used only a 123-base DNA fragment. We believe that the extraction efficiencies for a range of DNA fragment sizes would be similar to those reported here, provided the DNA fragments were greater than 100 bp in length. This is based on our previous work[203] and others[261, 262] showing it is difficult to efficiently extract and

recover short DNA fragments using chaotrope/silica chemistries. For example, Oreskovic *et al.* compared two published DNA extraction methods and three commercial kits to their hybridization-capture system for extraction of single-stranded IS*6110* TB DNA (25-150 base). While they found their 1.5 hour protocol performed most consistently of all methods across different fragment sizes, consistently isolating 73% to 84% of fragments.[262] The other method using Q Sepharose only performed well for larger fragments (63-75%), and was significantly reduced for 25-base fragments (9%).[262] We also believe that the extraction efficiencies reported for the HGMS-enabled extractions are not dependent on the spiked DNA concentration. Based on what we have observed previously, if bead concentration is sufficient to bind available nucleic acids, the extraction efficiency is preserved.[203]

There are two elements of our HGMS-enabled protocol that are critical for optimum performance. Our protocol used a one to two minute gravity-driven pooling step to remove residual liquid from the pipette tip before eluting the nucleic acids, and this was found to be critical for DNA detection. Though the beads themselves have low carry over, surface tension in the capture matrix has the potential to retain liquid. Specifically, this step removed approximately 100 μL of the residual ethanol wash from the sample chamber. Ethanol contained in this wash is known to inhibit PCR and other downstream detection methods. Therefore, ethanol removal is critical. Second, we found that it was important to include a rapid 100 μL TE rinse for sputum samples, and have seen this to be beneficial under specific conditions in prior work.[208] We found that while this rinse can lead to some nucleic acid loss (data not shown), this rinse helps remove excess PCR contaminants (e.g. residual proteins, salts, alcohols) and allows for improved detection. The total rinse time appears to be critical too. If the rinse time is too quick, the beads may be disrupted, resulting in DNA elution and reduced recovery. In addition, contaminants may remain in the system, inhibiting PCR. If the rinse is too slow, DNA can be partially eluted and recovery is reduced (data not shown). Use of an alternative processing chemistries or DNA detection strategies may allow for the elimination of these two steps.

Our HGMS-enabled magnetic separation system, combined with chaotrope/silica binding chemistry, resulted in a flow through design for magnetic bead extraction of nucleic acids that performed as well as available commercial kits. A set of optimal physical features related to maximizing HGMS capture capabilities were identified as a high magnetic susceptibility steel wool matrix with a mass of at least 7.5 mg, packed at a density of 0.91 g/mm^3 under a 6180 G field (**Figure 3.4**). These consistently captured ~100% of paramagnetic beads. Variation around these values did not significantly reduce capture. For example, the same percent capture is achieved with a

35 mg matrix in an externally applied field of at least ~1700 G (**Figure 3.6**). The HGMS-enabled system can also capture essentially all beads from solution flows up to 45 mL/min and viscosities up to 55 cP (**Figure 3.7**). Our methods characterized the effect of each variable individually, however, the interplay between multiple variables will need to be further elucidated for final optimization for potential applications.

Although previous studies were limited in their scope of investigation there are some clear differences between our system and previously described HGMS systems. For example, the packing density of 0.91 mg/mm^3, or ~11.5% packing volume used in these experiments, is slightly higher density than previous work, where HGMS was used to efficiently isolate cells with columns typically packed at 2-5% of the total volume.[119, 122, 123] Owen *et al.* reported capture of up to 92% of paramagnetic erythrocytes using 1 g of magnetic stainless steel wool at flow rates less than 2 mL/min in an applied magnetic field of 33,000 G.[263] Molday and Molday reported 96% ± 2% capture of red blood cells using immunospecific magnetic nanoparticles at 2 mL/min in a 7,500 G field.[122] Miltenyi *et al.* only looked at relative proportions of cell mixtures before and after MACS®, but demonstrated that two different cell populations could be efficiently separated, with the retained cell type generally making up < 2% of the cells that were not captured in MACS® matrix. Miltenyi *et al.* used flow rates between 0.16 mL/min and 8 mL/min, most often less than 2 mL/min.[123] Despite these differences, these systems demonstrate similar capture efficiencies to the ones reported here, albeit at lower flow rates, greater applied fields, and with more steel wool than used in our system.

As far as we can tell, there have been no other studies specifically looking at the effect of sample viscosity in biological applications, since prior studies used aqueous solutions, such as saline.[119, 123] Our viscosity results are consistent with the industrial application of mineral particle separation by Dobby *et al.*, which demonstrated that viscosity plays a minor role in capture.[264]

Prior work performed limited studies looking at the effect of magnet surface field, typically only looking at two different fields.[105, 119] For example, Owen *et al.* investigated the effect of field strength on capture, demonstrating that capture efficiencies are proportional to the magnetic moment of the beads captured divided by the flow rate through the magnetic column.[119] Our data are consistent with Owen's findings, in that capture efficiency decreased with decreasing magnetic field. In addition, assuming the magnetic moment of the magnetic beads is constant and uniform, the flow rate data collected is consistent with Owen's findings, with capture efficiency decreasing with increasing flow rate; this is obvious when there is no ferromagnetic matrix present in the

path of fluid flow, and more subtly observed at high flow rates with the presence of ferromagnetic matrix (**Figure 3.7A**). These findings are consistent with available theory.[250, 264] We also note that prior work fully immersed and maximally saturated the entire steel wool matrix in the applied magnetic field, but did not assess the effect of magnet size specifically on a single system. This is likely because it was much more common to use electromagnets for HGMS systems when first implemented,[119, 122] with an exception to this being Miltenyi.[123]

The differences in capture effect with changes in matrix magnetic susceptibility suggests that the feature dominating paramagnetic bead capture is the matrix itself. However, the fact that there is a difference in capture efficiency between the two diamagnetic materials, copper ($\chi = -9.36\times10^{-6}$) and water/no matrix ($\chi = -9.05\times10^{-6}$),[257] suggests that just the presence of a metal matrix, even when traditionally identified as "non-magnetic," has an impact on capture. We and others have observed that the micron-scale paramagnetic beads can form chains while in a magnetic field[265, 266] and can form complex, magnetically anisotropic structures that could potentially further contribute to increasing bead capture. The importance of the chaining phenomenon is unclear. Further, flow likely remains laminar for all of the flows achievable in this system. Treating a single strand of the 35 μm steel wool matrix wire as a cylinder sitting perpendicular to the path of the fluid flow at a flow rate of 15 mL/min (fluid velocity of 7.29 cm/s) yields a cylinder Reynolds number (Re) of 2.58 in the laminar range.[267]

In general, manual extraction methods are not as desirable as automated systems, which require less training and are more reproducible. However, when the processing instruments and/or training are unavailable simple manual methods may fill a critical gap. In this report we describe the details of an HGMS-based manual approach. This manual system performs similarly to other manual systems, has some attractive features for low-resource use particularly in the areas of cost and robust operation, and has potential for further improvement to make even more suitable for low-resource settings. One of the attractive features of HGMS-enabled extraction is its robust performance is less dependent on user training. In our experience, the range of flow rates produced by different users expelling the transfer pipette is no greater than 20 mL/min (data not shown), and the capture of magnetic beads in the steel wool matrix is not affected by a range of flows up to 45 mL/min (**Figure 3.7B**). For highly viscous samples, the maximum flow rate of a liquid sample through the device primarily depends on viscous shear forces within the magnetic matrix material. Therefore, variations in flow rates produced by a user squeezing the pipette bulb as quickly possible are limited. The two dominant forces acting in a magnetic bead in a high-gradient magnetic separator are the hydrodyanamic drag force and the magnet force; all other forces are negligible.[250] For samples with

viscosities near that of water, the hydrodynamic drag force has the potential to overcome the magnetophoretic force at sufficiently high flow rates, reducing the capture efficiency of beads from solution.[268] It is our conclusion that HGMS-enabled capture demonstrated a robustness against potential operator variability, which could occur from variations in squeezing pressure and the resulting flow produced from different users and samples with a range of viscosities.

In addition, though the applied magnetic field needs to encompass the steel wool matrix for bead capture, a user can see the matrix inside of the pipette tip, and the magnet is the same size or larger than the steel wool matrix. Because a surface field of only ~1700 G is needed to efficiently capture particles (**Figure 3.6A**), the magnet does not need to be held in a precise location and can be a distance away from the steel wool matrix, with the condition that the magnet has a strong enough surface field. In the DNA extractions, the magnet was applied through an microcentrifuge tube wall with the pipette tip resting inside, and the steel wool separator was able to efficiently capture magnetic particles repeatedly during each wash step. While robust, it is still possible for a user to make an error. If a mistake is made and magnetic beads are lost, which would be visible due to the brown color of the magnetic beads, it is quick and easy to redraw the solution into the transfer pipette and repeat the magnetic bead capture. Repeating this step to overcome a processing error without loss is another major advantage of HGMS-enabled extraction.

The HGMS separator described here could potentially be used for sample preparation in a low-resource setting, where the cost of a point-of-care assay is a significant contributor to use and adoption. With the steel wool and transfer pipettes costing just pennies, the most expensive component of the assay described are the magnetic beads at $3.30/assay at the time of publication. This large number of beads was kept constant because we sought to describe the methods that closely match the method used in Beall *et al.*,[251] which were designed to maximize performance, rather than minimize cost. Further assay optimization could reduce cost, and it is believed that the resulting extraction kit will likely cost under $1.00 per test. Real-time PCR was used as the readout and was not inhibited by the extraction methods. We expect methods such as loop-mediated isothermal amplification (LAMP), or other nucleic acid amplification methods in development, with lateral flow assay readout would also perform well and might serve as a more suitable detection method in resource-limited settings.

Another important consideration for low-resource use is the identification of less hazardous extraction chemistry. There are alternative methods to guanidinium-based methods, such as the Chargeswitch™ system

(ThermoFisher). Claremont BioSolutions has also developed an extraction method that does not use hazardous extraction chemistry.[269] A compelling future direction is testing of the Chargeswitch™ chemistry using the HGMS-format. This potentially could eliminate the critical timing step currently required for maximum recovery from sputum. Improved reagent storage could also be achieved. For example, the transfer pipette bulb allows for future lyophilization of reagents within the extraction device,[211] further simplifying the assay protocol and reagent packing; this would also allow for inclusion of poly-A carrier RNA, which helped significantly improve the extraction efficiency of DNA from urine. Other liquid-phase processing solutions and containers could be packaged and arrive in a disposable, single-use "kit" format, with all components pre-aliquotted or individually wrapped. The user would simply remove the assay components from their packaging and quickly start performing extraction(s) without any pre-processing steps. The use of a single inlet and outlet of the transfer pipette, rather than separate entry/exit ports in flow through systems, yields additional mixing potential that could improve biomarker yield.

The use of a larger sample can increase the sensitivity of low-resource detection methods.[211, 270] This is simple to do with HGMS-enabled extraction. Pipettes with different sized bulbs or syringes could be easily interchanged for application-specific design, with larger, more dilute samples using larger volume actuators. While we only processed 100 µL for these proof-of-principle studies, we demonstrate that larger sample volumes, up to 3 mL can be processed using the HGMS-enabled transfer pipette system. Further, it is the maximum number of beads that can be captured in a matrix that limits a HGMS's performance, not the volume in which these beads are suspended; this was demonstrated by Miltenyi[123] and in industrial applications as discussed. The large number of beads captured in our baseline design suggests that the small amount of steel wool used in these studies is still well below the load limiting capacity. This implicates potential for very large volumes or dilution, though overzealous dilution can reduce bead-biomarker interactions necessary for DNA isolation.

With modifications, this approach can be adapted for other sample types. In Beall *et al.*, the methods described here were successfully modified with a proteinase K treatment for successful extraction from whole blood and stool. This shows that the HGMS-enabled extraction can be adapted for other sample types at clinically relevant concentrations. Further optimization may be required, however. For example, we tried to adapt our previous sputum protocol,[209, 210] but the high detergent concentration in the lysis/binding buffer resulted in significant bubble formation using the HGMS-enabled device. In addition, we hypothesize that our sensitivity for *M. tuberculosis* detection was only 76% because our guanidine buffer did not lyse all spiked *M. tuberculosis* cells, which are known

to be difficult to chemically lyse without use of organic solvents.[72] These examples demonstrate the need for buffers tailored to the extraction system design as well as the application.

Additional processing strategies are possible with this approach and have not been explored. The initial capture of biomarkers onto the magnetic beads is an area where we speculate this HGMS-based approach may significantly improve performance. In this alternate approach, magnetic beads could be transiently captured within the steel wool and the entire sample passed through it multiple times to accelerate the binding of the nucleic acid biomarkers to the surface of the magnetic beads. This is likely to have advantages over other bead-sample mixing strategies in that extraction efficiency can be maintained while bead number and initial binding times are reduced. This could also be implemented during the processing steps. Instead of releasing and re-capturing beads in the steel wool matrix during each step of the extraction processes the magnet could be applied throughout. However, if beads are non-uniformly distributed through the steel wool matrix, there is the possibility that not all beads will receive sufficient contact with the processing solutions. Another future direction may to incorporate this processing method into a simple instrument to reduce the number of manual steps and operational errors.

This study did not look at the effect of bead magnetic susceptibility or size, which would also influence the capture efficiency of beads in the steel wool matrix The size of the beads used, if at all,[118, 119, 263] across previous studies were also smaller than 200 nm,[122, 123] giving the beads a smaller magnetic susceptibility than the 1 μm beads used in our study due to their reduced iron content. Nevertheless, the use of smaller beads would increase the surface area available for capture potentially reducing the cost of the system while maintaining capture efficiency.

Conclusions

In summary, the proposed HGMS-enabled nucleic acid extraction method is an effective alternative for magnetic bead-based sample processing that is as efficient as gold standard commercially available systems, but also inexpensive, rapid, and simple. We have shown that the device offers advantages over existing magnetic extraction methods, including magnetic separation of beads from viscous and large-volume samples without the use of specialized laboratory equipment, making the approach potentially useful in resource-limited applications. With changes in the surface chemistry of the beads, we expect that this robust HGMS-enabled system can be applied to extraction and purification of other biomarkers of interest.

Acknowledgements and Funding

The authors would like to thank Jami Hamman of Harpeth Hall and Christia M. Victoriano of Vanderbilt University for their efforts in assisting with data collection. They also thank John Albert Rector IV of Vanderbilt University for assistance collecting Supporting Information.

This work was funded in part by the Bill and Melinda Gates Foundation, OPP1172605, and the National Institutes of Health, R01 AI135937.

CHAPTER 4 : CONTROLLING DROPLET MARANGONI FLOWS TO IMPROVE MICROSCOPY-BASED TB DIAGNOSIS

Adapted from: Pearlman, S. I.; Tang, E. M.; Tao, Y. K.; Haselton, F. R., Controlling Droplet Marangoni Flows to Improve Microscopy-Based TB Diagnosis. *Diagnostics (Basel)*. **2021,** *11* (11), 2155., with permission from *Diagnostics (Basel)* and coauthors. Article published under Creative Commons CC BY 4.0 license.

Abstract

In developing countries, the most common diagnostic method for tuberculosis (TB) is microscopic examination sputum smears. Current assessment requires time-intensive inspection across the microscope slide area, and this contributes to its poor diagnostic sensitivity of ~50%. Spatially concentrating TB bacteria in a smaller area is one potential approach to improve visual detection and potentially increase sensitivity. We hypothesized that a combination of magnetic concentration and induced droplet Marangoni flow would spatially concentrate *Mycobacterium tuberculosis* on the slide surface by preferential deposition of beads and TB-bead complexes in the center of an evaporating droplet. To this end, slide substrate and droplet solvent thermal conductivities and solvent surface tension, variables known to impact microfluidic flow patterns in evaporating droplets, were varied to select the most appropriate slide surface coating. Optimization in a model system used goniometry, optical coherence tomography, and microscope images of the final deposition pattern to observe the droplet flows and maximize central deposition of 1 μm fluorescent polystyrene particles and 200 nm nanoparticles (NPs) in 2 μL droplets. Rain-X® polysiloxane glass coating was identified as the best substrate material, with a PBS-Tween droplet solvent. The use of smaller, 200 nm magnetic NPs instead of larger 1 μm beads allowed for bright field imaging of bacteria. Using these optimized components, we compared standard smear methods to the Marangoni-based spatial concentration system, which was paired with magnetic enrichment using iron oxide NPs, isolating *M. bovis* BCG (BCG) from samples containing 0 and 10^3 to 10^6 bacilli/mL. Compared to standard smear preparation, paired analysis demonstrated a combined volumetric and spatial sample enrichment of 100-fold. With further refinement, this magnetic/Marangoni flow concentration approach is expected to improve whole-pathogen microscopy-based diagnosis of TB and other infectious diseases.

Introduction

The leading cause of infectious disease death worldwide, the global burden of tuberculosis (TB) disease today stands at 10 million cases per annum, with 12% of those individuals dying from the disease. The causative bacterial agent of TB, *Mycobacterium tuberculosis* (*M.tb*), is also the most common opportunistic infection and leading cause of death in HIV-infected persons in developing nations.[2] The inability to rapidly and accurately diagnose TB disease and evaluate resistance with high sensitivity and specificity at the point-of-care (POC) continues to be a confounder in disease transmission, patient mortality and morbidity, and time to treatment initiation in the developing world; this is a major barrier to effective control of TB.

In 2012, the World Health Organization endorsed the nucleic acid amplification-based GeneXpert MTB/RIF assay as a frontline diagnostic and drug resistance test for TB in endemic settings.[51] Unfortunately, reliance on a special instrument possesses significant limitations that hinder its capacity to serve as a comprehensive screening tool. Most crucially, for example, in South Africa where Xpert is widely used, Xpert devices are commonly located in centralized tertiary health care facilities in densely populated areas.[59] This leaves individuals in rural, sparsely populated areas without immediate access to Xpert testing, requiring patient specimens be shipped from remote clinics to testing centers, imposing a lengthy turnaround time (days to weeks) for what should be a two hour diagnostic test. This exacerbates pre-treatment loss to follow-up rates, which can be up to 38% for patients diagnosed with TB in both rural and urban pats of the developing world.[4] In addition, Xpert cartridge stock-outs and supply chain mismanagement, interruptions in electricity, unpredictable transport of patient specimens from off-site locations, and high start-up costs have impeded implementation of Xpert.[271] Knowing these barriers, it has been shown that case detection has not significantly improved with the rollout of Xpert, and that the number of patients lost to follow-up did not decrease following TB diagnosis with Xpert.[271-273] Thus, empiric treatment without molecular diagnosis remains commonplace.[4]

In the absence of any reliable biomarker-based POC diagnostic test for TB, the gold standards for accurate TB diagnosis continue to rely on microscopic pathogen detection paired with diagnostic confirmation using bacterial culture methods.[2] Sputum smear staining and microscopy has the advantages of having high specificity (~100%) while being inexpensive and easy to perform. Unfortunately, these advantages do not overcome poor diagnostic sensitivity (~50%), subjectivity, and laboriousness. Manual inspection of stained sputum smear slides requires visual inspection of a minimum 100 fields-of-view using high-power magnification, which can take up to three hours,

depending on the degree of infection and the microscopist experience.[240] Understaffed and busy clinics that continue to rely on smear inspection are especially prone to false negatives resulting from improper examination.[183]

Spatial concentration of TB bacteria has the potential to reduce inspection time of patient samples, which could be further improved when paired with TB-specific volumetric concentration strategies. Using what is known about the hydrodynamics of an evaporating drop, spatial concentration is theoretically achievable without the need for specialized equipment. Our group and others have extensively studied the flow and deposition patterns of particles in drying drops, and have shown that these microfluidic properties can achieve spatial concentration at the edge or center of the drop.[135, 142, 145, 146]

Our group has previously published two biosensor designs that make use of the radial flows found in evaporating sessile droplets.[145, 146] The first design used the primary radial flow to deposit polystyrene particles at the edge of an evaporating drop, creating what is colloquially known as a "coffee ring." [146] Our second published design used secondary radial flows, known as a Marangoni flows, to concentrate particles in the center of a drying drop. This design used an antibody recognition system to induce particle aggregation in the presence of biomarker, followed by deposition in the center of the evaporating drop.[145] A larger deposition pattern in the center of the drop corresponded to a greater biomarker quantity, and this could be quantitatively measured. The assay also achieved a limit-of-detection (LOD) of picomolar biomarker concentrations. The system included glycerol to remove interference of salt crystallization and enhance the Marangoni flows. It also used a polydimethylsiloxane (PDMS) substrate instead of glass, which has the required material properties for production of Marangoni flows radially inward along the substrate. Unfortunately, both the substrate and solvent material properties that made this assay work are not compatible with acid-fast staining protocols used at the POC. In addition, both assays use 1 μL drops, a volume too small for suspension of a large-volume sample after volumetric concentration.

Here we describe a different design for spatial concentration of *M.tb* bacilli for use in microscopic sputum smear inspection using Marangoni flow (**Figure 4.1**). In this report, we detail the design and testing of potential materials before comparing our method to direct sputum smear. **Figure 4.2** demonstrates combined magnetic enrichment and spatial concentration using nanoparticles (NPs) and Marangoni flows, achieving a simple workflow for use in low-resource settings.

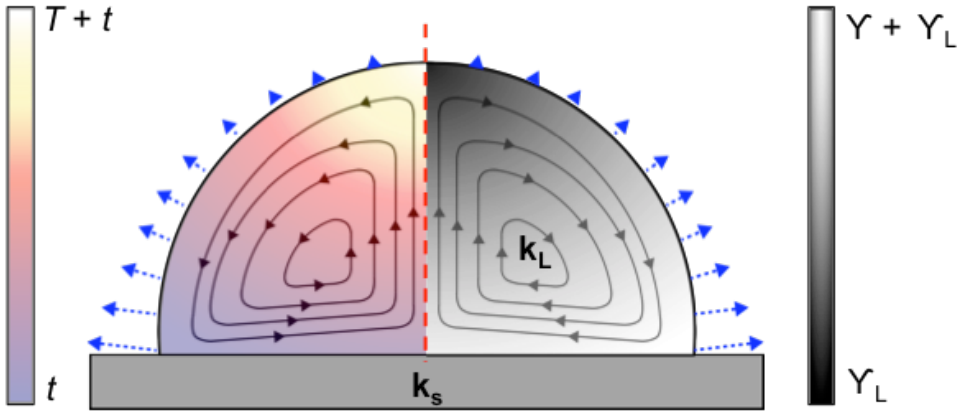

Figure 4.1. Physical phenomena that contribute to Marangoni flow formation and direction. Surface tension (ϒ) and thermal conductivity (k) of the surface (k_s) and droplet solvent (k_L) can be manipulated to create inward or outward-oriented Marangoni flow patterns in an evaporating droplet. In this case, nonuniform evaporation along the liquid-air interface of the droplet (blue dashed triangle arrows) occurs. This creates a temperature gradient (T) resulting in the nonuniform surface tension gradient. When $k_s < 1.45k_L$, where the temperature at the top of the droplet is warmest, while the contact line is coldest (indicated by the color gradient, the microfluidic flows within the droplet circulate radially inward along the solid substrate (black triangle arrows) independent of surface tension.[142]

Materials and Methods

Mycobacterial strains, culture conditions, and electroporation.

Mycobacterium bovis Karlson and Lessell TMC 1011 [BCG Pasteur] (ATCC® 35734TM) is referenced here as *M. bovis* BCG (BCG), and *Mycobacterium smegmatis* (Trevisan) Lehmann and Neumann mc(2)155 (ATCC® 700084TM), referenced here as *M. smegmatis* (*M. smeg*) were cultured in BD DifcoTM Middlebrook 7H9 Broth (FisherSci, Cat# DF0713-17-9) supplemented with 10% BD BBLTM Middlebrook OADC Enrichment (FisherSci, Cat# B12351) and 0.05% glycerol, or on BD DifcoTM Middlebrook 7H10 agar (FisherSci, Cat# DF0627-17-4) supplemented with OADC and glycerol. All BCG cultures were grown at 37°C with constant shaking at ~200 rpm, and *M. smeg* cultures grown at 20°C with constant shaking at ~200 rpm. *M. smeg* was cultured at room temperature as a preventative measure to reduce contamination potential of the incubator and BCG cultures with the faster growing mycobacterial strain. Following electroporation, outlined below, transformed *M. smeg* were grown using the indicated media with 100 µg/mL Hygromycin B (RPI Corp., H75020) supplement to maintain selection of bacteria expressing the plasmid.

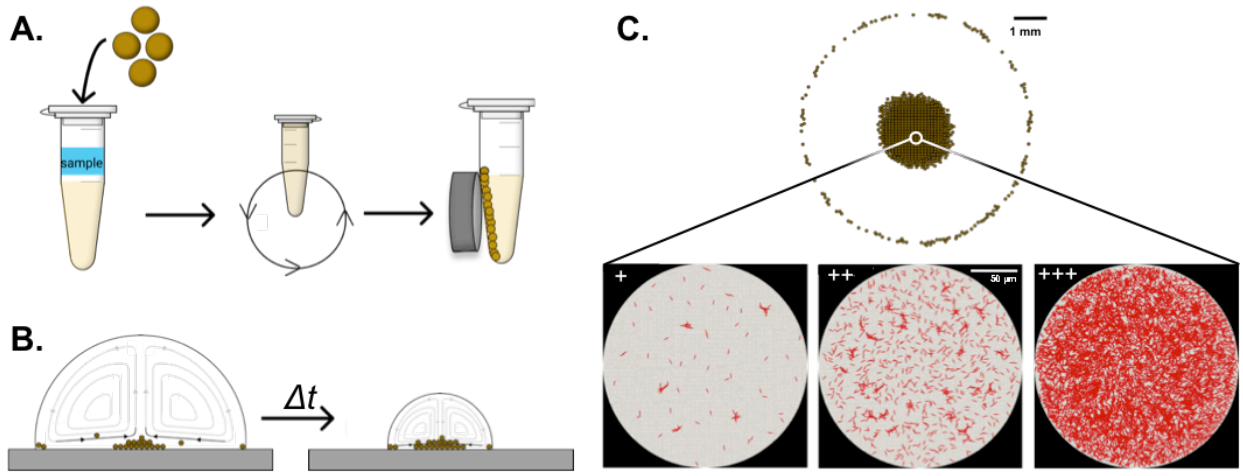

Figure 4.2. Workflow for combined volumetric and spatial concentration of *M.tb*. **A.** Magnetic nanoparticles are added, incubated with the sample to capture bacilli, and then magnetically separated from the sample. After washing, the bound sample and nanoparticles are recovered in 50 µL PBS-T. **B.** The recovered sample is deposited on the Rain-X® + poly-L-lysine coated microscope slide and evaporated at room temperature. **C.** The dried sample is stained using the Ziehl-Neelson method, and the central Marangoni deposition area is inspected using microscopy at 1,000x magnification. Representative positive samples with increasing *M.tb* concentrations are shown. (+) – 10^4 bacilli/mL; (++) 10^5 bacilli/mL; (+++) 10^6 bacilli/mL. Black scale bar – 1 mm; white scale bar – 50 µm.

Plasmid pMyCA-mCherry was a gift from Young-Hwa Song (Addgene plasmid #84272; http://n2t.net/addgene:84272; RRID: Addgene_84272).[274] This plasmid was used to create fluorescent *M. smeg* bacilli for imaging. The plasmid arrived as a bacterial stab of transformed *Escherichia coli* DH5α, which were expanded into 100 mL cultures in LB (Lysogeny Broth) liquid culture medium (RPI Corp., L24040) containing 100 µg/mL Hygromycin B at 37°C with shaking at 200 rpm. The plasmid was isolated from the cultures using the QIAprep® Spin Miniprep Kit (Qiagen, Cat# 27104).

M. smeg was electroporated as indicated by Goude and Parish,[275] substituting the culture media above into the *M. smeg* electroporation protocol. Following electroporation and plating on selection agar, *M. smeg* was cultured at 37°C for three to five days, before transformed colonies were transferred into liquid culture. *M. smeg* electroporated with water instead of plasmid DNA did not grow on the Hygromycin B selection plates. Pink colonies only grew on the selection plates that were electroporated with plasmid DNA.

Microscope slide coating with candidate substrate materials.

Fisherbrand™ Premium Plain Glass Microscope Slides (Fisher Scientific, 12-544-1) or Fisherbrand™ ProbeOn™ Slides (Fisher Scientific, 15-188-51) were cleaned using 70% ethanol/30% 1 N HCl, rinsed generously with MilliQ water, and dried at room temperature before use. Indium tin oxide (ITO) glass (MilliporeSigma, 703192-10PAK) was untreated and used directly from packaging. Krayden Dow Corning Sylgard 184 Silicone Elastomer Kit (Fisher Scientific, NC9285739), referred to here as PDMS, was prepared using a 10:1 Base Polymer (Part A) to Curing Agent (Part B) ratio, poured into a flat aluminum foil-lined tray, degassed under vacuum, and placed at 65°C overnight to cure. PDMS was wiped cleaned with 70% ethanol before use to ensure any residual contaminates from handling were removed. The thermal conductivity of each material can be found in **Table 4.1.**

All coatings were applied to plain glass microscope slides after washing. Rain-X® Original Glass Water Repellent (US# 800002242) and Rain-X® Interior Glass Anti-Fog™ (US# 21106DW) are polysiloxane coatings that covalently modify glass surfaces to which they are applied.[276, 277] Rain-X® coatings were poured onto a clean microfiber cloth, and applied to the surface of the microscope slide in a circular motion three times, allowing the coating to dry between coats. Residual Rain-X® was removed using a clean, dry microfiber cloth. WD-40® Specialist® Dirt & Dust Resistant Dry Lube PTFE Spray (WD-40, 300059) was applied by spraying onto the surface of an upright microscope slide for 1 to 2 s, and allowing excess liquid to drip down the slide onto a Kimwipe®. With the excess removed, the slides were placed horizontally to finish drying. DuPont® Non-Stick Dry Film Lubricant with Teflon® fluoropolymer (DNS040101), and Sigmacote® (SigmaAldrich, SL2-100ML), a glass siliconizing agent, were poured into a 50 mL conical, and microscope slides were submerged upright for 1-2 s, and then removed. Excess liquid was allowed to drip off the end of the upright microscope slide onto a Kimwipe®. With the excess removed, the slides were placed horizontally to finish drying.

Contact angle measurements of candidate substrate materials.

Contact angle of MilliQ water was measured on each substrate material using a ramé-hart Model 200-F4Goniometer (Succasunna, NJ) and DROPimage Advanced Software v2.6.1. The instrument was used as per the manufacturer's instructions for measurement of contact angles on a level surface (CA Tools>Contact Angle) and calibrated using the 4 mm ball before use. The Baseline setup for the Tilt of the substrate had no more than ±0.02%

difference between the left and right intercepts for all droplets measured. A minimum of thirteen ($n \geq 13$) 2 µL MilliQ water droplets were measured for each substrate.

Table 4.1. Thermal Conductivities of Candidate Substrate Materials.

Material	Thermal Conductivity (W m^{-1} K^{-1})
Polysiloxanes[§§]	0.077 – 0.150 [278, 279]
Sylgard 184 polydimethylsiloxane (PDMS)	0.27 [280]
Polytetrafluoroethylene (PTFE)	0.245 [281]
Borosilicate Glass	1.21 [282]
Indium Tin Oxide (ITO)	10.2 [283]

Droplet deposition pattern screening of candidate substrates.

To assess the final deposition of particles in a drying droplet on each substrate, solutions were prepared containing either 1 µm yellow-green fluorescent polystyrene particles (PS) (ThermoFisher, Cat# F8768, Lot# 1878394) at a concentration of 10^6 particles/µL, or 200 nm streptavidin-coated magnetic NPs (OceanNanotech, SV0200) at 0.5 µg/µL, in 0.5x PBS + 0.01% Tween-20 + 8% glycerol.[145] Two-microliter (2 µL) droplets were deposited in triplicate on each substrate and allowed to dry while covered with a box to prevent environmental airflow variations during evaporation. Droplets were imaged on a Nikon TE-200U microscope using a 2x objective and DS-U3 Color Camera in Nikon NIS Elements AR 4.13. NP droplets were measured using white light. The fluorescent polystyrene particles were imaged using a fluorescent bulb and filter cube with FITC Ex/Em filters.

Droplet deposition pattern screening with decreasing concentrations of glycerol.

Using the same particle concentrations listed, 0.5x PBS + 0.01% Tween-20 (PBS-T) [145] with either 0%, 2%, 4%, and 8% glycerol were made, 2 µL droplets deposited on Rain-X® Original Glass Water Repellent coated microscope slides in triplicate, and allowed to dry, covered, and imaged as previously indicated. In addition, the same protocol was repeated with mCherry *M. smeg* at a concentration of 10^6 bacteria/µL (estimated using absorbance at 600 nm), which were washed once in 1x PBS (137 mM NaCl, 2.7 mM KCl, 10 mM Na_2HPO_4, 1.8 mM KH_2PO_4, pH = 7.4) before suspension in the droplet solutions. The *M. smeg* evaporated droplets were imaged

[§§] Exact composition of Sigmacote® and Rain-X® polysiloxane coatings are trade secrets and unavailable from the manufacturers.

using a Texas Red® Ex/Em filter, and were imaged using a 4x objective instead of 2x to improve visualization of the bacteria deposition in the droplet given their small size and lower fluorescence, relative to the PS particles.

Imaging and analysis of evaporating droplet Marangoni flow fields using optical coherence tomography.

Droplet flow imaging was performed using a custom spectral-domain optical coherence tomography (OCT) system. OCT is an interferometric imaging technique that allows for the acquisition of a single line in depth for each laser beam position on the sample.[284] By raster scanning the laser beam using mirrors, 2D cross-sectional and 3D volumetric images can be rapidly constructed. A super-luminescent diode (Superlum) centered at a wavelength of 889 nm with a 93 nm bandwidth was used for illumination. The resolution of the system was measured to be 4 μm in the lateral dimension and 2 μm in the axial dimension. The imaging system was tilted slightly to reduce the effects of specular reflection during manual alignment to the diameter of a 1 μL droplet. Backscattered light was detected using a CMOS camera (Basler Sprint, spL4096) running at a line rate of 45 kHz. Cross-sectional images were acquired with 2048 pixels in depth and 2000 lines per frame over a 5 mm field-of-view. Due to improvements in hardware and software, the temporal sampling rate was increased from the method reported in Trantum *et al.*[135] A total of 800 repeated frames were taken at the same position for a total acquisition time of 36 s per measurement in order to monitor the changes in particle flow and droplet evaporation. For each droplet, measurements were taken at two minute intervals beginning at one minute following droplet placement until complete evaporation.

Raw OCT spectral data was converted to tagged image file format (TIFF) using conventional post-processing techniques that include linearizing the spectrum with respect to wavenumber, performing dispersion compensation to reduce axial distortions, and finally converting wavenumber to depth using the Fourier transform. TIFF images were then imported into ImageJ for analysis. Time-lapse composites were created for each measurement by averaging the corresponding 800 frames acquired at the same position and adjusting contrast to better visualize particle flow.

Preparation and spot size assessment of Rain-X® coated slides with poly-L-lysine layer for improved heat fixation of magnetic nanoparticles.

Water Repellent Rain-X® was applied to microscope slides as indicated. A grid was drawn onto paper and attached to the back of the microscope slide using transparent tape. Where indicated by the grid, droplets of 1-10 μL

containing 0.01% poly-L-lysine (PLL) (MilliporeSigma, P8920-100ML) were applied, and allowed to rest for 5-10 min (**Figure 4.3**). For a negative control, 10 µL of MilliQ water was placed on the grid in place of PLL. Excess PLL solution was carefully removed through capillary action using a dry Kimwipe®, and the slides baked at 65°C for one hour and stored in a closed container at room temperature until use. The positive charge of the PLL polymer helps enhance electrostatic interactions between the positively charged surface and negative charges of in the sample, usually located on cell or tissue membranes.

After, a solution of 0.2 µg/µL of 200 nm streptavidin-coated magnetic NPs was prepared, and 50 µL droplets were deposited over the grid (**Figure 4.3**). The droplet was positioned such that the center of it was centered over the applied PLL spot coating. Drops were allowed to evaporate uncovered at room temperature until dry. Bright-field microscope images of the dried spots were taken at 1x magnification. Particle deposition area in the center of each droplet was measured by drawing a "polygon" around the outer edge in the raw image in NIS Elements.

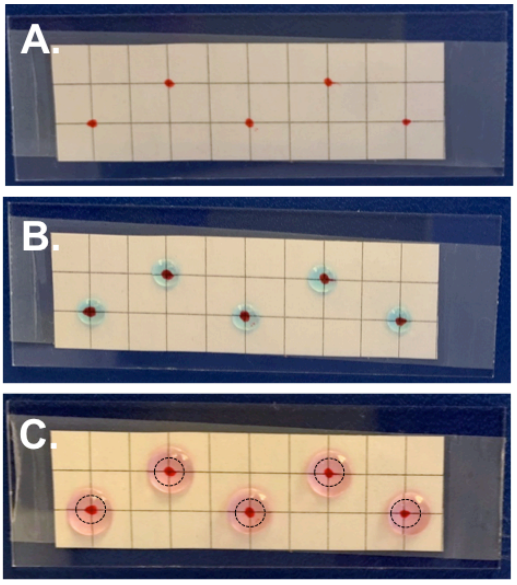

Figure 4.3. Deposition of poly-L-lysine onto Rain-X® coated slide. **A.** A marked grid is affixed to the back of the microscope slide using tape. **B.** 10 µL droplets containing 0.01% poly-L-lysine were spotted onto the microscope slide where indicated. **C.** After removing excess poly-L-lysine, 50 µL droplets containing the volumetrically concentrated samples were placed over the poly-L-lysine landing zone and allowed to dry. Location of landing zone in center of droplets indicated by dashed circle. Dyes added to droplets for visualization.

Preparation of pure mycobacterial samples.

Mycobacteria have a propensity to clump in culture, and it is necessary to dissociate these clumps to obtain a primarily unicellular suspension. Suspension mycobacterial cultures were collected and centrifuged in 50 mL volumes at 1200 rcf for 5 min. The supernatant was removed, and ten 3 mm glass beads were added to the cells, and shaken vigorously for 1 min. After allowing the aerosols to settle, 6 mL of 1x PBS were added to the cells. The sample was rocked back and forth to wash the walls of the tube, and then allowed to sit for 5 min. After, the upper 5 mL of cell suspension was removed and filtered through a 70 μm cell strainer (FisherSci, 22363548). New glass beads were added to the cell solution and shaken a second time for 1 min. After shaking, the cell solution was allowed to stand for 10 min, and the upper 4 mL suspension was recovered and used for experiments.

Optical density measurements at 600 nm (OD600) were taken using a Go Direct® SpectroVis® Plus Spectrophotometer (Vernier, GDX-SVISPL), and were used to estimate the number of cells/mL. Because of the difficulty accurately counting bacterial cells, cell solutions at various optical density measurements were counted on a BD FACSAria™ III flow cytometer alongside a known quantity of Countbright™ Absolute Counting Beads (ThermoFisher, C36950**).** It was assumed that one event corresponded to one bacterial cell, and a standard curve correlating Flow Cytometry Events vs. OD600 was created. This was used to estimate the number of cells in a suspension before each experiment (**Figure B1**). A 10-fold dilution series of bacteria containing 10^6 bacilli/mL down to 10^3 bacilli/mL was created, and direct smears of the dilution series were created to determine that the estimated amount of bacteria corresponded to what was present on the slide before use.

Processing of pure mycobacterial samples.

All stains and buffers used were 0.22 μm sterile filtered before use. Each 2.020 mL sample was split into three parts for a paired comparison. First, 20 μL was removed and applied to a 2 cm^2 area of a plain glass microscope slide treated with 0.01% poly-L-lysine, creating a direct smear, or unprocessed control. This is the same volume of sputum that is sampled, smeared, and stained for diagnosis.[285] The remainder of the sample was split into two individual 1 mL fractions. Both fractions underwent the same volumetric concentration protocol. The volumetric only control sample was recovered into a final volume of 20 μL and applied to a 2 cm^2 area of a plain microscope slide. A 20 μL volume was chosen as the volumetric-only control resuspension volume because it is the same volume of liquid used in a direct smear.

The second sample, which used combined volumetric concentration + Marangoni enrichment was recovered into a final volume of 50 µL, and had the entire 50 µL of the recovered sample placed onto a Water Repellent Rain-X® treated slide with 10 µL spots of PLL; droplets were placed on the grid indicating where the PLL spots were located, as described previously, and allowed to dry completely at room temperature in a closed biosafety hood, with airflow turned off. All samples were placed on their own microscope slide to ensure that no contamination occurred between samples. With all samples dry, slides were heated on a heat block at 65°C for 2 h to completely inactivate and heat fix the BCG onto the slide, followed by Ziehl-Neelsen staining using a BD BBL/Difco TB ZN Stain Kit, according to the manufacturer's directions (fishersci.com, B12520). A piece of blotting paper (GE Lifesciences, 3030-861) was used to prevent the sample from drying out while heating the sample with the first carbol fuschin stain. All samples were glycerol mounted in 90% glycerol, 10% 10x PBS under a #0 cover glass (Thor Labs, CG00K), and sealed with nail polish in preparation for imaging.

For the samples that underwent volumetric processing, 10 µL of 200 µm streptavidin NPs (OceanNanotech, SV0200) were added to the BCG containing samples, briefly vortexed, and then placed on a lab rotisserie for 1 h. These sized nanoparticles were selected because individually they are smaller than the diffraction limit of light and would not obscure bright-field visualization of bacteria. Samples contained 10-fold dilutions of BCG bacteria as specified. After binding, samples were magnetically separated on a magnetic tube rack for a minimum of 30 min. The unbound supernatant was removed, and the samples were washed twice with 1 mL of 1x PBS + 0.01% Tween-20. Finally, volumetrically concentrated samples were suspended in 0.5x PBS + 0.01% Tween-20 (PBS-T), as previously indicated, placed onto the Rain-X® + PLL prepared slide, and allowed to dry overnight in a closed biosafety cabinet with the airflow turned off (**Figure 4.2**).

Microscope image post-processing.

Images were altered post-collection to improve visual appearance for publication as follows. To reduce the effects of uneven illumination using ImageJ,[286] NP droplets had a representative background image subtracted from the original deposition image. All images had brightness and contrast adjusted as needed to improve image visualization/printing for publication. Differences in the "Auto White" setting of NIS Elements during image collection resulted in varied color of the PS particle images; for this reason, all PS fluorescent images were recolored green in Microsoft PowerPoint for consistency in the final manuscript image. No specific quantitative data was

taken from any of the images pre- or post-processing, except for the particle deposition area, which was measured in NIS Elements from the raw image in pixels^2.

Imaging of paired processing methods.

BCG processed samples were imaged on an Olympus CX23. This is a model of microscope that is commonly available in primary rural clinics in low-resource areas of the world (W. Silva, personal communication, March 19, 2019),[184] and this is why it was chosen for final sample imaging in place of the Nikon TE-200U. Samples were manually inspected at 1,000x total magnification under oil immersion, and assessed by inspecting up to 100-fields of view and recording the number of acid-fast bacilli visualized using the semi-quantitative method outlined in the Global Edition of the Laboratory Diagnosis of Tuberculosis by Sputum Microscopy Handbook.[151] Cells had to be stained a dark pink or red to be considered "positive" for a BCG cell. Poorly stained cells or contaminants were not counted towards the cell count, ensuring conservative estimates. Images were taken using a Gotsky Microscope Lens Adapter with WF 10X Eyepiece with 30 mm Tube Smartphone Camera Adapter (Amazon.com, https://www.amazon.com/gp/product/B085C6ZKSL/ref=ppx_yo_dt_b_asin_title_o00_s00?ie=UTF8&psc=1) and an iPhone XR, Model MT3L2LL/A. All samples were imaged at 1,000x under oil immersion, and images were selected to be representative of the all samples inspected. Top view images of the Marangoni droplets were also taken at 40x total magnification for a global view of the evaporated droplets. A microscope micrometer was used to determine scale.

Results

There are two types of radial flows observed in an evaporating sessile droplet.[132-134, 140, 287, 288] The first, which are found in droplets containing pure water, are capillary flows responsible for the "coffee ring effect," carrying suspended colloids to the edge of the droplet radially outward along the substrate, resulting in a nonuniform deposition pattern across the droplet area upon complete drying, with particles at the edge of the droplet upon drying.[132-134] A secondary radial flow forms when the nonuniform evaporation rate (indicated by blue arrows in **Figure 4.1**) of the sessile drop, thermal conductivities of the substrate and droplet solvent, and surface tension of the drop all interact synergistically, resulting in a temperature gradient across the droplet volume. This creates predictable, specific flow patterns, known as Marangoni flows (**Figure 4.1**).[142, 279] Marangoni flows can move in the

same direction or opposite direction of the fluid stream in the coffee ring effect, and can result in particles depositing at the edge or center of the drop, or across the entire liquid-solid interface. Based on our prior work, we know that when Marangoni flows move inward along a hydrophobic substrate, a clearly defined central deposition of 1 μm particles occurs, forming what is essentially a reverse coffee ring. In addition, Marangoni flows can also be influenced by a nonuniform surface tension gradient.[133]

While there are a variety of biological applications using Marangoni flows in evaporating sessile droplets,[145, 289-292] unfortunately, previous work does not use materials compatible with many microbiological staining protocols. Knowing this, we sought to use established knowledge to intelligently design a new system compatible with cellular biomarkers. This system can then be paired with a volumetric concentration strategy to further improve the results of the method.

We first focused on identifying a new substrate material. Identifying the substrate required that multiple design requirements be taken into consideration. For acid-fast staining, materials should be optically clear, flame resistant (will not burn with prolonged flame exposure), nonporous, inexpensive and readily available. It was also important that we preferentially concentrate the NPs and bacteria into the center of the drying droplet, since this would create a small, well-defined area for inspection under a microscope.

Effect of candidate substrate physical characteristics on particle deposition patterns.

It is known that both the droplet contact angle and the ratio of the substrate, k_s, and droplet solvent, k_L, thermal conductivities are important in determining the circulation direction of Marangoni flows (**Figure 4.1**)[142] in evaporating droplets. Established theory by Ristenpart *et al.* states that for the Marangoni flows to move inward along the liquid-solid substrate interface and outward along a drop's liquid-air interface (referenced from here on as the direction of fluid flow along the substrate) can be achieved by keeping the ratio of the thermal conductivities k_s/k_L less than 1.45. When the ratio is greater than two, the flow field reverses and instead flows outward along the substrate surface. When a ratio between 1.45 and two is achieved, the Marangoni flow direction is dependent on the droplet contact angle.[142, 287] The direction of the fluid flow[142] and forces applied to the colloids ultimately impact where colloids deposit, and for this reason it was critically important to maintain fluid flow inward along the substrate. Though the contact angle is irrelevant for Marangoni flow direction when k_s/k_L is less than 1.45 or greater than 2, it can also impact the final particle deposition pattern,[142] so we preserved both the contact angle and

Marangoni flow direction in our new design. Logically, glass slides used for sputum smear microscopy, and PDMS, the substrate known to yield the desired Marangoni flow patterns[145] were chosen as candidate substrates. Beyond those, surface coating materials containing PTFE or polysiloxanes were selected for initial testing because of their low thermal conductivity (**Table 4.1**) and high heat resistance. ITO coated glass, which meets all the design criteria, with the exception that its high thermal conductivity would produce outward-oriented flow patterns in aqueous droplets, was selected for comparison to the candidate substrates with lower conductivity.

We started substrate characterization by measuring the contact angle of water on the substrates. This gave information about how a substrates' hydrophobicity/hydrophilicity will impact surface tension of the droplet. **Figure 4.4A** plots the measured contact angle of 2 µL water droplets on the candidate substrates. The contact angles measured for PDMS (109.6° ± 1.9°), DuPont® PTFE (104.6° ± 6.1°), Water Repellent Rain-X® (101° ± 1.8°), Sigmacote® (86.3° ± 1.2°), plain glass (23.5° ± 4.7°), and Probe On™ glass (53.1° ± 5.6°) are consistent with literature values.[293-295] The positive charge of the Probe On™ slides creates a more hydrophobic surface, with polar water molecules being partially repelled by the surface, creating a larger contact angle when compared to a standard glass microscope slide.

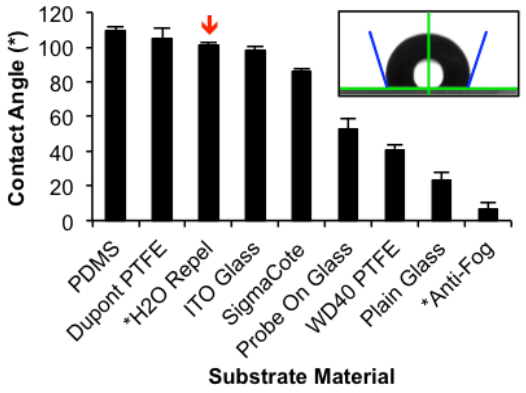

Figure 4.4. Contact angle measurements, as shown in insert, of 2 µL MilliQ water droplets on each candidate substrate (mean ± s.d.; n ≥ 13). Coatings with a contact angle less than 85° did not centrally deposit particles during evaporation. Red downward arrow indicates substrate selected for final design (H2O Repel). *Indicates Rain-X® product.

When measuring the contact angle for the WD-40® PTFE coating, the dried film was readily rehydrated upon drop deposition, and vortices of PTFE coating mixing into the droplets were observed through the side of the

droplet on the goniometer during measurement (data not shown). This would explain the smaller contact angle (40.8° ± 2.6°) compared to the DuPont® PTFE coating and reported literature values.[295]

The Anti-Fog Rain-X® performed as intended in everyday usage, such as on windshields or glasses, though this was the opposite of the other polysiloxane coatings; by creating a superhydrophilic surface, any water droplets that form on the glass surface are flattened to reduce visual interference. Anti-Fog Rain-X® had the smallest reported contact angle (6.9° ± 3.5°), though within 10 s of droplet deposition the contact angle was reduced to 0°.

Our goal was to create a highly repeatable, well-defined, small central deposition area that was also easy to find under a microscope, so it was important that we observed central deposition for both nano- and micron- scale particles, colloid sizes expected to be in our final droplet, before moving forward to biological experiments using rod-shaped bacilli. After measuring the contact angle of the selected substrates, particle-containing drops were allowed to evaporate, and the deposition pattern of PS particles and magnetic NPs were assessed. As shown in **Figure 4.5**, the materials with contact angles less than 85° failed to concentrate particles in the center of the evaporating droplet. The contact angle is dependent on cohesive and adhesive intermolecular forces within the liquid and between the liquid-solid interfaces. These forces are also at play between the liquid and suspended colloids. These can influence particle deposition directly based on the particles' chemical composition, not just indirectly by changes in the contact angle and surface tension. Furthermore, surface forces and inertial body forces acting on the particles control the particle trajectory within the flow velocity field and their deposition location. The balance of these forces change with the size, density, shape, and surface composition of the particles, as well as the velocity of the fluid flow, which result in different particle deposition patterns upon drying.

Three substrate surfaces in **Figure 4.5** showed deposition in the center of the droplet for both 1 μm and 200 nm colloidal solutions: Water Repellent Rain-X®, PDMS, and Sigmacote®. Water Repellent Rain-X® was ultimately selected as the final substrate coating for the design for a few reasons. First, Water Repellent Rain-X® covalently modifies the surface of glass without leaving a residue behind, which is a beneficial design for downstream assay packaging; the slides could be prepared by the manufacturer, and would be stable for long term storage. Second, unlike the Rain-X®, Sigmacote® left a residue on the slide that could be disturbed during handling. This would make pre-coated slides more difficult to package in a deliverable assay. It also increases the chance that

a sample is lost during the staining process after deposition and drying, and makes it more difficult for the sample to physically heat fix to the glass. And simply, Water Repellent Rain-X® is less expensive and very easy to acquire.

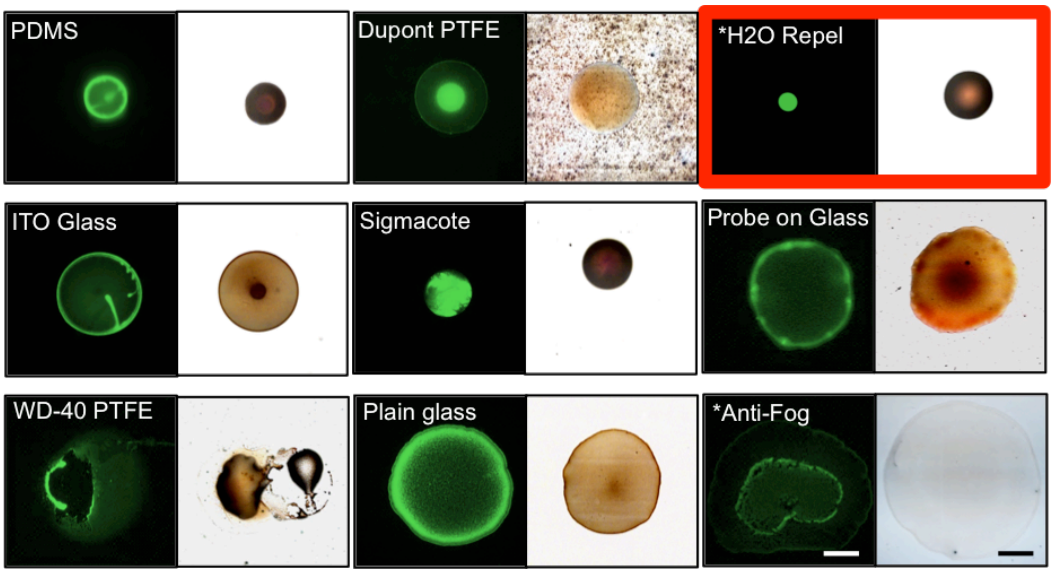

Figure 4.5. Particle deposition patterns of 2 µL droplets containing green fluorescent polystyrene particles (left of each pair) or 200 nm magnetic nanoparticles (right of each pair) in order of decreasing contact angle. Theory states that Marangoni flows in all droplets are oriented radially inward along the substrate, with the exception of ITO, which is oriented radially outward along the substrate. Because of the strong central deposition pattern, we selected Water Repellent Rain-X® (H2O Repel) to covalently coat microscope slides, creating our solid substrate. Scale bar = 500 µm, n = 3. *Indicates Rain-X® product.

ITO coated glass demonstrates how the reverse flow pattern changes the applied forces and impact on colloidal deposition. With a high thermal conductivity, theory states that the Marangoni flows are oriented outward along the substrate,[142] not inward as desired. This is regardless of its measured contact angle (98.5° ± 1.9°), which is similar to that of PDMS and other candidate surfaces that had highly efficient central deposition. As shown in **Figure 4.5**, PS particles (a similar size to individual bacteria) settle at the edges of the drop and NPs are deposited across the total drop interface, though with some concentration in the middle of the drop.

Effect of droplet solvent glycerol concentration on particle deposition patterns.

With a microscopy-compatible substrate determined, testing was then performed to establish a compatible solvent system. Trantum *et al.* had demonstrated that glycerol was important, though not necessary, for formation of

Marangoni flows. In addition, glycerol was added to prevent salt crystallization that interfered with imaging.[145] Unfortunately, glycerol is difficult to remove or evaporate due to its viscosity and high boiling point, making it incompatible with microscopy staining. Because of the acid-fast staining process, salt crystals are rinsed away, eliminating this problem. As shown in **Figure B2** and as observed by Trantum *et al.*, removal of glycerol from the droplet still formed centrally located Marangoni deposition in 2 μL droplets of 1 μm PS particles, 200 nm NPs, and *M. smeg*, a nonpathogenic mycobacterial cousin of *M.tb*. Again, theory states that these flows should be directed radially inward along the substrate.

Visualizations of inward-oriented Marangoni flows using OCT and microscopy.

After identifying a new substrate material and new solvent system that were both compatible with microscopic staining techniques and met the criteria established by Ristenpart *et al.*, we further confirmed that the final deposition pattern was due to Marangoni flows oriented inward along the substrate using OCT, as we have demonstrated previously.[135, 145] **Figure 4.6A** shows composite, time-lapse images through the diameter of a 1 μL evaporating droplet containing 10^6 polystyrene particles/μL. **Video B1** uses the same image series to dynamically show that the flow fields are oriented as expected in the inward direction along the substrate, the same direction shown by the black arrows in **Figure 4.6**. Reflection off the particles is indicated by the white dots moving within the droplet. During the first minute of evaporation, the microfluidic flows produced by the thermal gradient are initially unstable, possibly due to Bénard-Marangoni instability, though this is just speculative.[296] As time progresses, the chaotic flows stabilize into radially symmetric flows, as seen at 3 min. Due to the small size of the droplet, the accumulation of particles in the center of the droplet is not visible via OCT, but it is clearly observed upon total drop evaporation.

Microscopy was also used to visualize the microfluidic flows. While microscopy cannot image the entirety of droplet flows vertically, the images and videos gathered help support the data shown in **Figure 4.6A**. In **Figure 4.6B** a singular image with a 4 s exposure time was taken near the solvent-substrate interface of a 5 μL droplet containing 10^4 particles/μL, demonstrating movement radially inward. **Video S2** captured a series of images of the same droplet, which dynamically shows the flow field orientation. Images for **Video B2** were taken at 1 fps for 40 s.

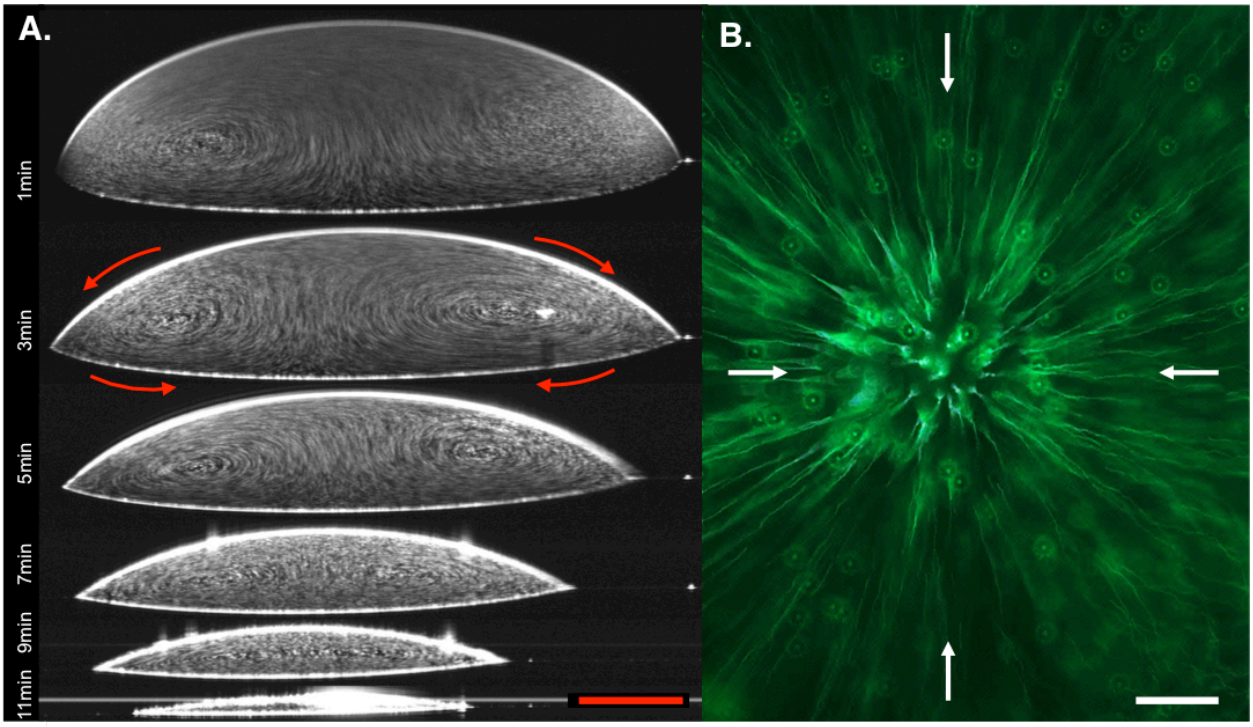

Figure 4.6. Time-lapse images demonstrate formation of Marangoni flow patterns oriented radially inward along the substrate. **A.** Starting at 1 min, and every 2 min thereafter until the droplets dried, composite images containing 800 repeated frames in 36 s were taken at the diameter of the 1 µL droplet to image the flow fields produced in the droplet using optical coherence tomography. Flow direction is indicated by red arrows. **B.** Top-view microscopy image showing movement of particles inward along the substrate surface of a drop in a 5 µL droplet. A single image was captured using fluorescent imaging with an exposure time of 4 s. White arrows indicate flow direction. Sample contains 10^6 and 10^4 particles/µL respectively. Composite videos for OCT and microscopy series can be found in Supplementary Information, and video captions can be found in Appendix B (**Video B1** and **Video B2**). Red scale bar = 125 µm. White scale bar = 100 µm.

Impact of droplet volume on particle deposition patterns.

With promising results in scale experiments and flow confirmation using OCT and microscope, we performed trials with larger volume droplets containing NPs to confirm that the Marangoni flows occurred independently of droplet size, using the final deposition pattern to assess performance (**Figure B3**). For droplets 1-100 µL in diameter, all drops exhibited central deposition of the suspended NPs. A 50 µL drop was chosen because it created a small enough central inspection area for efficient inspection without completely obstructing view, whereas smaller droplets resulted in central areas that were too dense to observe bacterial clusters among the NPs. Droplets larger than 50 µL had an extremely long drying time, making it not feasible to perform, given the drying

time for a 50 uL droplet already takes a minimum of 5 h. A time series showing the evaporation of a 50 μL drop, demonstrating the formation of the concentrated area during evaporation can be found in **Figure B4**.

Effect of poly-L-lysine substrate landing zone on particle deposition and sample adherence.

While it seemed the system was ready for use, a critical flaw in the substrate design, which was previously alluded to, became clear and required further design refinement. Because the surface of the microscope slide was covalently modified to become hydrophobic, even with heat fixation, the samples of NPs with and without bacteria were almost completely lost during the staining process; this required testing of a variety of fixation techniques to solve the problem. Specialty microscope slides provided inspiration. Specifically, companies commercially make positively charged slides that aid in sample adherence (such as the Probe-On^{TM} slides used earlier in this study), and at-home recipes for coating slides in poly-L-lysine (PLL) are readily available online. The PLL polymer helps enhance electrostatic interactions between the microscope slide surface and applied sample. We found that coating the entire Rain-X® coated slide in PLL impacted the deposition pattern leading to uniform deposition across the liquid-solid interface of the drop, likely caused by the positive charge of PLL ionically attracting the bacteria and NPs to the surface with enough force to overcome forces exerted by the radial Marangoni flows.

We then investigated if functionalizing the Rain-X® coated slides in the center of the droplet deposition area with PLL, not the entire slide, could create a "landing zone" for the sample, helping secure it for staining while not significantly changing the deposition pattern. With this, arrays of increasing size PLL spots were placed onto Rain-X® coated slides, followed by NP deposition on top of the array, ensuring the center of the drop was placed over the PLL spot, as indicated by graph paper taped the back of the microscope slide (**Figure 4.3**). The grid was removed for staining and imaging, and after analysis of the droplets, we determined that depositing a 10 μL PLL spot in the center of the 50 μL drop deposition area was the best option, because it resulted in improved uniformity of the central deposition area (**Figure B5**). The drawback to using such a large PLL spot is that a small amount of sample does deposit outside the most centrally concentrated area, across other regions of the liquid-solid interface of the drop. However, it was decided that this trade-off is worthwhile, since a larger PLL spot size allows for error as the operator manually deposits the final sample on the microscope slide. The implication is that the most concentrated center created by the Marangoni flows will still land on the PLL area, ensuring the majority of the sample is not lost. Though there are alternative methods to functionally achieve the same thing, such as derivatizing

the surface of the microscope slides with antibodies that target both the bacteria or NPs, the protocols to perform this are much more complex, require specialized reagents, and could require specialized storage conditions that in our opinion negate any potential selectivity it would provide.

Qualitative effect of volumetric concentration and Marangoni spatial enrichment of M. bovis *BCG using microscopic visualization.*

With the Marangoni flow system finally designed, combined volumetric concentration and spatial enrichment of *M. bovis* BCG was performed. The bacteria were nonspecifically captured on streptavidin-coated NPs, and isolated on a stationary magnet. After washing the particles, they were either applied over the standard 2 cm^2 area, creating a volumetric concentration-only control, or were suspended in 50 μL and applied as a drop to the PLL-Rain-X® functionalized slide. These were both visually and semi-quantitatively compared to a direct, unconcentrated smear (**Figure 4.7**). All samples regardless of processing method were stained using the gold standard Ziehl-Neelsen staining protocol. Initially, we had designed the method using anti-*M.tb* immunospecific NPs, but found that for both naked NPs and isotype control NPs, just as many bacteria were nonspecifically captured by the NPs during volumetric concentration. Those with experience working with mycobacteria know that they are extremely "sticky," and it can be difficult to prevent nonspecific binding of bacteria to surfaces. It is likely that creating an immunospecific particle will further improve the results shown here.

With the current limit-of-detection for sputum smear microscopy being 10^4 bacilli/mL,[297] as expected it is generally difficult to find any bacteria on the direct smears for all samples except 10^6 bacilli/mL. When samples were volumetrically concentrated, higher concentration samples benefitted significantly more than lower concentration samples. Even with volumetric concentration, only 2% of the smear area is inspected, and there were few or no bacteria seen by microscopy in the 10^3 bacilli/mL and 10^4 bacilli/mL samples. When volumetric concentration and spatial enrichment were combined, the 10^3 bacilli/mL and 10^4 bacilli/mL samples had visible, stained mycobacterial clusters in the central deposition area of the droplet. No bacteria were seen in any of the samples containing 0 bacteria. On a plain glass slide, central deposition of a sample NPs not occur (**Figure 4.5**, **Figure B1**).

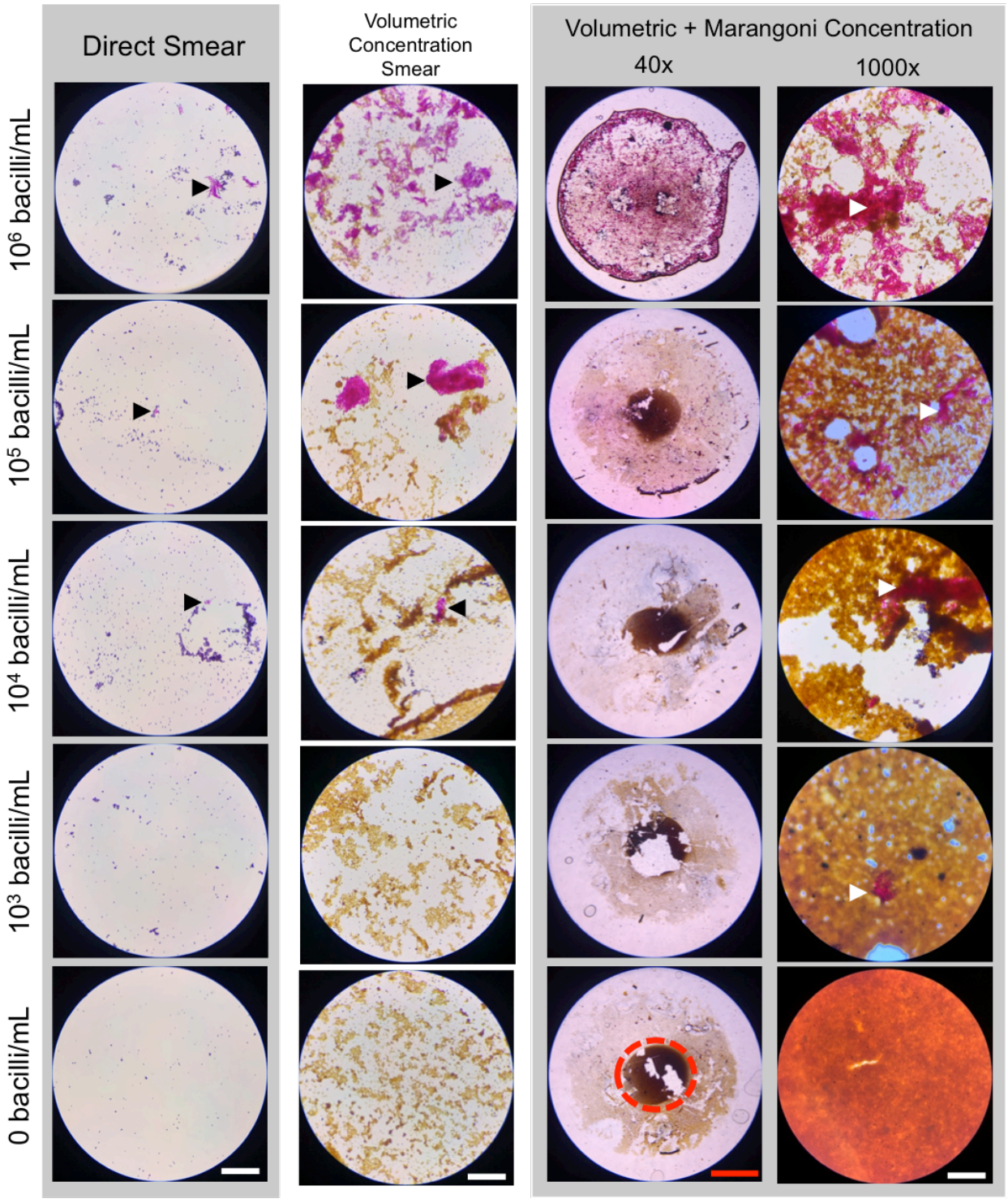

Figure 4.7. Effect of volumetric concentration and Marangoni spatial enrichment of 50 µL droplets on smear microscopy (n = 3). BCG-stained pink/red with Ziehl-Neelsen stain. Nanoparticles are brown, or may appear as red-orange if extremely concentrated, as seen in the lower right most image. Counterstained objects appear dark blue-purple. The most central deposition area inspected for combined volumetric + Marangoni concentration is indicated by a dashed red circle on the 0 bacilli/mL whole drop image at 40x magnification.

In the high magnification columns 1, 2 (black), and 4 (white) arrows indicate a positive smear. Images selected were representative of the samples inspected. White scale bar (columns 1, 2, 4) = 30 μm. Red scale bar (column 3) = 300 μm.

Semi-quantitative sputum grading of paired processing methods.

The benefit of combining spatial and volumetric concentration is further seen when samples were semi-quantitatively analyzed using the same examination methods used for diagnostic sputum grading during sputum smear microscopy (**Table 4.2**).[151] Grading of the smears was performed conservatively, given the difficulties of achieving a uniformly single-bacillus suspension with accurate quantification of bacteria in the sample. For the samples with higher concentrations of bacteria, volumetric concentration improved the grading by one grading, but this was not seen in lower concentration samples, particularly the 103 bacilli/mL. Specifically, volumetric concentration on its own failed to improve detection of these samples. With the addition of spatial concentration, these samples all had detectable amounts of bacteria even with some visible sample loss during staining. Even in areas where bulk sample was lost, stained bacteria were observed, showing that the addition of the PLL spot helped prevent sample loss not just macroscopically, but microscopically (data not shown).

Table 4.2. Semi-quantitative Grading for Each Sample Processing Method.[151]

		Sample Type		
		Direct Smear	Volumetric Concentration	Volumetric and Marangoni Concentration
Bacteria/mL	10^6	2+, 2+, 2+	3+, 3+, 3+	3+, 3+, 3+
	10^5	Sc(4),[***] 1+, 1+	2+, 2+, 2+	3+, 3+, 3+
	10^4	Neg,[†††] Sc(7),[***] 1+	1+, 1+, 1+	1+, 1+, 2+
	10^3	Neg, Neg, Neg[†††]	Neg, Neg, Neg[†††]	Sc(8),[***] 1+, 1+
	0	Neg, Neg, Neg[†††]	Neg, Neg, Neg[†††]	Neg, Neg, Neg[†††]

Discussion

Our Marangoni flow-enabled spatial concentration system, combined with volumetric magnetic NP concentration, resulted in a design that outperformed the current technique and was able to visualize bacteria in samples that contained 10x fewer bacteria than the current limit-of-detection for direct sputum smear microscopy

[***] *Sc(#) = Scanty (# cells counted).*

[†††] *Neg = Negative. See cited reference for sputum grading criteria.*

(**Table 4.2**). This study is the first of its kind to use the microfluidic principles of Marangoni flows to improve microscopic visualization of whole pathogens using standard microscopic staining techniques.

We designed the method with the goal of introducing an improvement to the current workflow, rather than establishing an entirely new diagnostic method. Unlike our previous design, particles that do not aggregate are designed to still deposit in the center of the droplet. We chose this design because it creates a clearly defined, small area for inspection for the presence or absence of *M.tb* bacilli under the microscope. A significant majority of the time and labor that goes into sputum smear microscopic diagnosis of TB is inspection of the smear itself, which is applied over a large 2 cm^2 area. Concentrating the sample into a smaller known area increases the chances of observing TB bacilli, especially when paired with volumetric concentration. Current smear inspection looks at 100-fields of view, which is equivalent to 2% of the standard smear area. Use of Marangoni concentration deposits the majority of the sample into the most central deposition area (as indicated in **Figure 4.7**), increasing the inspected sample area to ~90%. For a 1 mL sample, volumetric concentration alone into a 20 μL smear concentrates the sample 50x. Spatially, while the sample is primarily concentrated into the center of the droplet, the total area occupied by the sample is 5.3x smaller than the standard smear area, while the most central deposition area is 45x smaller. Combined volumetric and spatial concentration into a 50 μL droplet yields a sample that is enriched 105-fold. If the method were improved to concentrate 100% of the sample in the most central deposition area of the droplet, perhaps through improvements in the fixation protocol, total enrichment could be up to ~900x.

To overcome the limitations of bright-field microscopy-based inspection of sputum smears, there has been substantial effort to develop fluorescence microscopy (FM) for use with volumetric sample concentration-based methods for TB detection.[62, 152, 298-300] These approaches, centrifugation and magnetic bead separation, unfortunately use time-intensive and nonspecific isolation procedures, increasing labor requirements to the already lengthy inspection protocols. As a consequence, these concentration-based FM smear methods show only modest improvements in clinical sensitivity,[301] but reduced specificity.[301, 302] In addition, FM inadvertently creates a second barrier for implementation because of its reliance on FM technology that is frequently unavailable in low-resource settings.[183] Other magnetic bead separation strategies use larger particles that obscure visualization of the bacteria, requiring that FM be used for visualization. While these methods have failures that prevent implementation, our design works to overcome the barriers presented. Our method demonstrates the potential for what is achievable with further design of an antigen-specific NP. For the purposes of this study, the "stickiness" of mycobacteria allowed for

use of nonspecific isolation on a simple streptavidin particle, but in practice, other contaminants, such as non-tuberculous bacteria and human cells found in the airways, would also stick to the particles, creating a sample that is impossible to accurately and effectively visualize without providing any specificity. The use of NPs smaller than the diffraction limit of light enabled improved visualization of the sample using bright-field microscopy and gold standard acid-fast staining techniques. Though not demonstrated, fluorescent-staining techniques such as auramine O[184] could theoretically be used with our concentration method, but it is not a requirement for implementation like prior methods. The newly developed DMN-tre stain would provide the added benefit of not subjecting the sample to repeated harsh chemicals as occurs with acid-fast staining techniques; this would help resolve the issue of sample loss, but fluorescence microscopy would be required for visualization.[303]

There are two core phenomena that are important elements of our method. First, during volumetric concentration, the capture of bacteria on NPs form aggregates which are clearly visualized upon staining. Second, thermocapillary Marangoni flows oriented inward along the substrate are important for ensuring central deposition of captured bacteria and NPs. The formation of bacterial aggregates aid in the final visualization of the bacteria in the center of the drop, which are seen as large, three-dimensional pink or red networks of bacteria amongst the NPs (**Figure 4.7**). Regardless of the presence or absence of bacteria, the NPs settle in the center of the droplet during evaporation, creating a clearly defined area for inspection.

This study was designed to use known principles of Marangoni flow formation to engineer a new design for microscopic application. Changes from our prior work in both the substrate and solvent were determined. The solutions tested were based on the work of Ristenpart *et al.*[142] and our prior work[135, 145, 146]. Having clearly defined goals and design constraints allowed us to focus materials testing while also easily identifying inexpensive solutions for these improvements. The knowledge that Marangoni flows are not formed in pure water[139, 149] helped us in modifying the droplet solvent, allowing us to remove what was incompatible with microscopy while maintaining a system that created the desired flow pattern. The addition of the PLL droplet array was a critical design requirement for making our chosen substrate and solvent system useable.

The use of inexpensive, commonly available PLL and Rain-X® for the microscope slide substrate means the cost of the microscope slide is nominally more expensive. Also, the cost of the magnetic NPs was only $0.56/test at time of publication. Even with the addition of an antigen recognition system to the NPs, this assay could easily be produced at <$1.00/test, in addition to the cost of staining reagents already used at the POC. In addition, because

Rain-X® covalently modifies the surface of the microscope slide, and PLL-coated slides have a year-long shelf life if stored in a closed container, the slides could ship to decentralized testing sites prepared and ready for use with no required preparation. While PLL spots were applied by hand in this study, automated processing could create highly repeatable and reproducible microscope slides.

This report was designed to be a "proof-of-principle" study, and some limitations remain. As mentioned, it is important that the NPs be immunospecific in the final application, because as prior work demonstrates, nonspecific volumetric concentration of samples does not significantly improve sensitivity and also reduces specificity.[301, 302] The use of nonspecific isolation techniques in prior studies and the continued issues seen here demonstrate the difficulty in creating an immunospecific particle for specific capture of mycobacteria. The gap that remains by not solving this problem is not lost, since failing to specifically isolate mycobacteria from a sputum sample will make it impossible to visualize bacteria. Specifically it is extremely common for other biological contaminants to significantly outnumber TB bacteria in sputum samples; isolation of all biological contaminants will result in a dark blue stain that cannot be accurately read by the microscopist. For methods such as this to work, it is imperative that more development focus on methods to rapidly and specifically isolate mycobacteria. Even better, design and use of an antigen recognition element that can discern between tuberculous and nontuberculous infections would create a diagnostic that satisfies another diagnostic need that is currently insufficiently met using culture.[304]

Second, magnetic NPs were chosen specifically because they are smaller than the theoretical diffraction limit of light and are unable to individually obscure bacilli visualization like larger magnetic particles. However, together, if spatially concentrated enough, they can obscure imaging. The particle volume used in this study was chosen to yield efficient volumetric concentration while not completely obscuring visualization following spatial enrichment, but in other applications, these parameters would need to be optimized to prevent bulk NP imaging interference.

Third, given this is study intended to demonstrate the improvement of a rapid, POC diagnostic method, it is important that it can be performed in a period no greater than a few hours. In the current iteration, both the time it takes for magnetic separation, and the amount of time it takes for the droplet to dry are too long to meet this requirement, and changes to the method design are required. The lower magnetic susceptibility of the NPs, compared to more common ≥1 μm magnetic microparticles used in magnetic bioseparations significantly extends

the time it takes to magnetically separate the sample. When adding the increased viscosity of sputum in a patient sample, the separation using a stationary magnet is not feasible for use at the POC. The use of high-gradient magnetic separation, a technique that has been shown to rapidly and efficiently separate both micro- and NPs from large volume, high viscosity samples,[123, 238] has the potential to solve this problem and should be explored as an alternate to stationary magnetic pooling. This technique may also allow for use of even smaller NPs, providing another solution to bulk NP imaging issues. The use of entire sputum samples, which averages 3 mL in volume,[305] can further improve method sensitivity.

To solve the issue of the droplet drying time, the use of multiple smaller droplets instead of a single large droplet can significantly reduce the time to dry, though this could increase the inspection time and/or area. In addition, as demonstrated in microarray development, the use of a greater number of smaller drops rather than fewer larger drops can improve the sensitivity of the method [306]. Further studies should be performed to determine if this theory applies to our application and what the trade off between inspection area and sensitivity is. It also may provide a solution to potential NP visualization issues previously mentioned.

Conclusions

The proposed volumetric magnetic enrichment with Marangoni flow concentration is an effective alternative to the current method of sputum smear microscope-based inspection for TB diagnosis. We have shown that our method outperforms the current gold standard sputum smear method, and has advantages over other magnetic bead-based volumetric concentration strategies, namely the use of smaller particles that do not inhibit bright-field imaging. In addition, other methods fail to provide any type of significant spatial concentration after volumetric enrichment. The method is inexpensive, simple, fits within current smear and staining protocols, and does not require any additional specialized equipment that is not already available or easily obtainable and used at the point-of-care where sputum smear inspection is already performed. With further refinement, we expect that this technique can be applied to isolation and microscope-based inspection for other whole pathogens.

Acknowledgements and Funding

The authors thank Dr. Raymond L. Mernaugh, Dr. Patricia K. Russ, and Lejla Pasic of Vanderbilt University for insightful conversations regarding study design and thank Lejla M. Pasic for assistance with bacterial

electroporation**.** The authors thank the Blackburn Lab at University of Cape Town for assistance developing our mycobacteria-dissociation protocol, and thank Young-Hwa Song for the gifted plasmid. Flow Cytometry experiments were performed in the Vanderbilt Flow Cytometry Shared Resource Core. The Vanderbilt Flow Cytometry Shared Resource Core is supported by the Vanderbilt Ingram Cancer Center (P30 CA068485) and the Vanderbilt Digestive Disease Research Center (DK058404).

This work was funded in part by the US National Institutes of Health Grant No. R01-AI135937, R01-EY030490 and R01-EY031769 and in part by the Vanderbilt Institute for Surgery and Engineering (VISE).

CHAPTER 5 : IMPACT OF MECHANICAL AND ENZYMATIC CELLULAR DISSOCIATION METHODS ON CELLULAR DE-CLUMPING AND SURFACE ACCESSIBILITY OF LIPORARBINOMANNAN ON *M. TUBERCULOSIS*

Adapted from: Pearlman, S. I.; Pasic, L.; Blackburn, J.; Haselton, F. R., Impact of mechanical and enzymatic dissociation methods on cellular de-clumping and surface accessibility of lipoarabinomannan on M. *tuberculosis*; with permission from coauthors. In preparation.

Abstract

Tuberculosis (TB) remains a major global health problem, partially because of a lack of access to sensitive and specific diagnostic tests by those who need them most. Lipoarabinomannan (LAM) is a TB surface glycolipid virulence factor that has become a significant biomarker of interest in molecular TB diagnostics throughout the last few decades. However, most of what we know and understand about LAM and the mycobacterial cell surface comes from in vitro culture studies, not in vivo data. These results are confounded because mycobacterial cultures clump and therefore must be mechanically dissociated or grown in the presence of detergents to achieve unicellular suspensions. While the effect of culture additives on LAM surface expression is understood, nothing in the literature has characterized how mechanical or enzymatic dissociation methods alter the cell surface. We hypothesized that mechanical and enzymatic treatment of *M. tuberculosis* (*M.tb*) would change the cell surface features and impact the number of recoverable cells. Needle dispersion and glass bead beating created unicellular suspensions while enzymatic treatment with trypsin, lysozyme, lipase, or amylase did not de-clump *M.tb* on their own. To quantify LAM surface expression, we used newly identified LAM recognition elements that bind to its different structural regions; either the conserved arabinose backbone or TB-specific terminal mannose carbohydrate-capping motif. Both needle dispersion and glass beads improved LAM surface accessibility compared to cells recovered from simple surface washing; this was attributed to unprocessed cells exhibiting low expression levels of surface LAM, while cells found in clumps had a statistically higher LAM-surface expression. We also found that shear force from centrifugation removes the *M.tb* capsular layer, reducing the surface-accessible LAM. As more of the capsule is removed, LAM anchored to the outer cell envelope is exposed, recovering the LAM expression level seen before centrifugal processing. Even after a 60 minute digestion, none of the enzymatic processing methods impacted LAM

surface accessibility. To our knowledge, this is also the first study to show the binding of α-(1, 2)-mannobiose-binding cyanobacterial lectin microvirin-N to the surface of *M.tb*. We believe these detailed preparations methods will interest those studying or looking to preserve surface accessible structures of *M.tb* or those looking to use cultured cells for simulated samples in whole-cell diagnostic assay development.

Introduction

With 10 million cases annually worldwide, tuberculosis (TB) remains a significant public health issue, with individuals in developing nations disproportionally affected by TB disease.[2] While there are multiple methods to diagnose TB, these methods suffer from poor diagnostic sensitivity or are not available at the point-of-care (POC), exacerbating pre-treatment loss to follow-up rates, which are as high as 38% in low-income countries.[4] As a result, empiric treatment without molecular diagnosis or bacteriologic confirmation remains commonplace.[2, 4] The inability to rapidly and accurately diagnose TB disease with high sensitivity and specificity at the point-of-care (POC) continues to be a confounder in disease transmission, patient mortality, and morbidity, and time to treatment initiation in the developing world. Therefore, there is a significant need for rapid and straightforward POC diagnostics development to improve TB care for those who need it most.

Lipoarabinomannan (LAM) is a glycolipid virulence factor (**Figure 5.1**) highly expressed on the surface of *Mycobacterium* spp. (**Figure 5.2**).[219] LAM is a biomarker of interest for rapid molecular tuberculosis diagnostics for a few different reasons. First, *M. tuberculosis* (*M.tb*) and other *Mycobacterium* spp. actively shed LAM from their surface during active metabolic processes, and it is detectable in patient samples, eliminating the need to detect whole cells or DNA.[226] Most notably, LAM has been used to diagnose TB from urine in a lateral flow platform, with examples including the Alere™ Determine™ TB LAM Ag Test[221] and Fujifilm SILVAMP TB LAM.[213] Unfortunately, these tests reduce mortality and improve patient outcomes only in severely immunocompromised patients with HIV (CD4 count <100 cells/μL).[307] Therefore, the World Health Organization endorses using the Alere™ test only in this patient population.[223] More recent studies suggest LAM urine lateral flow tests may aid TB diagnosis in severely malnourished children, but broader studies are needed.[212, 213] Given the limited size of these two patient populations, LAM urine lateral flow tests these tools have not been helpful screening tools for most populations.

The second reason LAM is a biomarker of interest is because of the structural variability of the carbohydrate-capping motif on LAM (**Figure 5.1**). Specifically, LAM has three structural regions. The two structures that make up the anchor and backbone of the molecule, the mannosyl-phosphatidyl-*myo*-inositol surface anchor and a polysaccharide backbone composed of D-mannan and D-arabinan branches, are conserved structures across all *Mycobacterial* spp.[219] The third domain, the capping motif of LAM, varies based on the species. Slow-growing pathogenic species, including *M. tuberculosis* complex species (MTBC; e.g., *M. tuberculosis*, *M. bovis*, *M. bovis* BCG, *M. canetti*, *M. africanum*), are capped with one to three α-D-Man*p* residues linked through α-(1→2)-glycosidic linkages,[308] referred to herein a ManLAM. Fast-growing and NTM-associated species have LAM capped with a phosphatidyl-*myo*-inositol cap called PILAM. The third capping motif lacks any cap terminal cap, known as AraLAM.[219] Even though the number of mannose and phosphoinositol carbohydrate caps on each LAM molecule is highly variable across each species, the structural differences in this terminal cap make it an attractive biomarker for differentiation between TB disease and NTM infection.

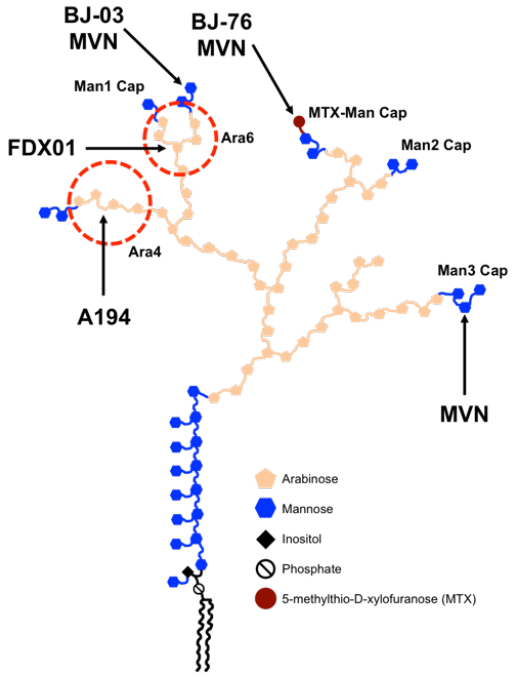

Figure 5.1. The structural motifs of ManLAM, with LAM recognition element target structures indicated. Man1 = mannosyl monomer cap. Man2 = mannosyl dimer cap. Man3 – mannosyl trimer cap. MTX-Man – Man2/3 cap with the single terminal mannose residue substituted with an α-(1,4)-linked methylthio-D-xylofuranose (MTX).

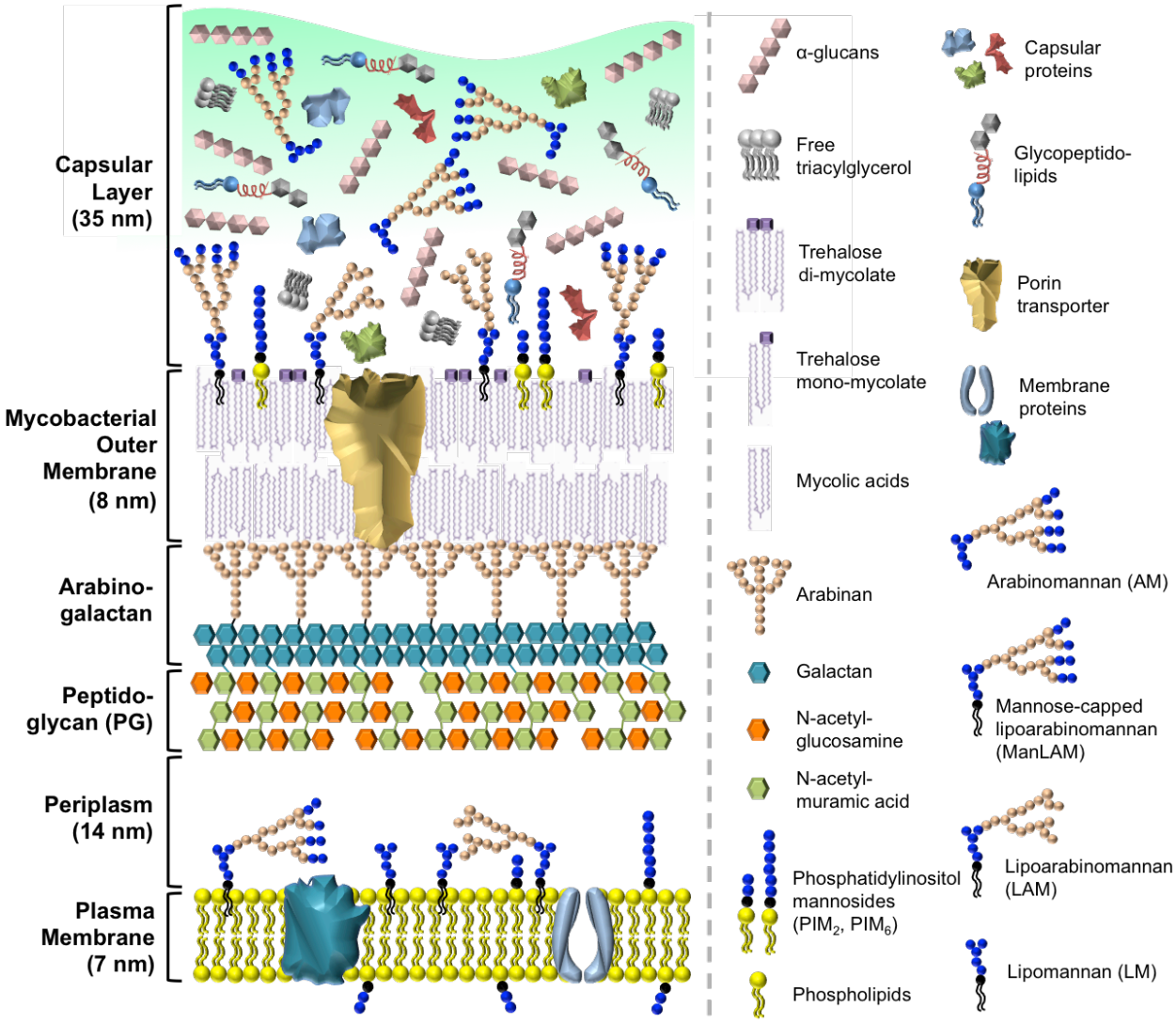

Figure 5.2. Cross-sectional drawing of *M. tuberculosis* cell envelope. There are four main components of the mycobacterial cell envelope. Working from the inside to outside of the cell, they are (**I**) the plasma membrane, (**II**) peptidoglycan (PG) and arabinogalactan complex, (**III**) the mycobacterial outer membrane, and (**IV**) the outer capsular layer. The plasma membrane is composed of standard phospholipids, membrane proteins, and phosphatidylinositol mannosides, which include lipoarabinomannan (LAM), its precursors lipomannan (LM), PIM_2, and PIM_6, and arabinomannan (AM), a lipid-free antigen similar in structure to LAM. The peptidoglycan and arabinogalactan complexes help stabilize the outer mycobacterial membrane against osmotic pressures. The outer membrane is covalently esterified to the arabinogalactan layer and is composed of mycolic acids. These waxy molecules make *M.tb* challenging to penetrate, with the surface of this outer membrane having trehalose mono- and di-mycolate modified mycolic acid. Most notably on the outer surface is LAM, which makes up 15% of the total bacilli mass, in addition to LM, PIMs, and transporter proteins. The outer capsular layer contains LAM and its precursors, which are shed from the surface of *M.tb*. It also contains polysaccharides, including α-glucan, capsular proteins, and small amounts of glycopeptidolipids and triacylglycerols.

There also exists a chemically distinct version of the ManLAM cap in *M.tb*. This 5-methylthio-D-xylofuranose (MTX) mannose cap has the single terminal mannose residue substituted with an α-(1,4)-linked methylthio-D-xylofuranose (MTX) residue.[309] Generally, there is only a single MTX-Man Cap on each ManLAM molecule, making it an unlikely diagnostic target due to its low abundance.[310] Nonetheless, multiple antibodies have been developed to target the MTX-Man cap decidedly because of the extremely high specificity it would provide new tests.[224, 226]

Even though LAM is an excellent candidate biomarker, developing LAM-based diagnostics continues to be complicated. For decades, knowledge about LAM structure and function came exclusively from lab cultures, raising the question of how relevant this knowledge was to *M.tb* in vivo. The high heterogeneity of LAM has made it difficult to understand these characteristics fully. In addition, the propensity for *M.tb* in culture to stick together in millimeter-sized means cells directly from culture are unusable, and de-clumping is required to obtain individual cells or small aggregates usable for study.

Attempts to solve the cell clumping problem by including chemical and biological (e.g., enzymes, blocking proteins) flocculants or additives in culture media have been explored. The most common culture additive used is Tween-80. While addition makes working with cultures reduces clumping,[311] inclusion of Tween-80 also reduces the abundance of detectable arabinomannans (AMs) on *M.tb*'s surface, including LAM. In addition, Tween-80 destabilizes the capsular layer (**Figure 5.2**) of *M.tb*.[89 88, 89] However, for those studying the *M.tb* capsule or surface-bound structures, including Tween-80 in culture can be more detrimental than beneficial.

Without culture additives, cell clusters must be isolated from culture and pre-processed to reduce the difficulty of working with the slow-growing cultures. Mechanically dissociating mycobacterial clumps using glass beads or needles is not new and is commonly used to avoid the stability issues observed with Tween-80.[88, 89] Enzymatic digestion could also be performed, but this is uncommon given the risk of cell lysis and general difficulty of physically penetrating the *M.tb* surface. Regardless of the cell dissociation method, beyond the influence of detergents or other additives used during growth in suspension culture, little is known about how post-culture mechanical and enzymatic dissociation techniques influence *M.tb* surface structure accessibility before downstream use of recovered bacteria.

This study uses several newly available LAM recognition elements to characterize LAM surface accessibility on *M.tb* following mechanical and enzymatic dissociation. With limited knowledge on how these often

necessary post-culture processing methods influence *M.tb* surface marker expression levels, we hypothesized that different mechanical and enzymatic treatments would (**1**) impact the recovery of usable, quantifiable cells from clumps formed in culture and (**2**) change the density of surface biomarker found on the cell surface. With significant interest in using LAM for TB diagnosis, this study aims to provide important information to researchers interested in *M.tb* surface-accessible structures.

Materials and Methods

Microvirin-N biotinylation.

Dr. Megan van der Horst (Department of Chemistry, Vanderbilt University) generously gifted us microvirin-N (MVN)[312] previously purified using His-tag purification. Production is described in van der Horst *et al.* 2021.[86] MVN was reacted with 20x molar equivalents of EZ-Link™ NHS-PEG_{12}-Biotin (ThermoFisher, A35389) for one hour at room temperature on a lab rotisserie according to the manufacturer's protocol. Zeba™ Spin Desalting Columns, 7K MWCO (ThermoFisher, 89882) removed unreacted NHS-PEG_{12}-Biotin following reaction incubation. The final concentration of biotin-conjugated MVN was determined using absorbance at 280 nm on a Nanodrop™ Spectrophotometer ND-1000.

Preparation of gamma-irradiated Mycobacterium tuberculosis *(*M.tb*).*

Mycobacterium tuberculosis, Gamma-Irradiated Whole Cells of Strains H37Rv, (NR-49098, Lot# 70042402), East African Indian 91_0079 (NR-49102, Lot#63648741), HN878 (NR49001, Lot# 70005745, 70045520), Indo-Ocean (NR36491, Lot# 62554359), and Indo-Ocean T17X (NR-49101, Lot# 63648740) were obtained from the Biodefense and Emerging Infections Research Resources Repository (BEI Resources, Manassas, VA), NIAID, NIH. *M.tb* H37Rv cells were used for mechanical dissociation and centrifugation experiments. For enzymatic dissociation experiments, HN878, East African Indian, and both Indo-Ocean strains were pooled into a single population containing ~20% HN878, ~20% East African Indian, ~50% Indo-Ocean, and ~10% Indo-Ocean T17X to reduce sample variability. The cells were thawed at room temperature, pooled into a single 50 mL conical, and suspended in 10 mL of 1x PBS (137 mM NaCl, 2.7 mM KCl, 10 mM Na_2HPO_4, 1.8 mM KH_2PO_4). Large aggregates of cells were allowed to settle for 5 min, and the upper 5 mL of supernatant was removed. These cells

were saved and used as an “unprocessed control” for comparison. The remaining cell aggregates were divided into populations containing approximately 0.2 g of cells (estimated by cell volume) each in 50 mL conical tubes and centrifuged at 1,100 x rcf for 5 min in Beckman Coulter™ Allegra™ X-22R Centrifuge. The supernatant was removed, and the cells were processed according to the described chemical or mechanical dissociation protocols (below). At no point during ANY preparation/dissociation/antibody staining was a Vortex-style mixer used to mix cell solutions to prevent the additional and uncontrolled application of shear forces to the cells. All mixing was done through gentle inversion or pipetting.

Mechanical dissociation of M.tb.

For glass bead processing, ten acid-alcohol (fuming HCl, followed by 70% ethanol, then MilliQ water)-washed and autoclaved three mm glass beads (MilliporeSigma, 1040150500) were added to the 50 mL conical tube of cells vigorously shaken for 1 min. After allowing aerosols to settle for at least 1 min, 6 mL of 1x PBS were added, and the tube gently rocked to wash cells off the tube walls. The large aggregates were allowed to settle for 5 min, and the upper 5 mL was transferred into a clean 50 mL conical tube and processed as described.

For needle dispersion, 1 mL of 1x PBS was added to cells. An autoclaved 1” blunt-tipped 21-gauge needle (FisherSci, NC1507901) was placed onto a 1 mL tuberculin syringe (BD, 309659). The syringe was used to draw the cell solution up and down through the needle 20-25x, approximately 2 min. An additional 5 mL of 1x PBS were added to the cells, and they were then allowed to settle for 5 min. The upper 5 mL of cells were then transferred into a clean 50 mL conical tube.

Following each mechanical processing method, the retained 5 mL fractions of cells were centrifuged at 378 x rcf for 10 min, and the upper 4 mL of supernatant were removed, which contained the cells used in the experiment. Triplicate optical density measurements at 600 nm (OD600) were collected for each population using a Vernier Go Direct® SpectroVis® Plus Spectrophotometer (Vernier, GDX-SVISPL). These readings' were averaged and then used to estimate the number of recovered cells. Because of the difficulty of accurately counting the total number of cells, cell solutions at various optical density measurements were counted on a BD FACSAria™ III flow cytometer alongside a known quantity of Countbright™ Absolute Counting Beads (ThermoFisher, C36950). Because of their small size and rod shape, there were no distinct populations discriminating events containing single cells vs. double cells. For this reason, it was assumed that one event corresponded to one bacterial cell, and a standard curve

correlating Flow Cytometry Events vs. OD600 was created (**Figure B1**). Cell-staining with the LAM recognition elements was then performed as described below.

Enzymatic dissociation of M.tb.

Trypsin-EDTA, 0.25% Trypsin/2.21 mM ethylenediaminetetracetic acid (EDTA) in Hank's Balanced Salt Solution (MediaTech/Cellgro-Corning, MT25053CI) was placed into 5 mL sterile aliquots upon receipt and frozen at −80°C until use. α-Amylase from porcine pancreas (MilliporeSigma, A3176-500KU), Lipase from *Aspergillus niger* (MilliporeSigma, 62301-100MG-F), and Lysozyme were reconstituted at 5 mg/mL, 10 mg/mL and 10 mg/mL respectively in 10 mM Tris-HCl, pH = 8, based on the recommendation by SigmaAldrich.[313] The lysozyme was frozen in aliquots at −80°C until use. Lipase and amylase were prepared fresh and used within 3 h of preparation.

All enzymes and cells were pre-warmed to 37°C before digestion. The amylase, lipase, and lysozyme samples were suspended in a total volume of 2 mL of 1x Tris-buffered saline (TBS; 50 mM Tris HCl, 150mM NaCl; Corning, Cat# 46-012-CM) containing 200 µg of lysozyme (pH = 8),[88, 314] 2 µg amylase (pH = 7.4),[315, 316] or 5 µg of lipase (pH = 7.4).[317, 318] A final concentration of 1 mM $CaCl_2$ was included in the amylase-digested samples, since Ca^{2+} is required for enzymatic activity. Cells treated with trypsin were directly suspended in 2 mL (5 mg) of stock trypsin/EDTA. Cells were placed in a 15 mL conical tube, and the tube was positioned on its side on a shaker set at ~200 rpm for 60 min at 37°C to provide some mechanical agitation to aid in enzymatic digestion.

Trypsin was inactivated by adding 5 mL of 1x PBS + 10% Fetal Bovine Serum (Summit Biotechnology, FP-100-03) to each sample. Amylase was inactivated by adding 6 mL of 1x TBS, 15 mM $CaCl_2$ (pH = 7.4) to each sample since a high calcium concentration is known to inhibit amylase.[315] Lysozyme and lipase were inactivated by adding 1x TBS containing a final sample concentration of 0.25 mM or 0.5 mM, respectively, of $FeSO_4 \cdot 7H_2O$ (Alpha Chemicals, B007ODUI76), pH = 7.4 in a total volume of 8 mL.[319, 320] Following inactivation, the cells were centrifuged at 1,100 rcf x 10 min and washed two times in 6 mL of 1x PBS. The cells were suspended in 6 mL 1x PBS again after removing the supernatant. Enzymes alone universally failed to de-clump cell aggregates. In an attempt to improve cell cluster dissociation, enzymatically-digested cells were dispersed using a 21-gauge needle as described for mechanical processing. The remaining clumps were used for analysis since enzymatic dissociation did not produce any significant quantity of single cells.

Because $FeSO_4$ precipitates in an aqueous solution, both cells and the brown precipitate pelleted in the tube during centrifugation, making complete $FeSO_4$ removal near impossible. Instead, cell clumps were settled using gravity for 1 h. The supernatant containing $FeSO_4$ was then carefully removed without disturbing the loosely-packed cell clumps. After adding a new volume of wash buffer, the process was repeated a second time to reduce $FeSO_4$ contamination before surface staining.

Antibody staining controls containing 0.02 mM and 0.05 mM $FeSO_4$ were run in parallel on unprocessed cells to elucidate better the impact of $FeSO_4$ on antibody binding and detection (**Figure C1**). Because of the difficulty separating cells and $FeSO_4$ precipitate, the exact concentration of $FeSO_4$ in each cell population was unknown. We considered using absorbance to measure the $FeSO_4$ concentration, but cell clumps in the samples made accurate measurement difficult. Based on the visual appearance of the brown-tinged buffers relative to known concentrations of $FeSO_4$, we do not believe the concentration of $FeSO_4$ was higher than 0.02 mM for all samples.

Triplicate OD600 measurements for each population were measured using a Vernier Go Direct® SpectroVis® Plus Spectrophotometer, and the number of cells recovered was estimated using the standard curve (**Figure B1**). Because the standard curve was established using a known single-cell suspension, and the enzymatically-treated cells still contained clumps of cells, the exact number of cells in each sample was not known. Cells were then stained with LAM recognition elements as outlined below.

Impact of centrifugation speed in LAM surface expression.

Leftover unprocessed cells were for these experiments. The cells were divided into tubes containing 1.3 million cells per 650 µL sample, and centrifuged 1x, 3x, or 5x at 1,230 x rcf, 4,800 x rcf, for 10 min or 10,000 x rcf, or 20,800 x rcf for 2 min in an Eppendorf® Centrifuge 5417R (Hamburg, Germany) in 2 mL microcentrifuge tubes. Three tubes were processed in parallel for each condition. All samples independent of centrifugation conditions were inverted to resuspend cells between each step to ensure equal mechanical agitation outside of centrifugation across all conditions. Following centrifugation, cells were stained with LAM recognition elements as outlined below.

Acquisition and titration of antibodies for cell surface staining of LAM.

Anti-LAM antibodies A194 and FDX01 (raised in human), and BJ-03 and BJ-76 (raised in rabbit), were generously gifted by Foundation for Innovative and New Diagnostics (FIND). A194,[226, 321] BJ-03 and BJ-76[322] are previously been described in the literature. Measured primary antibody concentrations and antibody and MVN titrations are found in **Table C1** and **Figure C2**. All antibodies and MVN titrations were performed with *Mycobacterium tuberculosis*, CDC1551, Gamma-Irradiated Whole Cells (BEI Resources, NR-49009, Lot# 70037237) following dissociation using glass beads, as described. This optimization helped identify appropriate working concentrations. For final experiments, primary antibodies BJ-03, BJ-76, FDX01, and A194 were used at 1:2,000, 1:4,000, 1:2,500, 1:1,000 dilutions, respectively. Secondary antibodies goat anti-Rabbit IgG H+L conjugated to Horseradish peroxidase (HRP; abcam, ab205718), goat-anti-Human H+L HRP (abcam, ab6858), and anti-Biotin (abcam, ab53494) were used at 1:2,000, 1:3,500, and 1:1,000 dilutions, respectively. For MVN, 2 µg of MVN-Biotin was applied to each sample. Goat anti-Mouse IgG Fc-specific HRP (SigmaAldrich, A2554) was substituted as an isotype control for the HRP-conjugated detection antibodies. Human IgG1 Lambda Myeloma Purified Protein (SigmaAldrich, I4014) was the isotype control antibody for FDX01 and A194. Dr. Raymond L. Mernaugh (Department of Biochemistry, Vanderbilt University) generously gifted a purified rabbit polyclonal IgG antibody used as the isotype control antibody for BJ-03, BJ-76, and anti-Biotin.

The measured Normalized Absorbance for each isotype control condition is shown in **Figure C3**. When the secondary anti-Mouse-HRP isotype control was applied for detection for all LAM recognition elements, under no conditions was nonspecific binding observed. All samples had lower absorbance than samples treated with anti-Mouse-HRP only (**Figure C3A**). When isotype antibody controls replaced the primary LAM antibodies (or anti-Biotin for MVN), all conditions showed some nonspecific binding compared to secondary-only control samples (**Figure C3B**). For this reason, in analysis, the isotype control was generally used for background subtraction unless the secondary-only control value had a higher measured absorbance, such as in samples treated with $FeSO_4$.

Antibody surface staining of M.tb.

Binding assays were performed in a Corning® 96-well Clear Flat Bottom Polystyrene Not Treated Microplates (Corning, 3370) pre-blocked overnight at 4°C in 1x PBS + 0.1% Tween-20 + 1% BSA; this blocking step prevented nonspecific binding of the antibodies to the plate during staining and allowed for efficient processing

of samples. A total of 200,000 cells/sample were dispensed in each well, stained, and washed in 200 µL volumes of 1x PBS + 0.02% Tween-20 + 0.1% BSA (PBS-T-BSA) with antibody or MVN at given dilutions. Cells were incubated with antibodies at room temperature for one hour on a shaker set to 150 rpm. Cells were then washed three times in PBS-T-BSA after each staining step, using centrifugation in a Beckman Coulter™ Allegra™ X-22R Centrifuge at 1,100 x rcf for 5 min to pellet the cells between each wash. For enzymatically dissociated cells, the optical density of the cell clumps was used to estimate the volume that contained 200,000 cells. While internally consistent, the actual number of cells each analyzed sample contained could not be accurately quantified for previously specified reasons. The enzymatically-treated samples were also left to sit in the wash buffer for 5-10 min before each centrifugation to provide extra time for unbound antibodies to diffuse from cell clumps. The clumped samples likely contain metabolic waste products inadequately washed from the clumps, which increased the probability for nonspecific staining.

Development and quantification of LAM recognition element binding to the M.tb *cell surface.*

A total of 9.605 g of anhydrous citric acid (MilliporeSigma, 251275) was first dissolved in 1 L MilliQ water in an acid-washed glass bottle. Then, 6 mL of 10 N NaOH was added and adjusted to pH = 4.4. A total of 0.5 g of 2,2'-azino-bis(3-ethylbenzothiazoline-6-sulfonic acid) diammonium salt (ABTS; MilliporeSigma, A1888) was added to the buffer, and the solution was stored at 4°C protected from light until use.

Immediately before application to stained cells, 30% hydrogen peroxide (H_2O_2) was added to the ABTS stock at a ratio of 1.8 µL H_2O_2 to 1 mL of ABTS. A 200 µL volume of this working solution was applied directly to cells. The HRP conjugated to the detection antibodies readily reduced H_2O_2 into water and oxidized the ABTS, producing a soluble green end product that can be read spectrophotometrically at 405 nm. After allowing the reaction to proceed for 30 min, the reaction was stopped by adding 100 µL of 10% sodium dodecyl sulfate (SDS). The absorbance was measured on a BioTek® Synergy™ HT Microplate Reader with BioTek® Gen5™ ver.1.11 software. When the absorbance readings were out of range for the plate reader, 100 µL of the ABTS/SDS reaction mixture was diluted into 100 µL stock ABTS without peroxide on a clean microplate, and the diluted samples were measured. In the event that this dilution was necessary, all samples within the experiment were diluted, not just the high-absorbance samples, maintaining internal relative expression levels across all conditions for each experiment.

Data and statistical analyses.

The absorbance values had background-subtracted as described from their raw measured absorbance. Values were normalized to the unprocessed control sample for mechanical dissociation. Values derived from enzymatically-dissociated cells were normalized to cells that underwent mechanical dissociation only using needle aspiration (as described). Antibody titration plots (**Figure C2**) were normalized to the maximum measurable value. All samples used in mechanical dissociation experiments were processed in parallel on the same day to reduce experimental variability. Samples undergoing enzymatic dissociation were also processed in parallel on the same day.

All statistical analyses were performed using MATLAB on background-subtracted data (not normalized). One-way analysis of variance (ANOVA) determined statistical significance for data containing three or more groups. Unpaired t-tests were performed for data sets including only two groups. Statistical significance was defined as $p < 0.05$. Tukey's range test identified which specific conditions were statistically different following ANOVA. Experimental variation was compared to the unprocessed control unless otherwise stated. Standard error of the mean (SEM) is reported for relative expression levels of LAM for each cell population, plotted as the Normalized Absorbance.

Results

Effect of dissociation method on cell recovery.

The mechanical dissociation protocol performed statistically impacted the number of recovered single cells. As shown in **Figure 5.3A**, the total cell counts recovered by shaking *M.tb* with glass beads (3,049,750 cells ± 499,735 cells) were statistically higher than those recovered from needle aspiration (667,256 cells ± 198,241 cells) or the number of single cells gently washed from the sample prior to dissociation (1,151,649 cells ± 187,973 cells), as identified by Tukey's range test.

For the enzymatically-digested cells, OD600 was used to determine the relative sample recovery for each processing method (**Figure 5.3B**). Because of the lack of single-cell recovery, relative absorbance replaced cell counts for recovery determination. Specifically, while enzymatic dissociation did help break apart the clusters of *M.tb* in the sample, the final samples still contained sizeable clumps of cells visible to the naked eye, with negligible

quantities of single cells. Tukey's range test showed that lysozyme statistically freed more cell clumps than trypsin or amylase. There was no significant difference between lipase recovery and recovery from other enzymatic digestion methods. It is important to note that cell lysis may have influenced the cell recovery in varying degrees for each enzymatic treatment, not just the efficiency of de-clustering.

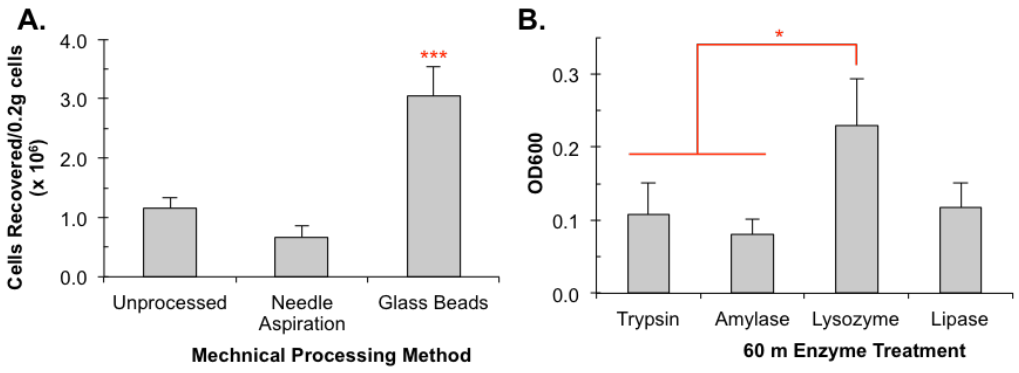

Figure 5.3. Cell recovery for each processing method. **A.** Single cell recovery of each mechanical processing method. **B.** Measured OD600 for each enzymatic processing method. A greater OD600 corresponds to a greater number of cells. n = 3. (mean ± s.d.). *Indicates statistical significance at $p < 0.05$. ***Indicates statistical significance at $p < 0.0005$.

Impact of mechanical dissociation method on surface expression of LAM.

As shown in **Figure 5.4**, the method used to process cells statistically increases the relative level of LAM features on the *M.tb* cell surface. The surface accessibility of LAM was measured using antibodies FDX01, A194, BJ-03, BJ-76, and MVN. Dissociation using a 21-gauge needle resulted in higher relative levels of LAM than the unprocessed control for BJ-03 (which binds unmodified mannosyl caps) and both antibodies that bind the arabinose backbone (FDX01, A194) of LAM. Dissociation using glass beads also resulted in a statistical increase in LAM accessibility on the surface of *M.tb* for A194 (Ara4). For BJ-76 (MTX-Man), while there was no statistical difference between unprocessed cells and those dissociated using glass beads, there was a statistical difference between LAM surface accessibility for cells processed using glass beads and needle aspiration. MVN binding to the *M.tb* cell surface was not statistically impacted by either mechanical processing method. It is interesting to note that while needle aspiration resulted in a lower yield of cells compared to glass bead dissociation, it does have higher expression levels of LAM for all characteristic features. We theorize that the glass beads impart a greater mechanical force on the cells than needle aspiration, and while this helps improve the recovery of usable cells, it

also likely shears LAM off the surface. Experiments assessing how applied shear forces change LAM surface expression are needed to confirm this hypothesis, such as with a constant shear force viscometer.

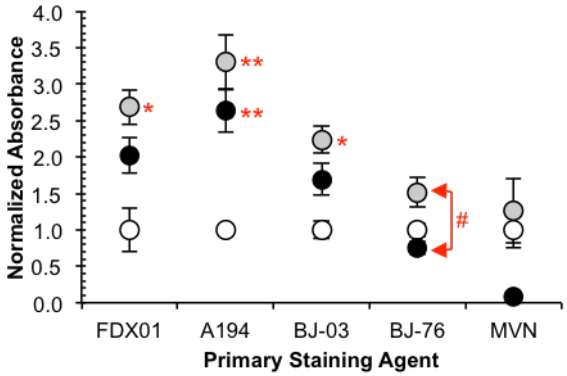

Figure 5.4. Mechanical dissociation significantly impacts relative expression levels of LAM on the surface of *M.tb* post-processing. Values were normalized to the unprocessed control (white circle), and each sample contained 200,000 cells/sample. White circle = Unprocessed Control. Grey circle = Needle dispersion. Black circle = Glass bead dissociation. n = 3. (mean ± SEM). (*, #) Indicate statistical significance at $p < 0.05$. **)Indicates statistical significance at $p < 0.005$.

Assessing the structure of *M.tb*'s cell surface, there are a few potentials as to why LAM accessibility would increase after dissociation. One possibility is that the unprocessed cells recovered directly from the sample have less surface LAM than cells recovered from the cell clumps using mechanical dissociation. If correct, it could also suggest why they were not attached to the larger cell clumps.[90] The other hypothesis predicts that mechanical dissociation changes the capsular layer of the cell, improving accessibility of LAM anchored to the outer membrane.[323] To determine the correct hypothesis, we subjected unprocessed (already dispersed) single cells to the needle aspiration protocol and directly compared the LAM expression of the two populations. As shown in **Figure C4**, detection of LAM is not statistically different on initially recovered initial single cells compared to needle-aspirated initial single cells. All but one LAM recognition element showed a lack of statistical difference between pre and post-processing. The exception is FDX01, which borders statistical significance ($p = 0.046$). However, if this difference is significant, needle aspiration appears to reduce the level of surface LAM detected by FDX01. These data oppose the hypothesis that mechanical dissociation improves accessibility to LAM by simply changing the capsular layer of a single cell. Rather, the results support the idea that cells need to become dissociated from previously existing clumps to display originally buried LAM epitopes.

Impact of centrifugation speed and frequency on LAM surface expression.

When working with bacterial cells, it is not uncommon to use centrifugation to wash and process cells. Commonly, cells are centrifuges for short periods at high speeds to concentrate bacteria rapidly. Alternatively, cells can be treated more gently by centrifuging at lower speeds for prolonged periods, reducing the applied centrifugal force. Because both LAM and the capsular layer can be stripped from the surface of mycobacteria,[323] it is essential to understand how centrifugal processing may change surface LAM accessibility.

Figure 5.5 shows the impacts of centrifugation speed and successive centrifugation prior to antibody staining. Focusing on the centrifugation speed, accessibility of Ara6 (FDX01) structures did not statistically vary with increasing centrifugation speed or repetition. In contrast, MVN binding was almost universally statistically reduced following centrifugation at all speeds and frequencies, even when the accessibility of mannosyl-cap targeting antibodies (BJ-03, BJ-76) was not statistically impacted. This observation is interesting, and a few different explanations exist. Centrifugation could have damaged the mannosyl caps and the α-(1,2)-glycosidic linkages MVN binds. If this were true, these linkages either (**1**) no longer exist because mannosyl residue(s) were removed entirely, leaving Man1 motif-exclusive ManLAM, or (**2**) are physically distorted in a way that inhibits MVN binding but does not remove mannosyl residues, leaving Man2/3 structures intact. If hypothesis (**1**) were correct, BJ-03 would have to bind both Man1 and Man2 motifs, and BJ-76 would have to bind Man1 and MTX-Man2/3 motifs on the arabinose terminal LAM structure. According to FIND, BJ-03 and BJ-76 are targeted only to di-mannosyl caps and MTX-di/tri-mannosyl caps, respectively, and they do not bind mannose monomer caps. If this data is reliable, hypothesis (**1**) is much more unlikely, and hypothesis (**2**) is likely to be more accurate. Though the generation of BJ-03 and BJ-76 have been published, there is no publically available or information that could help confirm or refute these hypotheses.[322] A LAM glycan-binding array confirming the FIND's data would help elucidate what is most likely happening. Alternatively, an undetermined co-factor on the cell's surface and capsule may exist and enhance MVN binding, but centrifugation removed this co-factor from the cell surface. However, we believe this to be unlikely because MVN efficiently binds purified *M.tb* ManLAM in ideal buffer systems (data not shown).[86] van der Horst *et al.* reported the affinity of MVN for ManLAM, as determined by the equilibrium dissociation constant (K_D), as less than 10^{-12} M, which is three to six orders of magnitude better than typical antibody K_D values.[86]

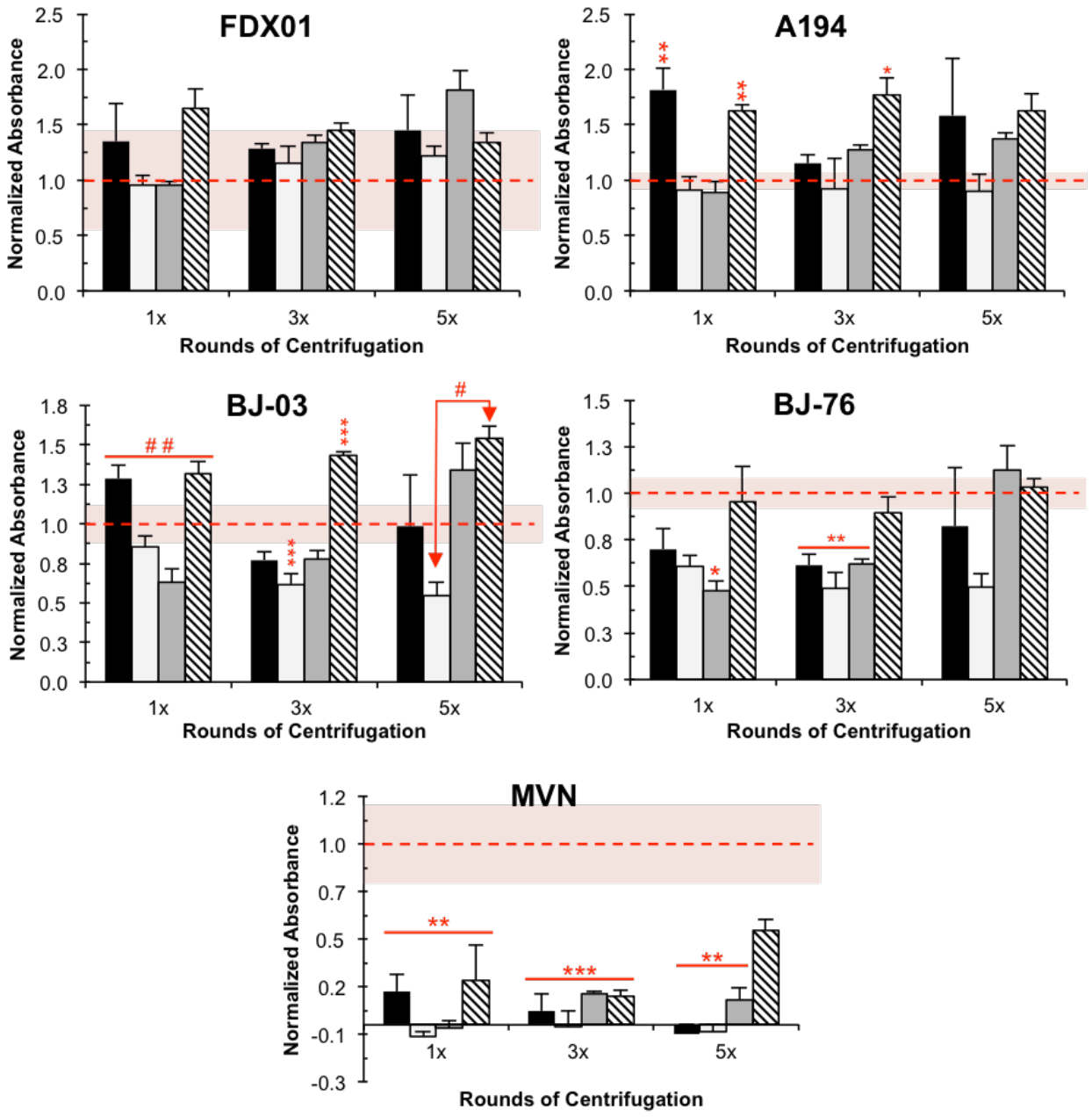

Figure 5.5. Centrifugation speed universally changes the accessibility of mannosyl-capping motifs on LAM, but the impact on the arabinose backbone depends on both speed and centrifugation repetition. Samples were centrifuged at the indicated speeds once, thrice, or five times. The red dashed line indicates the normalized mean absorbance for the unprocessed control; the pink shaded box the graphs are superimposed over indicates the ± SEM. Black bar = 1,230 rcf. White bar = 4,800 rcf. Grey bar =10,000 rcf. Diagonally striped bar = 20,800 rcf. n = 3. (mean ± SEM). (*, #) Indicate statistical significance at $p < 0.05$. (**, ##) Indicate statistical significance at $p < 0.005$. *** Indicates statistical significance at $p < 0.0005$. (*, **, ***) Indicate statistical difference between control and treated sample(s). (#, ##) Indicate statistical difference between treated samples, though none were statistically different from the control.

Looking at the impact of repeated centrifugation at each speed, for cells centrifuged once (**Figure 5.5**), there was a statistical increase in the accessibility of Ara4 (A194) structures on the arabinose backbone at both 1,230 rcf and 20,800 rcf. While there was also a statistical difference on di-mannosyl cap accessibility (BJ-03), none of the centrifuged groups were different from unprocessed cells; instead, 1,230 rcf and 20,800 rcf were statistically different from 4,800 rcf and 10,000 rcf. A statistically reduced number of MTX-Man caps (BJ-76) were measured following single centrifugation at 10,000 rcf. For cells centrifuged three times, antibody binding to mannose caps was statistically reduced, except for repeated centrifugation at 20,800 rcf, which was either statistically the same or higher than the control population. Ara4 backbone accessibility (A194) was statistically increased at 20,800 rcf. For cells centrifuged five times, there was a statistical difference between the 4,800 rcf and 10,000 rcf relative expression values for detecting di-mannosyl caps (BJ-03), but there was no difference for the MTX-Man caps or Ara4/Ara6 structures.

Impact of enzymatic dissociation on LAM surface accessibility.

Knowing that the capsular structure consists primarily of glucans, followed by proteins and lipids, we hypothesized that enzymatic digestion of *M.tb* may help aid in clump dissociation and may also effect the surface accessibility of LAM. For this reason, we tried digesting cells in the presence of amylase, trypsin, and lipase. Also, given the importance of peptidoglycan (PG), the balance of cell wall breakdown and regrowth throughout cell metabolism, and evidence showing some mycobacterial species can be susceptible to lysozyme-based damage, we investigated how lysozyme digestion on cell recovery and LAM accessibility.

While proteins and glucans make up the two major constituents of the capsular layer, neither trypsin nor amylase statistically impacted the surface accessibility of any LAM structures following digestion (**Figure 5.6**). Lysozyme treatment statistically increased Ara4 accessible structures bound by A194 but otherwise did not modify LAM accessibility. Lipase was the only enzyme to show any statistical increase on LAM structure accessibility for both the backbone and mannosyl caps, with increased signal from increased binding of all LAM recognition elements' to the cell surface. The relative increase in arabinan backbone accessibility is at least 60-fold. Unfortunately, it is unlikely that this signal increase is because lipase improved surface LAM accessibility. As shown in **Figure C1**, the use of $FeSO_4$ for inactivation of both lysozyme and lipase has statistically increased the ABTS signal observed for stained cells treated with only $FeSO_4$ compared to untreated cells; the lipase-associated

statistical increase occurred for all LAM recognition elements, including MVN. The $FeSO_4$ precipitates in solution and is readily pelleted alongside the recovered cells using centrifugation, making it difficult to remove all $FeSO_4$ from the cells. Iron anions in a solution can readily oxidize ABTS,[324] which could cause increased signal for both lipase and lysozyme. However, applying ABTS and peroxide to wells containing a final concentration of 0.05 mM $FeSO_4$ without cells did not significantly oxide the ABTS (**Figure C5**), nullifying this hypothesis. Instead, it is likely the $FeSO_4$ enhanced binding between LAM recognition elements and cells instead of causing nonspecific signal on its own, with more significant binding enhancement correlating with increasing $FeSO_4$ concentration. The high background measured in both sample sets inactivated with $FeSO_4$ suggests some signal augmentation results from nonspecific antibody binding.

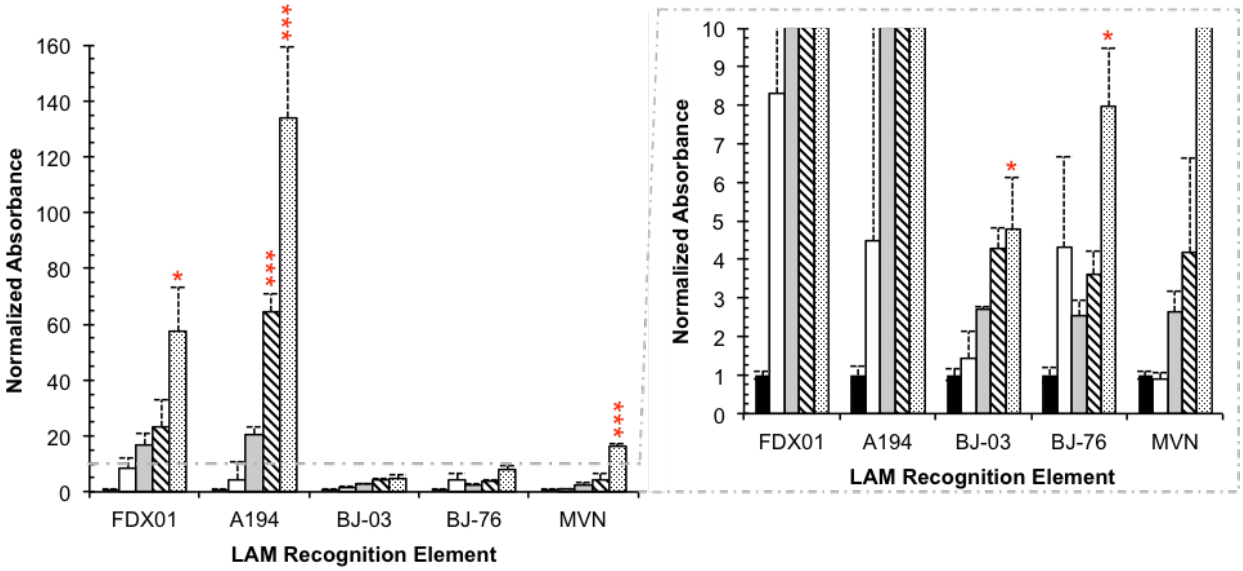

Figure 5.6. Lipase-treated cells significantly impacted detection signal for all LAM recognition elements, and lysozyme statistically increased signal for Ara4 backbone structures; however, enhanced binding of antibodies to cells, caused by the presence of $FeSO_4$ from enzyme inactivation, is the likely cause of this statistical increase (**Figure C1**, **Figure C5**). Amylase and trypsin did not statistically change LAM surface accessibility. The cutout shows values with a normalized absorbance value less than 10. Black bar = No enzyme treatment. White bar = Trypsin. Grey bar = Amylase. Diagonally striped bar = Lysozyme. Black and white polka dotted bar = Lipase. n = 3. (mean ± SEM). *Indicates statistical significance at $p < 0.05$. **Indicates statistical significance at $p < 0.005$. ***Indicates statistical significance at $p < 0.0005$.

Since the total amount of remaining $FeSO_4$ in each sample could not be easily measured (see Materials and Methods), for the conditions given in **Figure C1**, control samples containing 0.02 mM and 0.05 mM $FeSO_4$ were stained with each LAM recognition element and secondary antibody to estimate the impact $FeSO_4$ inactivation on the measured signal. Based on the visual appearance of cell solutions, which had a brown/rust color that positively correlated with increasing concentration, we believe the concentration of $FeSO_4$ in all lysozyme and lipase treated samples was less than 0.02 mM. Lipase was also the only condition that exhibited a surprisingly high background signal in secondary-only antibody-treated controls, supporting that the increased signal is due to $FeSO_4$. Lysozyme-treated cells also had a higher secondary-only control background signal than trypsin or lipase, but not to the same level as the lipase-treated cells.

Discussion

This manuscript demonstrates how in vitro processing methods impact *M.tb* surface marker accessibility by measuring the relative abundance of LAM structural features before and after processing. Newly developed structure-specific LAM recognition elements were used to quantify differences in surface LAM expression after processing. Because of their propensity to clump in culture, cells must be pre-processed and liberated from clumps for downstream use. The current hypothesis for why mycobacterial aggregation occurs suggests that they have adapted to grow as aggregates in aqueous culture environments. [88, 89] *M.tb* clumps grown in vivo are known to enhance pathogenesis, increase fitness, and quicken infection and inflammation compared to not clumped cells, supporting this hypothesis.[325] The processing methods investigated here can be avoided by including Tween-80 in the culture media at a concentration of 0.05%, but Tween-80 destabilizes the capsular layer of *M.tb*, which can impact antibiotic susceptibility testing results.[89] Furthermore, Tween-80 also reduces the abundance of LAM and its associated metabolites on the surface of *M.tb*.[90] The arabinomannan surface reduction and destabilization are not because detergent molecules block cell surface accessibility,[90] but the exact mechanism of how Tween-80 reduces clumping remains unknown. *M.tb*'s use of Tween-80 as a carbon source was recently linked to changes in the metabolome and carbon flux routing in *M.tb*,[326] but more data is needed to explain why these occur and how they reduce cell clumping. Another theory suggests that because Tween-80 can be toxic to *M.tb*, inducing stress responses and possible cell death may contribute.[326, 327] Regardless of the exact mechanism, *M.tb* exhibits reduced virulence in vivo after growth in Tween-80,[327] and these same culture conditions also reduce surface expression of

the crucial TB virulence factor ManLAM.[90] The possible association of decreased LAM with decreased in vivo virulence solidifies the argument that Tween-80 significantly impacts experimental results and our understanding of LAM, *M.tb*, and its surface, and science needs a better understanding of how the mechanical and enzymatic dissociation alternatives modify the *M.tb* cell surface.

Mechanical dissociation.

To assess how well these methods de-clump cells and change the relative abundance of surface LAM, we first looked at the impact of two standard mechanical dissociation methods.[88, 89] As demonstrated, for both needle aspiration and glass bead mixing, mechanical dissociation yields intact single cells following processing for both needle aspiration and glass bead mixing, and they have higher quantities of surface LAM following dissociation when compared to unprocessed single cells recovered initially by simple rinsing of the clumps. The additional data presented in **Figure C4** confirmed that the increase in LAM following dissociation is due to the unprocessed control cells initially containing low levels of LAM, not because LAM was liberated during processing. This is consistent with observations made in cultures containing Tween-80, where cell de-clumping correlates with decreased AMs, but the mechanism explaining this correlation is unknown and multifactorial. Additionally, arabinose-containing polysaccharides, such as AMs and LAM, significantly support *M.tb* aggregation.[328] Therefore, it is logical that the unprocessed cells not bound to the large, intact clumps would have significantly less surface LA. Combined, Efficient cell release and good LAM surface accessibility show mechanical dissociation using needle aspiration and glass beads compatible with downstream surface analysis. The required application should be considered when choosing the best processing protocol because each method has small trade-offs between the number of cells recovered and relative surface abundance of LAM.

Centrifugation and shear force.

Furthering our investigations into the mechanical processing of *M.tb*, we investigated the impact of centrifugation speed and frequency. Centrifugation did not statistically increase or decrease the accessibility of the conserved arabinan backbone of LAM (**Figure 5.5**), but there are more minor changes in the relative backbone abundance as centrifugation speed increases. Compared to unprocessed cells, centrifugation at 1,230 rcf increases expression of Ara4/6 structures, but they are then mildly reduced after centrifugation at 4,800 rcf and 10,000 rcf.

The relative abundance of these structures then increases in cells spun at 20,800 rcf. This pattern is independent of the number of centrifugation cycles performed up to five times before surface staining. LAM's vastly heterogeneous branching structure and high surface expression level and shedding means there is likely such a high density of Ara4/6 structures that even if centrifugation removed some from LAM from the cell surface, it might not be enough to impact measured expression levels statistically. Instead, more minor changes in surface LAM concentration may be seen. We made this hypothesis because the arabinose backbone makes up most of LAM's structure, and other mycobacterial AMs, including LAM precursors, have similar arabinose branching structures.[329] In addition, mechanical dissociation has been shown to remove shed ManLAM found at the very outer capsule surface. However, as the capsule is removed, arabinan-containing polysaccharides found in the inner compartment of the capsule are exposed, as is surface-anchored LAM.[323] A binding kinetics assessment of FDX01 or A194 for non-LAM mycobacterial AMs would show if these antibodies cross-react with other similarly structured mycobacterial AMs found in the capsule and on the cell surface, supporting our proposed theory.

In contrast, mannosyl cap accessibility statistically varied with both centrifugation speed and repetition. Depending on the conditions and structure, the relative abundance of mannose caps more often decreased than increased compared to unprocessed cells. For BJ-03 (Man2), there was no statistical difference when cells were centrifuged at different speeds one time or five times compared to unprocessed cells, but there was a statistical difference across the experimental conditions. A similar trend in the relative changes in Ara4/6 structures across centrifugation speeds is also seen in the amount of relative mannosyl-cap abundance with increasing centrifugation speed. For the mannosyl caps, the accessibility decreases as centrifugation speed increases to 10,000 rcf, but at maximum speed, the mannose cap abundance recovers to similar levels seen in unprocessed. MVN exhibited this same trend, and all but one condition had a statistical reduction in the accessibility of the glycosidic linkages.

The observed decrease followed by an increase in surface concentration for all carbohydrate structures suggests that the shear forces applied to the cells during centrifugation impact the surface-accessible structures. A likely explanation for this is that shear forces first strip the weakly bound capsular layer from the *M.tb* surface, where LAM is present at the outer surface of the capsule.[323, 330] The mannosyl cap structure may be more sensitive to the applied forces than the LAM backbone, physically disrupting the cap structure; the reduction in MVN binding supports this theory. Alternatively, because there is a lower starting quantity of mannosyl caps, the progressive

stripping of that capsular layer may cause more significant signal loss for each lost LAM molecule than the arabinan backbone. Realistically, a combination of these two mechanisms is likely responsible for the observed behavior.

If we look at the effect of total applied force during centrifugation, as more force is applied, the capsular layer containing LAM and other associated biomolecules should be stripped more rapidly, as seen through a LAM signal decrease. Nevertheless, removing more of the outer capsule also exposes constituents of the inner capsule and biomolecules bound to the outer mycobacterial membrane, more quickly "recovering" relative LAM abundance.[323] Even after removing the *M.tb* capsule, established literature states that the cell surface retains similar physiochemical properties because many of the capsule's carbohydrates, proteins, and lipids are also found anchored to the outer mycobacterial membrane.[329] Together, the combined impact of applied mechanical force, heterogeneous biomarker distribution throughout the *M.tb* capsule layers,[329, 330] under which surface-anchored LAM is located explains why LAM accessibility recovers after mechanical disruption of the capsule and why it occurs faster at higher centrifugal speeds.[329] This explanation is consistent with the current understanding of the mycobacterial capsule structure and composition[323, 329, 330]

Enzymatic digestion.

Because the *M.tb* cell envelope is a complex structure containing lipids, carbohydrates, and proteins, we chose investigated how different enzymatic treatments may help release cells from clumps in place of mechanical dissociation through cleavage and breakdown of the capsule and surface-bound biomolecules. Unfortunately, we found that enzymatic treatment with amylase, lipase, lysozyme, and trypsin did not release single cells from the culture clusters, and aggregates were still present. As discussed, the clumps of bacteria isolated from culture are much larger in diameter than the clumping observed in clinically relevant sputum samples, making them totally useless for clinical sample simulation. Cell aggregation also makes it impossible to accurately determine the number of cells in the sample and characterize cell surface biomarker levels. Therefore, the results obtained from these enzymatic dissociation experiments provide very-limited insight into the true impact these enzymes have on LAM surface accessibility. Dissociation with glass beads before enzymatic digestion, while a confounding factor, would have provided more apparent answers demonstrating how enzymes change surface LAM accessibility. Because we know mechanical dissociation alone efficiently breaks apart cell clumps, using enzymatic digestion afterward is redundant and therefore was not investigated.

Relatively, lysozyme recovered more cells than the other enzymatic treatments, which is interesting because lysozyme cannot easily access the internal PG layer of the cell wall. Further, there is no significant evidence in the literature suggesting any amount of PG in the *M.tb* capsule.[330-332] If lysozyme could access the PG layer, given its importance in stabilizing the cell wall, cell lysis and decreased cell recovery would be expected. Adequate data demonstrates the use of lysozyme for mycobacterial cell lysis,[88, 333] so it may be possible for lysozyme to pass through the outer cell wall using an unknown active transport mechanism.

The *M.tb* capsular layer is primarily made of α-D-glucans, which are homopolysaccharides composed of α-D-glucose residues connected by primarily α-(1,4) linkages. Since α-amylase from porcine pancreas hydrolyzes the α-(1,4)-glycosidic linkages, we predicted cells could be de-clumped using enzymatic treatment without significantly impacting LAM surface accessibility. Literature suggests, however, that this glucose-like glucan found in the capsule does not contribute to cell clumping in vitro; rather, it is arabinose-containing polysaccharides, such as AMs and LAM, that are the significant cause of clumping.[328] Trypsin, lipase, and lysozyme also did not improve LAM accessibility, but the $FeSO_4$ used to inactivate lipase and lysozyme did facilitate increased binding between the LAM recognition elements and the *M.tb* surface, some of which was nonspecific. Using a different enzyme that cleaves arabinose-containing polysaccharides would likely help break apart cell clumps, but the amount of LAM would likely be significantly reduced given the structural similarity.

Another possible explanation for the insignificant impact of enzymes on LAM accessibility is that the enzymes completely removed the capsular layer from the *M.tb* surface during the 60 minute digestions. As suggested by literature and demonstrated in our centrifugation studies, the similar physiochemical composition of the outer mycobacterial envelope should have comparable surface LAM density compared to unprocessed cells after capsule loss. Shorter digestions or different enzyme concentrations could potentially produce wider variations in surface LAM abundance. However, if all capsular components, including the arabinose-containing polysaccharides thought to be responsible for aggregation, were removed, we should expect to see better de-clumping of the cells. While the diameter of cell clusters decreased following enzymatic treatment, they were still large enough to be observed in solution with the naked eye; there were also no single cells recovered for any enzymatic processing method. Though entirely speculative, arabinose-polysaccharides on the *M.tb* surface may still facilitate clumping, but this would be inconsistent with cell behavior following mechanical dissociation. Exhaustive investigations are

needed to assess enzymatic alterations of the LAM surface accessibility accurately, with more questions generated than answers.

Alternative strategies likely exist to digest cell clumps from a culture with improved enzymatic efficacy. For example, adding amylase and lysozyme to the culture medium increases the effectiveness of antibiotic treatment and improves growth inhibition of *M.tb*. Individually, each enzyme marginally reduces cell growth, but both still help weaken the outer capsule and envelope.[89] However, as stressed in this report, there is no information demonstrating the impact on LAM accessibility. Testing established treatments known to influence *M.tb* virulence, antibiotic susceptibility, and growth, such as those cited in this report are excellent candidates for surface-accessible structure assessment. Hopefully, these analyses would broaden our scientific understanding of *M.tb* capsule destabilization and changes to the arabinose-polysaccharide surface density.

MVN as a LAM recognition element.

This report clearly shows that mechanical processing significantly reduces MVN binding to glycosidic linkages in the terminal ManLAM cap expressed on the surface of *M.tb*. This trend did not correlate with the two anti-ManLAM mannosyl-cap antibodies, and even when BJ-03 and BJ-76 binding was statistically changed, the relative difference was less than the disparity seen for MVN. In addition, the amount of MVN needed to label cells was excessive (2 µg/sample) compared to the antibody staining protocols (0.11 µg/sample to 1.19 µg/sample), and that was with an additional signal amplification step afforded by an anti-Biotin secondary antibody with the anti-Rabbit-HRP tertiary antibody. We also used MVN to fluorescently label single cells, using flow cytometry for fluorescence detection. Even after staining cells with ridiculous quantities of MVN and fluorescently-labeled secondary antibody for quantification of ManLAM surface density, more often than not, cell labeling with MVN was indistinct from cells labeled with only the fluorescent secondary antibody (data not shown).

Practically, this extensive testing has found that MVN does not reliably bind ManLAM on *M.tb*, and without further investigation as to why, it is unlikely MVN will become a novel LAM recognition element for detection of whole-cell *M.tb*. Structural damage to the glycosidic linkages may contribute, but this is pure speculation, and further studies were not performed to validate or nullify the hypothesis. Because MVN has such a high binding affinity for free ManLAM using biolayer interferometry, we hypothesize that MVN cannot stay bound

to the surface of *M.tb* because it only has one binding site. If this were proved true, MVN dimerization could drastically influence results.

Limitations and future directions.

While we aimed to provide a broad overview of the impact of different processing methods, there are many limitations to this study that must be addressed. First, as we established, culture conditions affect capsule structural integrity,[90, 331] and AM expression levels can vary considerably based on the growth phase of the culture.[334] These differences can completely disrupt multi-factorial processes, influencing drug susceptibility testing results[89] and BCG vaccine efficacy.[335] Therefore, we chose to use a readily available cell reagent to reduce culture variability. Gamma-irradiated strains of *M.tb* acquired through BEI Resources were grown in glycerol-alanine-salts without detergent until end-log phase growth. Knowing the disparities between cell culture conditions, the results presented here may not be directly applicable to *M.tb* grown in other recipes culture media. Feeding cells with minimal media instead of complete media can influence cell phenotypes, which again could significantly change experimental results. The use of gamma-irradiated cells is a confounding factor of the results presented here, since ionizing radiation can impact the stability of complex bioorganic structures,[336] which will influence molecular behavior under different physical and chemical conditions.

There are also significant differences in the surface-accessible structures found in different *Mycobacterium* spp., limiting study implications exclusively to *M.tb*, and possibly only to those strains used in the study. These variances go well beyond those discussed with the carbohydrate capping of ManLAM, PILAM, and AraLAM. Within NTM or MTBC species that express LAM with the same capping motif, the degree to which LAM is terminally-capped with mannose or phosphatidylinositol residues is species-dependent. For example, *M.tb* and *M. bovis* average seven to nine di-mannosyl caps per LAM molecule, but *M. leprae* averages only one.[337, 338] Different strains of *M.tb* also express different amounts of arabinomannans on their surface.[90] Variation in starting biomarker surface density can influence the net change that occurs with each protocol, with low-concentration biomarkers showing a more significant relative increase or decrease after processing; this phenomenon was previously alluded to in discussions of centrifugation impacts.

In addition, while the literature suggests that α-amylase did not successfully de-clumped *M.tb* because arabinose-polysaccharides are responsible for cell aggregation in *M.tb*, the α-D-glucans may be responsible for

clumping in *M. smegmatis*. These distinctions make it easy to speculate how enzyme digestion could produce total opposite results for *M. smegmatis* dissociation than *M.tb*; optimization may make it possible to completely digest the capsular layer with amylase, creating a single cell suspension while improving LAM surface accessibility.[328] The distribution of lipids and carbohydrates through the cell capsule is different for each mycobacterial species,[323, 329, 330] further adding to the heterogeneity within the different layers of the capsule itself. Altogether, outside of known differences in relative surface abundance, significant cell biology variations between different mycobacterial species will produce different results from the same processing protocols.

While statistically significant findings are presented and discussed throughout this report, the question arises; when these cases only exhibit a relative change of no more than two-fold or three-fold, is it important in practice? Typically, it is unlikely that mild increases or decreases in LAM surface expression are critical in practice, even when statistically different, because of the high abundance of surface LAM. However, if these small variations made a practical difference, they would most significantly impact the mannosyl caps because they are a minor part of ManLAM's structure. However, the mannosyl caps are entirely responsible for differentiation between MTBC and NTM differentiation, which makes them critically important for *M.tb* detection and diagnosis especially the rare and chemically distinct MTX-Man cap.

This report clearly shows that almost any processing significantly impacts MVN binding to the surface of *M.tb* via glycosidic linkages in the terminal ManLAM cap. In addition, the amount of MVN needed to label cells was excessive (2 µg/sample) compared to the antibody staining protocols (0.11 µg/sample to 1.19 µg/sample). We also used MVN to fluorescently label single cells, using flow cytometry for fluorescence detection. Even after staining cells with ridiculous quantities of MVN and fluorescently-labeled secondary antibody for quantification of ManLAM surface density, in most cases, there was no significant labeling of individual cells with MVN (data not shown). Practically, extensive testing has found that MVN does not reliably bind ManLAM on *M.tb*, and without further investigation as to why MVN is unlikely to become a novel LAM detection element for whole bacilli assays. Because MVN has such a high binding affinity for free ManLAM using biolayer interferometry, we hypothesize that MVN cannot stay bound to the surface of *M.tb* because it only has one binding site. If this were proved true, MVN dimerization could drastically change results.

Conclusions

Using newly available LAM recognition elements, we showed that *M.tb* dissociation methods impact surface accessible features and single-cell recovery, with data supported by established theory. Mechanical dissociation recovered more intact and usable single cells than enzymatic dissociation. Mechanical dissociation also improved surface LAM abundance, while treatment with four enzymes did not change accessibility. Relative differences in surface LAM showed that centrifugation speed and repetition likely stripped the cell capsule off *M.tb*'s surface, exposing the biomolecules anchored to the outer membrane. This is the first study to our knowledge that shows MVN binding to *M.tb*, but further investigation is needed to determine why MVN does not reliably bind *M.tb* even though it has such a high binding affinity for individual molecules of ManLAM. We expect this information will interest many TB investigators seeking detailed preparation methods that preserve as many surface-accessible biomarkers as possible.

Acknowledgments and Funding

We thank Dr. Raymond L. Mernaugh for their insightful discussions. The authors thank Dr. Megan van der Horst, Dr. Raymond L. Mernaugh, Dr. Carole Bewley, BEI Resources, and FIND for the reagents gifted for use in this manuscript. Flow Cytometry experiments were performed in the Vanderbilt Flow Cytometry Shared Resource Core. The Vanderbilt Flow Cytometry Shared Resource Core is supported by the Vanderbilt Ingram Cancer Center (P30 CA068485) and the Vanderbilt Digestive Disease Research Center (DK058404). The Vanderbilt Antibody and Protein Resource Core expressed MVN that Dr. van der Horst gifted.

This work was funded in part by the US National Institutes of Health Grant No. R01-AI135937.

CHAPTER 6 : DESIGN OF A CYANOBACTERIAL LECTIN SURFACE-FUNCTIONALIZED MAGNETIC BEAD FOR SPECIFIC ISOLATION OF TUBERCULOUS MYCOBACTERIA

Adapted from: (**1**) Pearlman, S. I.; Warren, C.; Pasic, L.; Blackburn, J.; Haselton, F. R., Cyanobacterial lectin microvirin-N specifically isolates tuberculous mycobacteria from a mixture; with permission from coauthors. In preparation.

(**2**) Pearlman, S. I.; Pasic, L.; Blackburn, J.; Haselton, F. R., Impact of mechanical and enzymatic dissociation methods on cellular de-clumping and surface accessibility of lipoarabinomannan on *M. tuberculosis*; with permission from coauthors. In preparation.

Abstract

While tuberculosis (TB) has killed more people than any other infectious disease in human history, nontuberculous mycobacterial (NTM) infections have recently become a significant public health concern, with the number of NTM cases now exceeding TB cases in the United States. These infections target similar patient populations and have similar symptoms but require different antibiotic regimens. Beyond bacterial culture, there is no diagnostic test available to differentiate between TB and NTM infections, and an estimated 10% of TB patients are misdiagnosed and instead have an NTM infection. To address this gap in care, we designed a magnetic capture bead for the isolation of only TB-causing mycobacteria. These beads were functionalized with cyanobacterial lectin microvirin-N (MVN), which binds the terminal mannose caps of lipoarabinomannan (LAM), expressed on the surface TB-causing mycobacterial species. NTM species instead express terminal phospho-*myo*-inositol caps on LAM. Using flow cytometry analysis of the interactions between fluorescent bacteria and beads, we demonstrated capture of *M. bovis* BCG (BCG) on MVN-functionalized beads. In creating a negative control. The capture efficiency of MVN-beads was dependent on the bead surface loading concentration. In creating an MVN negative binding control, we found that reduction and alkylation of MVN reduced its binding affinity for mannose-capped LAM by 100-fold, though improving the MVN purity could improve these results further. Though Galectin-1 exhibited some binding to the BCG surface, its structural similarity to MVN demonstrated that, with refinement, a non-mannose binding lectin could serve as an effective isotype-analog to MVN. Individual MVN molecules did not reliably bind to the surface of BCG, which we attribute to its monomeric binding site; surface loading of BCG

would likely improve with MVN re-engineering into a dimer. Though more work is necessary to overcome the identified development and implementation barriers, the use of MVN as a mycobacterial diagnostic tool remains promising.

Introduction

Tuberculosis (TB) is a major cause of death, particularly in low-income countries, with 10 million annual cases worldwide.[2] TB disease is well-known and studied worldwide, but few are aware of the sudden rise of nontuberculous mycobacterial infections (NTM, e.g., *M. abscessus, M. smegmatis*, *M. fortuitum*) in both immunocompetent and immunocompromised patient populations.[83] The difference in treatment regimens between TB disease and NTM infection create care gaps, with patients often being misdiagnosed with TB.[73] In 2009, the median time to diagnose NTM infection following symptom onset was two years.[81] This inappropriate care often leaves patients with permanent loss of lung function and, in some cases, results in patient death.

In resource-limited parts of the world, there is no readily available technique to determine the species-specific causative agent of mycobacterial infections. Culturing patient sputum can theoretically discern between TB and NTM.[339] However, for the same reasons it does not adequately work for the diagnosis of TB, namely the extensive time and infrastructure barriers required to implement culture are too slow and unavailable for use at the point-of-care (POC),[2] it also fails to diagnose NTM infections. Therefore, diagnosis is reliant on sputum smear microscopy. However, acid-fast staining and microscopic sputum observation cannot tell the difference between *M. tuberculosis* complex (MTBC, e.g., *M. tuberculosis*, *M. bovis*, *M. bovis* BCG, *M. canetti*, *M. africanum*) species, the causative agents of TB, and NTM infections.

Furthermore, the parts of the world using sputum inspection for diagnosis are also areas with high rates of TB disease, increasing the chances of misdiagnosis.[73] Multiple reports worldwide further demonstrate the need for mycobacterial species-specific diagnostics, with more than 10% of diagnosed TB infections truly caused by NTM in some parts of the world.[76, 339-342]

Lipoarabinomannan (LAM) is a glycolipid virulence factor found in *Mycobacterium* spp.[219] Up to 15% of the total cell mass of *M. tuberculosis* (*M.tb*) and other *Mycobacterium* spp. is composed of LAM, making it an extremely abundant surface biomarker.[87] What makes LAM an even more exciting biomarker choice is the structural variability across *Mycobacterium* spp. Specifically, LAM has three structural regions. The mannosyl-phosphatidyl-

myo-inositol surface anchor attaches the rest of the LAM structure to the outer cell envelope. Attached to this is a polysaccharide backbone composed of D-mannan and D-arabinan branches. The anchor and backbone are both conserved structures across all *Mycobacterial* spp.[219] The end of these branches are sometimes further modified with a carbohydrate cap structure, which makes up the third domain.

Interestingly, this capping motif varies depending on the species expressing it. Slow-growing MTBC species that cause TB disease have one-to-three terminal α-D-Man*p* residues linked through α-(1→2)-glycosidic linkages (ManLAM; **Figure 5.1**). Fast-growing NTM species have LAM capped with a phosphatidyl-*myo*-inositol cap (PILAM). AraLAM is devoid of any additional terminal carbohydrates and exists in only a few species of mycobacteria.[219] Even though the number of carbohydrate caps on each LAM molecule is highly variable across *Mycobacterium* spp., the structural differences in this terminal cap make it an attractive biomarker for differentiation between TB disease and NTM infection.

This report aims to create a simple method for differentiation between MTBC and NTM infections at the POC. Instead of using traditional immunoprecipitation, we describe a design for specific capture magnetic bead surface-functionalized with novel cyanobacterial mannose-binding lectin microvirin-N (MVN). Recently, van der Horst *et al.*[86] demonstrated that MVN specifically binds the mannose linkages found in ManLAM while not binding PILAM.[312, 343, 344] In this report, we detail the work completed towards achieving specific bead capture of MTBC species *M. bovis* BCG but not NTM species *M. smegmatis*. Barriers to completion and potential solutions for completion of the project are outlined. When implemented with POC sputum smear microscopy for bacteriological confirmation, we believe this MVN-magnetic bead could make a simple workflow for differentiation of MTBC and NTM infections in low-resource settings attainable.

Materials and Methods

Mycobacterial strains, culture conditions, and electroporation.

Mycobacterium bovis Karlson and Lessell TMC 1011 [BCG Pasteur] (ATCC® 35734TM) is referenced here as *M. bovis* BCG (BCG), and *Mycobacterium smegmatis* (Trevisan) Lehmann and Neumann mc(2)155 (ATCC® 700084TM), referenced here as *M. smegmatis* (*M. smeg*) were cultured in BD DifcoTM Middlebrook 7H9 Broth (FisherSci, DF0713-17-9) supplemented with 10% BD BBL™ Middlebrook OADC Enrichment (FisherSci,

Cat# B12351) and 0.05% glycerol, or on BD Difco™ Middlebrook 7H10 agar (FisherSci, DF0627-17-4) supplemented with OADC and glycerol. All suspension BCG cultures were grown at 37°C with constant shaking at ~200 rpm, and *M. smeg* suspension cultures at 20°C with constant shaking at ~200 rpm. *M. smeg* was cultured at room temperature as a preventative measure to reduce the chances of contaminating the incubator and BCG cultures with the faster-growing mycobacterial strain. Following electroporation, transformed BCG and M. smeg were grown using the indicated media supplemented with 50 µg/mL or 100 µg/mL Hygromycin B respectively (RPI Corp., H75020) to maintain the selection of bacteria expressing the plasmid.

Plasmid pMN437 was a gift from Michael Niederweis (Addgene plasmid # 32362; http://n2t.net/addgene:32362; RRID:Addgene_32362).[345] Plasmid pMyCA-mCherry was a gift from Young-Hwa Song (Addgene plasmid #84272; http://n2t.net/addgene:84272; RRID: Addgene_84272).[274] These plasmids were used to create fluorescent BCG and *M. smeg* bacilli respectively for imaging. The plasmids arrived as a bacterial stab of transformed *Escherichia coli* DH5α, which were expanded into 100 mL cultures in LB (Lysogeny Broth) liquid culture medium (RPI Corp., L24040) containing 200 µg/mL or 100 µg/mL Hygromycin B respectively at 37°C or 20°C, respectively, with shaking at ~200 rpm. The plasmids were isolated from the cultures using the QIAprep® Spin Miniprep Kit (Qiagen, 27104). The same stock of *E. coli* used to copy and isolate pMyCA-mCherry in preparation for electroporation was expanded and used in experiments using mCherry *E. coli*.

BCG and *M. smeg* were electroporated as indicated by Goude and Parish,[275] substituting the culture media above into the electroporation protocols. Following electroporation and plating on selection agar, BCG was cultured at 37°C for up to four weeks, and *M. smeg* was cultured at 37°C for three to five days before inoculating liquid culture media with transformed colonies. BCG and *M. smeg* electroporated with water instead of plasmid DNA did not grow on the Hygromycin B selection plates. Green or pink colonies only grew on the selection plates electroporated with the corresponding plasmid DNA.

Preparation of single-cell suspensions.

Because of mycobacterial cultures' sticky/clumping nature, it is necessary to use mechanical dissociation to liberate usable cells before use in experiments. A minimum of 50 mL of suspension culture for each strain was used in preparations to ensure enough cells were available for use. Suspension cultures were placed in 50 mL conicals and centrifuged at 1,100 x rcf for 5 min in Beckman Coulter™ Allegra™ X-22R Centrifuge. The supernatant was

removed, and the process was repeated for populations with culture volumes greater than 50 mL. Once complete and all supernatant was removed, ten acid-alcohol-washed and autoclaved 3 mm glass beads (MilliporeSigma, 1040150500) were added to the 50 mL conical and cells and vigorously shaken for 1 min. After allowing aerosols to settle for at least 1 min, 6 mL of 1x Phosphate-buffered saline (PBS; 137 mM NaCl, 2.7 mM KCl, 10 mM Na_2HPO_4, 1.8 mM KH_2PO_4, pH = 7.4) was added, and the tube was gently rocked to wash the cells off the tube walls. The large aggregates were allowed to settle for 5 min, and the upper 5 mL were filtered through a 70 μm cell strainer and into a clean 50 mL conical. The cells were centrifuged at 378 x rcf for 10 min, and the upper 4 mL of supernatant was removed, which contained single cells for the experiment. In some cases, the cell yield was low and more cells were needed to complete each experiment. Cells from the entire 5 mL volume following filtration were used in those cases. Only the single cells acquired after the second centrifugation step should be used in future experiments.

Triplicate optical density measurements at 600 nm for each population were measured using a Vernier Go Direct® SpectroVis® Plus Spectrophotometer (Vernier, GDX-SVISPL), and the number of cells recovered was estimated. Because of the difficulty of accurately counting the total number of cells, cell solutions at various optical density measurements were counted on a BD FACSAria™ III flow cytometer alongside a known quantity of Countbright™ Absolute Counting Beads (ThermoFisher, C36950). One event was assumed to correspond to one bacterial cell, and a standard curve correlating Flow Cytometry Events vs. OD600 was created (**Figure B1**).

MVN-His_6 production and purification.

Plasmid information.

The microvirin-N (MVN) DNA sequence was previously cloned into the pET15b vector as described by Kehr *et al.*,[312] resulting in the expression of an N-terminally His-tagged MVN protein. Dr. Carole Bewley generously gifted the cloned pET-15b-MVN plasmid (Laboratory of Bioorganic Chemistry, NIDDK, National Institutes of Health).[343] Cloning methods inserting the MVN into the pET-15b vector are described by Kehr *et al.*[312]

Expression of MVN-His_6.

The pET15b-MVN plasmid was transformed into One-Shot™ BL21 (DE3) pLysS *Escherichia coli* (*E. coli*; Invitrogen, C606010) with 190 ng plasmid per 100 μL of competent bacteria, according to manufacturer's instructions. Transformed bacteria were inoculated into a 50 mL culture of Lysogeny Broth with 100 μg/mL ampicillin, and cultures were then shaken at ~220 rpm overnight at 37°C. The following day, a 2 L baffled flasks

containing 1 L of Terrific Broth (1.2% w/v tryptone, 2.4% w/v yeast extract, 0.4% v/v glycerol, 17 mM KH_2PO_4, 72 mM K_2HPO_4) with 100 μg/mL ampicillin were each inoculated with the overnight starter culture at an initial optical density at 600 nm (OD600) of ~0.1. The culture was incubated at 37°C with shaking at ~220 rpm until the OD600 measured 0.6 – 0.8. The incubator and cultures were then cooled to 18°C. Isopropyl β-D-1-thiogalactopyranoside (IPTG) was added at a final concentration of 1 mM to induce MVN expression, and the cultures were incubated overnight at −18°C with shaking at ~220 rpm to complete the protein expression. Cultures were harvested the following day using centrifugation, at which point the supernatant was discarded, and the pellet was used fresh or frozen at 80°C until use.

Bacterial lysis.

The induced cells were resuspended in 150 mL of Resuspension Buffer (25 mM NaH_2PO_4, 500 mM NaCl, 10% glycerol, pH = 8) containing 2 μg/mL Lysozyme (SigmaAldrich, L6876), 1 mL Protease Cocktail (SigmaAldrich, P8849), and a skosh of powdered DNase I (SigmaAldrich, DN25) in a beaker using a stir bar for 15 minutes. The mixture was chilled on ice, and then passed through an Emulsiflex-C3 High-Pressure Homogenizer (Avestin, Mannheim, Germany) three times while maintaining lysis pressure at 15,000 psi. The lysate was clarified by centrifuging it at 35,300 x rcf, 4°C, for 45-60 min. The clarified supernatant was filtered through a 0.22 μm filter.

IMAC purification of MVN-His_6.

Protein purification was performed using Fast Protein Liquid Chromatography. A 5 mL HisTrap™ HP (Nickel Sepharose™ High-Performance Medium) column (Cytiva Life Sciences, 17524802) was equilibrated at 4 mL/min with 5 column volumes (CV) of Resuspension Buffer. The clarified bacterial lysate was loaded onto the column at a 4 mL/min rate. The column was washed with 20 CV of Resuspension Buffer at 4 mL/min, and the protein was eluted using a linear imidazole gradient from 0−500 mM, collecting 2 mL fractions using Resuspension Buffer + 500mM imidazole, pH = 8. Elution fractions were analyzed by SDS-PAGE using an Invitrogen™ NuPAGE™ 4–12% Bis-Tris gradient gel run in 1x Invitrogen™ NuPAGE™ MES SDS Running Buffer (NP0002, 50 mM 2-(N-morpholino)ethanesulfonic acid (MES), 50 mM Tris Base, 0.1% SDS, 1 mM EDTA, pH = 7.3) for the presence of the 14 kDa MVN monomer and dimer respectively under reducing conditions. The fractions with similar MVN profiles were pooled (**Figure D1**) and dialyzed against 1x PBS overnight. Protein concentration quantified following SDS-PAGE using Image Studio™ Lite Version 5.2 (LI-COR, Lincoln, NE) through densitometry (**Figure**

D2). Purified MVN was aliquotted and stored at –80°C until use. Pool 2 was used to maintain MVN consistency between experiments.

Optimization and functionalization of streptavidin magnetic beads with AlexaFluor™ 405.

To visualize individual binding interactions between bacteria and beads, they must be labeled with a distinct fluorophore, providing an additional distinct physical variable for gating alongside their inherent size and granularity. Therefore, we created fluorescent magnetic beads by covalently modifying the ε-amino R-group of lysine on the streptavidin bead surface with AlexaFluor™ 405 (AF405). After, biotinylated proteins were loaded onto the surface of the fluorescent magnetic beads using the noncovalent interaction between streptavidin and biotin (**Figure 6.1**).

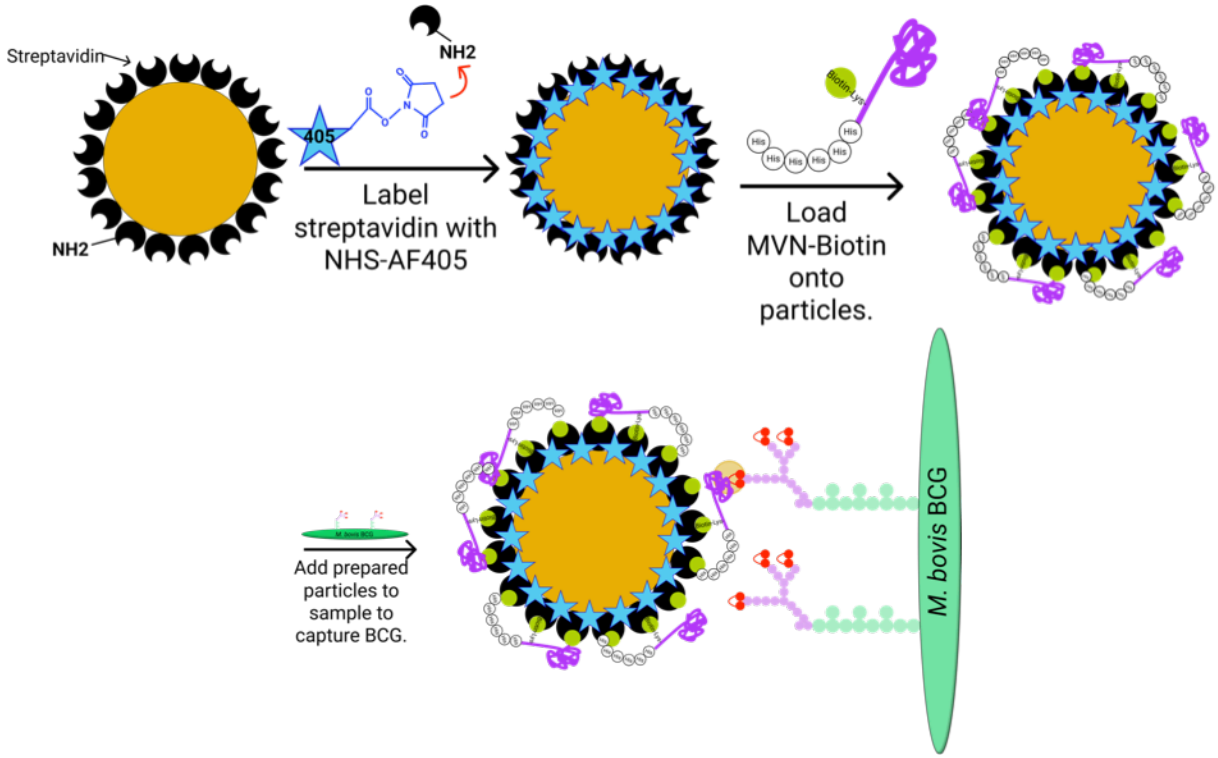

Figure 6.1. Design of heterofunctionalized MVN-capture bead. The streptavidin surface coating was first labeled with a carboxylic acid, succinimidyl ester of AlexaFluor™ 405. Covalent modification of the ε-amino R-group of streptavidin's lysines created a stable fluorescent bead that could then be loaded with biotinylated MVN and used to capture *M. bovis* BCG through the association of MVN and the mannosyl caps found on ManLAM. Loading of MVN-Biotin on the bead surface was confirmed by detecting the endogenous N-terminal His tag found on MVN.

MyOne™ Streptavidin T1 ™ (ThermoFisher, 65601; 1 μm diameter) and SuperMag Streptavidin Beads (OceanNanotech, SV0200; 200 nm diameter) were fluorescently labeled with AlexaFluor™ 405 (AF405) carboxylic acid, succinimidyl ester (ThermoFisher, A30000) before protein loading. AF405 was suspended at a 10 mg/mL concentration in dimethyl sulfoxide, aliquotted, and stored at –80°C until use to prevent ester hydrolysis.

Beads were washed three times with 1 mL of Conjugation Buffer (100 mM $NaHCO_3$, pH = 8.3) using a Vortex mixer to ensure adequate washing. ™ were magnetically separated on a fixed magnetic tube rack for at least 3 min between washes. Due to their small diameter low magnetic susceptibility, SuperMag Beads were concentrated via centrifugation at 17,500 x rcf for one to two minutes in an Eppendorf® Centrifuge 5430 (Hamburg, Germany), which significantly expedited the separation process during bead functionalization. In addition, the Conjugation Buffer and wash buffer listed included 0.01% Tween-20 for the SuperMag beads to help prevent intrabead aggregation and aggregation to the walls of the microcentrifuge tubes. When initially performed without Tween-20, the beads showed minimal conjugation at less than 10-fold molar excess, so Tween-20 was added, and the molar excess range increased. After washing, ™ and SuperMag beads were resuspended in Conjugation Buffer at concentrations of 5 mg/mL and 2 mg/mL, respectively, and briefly sonicated using a Vevor® 40 kHz Ultrasonic Jewelry Cleaner (Shanghai, China). AF405 was added to the beads and mixed using a Vortex mixer. Beads were incubated on a shaker at room temperature for 1 h at ~150 rpm protected from light in 2 mL microcentrifuge tubes. After, the beads were washed 1x in 1 mL of Conjugation Buffer, followed by two washes in 1x PBS. The beads were resuspended at their stock concentrations in 1x PBS + 0.02% Tween-20 and stored at 4°C protected from light until use. Conjugation of the streptavidin surface with AF405 was confirmed by measuring fluorescence using a Nanodrop™ 3300 Fluorospectrometer (ThermoFisher, Waltham, MA) before flow cytometric assessment.

To optimize the degree of surface modification of the ™ and SuperMag beads, the number of moles of streptavidin on each bead surface was first estimated. At the reported manufacturer's stock concentrations, we estimated Dynbeads has 2.56×10^{-12} mol streptavidin/μL beads (10 mg/mL stock), and SuperMag Beads have 1.71×10^{-13} mol streptavidin/μL beads (stock 1 mg/mL). Increasing molar equivalents of NHS-AF405 were added to beads for conjugation. The fluorescence intensity of the AF405-functionalized beads was measured and recorded on a BD FACSAria™ III. When the samples were analyzed on the cytometer, they were explicitly run in a specific order, starting with the unstained control, followed by the experimental conditions from the least to the greatest concentration of AF405 to ensure no contamination low-concentration sample measurements from high-

concentration sample measurements. A minimum of 5,000 beads were sampled for each condition. Conjugated beads were compared to unstained controls to determine which molar excess of AF405 produced a definitively positive AF405 signal without being hyper-intense (**Figure D3**). Based on these titrations, 6x and 100x molar equivalents of AF405 were selected for standardized fluorescent-tagging of ™ and SuperMag beads, respectively.

For the SuperMag beads, 10x molar excess increased the AF405 signal, but only 65% of beads were definitively positive. Therefore, a higher concentration of NHS-AF405 was needed to ensure complete bead labeling. However, even though the number of AF405-positive beads increased to >99%, the mean intensity decreased, likely because of self-quenching.[346] Because the total fluorescence intensity decreased at 40-fold molar excess, the AF405 titration should be repeated using smaller concentration difference intervals, explicitly looking at loading below 40x molar excess.

Acquisition of and titration of secondary His tag antibody.

Mouse monoclonal DyLight® 650 Anti-6x His tag® antibody [AD1.1.10] abbreviated anti-His_6-650 herein (abcam, ab117504) was purchased to detect MVN, specifically binding to the His_6 tag found on MVN. This antibody confirmed MVN loading on the magnetic bead and BCG surfaces. Mouse monoclonal DyLight® 650 Anti-DDDDK (Binds to FLAG® tag sequence) [M2] (abcam, ab117492) was purchased as an isotype control for the anti-His_6-650.

To titrate anti-His_6-650 for loading confirmation of MVN-Biotin on the bead surfaces, 5 µg of unaltered beads were mixed into 500 µL of 1x PBS + 0.02% Tween-20 (PBS-T) containing increasing quantities of anti-His_6-650. The samples were incubated for 30 minutes at room temperature on a lab rotisserie. The beads were washed three times in 1 mL of PBS-T, and the fluorescence intensity of at least 5,000 events was measured on the Allophycocyanin (APC) channel using the BD FACSAria™ III. Looking at the populations' intensity and spread changes aided in assessing nonspecific binding between the beads and anti-His6-650. The geometric mean (GMean), robust standard deviation (rSD), and % events DyLight® 650 positive were plotted here for analysis. The highest quantity of anti-His_6-650 that did not significantly increase the background signal was chosen for each titration (**Figure D4**). For Dynabeads™, this was a 1:1,000 dilution (0.5 µg/sample). For SuperMag beads, a 1:3,000 dilution (0.17 µg/sample) of anti-His_6-650 was chosen for loading quantification.

To titrate anti-His_6-650 for detection of MVN-His_6 or MVN-Biotin binding to the surface of BCG, approximately 2 million cells were resuspended in 500 uL of PBS-T with increasing amounts of anti-His_6-650 and incubated protected from light on a lab rotisserie at room temperature for 30 minutes. The cells were washed 3x using 1 mL of PBS-T in a 15 mL conical tube by centrifugation at 3,000 x rcf for 5 min in Beckman Coulter™ Allegra™ X-22R Centrifuge. Cells were resuspended in 200 µL of PBS-T, and the fluorescence intensity of a minimum of 5,000 events was measured using the BD FACSAria™ III (**Figure D5**). A dilution of 1:1,000 (0.5 µg/sample) was chosen. Some initial and troubleshooting experiments used other secondary antibody dilutions, and these instances are explicitly noted.

When analyzed on the cytometer for both titrations, samples were applied in a specific order. The unstained control was analyzed first, followed by the secondary-only control. Then, the experimental conditions were analyzed from the least to the greatest concentration of anti-His_6-650 to effectively prevent any contamination of low-concentration sample measurements from high-concentration sample measurements. The gating strategy for fluorescence analysis is shown in **Figure D6**.

MVN titration and binding to BCG surface.

BCG was prepared from culture as specified. An average of 2 million BCG or GFP BCG cells were suspended in 500 µL PBS-T with increasing amounts of MVN-His_6 or MVN-Biotin in a 1.5 mL or 2 mL microcentrifuge tube. The samples were mixed and incubated at room temperature for 30 min on a lab rotisserie. After, samples were transferred into a 15 mL conical tube and centrifuged at 3000 x rcf for 5 min. The samples were washed three times with 1 mL of 1x PBS + 0.02% Tween-20. The samples were then transferred into new microcentrifuge tubes containing 500 µL of 1:1,000 anti-His_6-650 and incubated again on a lab rotisserie for 30 min at room temperature protected from light. Samples were washed with 1 mL of PBS-T three times via centrifugation and suspended in 200 µL before analysis. The gating strategy for fluorescence analysis is shown in **Figure D6**.

Creation of an isotype-analogous control for MVN through irreversible intraprotein disulfide reduction of MVN.

Experiments with antibodies traditionally use an isotype control to determine how much nonspecific binding occurs through interactions with the conserved regions of an antibody. When isotype controls are loaded onto beads, it can serve as a control for nonspecific binding due to the antibody's conserved region and binding to

the bead's surface. MVN is a lectin, and therefore, an isotype control does not exist. As a result, nonspecific vs. specific binding cannot be accurately assessed during optimization experiments, such as when optimizing MVN surface loading for these beads.

MVN was biotinylated as described below with EZ-Link™ NHS-PEG$_4$-Biotin (ThermoFisher, A39259) and dialyzed into 150 mM NaCl in preparation for reduction using a Slide-a-Lyzer™ Dialysis Cassettes, 2K MWCO, 3 mL (ThermoFisher, 66203) according to the manufacturer's instructions. Tris(2-carboxyethyl)phosphine hydrochloride (TCEP HCl; ThermoFisher, 20490) was prepared in water according to the manufacturer's instructions at 100 mg/mL and stored at −20°C until use.

MVN has three disulfide bonds made from six cysteines to reduce. A 100-fold molar excess of the number of thiol groups of TCEP HCl is recommended for complete reduction. So, a total of 600-fold molar excess of TCEP HCl was added to MVN-Biotin, assuming that the total protein concentration measured using A280 was pure MVN and incubated on a lab rotisserie at room temperature for two hours. Leftover TCEP HCl was removed, and the buffer was exchanged into 1x PBS using Zeba™ Columns. The thiol groups on the free cysteines were alkylated with N-ethylmaleimide (NEM, ThermoFisher, 23030) to prevent any spontaneous oxidation. An equal mass of NEM was added to the reduced MVN-Biotin and reacted at room temperature on a lab rotisserie for 2.5 h. Unreacted NEM was also removed using Zeba™ Columns.

Three different methods assessed the outcome of the reduction and alkylation. First, an SDS-PAGE was performed to assess the protein content from MVN-Biotin fractions taken during each treatment step. A total of 5 μg of protein from each sample was separated on a 4-20% Mini-PROTEAN® TGX™ Precast Protein Gel (BioRad, 4561095) under reducing conditions at 100 volts for 80 min. According to the manufacturer's instructions, the protein gel was stained with GelCode™ Blue Stain Reagent (ThermoFisher, 24590) and imaged using a Gel Doc EZ Gel Documentation System (**Figure D7**).

Second, to determine if reduction and alkylation were successful, fractions from each process step were assessed for thiol concentration using molar absorptivity using Ellman's Reagent, 5,5'-dithiobis-(2-nitrobenzoic acid) (DTNB, ThermoFisher, D8451). DTNB reacts with free thiols in solution, producing a mixed disulfide product and 2-nitro-5-thiobenzoic acid (TNB), which is yellow-colored and can be quantified using spectrophotometry.[347] DTNB was prepared and mixed with known amounts (100 μL; variable concentration) of MVN-Biotin according to the manufacturer's instructions, and the absorbance of the TNB produced was measured in triplicate using a Go

Direct® SpectroVis® Plus Spectrophotometer at 412 nm. Using the extinction coefficient of TNB (14,150 M^{-1} cm^{-1}), the concentration of thiol groups within each sample was calculated and compared to the estimated number of thiols. A blank sample was also measured, and the average background signal was subtracted from the sample data.

Third, to assess if the reduced and alkylated MVN could bind ManLAM, as described in van der Horst *et al.,*[86] biolayer interferometry measured the binding kinetics of pre- and post- reduced + alkylated MVN-Biotin. Biolayer interferometry was performed using a ForteBio Octet RED96. Dip and Read Streptavidin Biosensors (ForteBio, 18-5019) were used in the binding experiments. *Mycobacterium tuberculosis*, H37Rv, Purified Lipoarabinomannan (NR-14848) was obtained from the Biodefense and Emerging Infections Research Resources Repository (BEI Resources, Manassas, VA), NIAID, NIH. All experiments were performed in 1x PBS + 0.02% Tween-20 + 0.1% Bovine Serum Albumin (BSA; MilliporeSigma, A7030). After a 10 min delay for sensor tip rehydration, as recommended by the manufacturer, the biosensor tips were moved into a well of PBS-T-BSA for a 300 s equilibration step. After, the biosensor tips were introduced into wells containing 0.1 μg/mL pf MVN-Biotin for 400 s, loading the streptavidin tips with the biotinylated lectin. The biosensors were then transferred into wells containing PBS-T-BSA for a 60 s baseline step, then transferred into wells containing 2-fold serially diluted ManLAM, starting at 20 nM, for 400 s. After this association, the biosensors were transferred back into the buffer-only sample well for 900 s to measure the dissociation between ManLAM and MVN-Biotin. A global 1:1 fit model calculated the binding kinetic and equilibrium constants (k_{on}, k_{off}, and K_D).

Bioconjugation of lectins.

Recombinant Human Galectin-1 (carrier-free) was purchased from Biolegend® (553506), aliquotted on arrival, and stored at –80°C until use. Both MVN-His_6 and Galectin-1-His_6 were reacted with 20x molar equivalents of EZ-Link™ NHS-PEG_{12}-Biotin (ThermoFisher, A35389) for one hour at room temperature on a lab rotisserie according to the manufacturer's protocol. Zeba™ Spin Desalting Columns, 7K MWCO (ThermoFisher, 89882) removed unreacted NHS-PEG_{12}-Biotin from MVN following reaction incubation. Galectin-1 was cleaned using 2K MWCO dialysis cassettes to reduce protein loss of the small quantity of Galectin-1. We have seen protein losses up to 50% with Zeba™ Columns. The final concentration of biotin-conjugated MVN (MVN-Biotin) and Galectin-1 (Galectin-1-Biotin) were determined using absorbance at 280 nm on a Nanodrop™ Spectrophotometer ND-1000.

MVN-Biotin was stored at 4°C until use. Galectin-1-Biotin was stored at –80°C until use. In some early experiments, EZ-Link™ NHS-PEG_4-Biotin was used to conjugate MVN instead of PEG_{12}.

Biotinylated lectin loading onto AF405-conjugated streptavidin beads.

This protocol applies to both MVN and Galectin-1. Dynabeads™ or SuperMag streptavidin beads conjugated with AF405 were washed three times in 1 mL of PBS-T. Dynabeads™ were resuspended at 10 mg/mL, and SuperMag beads at 1 mg/mL in PBS-T with a defined quantity of Lectin-Biotin (**Figure 6.1**). Samples were incubated at room temperature on a lab rotisserie for one hour. AF405-Lectin beads were washed three times in 1 mL of PBS-T. After, to block any free streptavidin binding sites, the beads were placed in 16 μM D-Biotin[86] in PBS-T and incubated on a rotisserie for one hour. The beads were washed three times with PBS-T to remove excess remaining biotin, and beads were used within 24 h of manufacture. In some initial experiments, naked beads were used as negative control beads. These beads were made similarly but did not include the Lectin-Biotin loading.

Capture of BCG, M. smeg*, or* E. coli *on fluorescent-MVN magnetic beads.*

The GFP BCG, mCherry *M. smeg*, or mCherry *E. coli* were used to assess the specificity of MVN-functionalized beads. MVN-Biotin was loaded onto AF405- Dynabeads™ or AF405-SuperMag beads as described at a 100% surface loading density. Naked streptavidin beads blocked in D-Biotin were used as a negative binding control. As specified, GFP BCG was stained with 5 μg of MVN-His6. The cells and beads were then stained with anti-His_6-650 to confirm MVN-Biotin loading.

Unfortunately, no notes indicated the quantity cells of *M. smeg* or *E. coli* were captured in this experiment; it was likely not recorded because the mCherry protein would interfere with an OD600 reading and was therefore not quantified. A standard curve for measuring the optical density of mCherry *M. smeg* at 700 nm should be made using the Counting Beads, similarly to that created in **Figure B1**. For this reason, each condition was normalized to capture the naked beads for each bacterial species and bead size. A total of 5 μg of naked beads or MVN beads were added to a 1 mL volume of 1x PBS + 0.02% Tween-20 containing GFP BCG, mCherry *M. smeg*, or mCherry *E. coli* and mixed on a lab rotisserie protected from light for 30 min. The samples were then staged on a fixed magnet tube rack and immediately taken to the cytometer for analysis. A minimum of 100,000 events were measured from each

sample. The collection parameters and fluorescence compensation matrix are listed in **Table D1** and **Table D2**, respectively. The gating strategy and FMO controls are shown in **Figure D8** and **Figure D9**.

Optimization of MVN loading concentration on AF405-conjugated SuperMag beads using isotype-analog control Galectin-1.

AF405-SuperMag beads were loaded with increasing amounts of MVN-Biotin or Galectin-1-Biotin as described. The reported bead surface loading density (% surface coverage) values were based on the size of MVN-Biotin. Galectin-1-Biotin was loaded at the molar equivalent of MVN-Biotin to take into account the difference in molecular weights. GFP BCG was prepared as described. One million GFP BCG bacilli were combined with 5 μg of MVN-AF405-beads or Galectin-1-AF405-beads in 500 μL of PBS-T in microcentrifuge tubes, and they were placed on a lab rotisserie to facilitate binding for one hour. The samples were then placed on a fixed magnet tube rack and immediately taken to the cytometer for analysis. A minimum of 100,000 events were analyzed for each sample. Collection parameters and fluorescence compensation matrix are listed in **Table D3** and **Table D4**, respectively. The gating strategy and FMO controls are described in **Figure D8** and **Figure D10**.

Flow cytometry data collection and analysis.

All experiments were performed in the Vanderbilt Flow Cytometry Shared Resource Core, and analyses were performed on a BD FACSAria™ III instrument using a 70 μm nozzle. Sample data was collected using BD FACSDiva™ Software Version 8.0.1. The fluorophores selected for this report used a different excitation/emission laser line on the instrument. Specifics regarding the optical components are in **Table 6.1**. Unstained samples of bacteria and beads were collected as unstained controls at each experiment. When multiple fluorophores were used together in an experiment, single fluorophore controls were used to perform fluorescence compensation within the FACSDiva™ software according to the manufacturer's instructions. For compensation, 5,000 events were collected for each control. Fluorescence Minus One (FMO) controls were created and collected after compensation. FMO controls were used to determine gating for post-collection analysis (**Figure D9** and **Figure D10**). A DyLight® 650 positive control bead was created by maximally loading anti-DDDDDK-650 onto Protein A ™ (ThermoFisher, 10001D). Forward scatter (FSC) and side scatter (SSC) thresholds were set to 500. Collection parameters for

channel voltage, gain, etc., for the MVN-Galectin-1 and BCG/*M. smeg*/*E. coli* capture experiments are in **Table D1** and **Table D3**. Compensation matrices are listed in **Table D2** and **Table D4**.

Table 6.1. Optical Hardware Specifications for Flow Cytometry.

Instrument: BD FACSAria™ III				
Laser Lines:	407 nm	488 nm	633 nm	561 nm
Long Pass Filter:	–	502 nm	–	600 nm
Emission Bandpass Filter:	450 nm ± 40 nm	530 nm ± 30 nm	660 nm ± 20 nm	610 nm ± 20 nm
Fluorochrome:	Pacific Blue (AF405)	FITC (GFP)	APC (DyLight® 650)	PE-TexasRed (mCherry)
Associated Reagent:	Streptavidin beads	BCG	His_6 antibody	*M. smeg*, *E. coli*

Post-collection analyses and gating were performed using FlowJo™ VX (v10.0.7) (FlowJo, LLC., Portland, OR). The size, granularity, and fluorescence distinguished between each population of beads or bacteria. The beads and bacteria showed similar sizing on forward scatter, but the magnetic beads had a higher granularity than the bacterial cells, creating distinct populations visualized on SSC-A vs. FSC-A plot. When bacteria and beads combine, they take on the other's size, granularity, and fluorescence characteristics. Therefore, when bound together, bacteria take on the granularity and AF405 fluorescence from beads, and the beads become GFP-positive or mCherry-positive. To detect bead-bacteria interactions, the bead population within each sample was gated, and the co-localization of the fluorophores (AF405 and GFP, or AF405 and mCherry) were assessed using the gates defined by FMO controls (**Figure D8**). The events definitively positive for both fluorophores were interpreted as a positive binding between a bead and bacteria. To quantify the degree of MVN-surface loading onto beads or bacteria, the population was gated on size and granularity, and the change in DyLight® 650 intensity and number of positive events for the gated population was calculated in FlowJo™ (**Figure D6**).

Statistical analyses.

Cell populations and expression levels follow a multiplicative relationship instead of a linear relationship, so geometric mean (GMean) and robust standard deviation (rSD) are reported. These statistics also resist outliers.

In sample sets where $n \geq 3$, statistical analyses were performed using MATLAB on background-subtracted data. One-way analysis of variance (ANOVA) determined statistical significance for data containing three or more groups. Statistical significance was defined as $p < 0.05$. Tukey's range test identified which specific conditions were statistically different post-hoc.

Results

Titration of MVN onto BCG surface.

Having a ManLAM surface expression level measured through MVN binding is essential for normalizing conditions across individual experiments before comparison and determining if binding events are because of MVN capture and not nonspecific interactions. Therefore, we titrated MVN onto the surface of BCG to identify an optimal staining concentration. As shown in **Figure 6.2**, the results varied significantly across each experiment. In some cases, the measured fluorescence intensity was relatively high, while other experiments showed essentially no binding under the same conditions. This variation was a substantial barrier to forwarding progress, and significant time was spent determining why so much variation occurred. We initially started by dissociating BCG using a 21 gauge needle and syringe instead of glass beads but found similar variations. There was no pattern observed between the age of the culture or time since the last split/feeding and the level of MVN binding. We did identify that the centrifuge conditions used for MVN and anti-His_6-650 impacted the ManLAM surface availability to MVN (**Figure D11**). The centrifugation conditions were adjusted to reflect this finding, but the reproducibility issue persisted. The findings outlined in Chapter 5, which demonstrate a significant impact on the surface binding of MVN with most treatments, highlight that the issue is not just a culture variation problem but an MVN problem. As shown in **Figure E3**, the monomer or dimer fraction of MVN used for surface staining *M.tb* impacts the degree of surface staining, which we hypothesize is due to the monovalent vs. divalent nature of the MVN monomer and dimer.

Capture of BCG, M. smeg, or E. coli on fluorescent-MVN magnetic beads.

Figure 6.3 and **Figure 6.4** outline experiments assessing the performance and specificity of MVN capture beads to GFP BCG, mCherry *M. smeg*, and mCherry *E. coli* on AF405 beads. These experiments were an initial survey of the fluorescent components once prepared for flow cytometry analysis, so surface loading of MVN-Biotin onto beads, binding time, and quantity of beads were not optimized. We first assessed the GFP BCG cultures for the presence of ManLAM through MVN binding and confirmed loading of MVN onto the bead surfaces before performing capture. As shown in **Figure 6.3A**, there was a negligible increase in the fluorescence intensity from 1.56 ± 74.6 to 18.4 ± 147 to 25.6 ± 179 between the unstained BCG, the secondary only control, and the cells tagged with 5 μg MVN-Biotin, respectively. Because ManLAM is highly expressed in BCG, this trivial difference in the

mean population intensity demonstrates minimal MVN surface binding and is consistent with the issues seen during MVN titration onto the BCG surface. More often than not, a minimal amount of binding of MVN to BCG occurred.

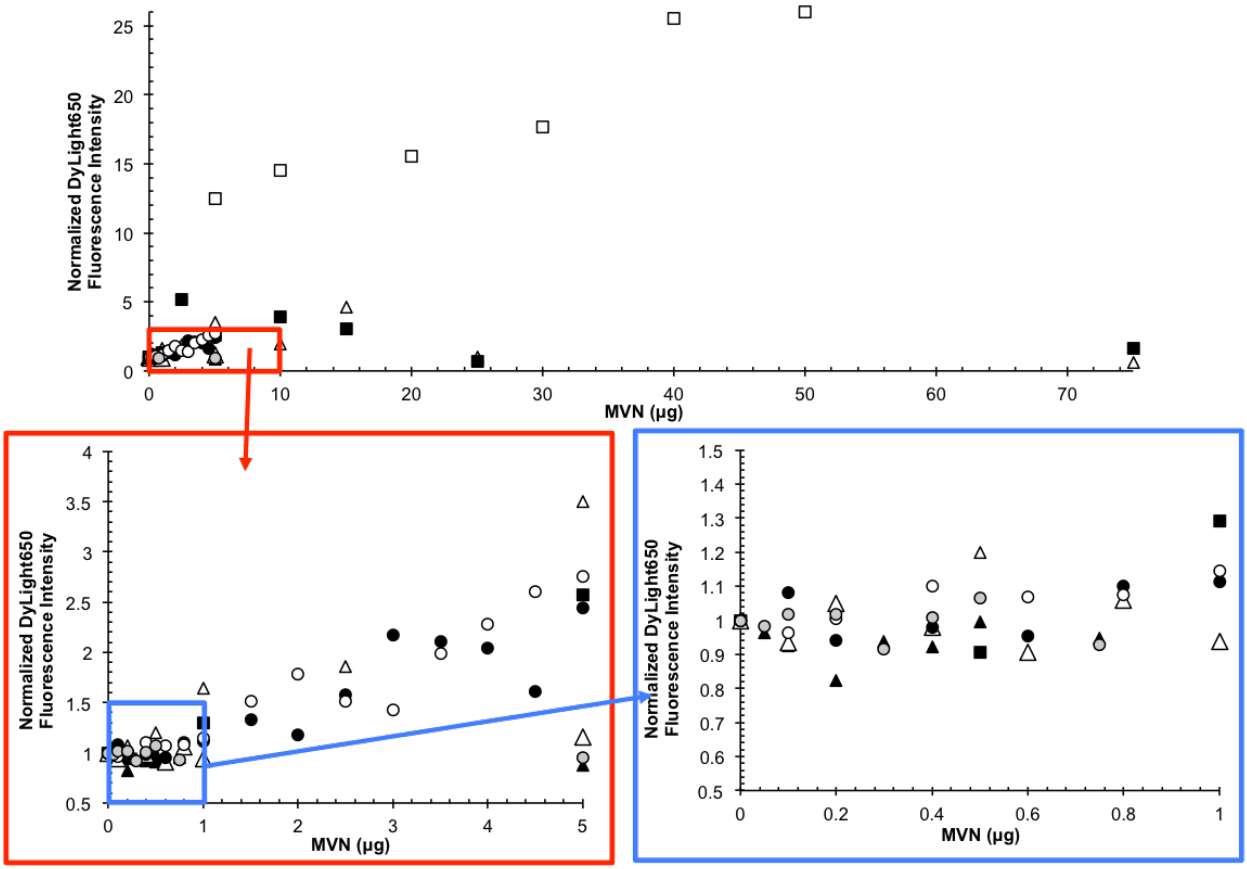

Figure 6.2. Titration of MVN binding to the BCG surface. Eight separate GFP BCG cell populations were titrated with increasing amounts of MVN (0.05 µg to 75 µg) using 1:1,000 anti-His6-DyLight® 650. Values for each experiment were normalized to the secondary-only control, stained only with anti-His_6-650. Each dot plot symbol (e.g., black circle, white triangle) represents a different population of cells. Normalized GMean values are reported for each population at each condition.

Figure 6.3B confirmed loading of MVN-Biotin onto the surface of both beads. Non-fluorescent beads had a mean DyLight® 650 fluorescence intensity of 10.5 ± 99.1 and 4.59 ± 89.5 for Dynabeads™ and SuperMag beads, respectively, and this changed to 6.1 ± 85.9 and 47.8 ± 95.2, respectively, for naked AF405 beads stained with anti-His_6-650 only. This shows some nonspecific binding of the secondary antibody for the naked SuperMag Beads. After maximally loading MVN-Biotin onto the surface of the beads, the DyLight® 650 fluorescence increased to 840 ± 625 and 451 ± 402, respectively, indicating the presence of MVN on the bead surface.

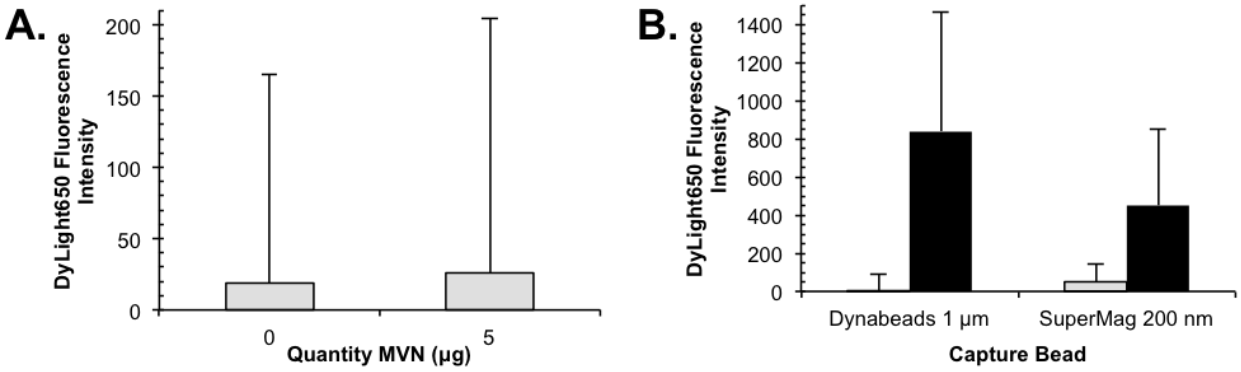

Figure 6.3. Confirmation of MVN-Biotin loading onto the surface of GFP BCG (**A.**) or AF405 capture beads (**B.**) Negative control capture beads (gray bars) were blocked in D-Biotin and otherwise left naked with no surface protein loaded. MVN-loaded beads (black bars) were loaded at 100% loading capacity. n = 1. (GMean ± rSD).

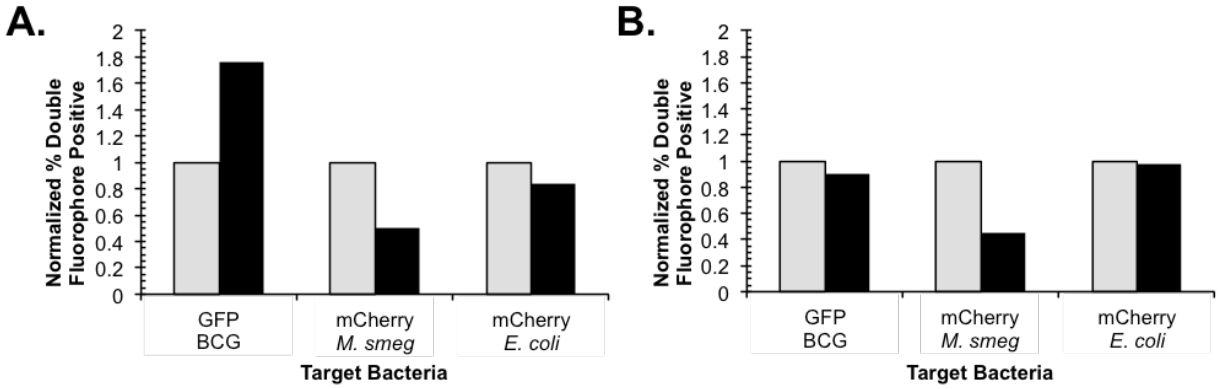

Figure 6.4. Normalized capture of GFP BCG, mCherry *M. smeg*, and mCherry *E. coli* each bacteria on AF405 Dynabeads™ 1 µm (**A.**) and AF405 SuperMag 200 nm beads (**B.**) surface-loaded with D-Biotin (gray bars) or MVN-Biotin (black bars). Values were normalized to the capture of each bacteria on D-Biotin beads. n = 1.

Despite the results showing no binding of MVN to the surface of GFP BCG, the prepared beads and bacteria were used in an initial capture experiment assessment for ManLAM-expressing BCG, PILAM-expressing *M. smeg*, and non-mycobacterial rod-shaped bacilli *E. coli*. The values reported in **Figure 6.4** were normalized within each experimental condition, and therefore extrapolation across different bacteria is not possible. Specifically, mCherry's fluorescence emission spectra significantly overlap with the measurements for OD600, and the number of bacteria used for these conditions was not specified.

It is interesting to note that almost universally, the amount of binding observed between beads and bacteria decreased when the beads were loaded with MVN, compared to the naked beads. The exception was Dynabeads™ capture of GFP BCG, which showed an almost 2-fold improvement in the capture of bacteria. This decrease in binding highlights the well-known issue of nonspecific binding between mycobacteria and capture beads and solidifies the need and importance of a negative control bead surface-functionalized with an MVN isotype-analog. Furthermore, **Figure D12** shows the non-normalized % Double Fluorophore Positive values for the same experiment. Even though the difference between the naked and MVN beads is insignificant, there is an extremely high amount of binding between the beads and the *E. coli* surface, particularly the Dynabeads™. Some nonspecific binding was also noted for mCherry *M. smeg*. The nonspecific binding issues across all conditions also establish the need for a bead design that reduces as many nonspecific interactions with the bead surface as possible and the need for an accurate isotype-analog control bead.

Reduction and alkylation of MVN-Biotin.

Because mycobacteria nonspecifically stick to beads, the surface of the negative control capture bead needed to be similarly loaded with protein to determine how much binding between beads and bacteria is specific vs. nonspecific. If the negative-control beads were left naked, as we saw previously, we could not assume that nonspecific capture on the naked bead was equivalent to that seen on a bead covered in the maximum theoretical amount of MVN-Biotin. MVN has a low isoelectric point (pI ~ 3.84, calculated using ExPASY)[348] which could further influence nonspecific interactions. Therefore, it was vital to identify a control that most closely recapitulated the structure of MVN without the function. We investigated two methods for the creation of an isotype-like control for MVN.

MVN has two different binding pockets that share a 35% sequence similarity,[349] and one of these pockets binds to the mannose-capping motif on ManLAM. Disrupting the structure of MVN would disrupt the carbohydrate-binding pockets and should prevent MVN from binding α-(1, 2)-mannobiose sugars and, therefore, ManLAM. The simplest way to achieve this is to permanently break the three disulfide bonds that maintain MVN's tertiary structure. If successful, this would create a protein similar in size and composition to MVN that does not bind ManLAM. Therefore, we tried reducing these disulfide bonds using Tris(2-carboxyethyl)phosphine hydrochloride (TCEP HCl). TCEP was chosen because reduction is considered irreversible because it does not regenerate any

competing disulfide bonds, such as those formed during dithiothreitol (DTT) and β-mercaptoethanol treatment.[350] For every disulfide bond, TCEP reduction creates two free hydrophilic cysteines that are more resistant to spontaneous oxidation than those created using DTT. It is also odor-free and effective under acidic and alkaline conditions. After reduction, the free cysteines were alkylated with N-ethylmaleimide (NEM) to ensure spontaneous oxidation did not reform the disulfide bonds.

To assess the impact of this reduction and alkylation on MVN-ManLAM binding, we first confirmed that the chemical reactions performed as expected. Using 5,5'-dithiobis-(2-nitrobenzoic acid) (DTNB), we confirmed the presence or absence of free cystines during each step of the reduction and alkylation process.[347] As seen in **Figure 6.5**, DTNB confirmed the reduction of MVN with TCEP, as seen by an increase in free thiols. However, there were almost 3x more thiol groups in the sample (388.84 nmol ± 2.52 nmol) than estimated (133.72 nmol), assuming the total protein consisted only of MVN-Biotin. Detecting 3-fold more thiol groups than estimated indicated the presence of contaminants in the IMAC-purified MVN sample; the contaminants were already known prior to reduction. Sample alkylation was also successful, as seen through a significant decrease in the number of thiol groups after adding NEM. A total of ~96% of free thiol groups were alkylated, but knowing other contaminating proteins are present in the MVN sample, it is not surprising that this small amount of thiols remained. A longer reaction time or NEM concentration adjustment would likely eliminate this.

SDS-PAGE analysis did not show any significant change in the molecular weight of the samples during each step (**Figure D7A**), though a few faint bands <14 kDa were noted following TCEP reduction and NEM alkylation. A precipitate formed during TCEP reduction (**Figure D7B**). Using an initial test sample of MVN, SDS-PAGE showed that MVN was present in both the soluble and insoluble fractions (**Figure D7C**). The insoluble fraction also contained contaminating proteins, consistent with the known protein concentration and results seen with DTNB thiol measurement. Because MVN was present in both, the soluble and insoluble fractions were not separated in the experiment reported in **Figure 6.5** and **Figure D7A**.

With the ultimate goal of creating an MVN-variant that does not bind ManLAM, we performed binding kinetic analysis on pre- and post- treatment MVN-Biotin using biolayer interferometry. The ability for MVN to bind ManLAM was measured using the equilibrium dissociation constant (K_D), which measures the propensity for the bound ManLAM to dissociate from the MVN. Ideally, if the reduction and alkylation worked, we would see no binding between MVN-Biotin and ManLAM. For untreated MVN-Biotin, the K_D was calculated at $<1\times10^{-12}$ M ±

9.7×10^{-12} M. For the reduced and alkylated MVN-Biotin, the K_D was calculated at 1.15×10^{-10} M ± 2.17×10^{-12} M. The plotted and processed data shows the binding association between MVN-Biotin and ManLAM (**Figure 6.5B**). While this result shows that MVN-Biotin can still bind ManLAM, the 100-fold reduction on the measured K_D nonetheless demonstrates some impact of reduction and alkylation. The contaminating proteins present in the IMAC purified MVN (see **Figure D1** and **Figure D2**) likely interfered with the reduction process and led to incomplete reduction of MVN-Biotin, since the number of additional disulfide bonds in those proteins was unknown, unaccounted for, and would have also reduced. Further purification of MVN following IMAC will be necessary to ensure that 100% of the sample is reduced and alkylated. The continued ManLAM-MVN association seen on biolayer interferometry is because the reduction and alkylation do not sufficiently disrupt the mannose-binding domain.

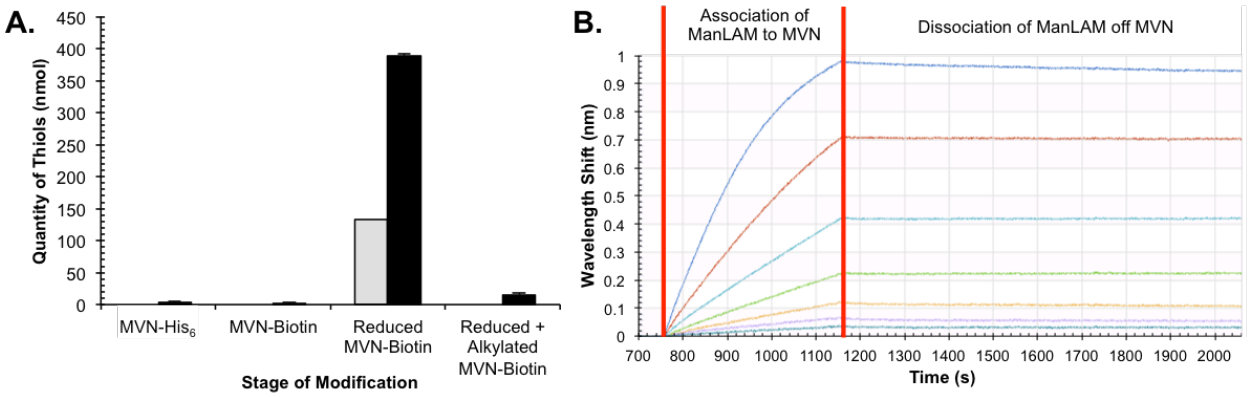

Figure 6.5. Reduction and alkylation of MVN-Biotin. **A.** Estimated quantity of thiol groups at each step of the reduction and alkylation process (gray bars) compared to the background-subtracted measured quantity (black bars) using DTNP (mean ± s.d. for triplicate sample measurements). **B.** Biolayer interferometry demonstrates binding between MVN-Biotin and ManLAM despite reduction and alkylation. Each colored line indicates a single well of the ManLAM dilution series, having been processed with background subtracted. n = 1.

Optimization of MVN-Biotin bead surface loading using Galectin-1 as an isotype control analog.

Because the MVN reduction and alkylation were unsuccessful, we explored using another lectin as an alternative to modifying MVN directly. It was imperative to use a lectin similar in size and structure to MVN that does not bind the mannose caps on ManLAM. Galectin-1 is a ~ 15 kDa lectin that binds β−galactosides with two binding domains. It also has a relatively low isoelectric point (pI ~ 5.3, calculated using ExPASY).[348] Similar to

MVN, the Galectin-1 was recombinantly expressed with an N-terminal His tag and linker sequence. It was selected for testing as a possible MVN-isotype control lectin for these reasons.

To the best of our knowledge, there is no data in the literature demonstrating binding of Galectin-1 to the mycobacterial cell surface, but we needed to confirm if Galectin-1 could bind to the surface of BCG given its complex capsular layer. Some binding of Galectin-1 was observed on the surface of BCG as determined by flow cytometry fluorescence analysis (**Figure 6.6**). The secondary-only control sample had a measured mean DyLight® 650 fluorescence intensity of 13.2 ± 76.0, and cells stained with Galectin-1 and MVN measured 92.9 ± 93.3 and 495 ± 771, respectively. MVN bound the surface of GFP BCG (thankfully!) and produced a more significant signal than Galectin-1 staining. This difference could be partially attributed to differences in the anti-His_6-650 accessibility of the N-terminal His tag on each protein, potentially confounding the results if this were true.

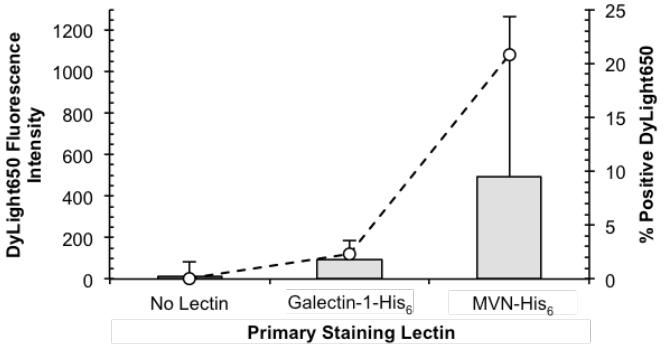

Figure 6.6. Binding of MVN-His_6 and Galectin-1-His_6 to the surface of GFP BCG through detection of the N-terminal His_6 tag on each protein. Accounting for the molecular weight difference between MVN and Galectin-1, cells were stained with a molar equivalent to that used in MVN staining. Gray bar − DyLight® 650 fluorescence intensity. (- -O- -) − % Cells positive for anti-His_6-DyLight® 650. n = 1. (GMean ± rSD).

Additionally, the observed Galectin-1 binding indicates the presence of a β−galactoside on the surface of BCG, which confounds capture experiment results and makes Galectin-1 a suboptimal isotype-analog for MVN. Rv1717 is a mycobacterial cell-wall associated β-galactosidase that breaks down an unknown substrate in the extracellular matrix.[351] The same substrate may be responsible for the signal observed, but this is purely speculative.

Despite the confounding factor introduced by Galectin-1 binding, we proceeded forward with an initial experiment aiming to optimize the surface loading density of MVN-biotin on SuperMag beads, using Galectin-1 as an isotype-analog control to assess specific vs. nonspecific binding of MVN-functionalized beads to BCG. We first

confirmed the loading of MVN-Biotin and Galectin-1-Biotin onto the surface of the AF405 SuperMag beads, as seen in **Figure 6.7**. Because the amount of MVN-Biotin or Galectin-1-Biotin varied, the difference in fluorescence intensity across surface loading density was expected. However, the difference in intensity seen between MVN and Galectin-1 beads is interesting, with lower fluorescence intensity seen for Galectin-1 beads. Because of the slight difference in molecular weight, the same number of Galectin-1 molecules were loaded onto the SuperMag beads rather than the same total mass. The minor differences between MVN and Galectin-1 explain variations in the fluorescence intensities but do not account for the up to 7-fold difference seen. This disparity suggests that the anti-His_6-650 does not have the same accessibility to the N-terminal His tag on both molecules once loaded onto the beads, but further experimentation would be required to validate this theory. It is also possible that Galectin-1 has a greater degree of biotinylation than MVN, and the practical surface loading density displays some variation. Optimizing the molar excess of NHS-Biotin used for labeling would reduce this impact.

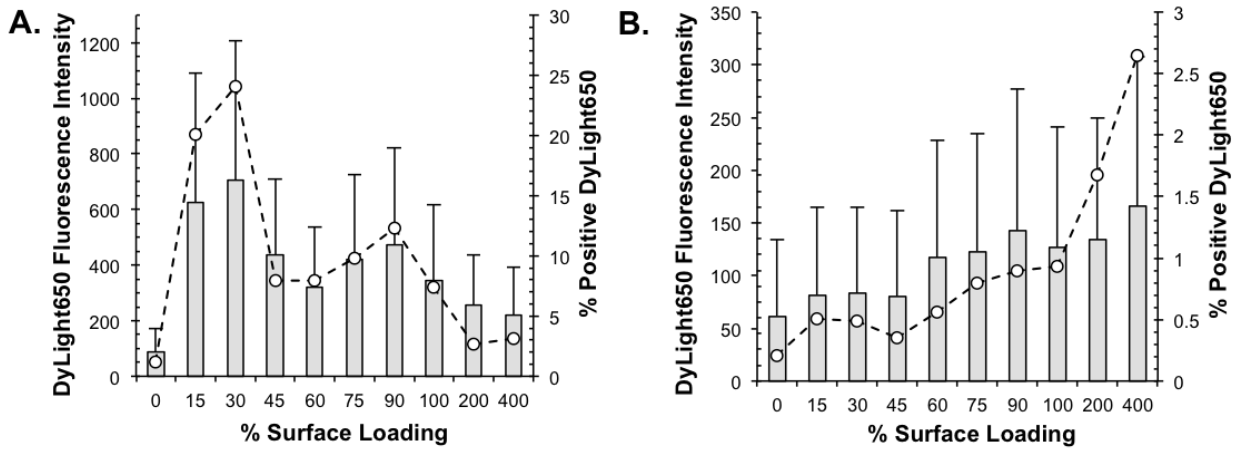

Figure 6.7. Confirmation of loading of MVN-Biotin (**A.**) and Galectin-1-Biotin (**B.**) on SuperMag 200 nm beads through detection of the N-terminal His_6 tag on each protein. Accounting for the molecular weight difference between MVN and Galectin-1, beads were loaded with a molar equivalent to that used for MVN loading. Gray bar − DyLight® 650 fluorescence intensity. (- -O- -) − % Beads positive for anti-His_6-DyLight® 650. n = 1. (GMean ± rSD).

With the confirmation of MVN and Galectin-1 loading on the surface of the AF405-SuperMag beads, both beads were used in a paired comparison assessing the impact of MVN surface loading density on BCG capture. As shown in **Figure 6.8**, varying the bead surface loading density impacted the % double-positive events by ≤6.3% within MVN and ≤4.72% within Galectin-1. Excluding the naked beads at 0% loading, the most significant

difference in the percentage of double-positive events between the lectins was at a surface loading density of 75%, with 11% MVN bead events AF405/GFP double-positive and 3.28% of Galectin-1 bead events. The least variability between the sample sets was observed at a 45% loading density, with double-positive events for MVN and Galectin-1 measuring 8.36% and 6.12%, respectively. Because of the confounding factors discussed to this point, the data presented does not provide sufficient insight into the optimal SuperMag bead surface loading density, and we cannot make any definite conclusions. After addressing the Galectin-1 confounding factors, or refining MVN reduction and alkylation, the experimental design will provide adequate information on specific vs. nonspecific binding observed as the experimental conditions vary.

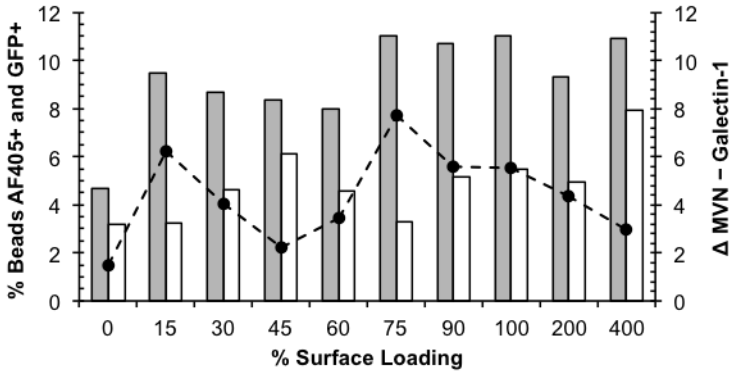

Figure 6.8. Impact of bead surface loading density on the capture of GFP BCG onto SuperMag beads loaded with MVN-Biotin (gray bars) or Galectin-1-Biotin (white bars). Difference (Δ) between MVN and Galetin-1 plotted in the line graph (- -•- -) Bead surface loading given in % coverage for MVN-Biotin, and to take into account the difference in molecular weight, Galectin-1-Biotin was loaded with the molar equivalent. See **Figure D8** and **Figure D10** for the gating strategy. n = 1. (GMean).

Discussion

This report aimed to design an *M.tb*-specific capture bead to isolate tuberculous mycobacteria, ultimately hoping it would provide a simple method for rapid differentiation between MTBC and NTM infections. By targeting LAM on the surface of mycobacteria, this highly abundant virulence factor is an excellent candidate for surface detection and immunoprecipitation, mainly when specificity is provided by different carbohydrate capping motifs on the terminal ends of LAM. Because so many anti-LAM antibodies bind the conserved structures of LAM, they do not provide specificity beyond confirmation of mycobacterial infection. Therefore, we hypothesized that we could instead use an α-(1→2)-mannobiose binding cyanobacterial lectin to specifically bind and capture mycobacteria

expressing the mannose-capped LAM associated with TB disease while leaving NTM species with phosphoinositol-capped LAM behind. However, using this lectin presented significant challenges to implementation, which made significant progress difficult with further difficulty establishing why the inconsistencies were observed. Here, we discuss the challenges encountered and possible solutions to overcome and complete the work outlined.

MVN reproducibility.

Throughout these studies, the binding of MVN to the BCG surface was highly variable and complex to consistently reproduce, and determining if the variability is an MVN problem, culture problem or both has been even more challenging. For consistency, the data presented in **Figure 6.2** only looked at titrations performed at the 1:1,000 anti-His_6-650 dilution identified during titration. However, titrations performed across secondary antibody dilutions from 1:2,000 to 1:250 showed the same inconsistencies, with MVN exhibiting high surface binding one day to showing no binding at all the next.

With our additional findings that the 24 kDa dimer binds the surface of whole cells better than the 14 kDa fragment (**Figure E4**), it may be necessary to stain cells specifically with dimerized MVN to achieve this normalization. Reserving SEC-purified 24 kDa MVN for cell staining could achieve this. Alternatively, an alkaline phosphatase sequence could be cloned into the pET-15b-MVN vector. When expressed, the single alkaline phosphatase protein attached to MVN will spontaneously dimerize with another MVN-alkaline phosphatase. One additional benefit is that the alkaline phosphatase can be used to directly quantify MVN loading into whole cells, eliminating the need for secondary antibodies. A third option would explore using the re-engineered MVN-variant LUMS1. MVN is unique from similar antiviral lectins because it exists as a monomer. Shahid *et al.* used cloning to modify the low-affinity binding domain B, replacing it with the sequence found in the high-affinity domain A. The modification of domain B increased the sequence identity between the domains from 35% to 100%, changing the binding stoichiometry for α-(1→2)-mannobiose glycan from 1:1 to 2:1.[349]

In addition to the issues with MVN surface binding, we could not determine if there was a pattern between culture conditions and MVN surface binding. For example, one experiment showed that stationary cultures did not bind MVN, but cultures grown on a shaker did (data not shown). However, many times the shaken cultures showed no surface binding of MVN. Sometimes, cultures that were 10-14 days out from their last split and feeding showed MVN surface loading, while others were only three days out; but most of the time, there was minimal surface

loading of MVN onto the BCG surface. Arabinomannan expression in *M.tb* and BCG is a highly dynamic process,[90] and a study likely needs to be designed and performed specifically to assess how culture conditions impact MVN surface binding. Using a pH indicator to monitor cultures for waste accumulation via acidification is an easy method to collect more information that aids in determining if culture conditions are partially responsible for influencing MVN surface binding. For example, *M.tb* has a narrow range for growth between pH = 6.2 and pH = 7.3 with significant impacts on growth and viability observed at pH = 5.0 and pH = 8.4,[352, 353] and BCG exhibits similar growth attenuation at similar pH ranges.[354] Two solutions of pH indicators, bromothymol blue (dynamic range pH = 6.0−7.6) and cresol red (dynamic range pH = 7.2−8.8), could be mixed with an equal volume of culture media for a colorimetric pH estimate.

In addition to the issues observed with inconsistent surface loading, we also observed long-term stability issues with MVN that impacted study progress. The study by van der Horst *et al.* demonstrated no change in the equilibrium dissociation binding constant after 100 days of storage in the fridge. However, we observed that MVN Pool 3 had no activity directly out of the freezer, and Pools 1 and 2 lost their activity after 10-14 days at 4°C, which was confirmed using biolayer interferometry (data not shown). The same technician performed these independent preparations using the same protocol at the Vanderbilt Antibody and Protein Resource Core. Looking across multiple preparations of MVN, we hypothesize that the purity of the MVN directly impacts its stability. Specifically, the MVN used in this report had a calculated purity of ~5%, calculated using the SDS-PAGE densitometry quantification for the MVN monomer concentration and the A280 total protein content measured on a Nanodrop™ (**Figure D1** and **Figure D2**). Even when we expressed and performed a version of the IMAC-only purification (protocol available in Appendix E) and achieved ~10% purity, MVN still lost its ManLAM-binding activity after a few weeks. Upon addition of SEC purification following IMAC, the MVN purity was >90%, and we no longer observed these stability issues, as confirmed on biolayer interferometry.

Dr. Megan van der Horst kindly gifted some of the purified MVN assessed in the van der Horst *et al.* study, and consistent with their results, we did not have any stability issues with it, and the MVN maintained activity past 14 days in a parallel analysis. Assessing the reported concentration of MVN relative to the total measured protein, we found that the van der Horst *et al.* MVN was ~25% pure. We also know through personal discussion with Dr. van der Horst that the study initially used an entirely different preparation of MVN, also expressed by the Vanderbilt Antibody and Protein Resource Core by the same technician using the same protocol also did not experience any

stability issues. While we do not have the total protein concentration on the other van der Horst *et al.* prep, we know from SDS-PAGE that the concentration of MVN monomer isolated was 3-fold higher than that isolated for our studies.

Assuming MVN purity is to blame, it raises the question: why is there variation between these preparations of MVN if they were prepared in the same way by the same person? We hypothesize that it relates explicitly to when and how the MVN was prepared. Through these discussions, we know that the initial preparation of MVN (not published in the van der Horst *et al.* study) was produced in July 2018, making it the first preparation of MVN by the Vanderbilt Antibody and Protein Resource Core. Because the same column should not be used to purify different proteins, the Core would have purchased a brand new IMAC column. The MVN used in this report was purified later in November 2018. Because IMAC columns are usually reused for the same protein, we believe the column was not adequately cleaned before reuse, and contaminants remaining from the prior purification could have made it into our preparation. Specifically, those skilled in the art know that insufficient chelation, washing, and recharging of the IMAC column can leave contaminants behind. Properly cleaning the resin involves using high-concentration imidazole, EDTA, and denaturing agents, and not every manufacturer suggests cleaning them between every single preparation. Some individuals will go so far as to remove the upper 1-2 mm of column material on the inlet side if the sludge cannot be removed. When van der Horst *et al.* went back in 2021 to acquire a new MVN preparation, even if the old column remained, after two and a half years, it would be ill-advised to try and chelate, recharge, and reuse, so a new, clean, and unused column would have been necessary for completing the new preparation. Our hypothesis that the IMAC column contained contaminants from the previous preparation is purely speculative. It cannot be confirmed, but we believe it is a reasonable explanation given the infrequency with which the Vanderbilt Antibody and Protein Resource Core recombinantly expresses and purifies proteins in *E coli*. Using a secondary chromatographic method for further purification would also remove most contaminants, as we saw with IMAC and SEC in combination.

MVN reduction and alkylation.

Though the reduction and alkylation of MVN were not entirely successful in disrupting the mannose-binding domain, the 100-fold decrease in binding affinity for ManLAM demonstrates promise that should be further explored for completion of an MVN isotype-analogous control. Specifically, the sample MVN used in this report

was only 5% pure, determined by comparing the SDS-PAGE quantification of MVN-His_6 band to the total protein measured via A280 on a Nanodrop™ Spectrophotometer ND-1000. These contaminating proteins likely interfered with complete MVN reduction and were reduced instead. Even though reduced MVN-Biotin still exhibited binding to ManLAM, the measured equilibrium dissociation constant was two orders of magnitude lower than untreated MVN-Biotin. Using SEC following IMAC purification will significantly improve the sample purity, as we saw an improvement in purity of the 14 kDa fraction to >90% following SEC (**Figure E2**) in our studies related to the impact of pre-processing on LAM surface accessibility (see Chapter 5). This high-purity MVN would provide more evident results on the impact of TCEP reduction and NEM alkylation of MVN-Biotin binding to ManLAM. It is possible that separating the insoluble fraction from the soluble fraction (**Figure D7C**) and performing independent alkylation and analyses could have changed the results on biolayer interferometry since the precipitated fraction contains the majority of the reduced proteins. However, the contaminating proteins were more concentrated and would continue to interfere with analysis and downstream use.

Galectin-1.

In addition to the reduction and alkylation of MVN, we investigated using a non-mannose binding lectin with a similar molecular weight, isoelectric point, and N-terminal His tag as an alternative isotype analog. While the initial results suggest this is a promising route, some Galectin-1 did bind the BCG surface. The fluorescent signal intensity observed was less than that seen for MVN staining; this confounding factor makes Galectin-1 a non-ideal candidate without further experimentation.

Galectin-1 binding can theoretically be blocked with lactose, the minimal carbohydrate ligand necessary for binding. A competitive binding assay containing 50 mM lactose (after pre-blocking lectin-functionalized beads in 150 mM lactose)[355] and BCG may prevent Galectin-1 binding to BCG and not inhibit MVN binding. If this were performed, it would be necessary to account for the potential hypertonicity from adding a high lactose concentration to 1x PBS. Therefore, it would be necessary to reduce the sodium chloride concentration to match the osmolarity of saline.[355] It is also known that galectins generally bind with a higher affinity to complex carbohydrates and lower affinity for disaccharides such as lactose, so there are likely better alternatives.[355, 356] There is also the option to explore other lectins in place of Galectin-1. However, the high carbohydrate content on the cell surface means it is likely that binding will also happen for the newly selected lectin, and the problem will not be solved.

If lactose blocking of Galectin-1 did sufficiently reduce binding to the BCG surface, there is still the issue that differences in accessibility of the anti-His_6-650 antibody on each lectin could be confounding the expression level results. Differences in the fluorescence intensity for SuperMag loading of molar-equivalent matched MVN and Galectin-1 suggest this is a definite possibility. Direct functionalization of MVN-His_6 and Galectin-1-His_6 with a fluorophore or other reporter molecule would eliminate the potential bias introduced from a difference in His tag accessibility, with the caveat that the functionalization protocol would need to be optimized to ensure both proteins have the same number of fluorophores on them. The degree of functionalization could otherwise vary and impact the total measured fluorescence because Galectin-1 would have more fluorophores per molecule.

There also remains the potential difference in the degree of biotinylation pf MVN and Galectin-1, which impact the surface loading of the two molecules. Specifically, MVN contains two available amine groups for NHS modification (N-terminal amine and single ε-amine lysine R-group), but Galectin-1 contains eight ε-amine lysine R-groups in addition to the N-terminal amine. While conjugation buffer pH can be adjusted to modify the N-terminus preferentially, it is not a perfect system, and ε-amine lysine R-groups can still be modified. Using a kit, such as the Pierce™ Biotin Quantitation Kit (ThermoFisher, 28005), to measure the degree of biotinylation at different treatment concentrations would provide quantitative information for optimizing lectin functionalization. This same optimization protocol would also apply to fluorescent modification, but the biotin should be attached using the same covalent modification chemistry and linker found on the desired reporter molecule label (e.g., NHS-PEG_4-Fluorophore labeling, with parallel labeling using NHS-PEG_4-Biotin).

Nonspecific binding to the bead surface.

One significant barrier that remains and has persisted across bead-based separations of bacteria is the issues with nonspecific binding. Even if specific immunoprecipitation using MVN-functionalized beads is successful, these advances would be entirely negated by nonspecific interactions with the bead surface. We found in independent experiments that passive blocking of the bead surface before and during cell capture with detergents, protein blocking agents such as bovine serum albumin or nonfat dry milk, changing the pH and salinity of buffers, and other blocking compounds such as polyvinyl alcohol (molecular weights ranging from ~9,000 to >200,000) and polyethylene glycol (chain lengths ranging from 200 to >20,000 repeats) does not solve the nonspecific binding problem (data not shown). Therefore, the successful implementation of this bead design hinges on developing a

"non-stick" bead, particularly given the heterogeneity and the high number of contaminants found in patient sputum. The design would critically depend on complete and uniform coverage with a molecule known to serve well as a blocking agent, such as polyethylene glycol or dextran-based organic polymer coatings,[357, 358] with the final conjugation molecule located at the outer end of the polymer coating. Because it is well-known that streptavidin can contribute to nonspecific binding, neutravidin or avidin may reduce nonspecific interactions because of their different isoelectric points. Using a covalent attachment instead of streptavidin-biotin affinity to load MVN onto the outer polymer would eliminate potential streptavidin-contributing nonspecific interactions.

Future Work

To summarize, the following experiments are needed to complete the studies described here:

- Use pH indicators to more closely monitor culture conditions and reduce potentially detrimental variations caused by waste accumulations.
- Create flow cytometry standard curve for quantification of mCherry *M. smeg* for accurate quantification using OD700 instead of OD600.
- Re-titrate NHS-AF405 on SuperMag beads to reduce self-quenching, increase fluorescence intensity, and improve the difference in population fluorescence intensity more defined.
- Create the MVN isotype control. Designing a competitive binding assay with lactose to prevent Galectin-1 binding to BCG may be one method to achieve this. It could also potentially be achieved by further purifying MVN using SEC following IMAC and performing a titration to optimize the concentrations for TCEP reduction and NEM alkylation.
- If Galectin-1 became the final isotype control, control the degree of biotinylation to match that of MVN-Biotin. Directly conjugate MVN and Galectin-1 with a reporter molecule to eliminate possible variation in the N-terminal His tag accessibility between the proteins.
- Titrate MVN binding to BCG surface. Explore creation and use of artificial MVN-dimers or re-engineered MVN-variant LUMS1.
- Repeat optimized anti-His_6-DyLight® 650 staining protocols on beads and bacteria with anti-DDDDK-DyLight® 650 isotype control antibody for scientific accuracy and integrity.

- The optimization of MVN-Biotin surface loading density must be completed upon validating an MVN isotype control.
- Optimize the number of capture beads and binding time for maximal BCG capture and compare this to the negative control MVN isotype bead.
- Upon completion of optimization, perform MVN surface staining and capture experiments using mCherry *M. smegmatis*.
- Perform MVN-bead capture from a mixture of BCG and *M. smegmatis*. Specific capture of BCG from a mixture of BCG and *M. smeg* would further solidify the specificity of the MVN-bead.
- Perform secondary analysis of flow cytometry samples to support further the specificity of MVN capture beads and the interactions seen between BCG and MVN-beads. Capture beads could be sorted and saved during cytometric analysis, and PCR and fluorescence microscopy could be used as secondary confirmation methods to verify capture specificity. PCR primer sets from Talbot *et al.*[359] and Plikaytis *et al.*[360] and gel electrophoresis could confirm BCG or *M. smeg* genomic DNA from the sorted samples, respectively.

Acknowledgments and Funding

We also thank Dr. Raymond L. Mernaugh for insightful discussions. The authors thank Dr. Carole Bewley, Dr. Megan van der Horst, Michael Niederweis, Young-Hwa Song, BEI Resources, and FIND for the reagents gifted for use in this manuscript. The authors thank the Vanderbilt Antibody and Protein Resource Core for expressing and purifying the MVN used in this study. Flow cytometry experiments were performed in the Vanderbilt Flow Cytometry Shared Resource Core. The Vanderbilt Flow Cytometry Shared Resource Core is supported by the Vanderbilt Ingram Cancer Center (P30 CA068485) and the Vanderbilt Digestive Disease Research Center (DK058404).

This work was funded in part by the US National Institutes of Health Grant No. R01-AI135937.

CHAPTER 7 : CONCLUSIONS AND FUTURE DIRECTIONS

Summary and Integration

The work presented in this dissertation designed and tested new solutions to obstacles that currently prevent effective TB diagnosis at the point-of-care in parts of the world with limited healthcare infrastructure. The goal was to design an assay with a diagnostic sensitivity of >85% and diagnostic specificity of >95%, equivalent to the reported values for the WHO-endorsed MTB/RIF assay, while also designing the tests to meet WHO's ASSURED criteria: **A**ffordable, **S**ensitive, **S**pecific, **U**ser-friendly, **R**apid and/or **R**obust, **E**quipment-free, **D**eliverable.

The first barrier identified a lack of molecular techniques for TB diagnosis at the POC, specifically nucleic acid-based testing. While independent of the first obstacle, the other identified problems support the need for improved non-genetic molecular detection techniques at the POC. The poor diagnostic sensitivity of sputum smear microscopy is the second identified obstacle because it is the most widely accessible method for diagnosis but misdiagnoses approximately half of TB cases as false negatives. Because there are no molecular tests available at the POC, and conventional microscopy has multiple diagnostic limitations, the complete absence of methods available for POC differentiation between TB disease and NTM infections is the third problem identified. MTBC and NTM infections require different antibiotic treatments, and both have serious health consequences if not treated. Identifying possible solutions to these three issues continues to be critical for reducing TB reservoirs and ultimately complete elimination of TB.

In Chapter 3, I tackled the first challenge by developing a nucleic acid extraction method based on high-gradient magnetic separation. This method is **A**ffordable, using readily available bulk transfer pipettes and steel wool; **E**quipment-free, relying on only a stationary magnet for performing extraction while not needing specialized reagent storage; and is **U**ser-friendly and can be **R**apidly performed by someone with little training in 15 minutes. In addition, the method recovered comparable quantities of cell-free DNA as two commercially available nucleic acid kits for both sputum and urine. Additionally, this method was adapted for total nucleic acid extraction from blood, sputum, and stool, which was implemented in a nucleic acid extraction challenge with the CDC and the Bill and Melinda Gates Foundation; our method outperformed three other commercially available methods in this challenge because of its superior **S**ensitivity, **S**pecificity, and ASSURED-based design. It also recovered more nucleic acid per sample volume used than any other group. In addition, I characterized the impact of various physical system

characteristics that may be of interest to those looking to adapt the method to other applications. With these characterizations, I demonstrated that HGMS-enabled extraction improved sample handling for the user for both large-volume and viscous samples. The system was **R**obust to user variability, with no observed difference in performance between users regardless of training. Publication of this work in *ACS Applied Materials and Interfaces* makes this the first publication to our knowledge to use HGMS to perform total nucleic acid recovery for infectious disease diagnostic purposes.

In Chapter 4, I focused on addressing issues with microscopic sputum inspection and used the principles of microfluidic flow in evaporating droplets to autonomously spatially concentrate TB bacteria into a significantly smaller inspection area prior to staining and microscopy. The system needed to be designed around the physical characteristics necessary for the spatial concentration, but the assay also needed to integrate with Ziehl-Neelsen staining and microscopic inspection, **A**ffordable reagents, equipment, and protocols already **D**elivered and performed at the POC. I confirmed that inward-oriented Marangoni flows were responsible for the spatial enrichment achieved using OCT and microscopy. Spatial concentration was **R**obust, with particles and bacteria reliably depositing in the center of the evaporating droplet independent of droplet size and particle size and shape in scale trials. With most of the sample concentrating in the innermost portion of the droplet, spatial concentration was up to 45x, making the protocol more **U**ser-friendly by pre-defining and reducing the total inspection area. When this **E**quipment-free method was combined with simple magnetic volumetric concentration, samples were enriched at least 100-fold, detected TB in samples containing 10x fewer bacteria than the current LOD for direct smear microscopy; a significant step for improving the **S**ensitivity of the technique. The use of magnetic nanoparticles smaller than the diffraction limit of light for volumetric concentration reduced visual interference of the bacteria by the nanoparticles, something that other magnetic bead-based methods have failed to overcome while making microscopic inspection more **U**ser-friendly. Publication of this work in *Diagnostics* is the first of its kind to use known models of microfluidic flows in an evaporating droplet to spatially concentrate whole-cell pathogens for disease diagnosis.

In Chapter 5, I characterized several LAM recognition elements for their specificity to LAM found on fast-growing and slow-growing species of mycobacteria. LAM is of interest to TB diagnostic researchers because it is highly abundant on and shed from the surface of mycobacteria, and the carbohydrate-capping motif of LAM is species-specific. Existing LAM-based assays have low specificity because they cannot differentiate between TB and

NTM infections. Furthermore, without an adequate test, ~10% of patients with TB were misdiagnosed and instead had an NTM infection, delaying appropriate treatment. If these recognition elements were shown to bind the carbohydrate cap, they could improve the **S**pecificity of new and existing assays. For these reasons, this information would interest TB researchers developing molecular diagnostics using LAM as the chosen biomarker, especially because specific and quantitative kinetic binding information to ManLAM and PILAM was collected using biolayer interferometry.

I then used these LAM recognition elements to investigate the impact of different mechanical and enzymatic dissociation methods on total cell recovery and LAM surface accessibility using gamma-irradiated *M.tb* cultures. Those skilled in the art of mycobacterial culture understand how much the bacteria clump in suspension, forming 2-3 mm diameter clumps that must be dispersed to simulate anything clinically relevant, or if single bacilli are needed. Before this study, while it was known that chemicals, mechanical force, and enzymes could impact the surface of *M.tb*, no specific information was published in the literature. Because cell dissociation is required for in vitro use, I believed information on the impact of these processing methods on cell surface markers would interest TB researchers. I found that mechanical dissociation was more efficient at liberating cells from large clumps formed in culture and improving LAM accessibility on the cell surface. Enzymatic digestion with trypsin, amylase, lysozyme, and lipase did not liberate cells from clumps and did not significantly improve LAM accessibility on the *M.tb* surface. Centrifugation speed and repetition had varied impacts on surface feature detection, though mannosyl caps on ManLAM were impacted more frequently than the conserved arabinan backbone. Upon publication, this work will be the first standardized report quantifying the impacts of these processing methods on TB surface marker ManLAM.

As part of the investigations into new LAM recognition elements, I investigated the binding of novel cyanobacterial lectin, microvirin-N, to the surface of *M.tb*. With only a single publication describing potential applicability for improving urinary LAM detection specificity, no published investigations demonstrate MVN binding to ManLAM whole cells. Interestingly, while MVN is highly **S**pecific, has a high binding affinity for ManLAM, and does not bind PILAM in a system using purified biomolecules, any amount of enzymatic or mechanical processing significantly reduced MVN binding to ManLAM on the surface of *M.tb*. To clarify why MVN fails to bind *M.tb* reliably, major 14 kDa MVN monomer species of MVN was isolated from the minor 24 kDa dimer using size exclusion chromatography. In a parallel analysis, it was evident that MVN dimerization

significantly improved binding of MVN to ManLAM on the cell surface compared to the monomer. This is likely the case because monovalent MVN only has a single ManLAM binding site, but studies are needed to confirm this hypothesis. Finally, understanding why MVN did not consistently bind to the *M.tb* cell surface, further development can be made towards a TB diagnostic using MVN for bacilli capture from sputum. In Chapter 6, I detailed work performed toward developing an *M.tb*-specific MVN-functionalized capture nanoparticle. I also detail the barriers and work that remain to bring this project to completion.

With these four chapters focusing on different but potentially related aspects of improving TB diagnosis at the point-of-care, future work could encompass the complete integration of all methods discussed. Completing the TB-specific nanoparticle functionalized with MVN or another ManLAM-specific recognition element would improve the **S**pecificity of magnetic volumetric and spatial concentration of bacilli using Marangoni flows, methods reduce the labor required for microscopic inspection to make it more **U**ser-friendly. Based on the preliminary results, these concentration techniques are also likely to show a **S**ensitivity improvement of sputum smear microscopy with further testing and refinement. Further, using HGMS to rapidly perform volumetric concentration from patient sputum would significantly reduce the processing time of samples and provide a method to easily contains aerosols during parallel processing of different patient samples, ultimately making the method a more **U**ser-friendly process. Because HGMS is not volume-limited, the entire patient sputum sample, which averages 3 mL in volume but can be up to 8 mL could be used, a strategy that could further improve the sensitivity of sputum smear microscopy; with literature supporting that increasing the sputum volume to five milliliters increases the sensitivity of sputum smears.[67] This combined approach will likely improve the limit-of-detection of sputum smear microscopic inspection with refinement. Furthermore, the fact that HGMS volumetric concentration and Marangoni flow spatial enrichment are **E**quipment-free and make use of reagents and materials already **D**elivered to the POC means the combined assay is more likely to be adopted and make a significant impact for patients seeking TB diagnosis.

In addition, HGMS-enabled nucleic acid extraction from large volume urine extractions (≥ 200 mL) could potentially improve IS*6110*-fragment isolation and detection in urine beyond HIV+ patients, a limitation that the Haselton Group previously reported in initial clinical studies of a different volume-limited nucleic acid extraction technology.[211] Other urine-based TB assays have also shown limited efficacy, only providing significant benefit for

TB/HIV co-infected individuals with advanced immunosuppression (CD4 counts ≤100/μL) or in individuals that are severely ill or malnourished.[213, 221]

Limitations and Recommendations

Some shortcomings of the work presented in this dissertation are important to highlight, as they are essential for addressing significant gaps in care. Broadly, this work used idealized or simulated samples for proof-of-principle studies, which do not contain the same biological variability or contaminants seen in clinical samples. The ideal samples were not blinded, making any diagnostic sensitivity or specificity determinations significantly biased. Actual patient samples may not perform as well as the simulated samples presented here, and testing is needed to determine method implementation in clinical point-of-care settings. Nucleic acid extraction and the blinded sample preparation challenge using human sputum, blood, urine, and stool demonstrate that the HGMS-enabled extraction is compatible with patient samples.

Identification of latent tuberculosis.

Initially, I identified the complete lack of TB diagnostics available for LTBI diagnosis, and the methods I describe here rely on patient samples from individuals with ATB disease. Currently, the only methods available for LTBI diagnosis measure patient immune responses. However, as discussed, the TST can result in false-positive diagnoses when used alone in patients that have received the TB vaccine, and IGRA assays require a 24 hour incubation period in addition to the hand-on time and equipment needed to perform the assay. Since latent TB means patients have what is described as undetectable bacterial loads, until understanding latent TB and its pathogenesis is expanded, looking at the immune response is the only viable method for effective diagnosis.

Lateral flow assays are usually ASSURED criteria compliant and can be read and quantified using a smartphone or lateral flow reader. Because IGRA assays use antibody-based detection methods quantify the increased expression of IFN-γ from T-cells after exposing patient blood to TB antigens, future work could focus on adapting current methods using lateral flow assays as the readout method in place of, for example, the enzyme-linked immunosorbent assay used for QuantiFERON®-TB Gold. To achieve this assay adaptation, an antibody that binds IFN-γ (anti-IFN-A, raised in rabbit, mouse, goat, etc., but not human) could be functionalized with a hexahistidine tag and loaded onto IMAC magnetic beads through the formation of coordination bonds between the

His-tag and the column's metal ion. Following incubation of the patient's blood with the TB-specific antigens, these anti-IFN-A beads would capture, concentrate, and wash IFN-γ from the patient sample. Imidazole disrupts the coordination bonds formed between the His-tag and chelated metal ion, which releases the antibodies and bound IFN-γ from the bead surface. The concentrated sample could be mixed with gold nanoparticles functionalized to an orthogonal binding pair of anti-IFN-A (anti-IFN-B, raised in a different species from anti-IFN-A, but not human), creating an antibody sandwich. This sample mixture would then be applied to the lateral flow. A secondary antibody that binds to anti-IFN-A would be used for the test line and would be positive if a sandwich forms between anti-IFN-A + IFN-γ + anti-IFN-B. The control line would be a secondary antibody against anti-IFN-B. The smartphone or lateral flow reader would image the lateral flow for colorimetric quantification of the amount of IFN-γ in each control, negative, and test samples to determine if a patient has an adequate immune response for TB diagnosis.

Unfortunately, this proposed method would not solve the 24 h incubation step required for IGRA testing. However, simply by reducing the current barriers for assay implementation, a clear path is created for researchers to assess if the incubation step may be shortened or modified to make it accessible at the POC. In addition, if volumetric concentration could enhance the IFN-γ signal seen in treated samples, it may be possible to adapt the assay for incubation at ambient temperature instead of 37°C or reduce the incubation time by increasing the LOD of IFN-γ across the entire assay. Even if these modifications resulted in some reduction in diagnostic sensitivity compared to the manufacturer protocol (QuantiFERON®-TB Gold ≤92%;[234] T-SPOT®.TB ~97%),[236, 237] the fact that any method is available at POC for diagnosis of both LTBI and ATB disease, and would only require a simple blood draw, would still significantly improve what is currently available.

Problems with HGMS-enabled nucleic acid extraction.

In the blinded Bill and Melinda Gates Extraction Challenge, diagnostic sensitivity and specificity were assessed for both DNA- and RNA-based pathogens; samples were spiked with known concentrations of these inactivated pathogens in blood, sputum, or stool. For influenza extracted from sputum and MS2 bacteriophage and *S. pneumonia* extracted from whole blood, the sensitivity was at least 85%. For *M.tb* extracted from sputum and MS2 bacteriophage and *S. typhimurium* extracted from stool, the diagnostic sensitivity was below the target 85% sensitivity criteria outlined in this dissertation.

All extractions had a diagnostic specificity of 100% except for influenza extracted from sputum, which had a reported specificity of 93%. This decreased specificity and single false positive seen is consistent with a noted internal spike our group placed in two individual samples for our independent testing. One of those samples was coincidentally this false-positive sample, which we determined during post-analysis discussions with the Gates Foundation. This error is unfortunate for determining the final test specificity, and an unbiased analysis must assume this was accidental sample contamination. Nonetheless, some extractions did not meet the defined success criteria, demonstrating room for improvement. In addition, sufficient DNA is needed not just for accurate diagnosis but for accurate determination of antibiotic resistance. Additionally, low-concentration positive samples were misidentified as false negatives, further validating the need for improved extraction methodology, particularly in samples with low bacterial loads. Immunocompromised patients and children are most likely to have low bacterial loads, and they are also the patient populations disproportionately impacted by the lack of available and effective TB diagnostics at the POC.

Since the test sample extractions used small volumes of ≤100 μL, the most efficient method for improving diagnostic sensitivity for each extraction method would be to increase the sample volume used. HGMS is known to work well with large sample volumes, making the use of larger patient samples a non-issue for future developers. The number of beads and extraction buffer volumes may require re-optimization or changes to the formulation, though guanidine-based extraction chemistry is well studied and easily adapted to larger volumes; it does have the drawback of being hazardous and difficult to dispose of, however. In addition, lyophilizing water-soluble reagents in the transfer pipette bulb would reduce the dilution factor of large sample volumes during extraction. For example, lyophilized reagents would be beneficial when extracting from urine because it is already a large, dilute aqueous sample that would become even more difficult to handle if the volume increased. Initial studies presented here used stock concentrated 4 M guanidine thiocyanate solutions and pure alcohols to dilute the sample by at least 7.5-fold before concentrating, and removal of the liquid volume containing guanidine salts and silica beads reduces the volume increase to 4-fold from the original sample volume while maintaining the high salt concentrations necessary for extraction. Removing this water volume from the extraction buffers would also reduce reagents' shipping and packaging costs and the space occupied for storage at clinical sites.

Implementation of nucleic acid-based diagnosis, which generally requires the amplification of nucleic acids, will require the development of amplification strategies that completely mitigate these infrastructure

problems. While the HGMS-enabled nucleic acid extraction method provides an inexpensive method for nucleic acid isolation, it does not overcome the issues of intermittent electricity or lack of access to PCR equipment needed to perform the final step of nucleic acid amplification. Solutions to this amplification problem are beyond the scope of this dissertation, but solutions are currently in development. Lateral flow assays provide an alternative method for detection because they do not require expensive optical and thermal hardware but fail to perform well as a diagnostic tool without nucleic acid amplification. FISH also provides an amplification-free method of nucleic acid detection but requires access to fluorescence-reading equipment that is not widely available. The use of loop-mediated isothermal amplification (LAMP) may provide a reduction in the instrumentation requirements but still does not provide a permanent solution to issues stemming from an overall lack of basic infrastructure. Developing a handheld PCR or LAMP machine with independent backup batteries and an onboard computer is one potential method to improve accessibility. The included battery could be recharged using an external gas generator, solar panel, or the electrical grid during the limited periods it does provide power. Recombinase polymerase amplification can be performed at ambient temperature, albeit at a slower reaction rate, and may provide a more accessible amplification method that does not require fancy equipment or electricity.

Problems with Marangoni flow-based diagnostics.

There are two significant concerns with the current iteration of the Marangoni flow-based spatial concentration system that must be adequately addressed before clinical use, with the first issue being the length of the assay. Using nanoparticles smaller in size than the diffraction limit of light for volumetric concentration was critically important for microscopic sample visualization. However, nanoparticles are challenging to work with, mainly when performing magnetic separations. Their low magnetic susceptibility means a strong magnetic field is needed for efficient and rapid separation, and stationary magnets fail to provide the necessary field strength. As a result, a minimum 30 minute separation period was necessary between each step of volumetric processing, significantly increasing the length of the protocol.

When a sample, such as sputum, has a high viscosity, the separation time is even longer because the magnetic force applied to the particle needs to be strong enough to overcome viscous body forces from the sample. In some cases, separation may be downright impossible. Therefore, future iterations of this assay should use a high-gradient magnetic separator optimized for bacilli capture and concentration from sputum. The sharp edges of steel

wool and tight packing density could damage cells or make it difficult to efficiently recover the nanoparticles in small wash volumes, so steel wool coatings or alternative fluid manipulation strategies should be considered if the transfer pipette separator does not work this application.

In addition to the lengthy separation times, the 50 μL droplet volume used during spatial concentration takes hours to dry before performing staining and microscopic inspection. While heating the slide or incubating the sample at a higher temperature could expedite drying, it will also impact particle deposition and flow patterns, making this an unlikely solution. Instead of inspecting the deposition area of one large droplet, dividing the purified sample into smaller droplets could significantly decrease drying time. In this alternative design, multiple deposition regions would need to be inspected instead of one particular area. Unfortunately, this protocol change could increase the tedium of inspection, effectively creating the same problem this solution was trying to solve. However, the amount of time searching for each small deposition area is easily remedied by printing a grid on the back of the microscope slide and explicitly defining where to look for the sample. Microscope slides with predefined wells, created by coating specific slide regions. Commercially available slides coated in PTFE polymer exemplify what this design change proposes. It is easy to know where a sample is or is not located when PTFE blocks the microscope's light path. In addition, multiple smaller droplets instead of a single large droplet may improve assay sensitivity and the LOD, a phenomenon seen in microarray assays.

Second, the orientation of the Marangoni flows relies on the thermal conductivity of the droplet solvent and substrate, and the final deposition pattern relies on that specific flow direction the resulting surface tension gradient of the droplet. In the proof-of-principle studies, cells were prepared in buffer, and while Marangoni flows can be robust to some contaminants, such as salts, compared to the coffee ring effect, the presence of detergents or proteins can significantly change microfluidic flow fields and particle deposition patterns.[139, 150, 290] Given that this dissertation focused on developing and improving sample preparation methods, the significance of biomarker cleanup before detection does not need to be stated. When used in complex clinical samples, efficient cleanup of nanoparticles prior to recovery will be critical for the reliable formation of Marangoni flows. It will be necessary to explore new diluent or wash buffer chemistry, processing volumes, repetition, etc., to ensure the nanoparticles do not carry contaminants into the purified sample while also ensuring *M.tb* remains bound and intact.

As stated, high-gradient magnetic separation could make sample processing using nanoparticles more straightforward. However, difficulties observed with thoroughly removing captured nanoparticles in a small buffer

volume require the addition of detergents well above the 0.01% Tween-20 listed in the current solvent recipe. However, solving the sample recovery dilemma this way also creates a conflicting problem because, as we know, the added detergents will change Marangoni flows and deposition patterns in the evaporating droplets. There is no perfect solution to this predicament, and I cannot explicitly identify which design trade-offs are better than the others since some plausible solutions still need to be exhaustively explored and tested. Based on my understanding, a complete redesign of the HGMS matrix and fluid handing, such as those made for MACS columns, is more likely to solve this conflict than negating detergents' impact on flow fields by diluting or removing them. Increasing the recovery volume used for particle removal from the matrix is another alternative, but the volumetric concentration achieved using magnetic separation is negated. Careful and well-planned design changes and experimentation would provide the information necessary to find a compromising solution.

The 200 nm nanoparticle diameter makes it physically impossible to visualize each particle under the microscope using the white-light wide-view microscopes available at the POC for microscopy, side stepping the need to remove bacteria from the particle before microscopic inspection and the associated polyvalence issues that make *M.tb* release from the particle extremely difficult. However, the bulk population can obscure bacteria because the iron-containing particles are brown and not optically clear. The number of particles used for BCG capture was explicitly chosen to prevent this from happening. For maximal assay performance, the quantity of particles used in an immunoprecipitation assay should ideally optimize biomarker recovery, not microscopic visualization. Therefore, bulk particle density could obscure *M.tb* visualization, and designs to the Marangoni spatial concentration would be necessary before implementation. The use of multiple smaller droplets instead of one large droplet, as suggested, could solve this problem. An alternative solution could use smaller diameter nanoparticles, but reducing the particle size too much more and reducing the iron content may decrease the particle's magnetic susceptibility so much that they cannot be separated even with HGMS.

Problems with MVN as a diagnostic tool.

Identifying possible species-specific molecular recognition elements provides the first step towards a molecular test to determine if a patient is sick because of an NTM infection or TB disease, but it does not deliver a product that addresses this need. Progress completed towards the delivery of a TB-specific nanoparticle functionalized with MVN were detailed, and the work needed for completion is outlined in this dissertation, with the

goal that another researcher can complete this work. Given that the MVN 24 kDa dimer showed a higher relative amount of binding compared to the 14 kDa MVN, it is possible that creating artificial MVN dimers could improve surface binding. One option to achieve this is to add a single alkaline phosphatase subunit to MVN through cloning. Alkaline phosphatase spontaneously dimerizes in vitro, and therefore would create MVN dimers upon expression.[361] In addition, with fluorescent, colorimetric, or luminescent alkaline phosphatase detection reagents, there would be no reliance on secondary detection antibodies. Shahid *et al.* also recently engineered a variant of MVN containing two identical structural binding domains,[349] and while more preliminary work is needed to determine if the additional binding pocket improves binding to whole *M.tb* cells, potential for use of MVN use in whole-cell diagnostics remains.

Because MVN binds α-D-Man*p*-(1→2)-α-D-Man*p* carbohydrate linkages found on biomolecules other than ManLAM, MVN alone as a TB detection agent would not provide adequate assay specificity for TB diagnosis. On its own, visualizing a cell that is similar in size and shape to *M.tb* and binds MVN does not mean *M.tb* is causing the infection, and further confirmation is needed to ensure accurate diagnosis and treatment. Therefore, an MVN-based diagnostic needs to be paired with a secondary confirmation assay, such as highly specific ZN staining. Using a two-test combination to ensure adequate sensitivity and specificity for a diagnosis instead of one is recommended if the tests meet the WHO ASSURED criteria. Often a three-test combination is needed for case detection of HIV at the POC, so a third method for definite TB confirmation would not be unwarranted under specific conditions, especially if that third test could also provide information on drug susceptibility/resistance.

Problems with nonspecific binding between mycobacterial cells and capture particles.

One problem repeatedly observed throughout this work and has been by other researchers was the nonspecific binding of mycobacteria to capture particles. The nonspecific binding is likely a result of charged interactions between mycobacteria and polymers in the particles. As stated, it is a well-known problem, and it continues to be a barrier for developing an *M.tb*-specific whole-cell capture particle. However, the use of different detergents, buffers, and other blocking compounds such as polyvinyl alcohol (molecular weights ranging from ~9,000 to >200,000) and polyethylene glycol (chain lengths ranging from 200 to >20,000 repeats) alone did not solve this problem during troubleshooting (data not shown). Therefore, the design of a "non-stick" particle is (more likely than not) required to complete an *M.tb*-specific particle for sputum isolation.

Collaborators at the University of Cape Town have reported that polyethylene glycol prevents nonspecific binding of *M.tb* to their microarrays (J. M. Blackburn, personal communication, June 16, 2021). They and others have successfully demonstrated that polyethylene glycol or dextran-based organic polymer coatings are superior to protein blocking agents (e.g., nonfat dry milk or bovine serum albumin). The caveat is that the polyethylene glycol short-length chains must be in a perfectly uniform monolayer, or longer chains must be sufficient in length.[357, 358] Although initial experiments showed passive blocking with polyethylene glycol was ineffective at preventing nonspecific binding, physically blocking the particle surface could significantly increase the possibility of eliminating nonspecific binding due to interactions with polymers used for particle manufacturing. Using streptavidin for surface functionalization can also cause nonspecific interactions in biological samples. Hence, the bio-conjugation method must be assessed explicitly for nonspecific binding in addition to the capture molecule loading concentration to determine maximum performance with minimal nonspecific binding.

Contributions to the Field

Three innovations serve as the foundation for this dissertation. The first major innovation in this dissertation focused on designing and testing a high-gradient magnetic separation-based biomarker and nucleic acid extraction device, which can capture and concentrate biomarkers from diverse biological matrices. The Haselton Research Group has published several papers using magnetic beads in stationary fluids to concentrate biomarkers and remove sample contaminants.[91, 94, 203, 209] Examining the inverse problem, how to re-collect the magnetic beads from a flow, this dissertation developed and refined the application of HGMS for biological sample processing with a focus on complete capture of magnetic particles and efficient biomarker recovery. This work demonstrates that multiple users with varying levels of training can capture ~100% of magnetic beads in the device under aqueous conditions, demonstrating that the design reduces potential error by an untrained user. Notably, the second characteristic of this design is the use of transient magnetism, as the steel wool remains magnetized only when an external magnetic field is present. This dissertation shows that a majority of the paramagnetic beads are flushed out of the steel wool upon magnet removal. This is beneficial for the concentrated recovery of biomarker-loaded beads, and its performance was validated when used to extract nucleic acids from urine, sputum, blood, and stool. While this design used nucleic acids for biomarker concentration, surface modification of the magnetic particle would allow for immunospecific concentration of protein, carbohydrate, lipid, or whole pathogen biomarkers.

Publication of this work in *ACS Applied Materials and Interfaces* made this the first published study (to my knowledge) featuring an HGMS system that purified nucleic acids for infectious disease diagnosis. A comprehensive literature search identified only a few papers that utilize high-gradient magnetic separation for nucleic acid isolation,[144, 362-364] and most of these accomplish their studies using commercially manufactured HGMS systems. The most similar commercial application is Miltenyi Biotech's mRNA isolation kit, cited in publications not explicitly identified here.

The second major innovation of this dissertation used secondary radial microfluidic flows, known as Marangoni flows, found in an evaporating sessile droplet for enhancement of conventional microscopic sputum smear inspection for TB diagnosis. Specifically, many researchers have tried to improve sputum smear microscopy by using nonspecific volumetric concentration, and unfortunately, these methods have only led to modest improvements in diagnostic sensitivity while also reducing specificity. The work presented here used a combined concentration strategy, pairing volumetric concentration with spatial enrichment, improving the LOD of sputum smear microscopy, and demonstrating the potential for improved specificity.

Though this is not the first work to use radial flows in an evaporating sessile droplet for diagnostic purposes, as demonstrated by the publication history of the Haselton Research Group,[135, 144-146] publication of this work in MDPI's *Diagnostics* makes this the first published study (to my knowledge) to harness the described microfluidic flows for whole pathogen diagnosis using traditional microscopic staining techniques. Trantum *et al.* detected the whole M13K07 phage using microscopy using Marangoni flows in a model system, but he did not directly visualize the phage and instead correlated the deposition spot size with phage concentration.[145]

The third major innovation of this dissertation investigated the binding of cyanobacterial lectin, microvirin-N, to *M.tb* cells and its potential for use in LAM-based whole pathogen diagnostics. MVN was characterized alongside other newly developed LAM antibodies and assessed for specificity to MTBC species or NTM species using biolayer interferometry and direct cell staining. As established in literature[86] and observed through personal experience, many antibodies developed for use with mycobacteria are nonspecific, and cross-reaction between antibodies for pathogenic and nonpathogenic species is common. The knowledge that antibodies are not completely specific necessitates using a variety of controls to demonstrate its specificity and usually requires lengthy culture protocols to confirm test results.[73] Use of MVN alongside a second confirmatory assay could solve the MTBC/NTM infection specificity gap, particularly if paired with an already accessible confirmatory assay. Publication of this

work will make it the first report, to my knowledge, demonstrating the specificity of MVN for MTBC/NTM species. In addition, we demonstrated that monomeric MVN does not either adequately bind or remain bound to the *M.tb* cell surface, and divalent MVN with two mannosyl binding sites increases the relative amount of MVN bound to the surface of the cell. As stated, no information about MVN binding to *M.tb* cells is publically available in the literature, so this additional information will be particularly interesting to individuals studying MVN in the context of TB or to those that study lectins and their binding behaviors.

After investigating LAM specificity, I focused on studying the impact of in vitro processing methods that are mandatory for isolating single mycobacterial cells following culture. Without these processing methods, it is often impossible to get a large population of usable cells, and there is no information available for researchers interested in how these methods change surface biomarker expression or experimental results. Using LAM accessibility as the "readout" for investigating these effects is clinically significant due to its high abundance and implications in pathogenesis. Upon publication of this work, with the intent to submit for peer review to the *Journal of Microbiological Methods*, this report will be first assessing, to my knowledge, assessing the impact of mechanical or enzymatic dissociation methods on changes to the relative surface density of the most abundant TB cell surface marker, LAM.

In addition, this dissertation made significant progress in developing an MVN-conjugated magnetic nanoparticle for ultimate use in a diagnostic capture assay. Upon completion of this project, this will be the first TB diagnostic tool to capture whole-cell pathogens for differentiation between MTBC and NTM infections using MVN. Unlike work published by van der Horst *et al.*, which used large, 1 μm magnetic particles for the on-bead ELISA, this work used nanoparticles compatible with microscopic visualization of whole cells.

Societal Impact

A new POC diagnostic TB test will positively impact individual patients since TB disease diagnosed earlier is simpler to treat. It will also impact patient communities since individuals with TB disease (or misdiagnosed NTM infection) will be identified and put on appropriate chemotherapeutic treatment sooner, curbing the transmission of TB disease and deaths caused by mistreated or untreated TB disease or NTM infection. These approaches could notably assist TB control programs by providing a major interrupter of *M.tb* transmission, especially in combination. Moreover, this diagnostics-based approach will be quicker and more effective than the finding, developing, and

testing new antibiotic classes that only temporarily overcome drug resistance. The fact that the most significant declines in TB mortality and incidence in industrialized countries occurred before the advent of effective anti-TB chemotherapy shows that social and environmental factors – especially active case finding – can dramatically influence TB transmission.[365, 366]

Because healthcare quality and accessibility are multi-factorial problems, one needs to consider the question, "Why is improving TB diagnosis in low-resource settings *specifically* a biomedical engineering problem?" With demonstrated supply chain mismanagement, high operating costs, known transportation issues getting both patients and samples to testing sites, and accessibility impacted by politics, there are other potential avenues to solve this problem beyond biomedical engineering. Unfortunately, it is well known that changes to socio-political situations similar to those mentioned happen at a glacial speed or are often globally insignificant and require operational changes to thousands or tens of thousands of employees outside of the POC diagnostic setting. The endorsement and implementation of Xpert have shown how quickly new diagnostics can be acquired, but how the continued socio-political and supply issues continue to impact its effectiveness at case detection, even with financial subsides from the Gates Foundation reducing the cost of testing. By creating a diagnostic that uses techniques based around methods and equipment already implemented at the POC, there are fewer operational and financial challenges to overcome for implementation. The research methods presented here focus on developing techniques that, with further refinement, are composed of inexpensive and easily acquired reagent additions that could be delivered bundled to the already used ZN staining reagents, using the current supply and delivery chain. Working within the current system makes it more likely that significant impacts will be seen. For this reason, improving TB diagnosis is solvable using biomedical engineering and is more likely to result in significant improvement to TB case detection than other systemic operational changes.

In conclusion, my work presents new, novel methods that could help improve TB diagnosis in rural, low-resource areas of the world. The foundations established here offer unique opportunities for refined development and testing of methods with a significant potential for integration into the current POC workflow and significant impact on TB case detection.

REFERENCES

1. Global Health Estimates 2020: Deaths by Cause, Age, Sex, by Country and by Region, 2000-2019. World Health Organization: Geneva, 2020.
2. *Global Tuberculosis Report 2020*; World Health Organization: Geneva, 2020.
3. Dheda, K.; Limberis, J. D.; Pietersen, E.; Phelan, J.; Esmail, A.; Lesosky, M.; Fennelly, K. P.; Te Riele, J.; Mastrapa, B.; Streicher, E. M.; Dolby, T.; Abdallah, A. M.; Ben-Rached, F.; Simpson, J.; Smith, L.; Gumbo, T.; van Helden, P.; Sirgel, F. A.; McNerney, R.; Theron, G.; Pain, A.; Clark, T. G.; Warren, R. M., Outcomes, infectiousness, and transmission dynamics of patients with extensively drug-resistant tuberculosis and home-discharged patients with programmatically incurable tuberculosis: a prospective cohort study. *The Lancet. Respiratory medicine* **2017**.
4. MacPherson, P.; Houben, R. M. G. J.; Glynn, J. R.; Corbett, E. L.; Kranzer, K., Pre-treatment loss to follow-up in tuberculosis patients in low- and lower-middle-income countries and high-burden countries: a systematic review and meta-analysis. *Bull World Health Org* **2014,** *92* (2), 126-138.
5. Kritzinger, F. E.; den Boon, S.; Verver, S.; Enarson, D. A.; Lombard, C. J.; Borgdorff, M. W.; Gie, R. P.; Beyers, N., No decrease in annual risk of tuberculosis infection in endemic area in Cape Town, South Africa. *Tropical medicine & international health : TM & IH* **2009,** *14* (2), 136-42.
6. TB, G. P. t. S., The Global Plan to Stop TB (2011-2015): Transforming the Fight Towards Elimination of Tuberculosis. **2011**.
7. Jilani, T. N.; Avula, A.; Zafar Gondal, A.; Siddiqui, A. H., Active Tuberculosis. [Updated 2021 Oct. 19]. StatPearls (Internet): Treasure Island, FL, 2021. https://www.ncbi.nlm.nih.gov/books/NBK513246/.
8. Small, P. M.; Fujiwara, P. I., Management of Tuberculosis in the United States. *NEJM* **2001,** *345* (3), 189-200.
9. Sia, J. K.; Rengarajan, J., Immunology of Mycobacterium tuberculosis Infections. *Microbiol Spectr* **2019,** *7* (4).
10. Ernst, J. D., The immunological life cycle of tuberculosis. *Nat Rev Immunol* **2012,** *12* (8), 581-91.
11. Sterling, T. R.; Njie, G.; Zenner, D.; Cohn, D. L.; Reves, R.; Ahmed, A.; Menzies, D.; Horsburgh Jr., R.; Crane, C. M.; Burgos, M.; LoBue, P.; Winston, C. A.; Belknap, D., Guidelines for the Treatment of Latent Tuberculosis Infection: Recommendations from the National Tuberculosis Controllers Association and CDC, 2020. *MMWR Recomm Rep 2020* **2020,** *69* (No. RR-1), 1-11.
12. Moule, M. G.; Cirillo, J. D., Mycobacterium tuberculosis Dissemination Plays a Critical Role in Pathogenesis. *Front Cell Infect Microbiol* **2020,** *10*, 65.
13. Chackerian, A. A.; Alt, J. M.; Perera, T. V.; Dascher, C. C.; Behar, S. M., Dissemination of Mycobacterium tuberculosis is influenced by host factors and precedes the initiation of T-cell immunity. *Infect Immun* **2002,** *70* (8), 4501-9.
14. Wolf, A. J.; Desvignes, L.; Linas, B.; Banaiee, N.; Tamura, T.; Takatsu, K.; Ernst, J. D., Initiation of the adaptive immune response to Mycobacterium tuberculosis depends on antigen production in the local lymph node, not the lungs. *J Exp Med* **2008,** *205* (1), 105-15.
15. Reiley, W.; Calayag, M.; Wittmer, S.; Huntington, J.; Pearl, J.; Fountain, J.; Martino, C.; Roberts, A.; Cooper, A.; Winslow, G.; Woodland, D., ESAT-6-specific CD4 T cell responses to aerosol Mycobacterium tuberculosis infection are initiated in the mediastinal lymph nodes. *Proc Natl Acad Sci U S A* **2008,** *105* (31), 10961-10966.
16. Heemskerk, D.; Caws, M.; Marais, B.; Farrar, J., Tuberculosis in Adults and Children. In *SpringerBriefs in Public Health* [Online] Springer Publishing: 2015.
17. Gill, W. P.; Harik, N. S.; Whiddon, M. R.; Liao, R. P.; Mittler, J. E.; Sherman, D. R., A replication clock for Mycobacterium tuberculosis. *Nat Med* **2009,** *15* (2), 211-4.
18. Ford, C. B.; Lin, P. L.; Chase, M. R.; Shah, R. R.; Iartchouk, O.; Galagan, J.; Mohaideen, N.; Ioerger, T. R.; Sacchettini, J. C.; Lipsitch, M.; Flynn, J. L.; Fortune, S. M., Use of whole genome sequencing to estimate the mutation rate of Mycobacterium tuberculosis during latent infection. *Nat Genet* **2011,** *43* (5), 482-6.
19. Chowdhury, R.; Vallania, F.; Yang, Q.; Lopez Angel, C. J.; Darboe, F.; Penn-Nicholson, A.; Rozot, V.; Nemes, E.; Malherbe, S. T.; Ronacher, K.; Walzl, G.; Hanekom, W.; Davis, M. M.; Winter, J.; Chen, X.; Scriba, T. J.; Khatri, P.; Chien, Y. H., A multi-cohort study of the immune factors associated with M. tuberculosis infection outcomes. *Nature* **2018,** *560* (7720), 644-648.

20. Hunter, R. L., Tuberculosis as a three-act play: A new paradigm for the pathogenesis of pulmonary tuberculosis. *Tuberculosis* **2016,** *97*, 8-17.
21. Rao, M.; Ippolito, G.; Mfinanga, S.; Ntoumi, F.; Yeboah-Manu, D.; Vilaplana, C.; Zumla, A.; Maeurer, M., Latent TB Infection (LTBI) - Mycobacterium tuberculosis pathogenesis and the dynamics of the granuloma battleground. *Int J Infect Dis* **2019,** *80S*, S58-S61.
22. Saeed, W., Cavitating pulmonary tuberculosis: a global challenge. *Clin Med* **2012,** *12* (1), 40-41.
23. Rodriguez-Takeuchi, S. Y.; Renjifo, M. E.; Medina, F. J., Extrapulmonary Tuberculosis: Pathophysiology and Imaging Findings. *Radiographics* **2019,** *39* (7), 2023-2037.
24. Chapter 2: Transmission and Pathogenesis of Tuberculosis. In *Core Curriculum on Tuberculosis: What the Clinician Should Know*, Centers for Disease Control: 2013.
25. Sharma, S. K.; Mohan, A.; Sharma, A., Miliary tuberculosis: A new look at an old foe. *J Clin Tuberc Other Mycobact Dis* **2016,** *3*, 13-27.
26. Krishnan, N.; Robertson, B. D.; Thwaites, G., The mechanisms and consequences of the extra-pulmonary dissemination of Mycobacterium tuberculosis. *Tuberculosis* **2010,** *90* (6), 361-6.
27. Khan, F. Y., Review of literature on disseminated tuberculosis with emphasis on the focused diagnostic workup. *J Family Community Med* **2019,** *26* (2), 83-91.
28. Narasimhan, P.; Wood, J.; Macintyre, C. R.; Mathai, D., Risk factors for tuberculosis. *Pulm Med* **2013,** *2013*, 828939.
29. Mase, S. R.; Chorba, T., Treatment of Drug-Resistant Tuberculosis. *Clin Chest Med* **2019,** *40* (4), 775-795.
30. Nahid, P.; Dorman, S. E.; Alipanah, N.; Barry, P. M.; Brozek, J. L.; Cattamanchi, A.; Chaisson, L. H.; Chaisson, R. E.; Daley, C. L.; Grzemska, M.; Higashi, J. M.; Ho, C. S.; Hopewell, P. C.; Keshavjee, S. A.; Lienhardt, C.; Menzies, R.; Merrifield, C.; Narita, M.; O'Brien, R.; Peloquin, C. A.; Raftery, A.; Saukkonen, J.; Schaaf, H. S.; Sotgiu, G.; Starke, J. R.; Migliori, G. B.; Vernon, A., Executive Summary: Official American Thoracic Society/Centers for Disease Control and Prevention/Infectious Diseases Society of America Clinical Practice Guidelines: Treatment of Drug-Susceptible Tuberculosis. *Clin Infect Dis* **2016,** *63* (7), 853-67.
31. Gupta, K.; GUpta, R.; Atreja, A.; Verma, M.; Vishvkarma, S., Tuberculosis and nutrition. *Lung India* **2009,** *26* (1), 9-16.
32. Seung, K. J.; Keshavjee, S.; Rich, M. L., Multidrug-Resistant Tuberculosis and Extensively Drug-Resistant Tuberculosis. *Cold Spring Harb Perspect Med* **2015,** *5* (9), a017863.
33. Society, A. T.; Control, C. f. D.; America, I. D. S. o., Treatment of Tuberculosis. *MMWR Recomm Rep 2003* **2003,** *52* (RR-11), 1-77.
34. Story, A.; Aldridge, R. W.; Smith, C. M.; Garber, E.; Hall, J.; Ferenando, G.; Possas, L.; Hemming, S.; Wurie, F.; Luchenski, S.; Abubakar, I.; McHugh, T. D.; White, P. J.; Watson, J. M.; Lipman, M.; Garfein, R.; Hayward, A. C., Smartphone-enabled video-observed versus directly observed treatment for tuberculosis: a multicentre, analyst-blinded, randomised, controlled superiority trial. *The Lancet* **2019,** *393* (10177), 1216-1224.
35. Guidelines for treatment of drug-susceptible tuberculosis and patient care, 2017 update; World Health Organization: Geneva, 2017.
36. Imperial, M. Z.; Nahid, P.; Phillips, P. P. J.; Davies, G. R.; Fielding, K.; Hanna, D.; Hermann, D.; Wallis, R. S.; Johnson, J. L.; Lienhardt, C.; Savic, R. M., A patient-level pooled analysis of treatment-shortening regimens for drug-susceptible pulmonary tuberculosis. *Nat Med* **2018,** *24* (11), 1708-1715.
37. Dorman, S. E.; Nahid, P.; Kurbatova, E. V.; Phillips, P. P. J.; Bryant, K.; Dooley, K. E.; Engle, M.; Goldberg, S. V.; Phan, H. T. T.; Hakim, J.; Johnson, J. L.; Lourens, M.; Martinson, N. A.; Muzanyi, G.; Narunsky, K.; Nerette, S.; Nguyen, N. V.; Pham, T. H.; Pierre, S.; Purfield, A. E.; Samaneka, W.; Savic, R. M.; Sanne, I.; Scott, N. A.; Shenje, J.; Sizemore, E.; Vernon, A.; Waja, Z.; Weiner, M.; Swindells, S.; Chaisson, R. E.; Group, A. C. T.; Tuberculosis Trials, C., Four-Month Rifapentine Regimens with or without Moxifloxacin for Tuberculosis. *N Engl J Med* **2021,** *384* (18), 1705-1718.
38. Iacobino, A.; Fattorini, L.; Giannoni, F., Drug-Resistant Tuberculosis 2020: Where We Stand. *Applied Sciences* **2020,** *10* (6).
39. Klopper, M.; Warren, R. M.; Hayes, C.; Gey van Pittius, N. C.; Streicher, E. M.; Muller, B.; Sirgel, F. A.; Chabula-Nxiweni, M.; Hoosain, E.; Coetzee, G.; David van Helden, P.; Victor, T. C.; Trollip, A. P., Emergence and spread of extensively and totally drug-resistant tuberculosis, South Africa. *Emerg Infect Dis* **2013,** *19* (3), 449-55.
40. WHO consolidated guidelines on drug-resistant tuberculosis treatment. Organization, W. H., Ed. Geneva, 2019.

41. Snider Jr., D. E., Pyridoxine Supplementation During Isoniazid Therapy. *Tubercle* **1980,** *61* (4), 191-196.
42. Katelaris, A. L.; Jackson, C.; Southern, J.; Gupta, R. K.; Drobniewski, F.; Lalvani, A.; Lipman, M.; Mangtani, P.; Abubakar, I., Effectiveness of BCG Vaccination Against Mycobacterium tuberculosis Infection in Adults: A Cross-sectional Analysis of a UK-Based Cohort. *J Infect Dis* **2020,** *221* (1), 146-155.
43. Andersen, P.; Doherty, T., The success and failure of BCG - implications for a novel tuberculosis vaccine. *Nat Rev Microbiol* **2005,** *3*, 656-662.
44. Black, G. F.; Weir, R. E.; Floyd, S.; Bliss, L.; Warndorff, D. K.; Crampin, A. C.; Ngwira, B.; Sichali, L.; Nazareth, B.; Blackwell, J. M.; Branson, K.; Chaguluka, S. D.; Donovan, L.; Jarman, E.; King, E.; Fine, P. E. M.; Dockrell, H. M., BCG-induced increase in interferon-gamma response to mycobacterial antigens and efficacy of BCG vaccination in Malawi and the UK: two randomised controlled studies. *The Lancet* **2002,** *359* (9315), 1393-1401.
45. Venkataswamy, M. M.; Goldberg, M. F.; Baena, A.; Chan, J.; Jacobs, W. R., Jr.; Porcelli, S. A., In vitro culture medium influences the vaccine efficacy of Mycobacterium bovis BCG. *Vaccine* **2012,** *30* (6), 1038-49.
46. Trunz, B. B.; Fine, P. E. M.; Dye, C., Effect of BCG vaccination on childhood tuberculous meningitis and miliary tuberculosis worldwide: a meta-analysis and assessment of cost-effectiveness. *The Lancet* **2006,** *367* (9517), 1173-1180.
47. Marcus, A.; Rose, D.; Sacks, H.; Schechter, C., BCG Vaccination to Prevent Tuberculosis in Health Care Workers: A Decision Analysis. *Preventative Med* **1997,** *26* (2), 201-207.
48. Organization, W. H., Systematic screening for active tuberculosis: principles and recommendations. World Health Organization: 2013.
49. Person, A. K.; Pettit, A. C.; Sterling, T. R., Diagnosis and treatment of latent tuberculosis infection: an update. *Current Respiratory Care Reports* **2013,** *2* (4), 199-207.
50. TB Elimination Interferon-Gamma Release Assays (IGRAs) - Blood Tests for TB Infection. Prevention, C. f. D. C. a., Ed. 2011.
51. Policy Statement: Automated Real-time Nucleic Acid Amplification Technology for Rapid and Simultaneous Detection of Tuberculosis and Rifampicin Resistance: Xpert MTB/RIF System. World Health Organization: 2011.
52. A New Tool to Diagnose Tuberculosis: The Xpert MTB/RIF Assay. In *Centers for Disease Control*, National Center for HIV/AIDS, V. H., STD, and TB Prevention, Ed. 2013.
53. Helb, D.; Jones, M.; Story, E.; Boehme, C.; Wallace, E.; Ho, K.; Kop, J.; Owens, M. R.; Rodgers, R.; Banada, P.; Safi, H.; Blakemore, R.; Lan, N. T.; Jones-Lopez, E. C.; Levi, M.; Burday, M.; Ayakaka, I.; Mugerwa, R. D.; McMillan, B.; Winn-Deen, E.; Christel, L.; Dailey, P.; Perkins, M. D.; Persing, D. H.; Alland, D., Rapid detection of Mycobacterium tuberculosis and rifampin resistance by use of on-demand, near-patient technology. *J Clin Microbiol* **2010,** *48* (1), 229-37.
54. Miller, M. B.; Popowitch, E. B.; Backlund, M. G.; Ager, E. P., Performance of Xpert MTB/RIF RUO assay and IS6110 real-time PCR for Mycobacterium tuberculosis detection in clinical samples. *J Clin Microbiol* **2011,** *49* (10), 3458-62.
55. Kayigire, X. A.; Friedrich, S. O.; Venter, A.; Dawson, R.; Gillespie, S. H.; Boeree, M. J.; Heinrich, N.; Hoelscher, M.; Diacon, A. H.; Pan African Consortium for the Evaluation of Anti-tuberculosis, A., Direct comparison of Xpert MTB/RIF assay with liquid and solid mycobacterial culture for quantification of early bactericidal activity. *Journal of clinical microbiology* **2013,** *51* (6), 1894-8.
56. Lawn, S. D.; Mwaba, P.; Bates, M.; Piatek, A.; Alexander, H.; Marais, B. J.; Cuevas, L. E.; McHugh, T. D.; Zijenah, L.; Kapata, N.; Abubakar, I.; McNerney, R.; Hoelscher, M.; Memish, Z. A.; Migliori, G. B.; Kim, P.; Maeurer, M.; Schito, M.; Zumla, A., Advances in tuberculosis diagnostics: the Xpert MTB/RIF assay and future prospects for a point-of-care test. *The Lancet. Infectious diseases* **2013,** *13* (4), 349-61.
57. Theron, G.; Zijenah, L.; Chanda, D.; Clowes, P.; Rachow, A.; Lesosky, M.; Bara, W.; Mungofa, S.; Pai, M.; Hoelscher, M.; Dowdy, D.; Pym, A.; Mwaba, P.; Mason, P.; Peter, J.; Dheda, K.; team, T.-N., Feasibility, accuracy, and clinical effect of point-of-care Xpert MTB/RIF testing for tuberculosis in primary-care settings in Africa: a multicentre, randomised, controlled trial. *Lancet* **2014,** *383* (9915), 424-35.
58. Pravettoni, R., Working for the Environment, South Africa. *UNEP/GRID-Arendal* **2011**.
59. GeneXpert Xpert MTB/RIF National report. Africa, N. H. L. S. o. S., Ed. 2019; pp 1-8.
60. Cambanis, A.; Ramsay, A.; Wirkom, V.; Tata, E.; Cuevas, L. E., Investing time in microscopy: an opportunity to optimise smear-based case detection of tuberculosis. *The international journal of*

tuberculosis and lung disease : the official journal of the International Union against Tuberculosis and Lung Disease **2007,** *11* (1), 40-5.
61. Hanscheid, T., The future looks bright: low-cost fluorescent microscopes for detection of Mycobacterium tuberculosis and Coccidiae. *Trans R Soc Trop Med Hyg* **2008,** *102* (6), 520-1.
62. Lewis, J. J.; Chihota, V. N.; van der Meulen, M.; Fourie, P. B.; Fielding, K. L.; Grant, A. D.; Dorman, S. E.; Churchyard, G. J., "Proof-of-concept" evaluation of an automated sputum smear microscopy system for tuberculosis diagnosis. *PLoS One* **2012,** *7* (11), e50173.
63. Steingart, K. R.; Ng, V.; Henry, M.; Hopewell, P. C.; Ramsay, A.; Cunningham, J.; Urbanczik, R.; Perkins, M. D.; Aziz, M. A.; Pai, M., Sputum processing methods to improve the sensitivity of smear microscopy for tuberculosis: a systematic review. *The Lancet. Infectious diseases* **2006,** *6* (10), 664-74.
64. Steingart, K. R.; Henry, M.; Ng, V.; Hopewell, P. C.; Ramsay, A.; Cunningham, J.; Urbanczik, R.; Perkins, M.; Aziz, M. A.; Pai, M., Fluorescence versus conventional sputum smear microscopy for tuberculosis: a systematic review. *The Lancet. Infectious diseases* **2006,** *6* (9), 570-81.
65. Ghodbane, R.; Drancourt, M., Magnetic bead protocol for culturing Mycobacterium tuberculosis from sputum specimens. *J Clin Microbiol* **2013,** *51* (5), 1578-9.
66. Peterson, E. M.; Nakasone, A.; Platon-DeLeon, J. M.; Jang, Y.; de La Maza, L. M.; Desmond, E., Comparison of direct and concentrated acid-fast smears to identify specimens culture positive for Mycobacterium spp. *Journal of clinical microbiology* **1999,** *37* (11), 3564-8.
67. Warren, J.; Bhattacharya, M.; de Almeida, K.; Trakas, K.; Peterson, L., A Minimum 5.0ml of Sputum Improves the Sensitivity of Acid-fast Smear for Mycobacterium tuberculosis. *Am J Resp Criti Care Med* **2000,** *161* (5), 1559-1562.
68. Albert, H.; Ademun, P. J.; Lukyamuzi, G.; Nyesiga, B.; Manabe, Y.; Joloba, M.; Wilson, S.; Perkins, M. D., Feasibility of magnetic bead technology for concentration of mycobacteria in sputum prior to fluorescence microscopy. *BMC infectious diseases* **2011,** *11*, 125.
69. Wilson, S.; Lane, A.; Rosedale, R.; Stanley, C., Concentration of Mycobacterium tuberculosis from sputum using ligand-coated magnetic beads. *The international journal of tuberculosis and lung disease : the official journal of the International Union against Tuberculosis and Lung Disease* **2010,** *14* (9), 1164-8.
70. Shapiro, H. M.; Hanscheid, T., Fuchsin fluorescence in Mycobacterium tuberculosis: the Ziehl-Neelsen stain in a new light. *J Microbiol Methods* **2008,** *74* (2-3), 119-20.
71. Stitt, E. R., Practical Bacteriology, Blood Work and Animal Parasitology Including Bacteriological Keys, Zoological Tables, and Explanatory Clinical Notes. P. Blakiston's Son & Co.: Philadelphia, OA, 1918; Vol. Fifth Volume, p 598.
72. Marrakchi, H.; Lanéelle, M.-A.; Daffé, M., Mycolic Acids: Structures, Biosynthesis, and Beyond. *Chemistry & Biology* **2014,** *21* (1), 67-85.
73. Jeon, K.; Koh, W. J.; Kwon, O. J.; Suh, G. Y.; Chung, M. P.; Kim, H.; Lee, N. Y.; Park, Y. K.; Bai, G. H., Recovery rate of NTM from AFB smear-positive sputum specimens at a medical centre in South Korea. *Int J Tuberc Lung Dis* **2005,** *9* (9), 1046-1051.
74. Kinyoun, J. J., A Note On Uhlenhuths Method for Sputum Examination, For Tubercle Bacilli. *Am J Public Health* **1914,** *5* (9).
75. Griffith, D. E.; Aksamit, T.; Brown-Elliott, B. A.; Catanzaro, A.; Daley, C.; Gordin, F.; Holland, S. M.; Horsburgh, R.; Huitt, G.; Iademarco, M. F.; Iseman, M.; Olivier, K.; Ruoss, S.; von Reyn, C. F.; Wallace, R. J., Jr.; Winthrop, K.; Subcommittee, A. T. S. M. D.; American Thoracic, S.; Infectious Disease Society of, A., An official ATS/IDSA statement: diagnosis, treatment, and prevention of nontuberculous mycobacterial diseases. *Am J Respir Crit Care Med* **2007,** *175* (4), 367-416.
76. Maiga, M.; Siddiqui, S.; Diallo, S.; Diarra, B.; Traore, B.; Shea, Y. R.; Zelazny, A. M.; Dembele, B. P.; Goita, D.; Kassambara, H.; Hammond, A. S.; Polis, M. A.; Tounkara, A., Failure to recognize nontuberculous mycobacteria leads to misdiagnosis of chronic pulmonary tuberculosis. *PLoS One* **2012,** *7* (5), e36902.
77. Sarro, Y. S.; Kone, B.; Diarra, B.; Kumar, A.; Kodio, O.; Fonfana, D.; Achenbach, C. J.; Beavogui, A. H.; Seydi, M.; Holl, J. L.; Taiwo, B.; Diallo, S.; Doumbia, S.; Murphy, R. L.; McFall, S. M.; Maiga, M., Simultaneous diagnosis of tuberculous and non-tuberculous mycobacterial diseases: Time for a better patient management. *Clin Microbiol Infect Dis* **2018,** *3* (3), 1-8.
78. Nishiuchi, Y.; Iwamoto, T.; Maruyama, F., Infection Sources of a Common Non-tuberculous Mycobacterial Pathogen, Mycobacterium avium Complex. *Front Med (Lausanne)* **2017,** *4*, 27.
79. Daniel-Wayman, S.; Abate, G.; Barber, D. L.; Bermudez, L. E.; Coler, R. N.; Cynamon, M. H.; Daley, C. L.; Davidson, R. M.; Dick, T.; Floto, R. A.; Henkle, E.; Holland, S. M.; Jackson, M.; Lee, R. E.;

Nuermberger, E. L.; Olivier, K. N.; Ordway, D. J.; Prevots, D. R.; Sacchettini, J. C.; Salfinger, M.; Sassetti, C. M.; Sizemore, C. F.; Winthrop, K. L.; Zelazny, A. M., Advancing Translational Science for Pulmonary Nontuberculous Mycobacterial Infections. A Road Map for Research. *Am J Respir Crit Care Med* **2019,** *199* (8), 947-951.

80. Blakemore, R.; Story, E.; Helb, D.; Kop, J.; Banada, P.; Owens, M. R.; Chakravorty, S.; Jones, M.; Alland, D., Evaluation of the analytical performance of the Xpert MTB/RIF assay. *J Clin Microbiol* **2010,** *48* (7), 2495-501.
81. Ahmed, I.; Tiberi, S.; Farooqi, J.; Jabeen, K.; Yeboah-Manu, D.; Migliori, G. B.; Hasan, R., Non-tuberculous mycobacterial infections-A neglected and emerging problem. *Int J Infect Dis* **2020,** *92S*, S46-S50.
82. Esther, C. R., Jr.; Esserman, D. A.; Gilligan, P.; Kerr, A.; Noone, P. G., Chronic Mycobacterium abscessus infection and lung function decline in cystic fibrosis. *J Cyst Fibros* **2010,** *9* (2), 117-23.
83. Ratnatunga, C. N.; Lutzky, V. P.; Kupz, A.; Doolan, D. L.; Reid, D. W.; Field, M.; Bell, S. C.; Thomson, R. M.; Miles, J. J., The Rise of Non-Tuberculosis Mycobacterial Lung Disease. *Front Immunol* **2020,** *11*, 303.
84. De Las Cuevas, G.; Faraudo, J.; Camacho, J., Low-Gradient Magnetophoresis through Field-Induced Reversible Aggregation. *Journal of Physical Chemistry* **2008,** *112* (4), 945-950.
85. Berensmeier, S., Magnetic particles for the separation and purification of nucleic acids. *Appl Microbiol Biotechnol* **2006,** *73* (3), 495-504.
86. van der Horst, M.; Karamchand, L.; Bauer, W. S.; Nel, A. J. M.; Blackburn, J. M.; Wright, D. W., The cyanobacterial lectin, microvirin-N, enhances the specificity and sensitivity of lipoarabinomannan-based TB diagnostic tests. *Analyst* **2021,** *146* (4), 1207-1215.
87. Hunter, S. W.; Gaylord, H.; Brennan, P. J., Structure and antigenicity of the phosphorylated lipopolysaccharide antigens from the leprosy and tubercle bacilli. *Journal of Biological Chemistry* **1986,** *261* (26), 12345-12351.
88. Kanetsuna, F., Effect of Lysozyme on Mycobacteria. *Microbiol Immunol* **1980,** *24* (12), 1151-1162.
89. van Schie, L.; Borgers, K.; Michielsen, G.; Plets, E.; Vuylsteke, M.; Tiels, P.; Festjens, N.; Callewaert, N., Exploration of synergistic action of cell wall-degrading enzymes against Mycobacterium tuberculosis. *Antimicrob Agents Chemother* **2021,** *65* (10).
90. Schwebach, J. R.; Casadevall, A.; Schneerson, R.; Dai, Z.; Wang, X.; Robbins, J. B.; Glatman-Freedman, A., Expression of a Mycobacterium tuberculosis arabinomannan antigen in vitro and in vivo. *Infect Immun* **2001,** *69* (9), 5671-8.
91. Russ, P. K.; Karhade, A. V.; Bitting, A. L.; Doyle, A.; Solinas, F.; Wright, D. W.; Haselton, F. R., A Prototype Biomarker Detector Combining Biomarker Extraction and Fixed Temperature PCR. *J Lab Autom* **2016,** *21* (4), 590-8.
92. Drowe, S.; Turnbull, S.; Oelrichs, R.; Dunne, A., Monitoring of Human Immunodeficiency Virus Infection in Resource-Contrained Countries. *Clinical Infectious Diseases* **2003,** *37* (Suppl 1), S25-S35.
93. Wee, E. J.; Lau, H. Y.; Botella, J. R.; Trau, M., Re-purposing bridging flocculation for on-site, rapid, qualitative DNA detection in resource-poor settings. *Chem Commun (Camb)* **2015,** *51* (27), 5828-31.
94. Bauer, W. S.; Gulka, C. P.; Silva-Baucage, L.; Adams, N. M.; Haselton, F. R.; Wright, D. W., Metal Affinity-Enabled Capture and Release Antibody Reagents Generate a Multiplex Biomarker Enrichment System that Improves Detection Limits of Rapid Diagnostic Tests. *Anal Chem* **2017,** *89* (19), 10216-10223.
95. Frantz, S. G. Magnetic Separator. 1937.
96. Oberteuffer, J. A., Engineering Development of High Gradient Magnetic Separators. *IEEE Transactions on Magnetics* **1976,** *12* (5), 444-449.
97. Iannicelli, J., Development of High Extraction Magnetic Filtration By the Kaolin Industry of Georgia. *IEEE Transactions on Magnetics* **1976,** *12* (5), 489.
98. Watson, J. H. P., Hocking, D., The Beneficiation of Clay Using A Superconducting Magnetic Separator. *IEEE Transactions on Magnetics* **1975,** *11* (5), 1588-1590.
99. Iannicelli, J., High Extraction Magnetic Filtration of Kaolin Clay. *Clays and Clay Minerals* **1976,** *24* (2), 64-68.
100. Harland, J. R.; Nillson, L.; Wallin, M., Pilot Scale High Gradient Magnetic Filtration of Steel Mill Wastewater. *IEEE Transactions on Magnetics* **1976,** *12* (6), 904-906.
101. Parker, M. R., High gradient magnetic separation. *Physics in Technology* **1981,** *12* (6), 263-268.
102. Maxwell, E.; Kelland, D. R.; Akoto, I. Y., High Gradient Magnetic Separation of Mineral Particulates from Solvent Refined Coal. *IEEE Transactions on Magnetics* **1976,** *12* (5), 507-510.

103. Oder, R. R., Magnetic Desulfurization of Liqueified Coals: Conceptual Process Design and Cost Estimation. *IEEE Transactions on Magnetics* **1976,** *12* (5), 532-637.
104. Buerger, M. J., The cell and symmetry of pyrrhotite. *American Minerologist* **1947,** *32* (7-8), 411-414.
105. Maxwell, E.; Kelland, D. R., High Gradient Magnetic Separation in Coal Desulfurization. *IEEE Transactions on Magnetics* **1978,** *14* (5), 482-487.
106. Trindade, S. C.; Kolm, H. H., Magnetic Desulfurization of Coal. *IEEE Transactions on Magnetics* **1973,** *9* (3), 310-313.
107. Lin, C. J.; A., L. Y.; Vives, D. L.; Oak, M. J.; E., C. G.; Huffman, E. L., Pilot-Scale Studies of Sulfur and Ash Removal from Coals by High Gradient Magnetic Separation. *IEEE Transactions on Magnetics* **1976,** *12* (5), 513-521.
108. Luborsky, F. E., High-gradient Magnetic Separation for Removal of Sulfur from Coal. Bureau of Mines, U. S. D. o. t. I., Ed. Pittsburg, Pennsylvania, 1977.
109. Avens, L. R.; Worl, L. A.; de Aguero, K. J.; Padilla, D. D.; Prenger, F. C.; Stewart, W. F.; Hill, D. D.; Tolt, T. T., Magnetic Separation for Soil Decontamination. In *Waste Management*, International Nuclear Information System: Tuscon, AZ United States, 1993; Vol. 24, pp 787-789.
110. Petrakis, L.; Ahner, P. F., Use of High Gradient Magnetic Separation Techniques for the Removal of Oil and Solids from Water Effluents. *IEEE Transactions on Magnetics* **1976,** *12* (5), 486-488.
111. de Latour, C., Magnetic Separation in Water Pollution Control. *IEEE Transactions on Magnetics* **1973,** *9* (3), 314-316.
112. de Latour, C.; Kolm, H. H., Magnetic Separation in Water Pollution Control - II. *IEEE Transactions on Magnetics* **1975,** *11* (5), 1570-1572.
113. Thorup, R. T.; Nixon, F. P.; Wentworth, D. F.; Sproul, O. J., Virus Removal by Coagulation with Polyelectrolytes. *Journal (American Water Works Association)* **1970,** *62* (2), 97-101.
114. Bitton, G.; Mitchell, R.; De Latour, C.; Maxwell, E., Phosphate Removal by Magnetic Filtration. *Water Research* **1974,** *8* (2), 107-109.
115. de Latour, C., HGMS: Economics, Applications, and Seed Reuse. *Journal (American Water Works Association)* **1976,** *68* (9), 498-500.
116. Dauer, R. R.; Dunlop, E. H., High Gradient Magnetic Separation of Yeast. *Biotechnology and Bioengineering* **1991,** *37* (11), 1021-1028.
117. Bitton, G.; Mitchell, R., The Removal of Escherichia Coli Bacteriophage T7 by Magnetic Filtration. *Water Research* **1974,** *8* (8), 549-551.
118. Melville, D.; Paul, F.; Roath, S., Direct magnetic separation of red cells from whole blood. *Nature* **1975,** *255*, 706.
119. Owen, C. S., High gradient magnetic capture of red blood cells. *Journal of Applied Physics* **1982,** *53* (5), 3884-3887.
120. Nalbandian, R. M.; Sammons, D. W.; Manley, M.; Xie, L.; Sterling, C. R.; Egen, N. B.; Gingras, B. A., A Molecular-based Magnet Test for Malaria. *American Journal of Clinical Pathology* **1995,** *103* (1), 57-64.
121. Molday, R. S.; Mackenzie, D., Immunospecific Ferromagnetic Iron-Dextran Reagents for the Labeling and Magnetic Separation of Cells. *Journal of Immunological Methods* **1982,** *52* (3), 353-367.
122. Molday, R. S.; Molday, L. L., Separation of cells labeled with immunospecific iron dextran microspheres using high gradient magnetic chromatography. *FEBS Letters* **1984,** *170* (2), 232-238.
123. Miltenyi, S.; Muller, W.; Weichel, W.; Radbruch, A., High Gradient Magnetic Cell Separation With MACS. *Cytometry* **1990,** *11* (2), 231-238.
124. Radbruch, A.; Mechtold, B.; Thiel, A.; Miltenyi, S.; Pflüger, E., High-Gradient Magnetic Cell Sorting. In *Methods in Cell Biology*, Academic Press: 1994; Vol. 42, pp 387-403.
125. Miltenyi, S. Methods and materials for improved high gradient magnetic separation of biological materlas. 1993.
126. Miltenyi, S.; Radbruch, A.; Weichel, W.; Muller, W.; Gottlinger, C.; Meyer, K. L. Metal matricies for use in high gradient magnetic separation of biological materials and method for coating the same. 1995.
127. Himmelblau, D. A. Observation and Modeling of Paramagnetic Particle Entrapment in a Magnetic Field. Massachusettes Institute of Technology, 1973.
128. Ge, W.; Encinas, A.; Araujo, E.; Song, S., Magnetic matrices used in high gradient magnetic separation (HGMS): A review. *Results in Physics* **2017,** *7*, 4278-4286.
129. Multi-24 Columns - Data Sheet. Biotec, M., Ed. miltenyibiotec.com, 2013.
130. Miltenyi, S. Magnetic Separation Apparatus. 1998.
131. Miltenyi, S. Magnetic Separation Apparatus. 1998.

132. Deegan, R. D.; Bakajin, O.; Dupont, T. F.; Huber, G.; Nagel, S. R.; Witten, T. A., Contact line deposits in an evporating droplet. *Phys Rev E Stat Nonlin Soft Matter Phys* **2000,** *62* (1), 756-765.
133. Deegan, R. D., Pattern formation in drying droplets. *Phys Rev E Stat Nonlin Soft Matter Phys* **2000,** *61* (1), 475-485.
134. Deegan, R. D.; Bakajin, O.; Dupont, T. F.; Huber, G.; Nagel, S. R.; Witten, T. A., Capillary flow as the cause of ring stains from dried liquid drops. *Nature* **1997,** *389* (6653), 927-829.
135. Trantum, J. R.; Eagleton, Z. E.; Patil, C. A.; Tucker-Schwartz, J. M.; Baglia, M. L.; Skala, M. C.; Haselton, F. R., Cross-sectional tracking of particle motion in evaporating drops: flow fields and interfacial accumulation. *Langmuir* **2013,** *29* (21), 6221-31.
136. Sangani, A. S.; Lu, C.; Su, K.; Schwarz, J. A., Capillary force on particles near a drop edge resting on a substrate and a criterion for contact line pinning. *Phys Rev E Stat Nonlin Soft Matter Phys* **2009,** *80* (1 Pt 1), 011603.
137. Yunker, P. J.; Still, T.; Lohr, M. A.; Yodh, A. G., Suppression of the coffee-ring effect by shape-dependent capillary interactions. *Nature* **2011,** *476* (7360), 308-11.
138. Anyfantakis, M.; Geng, Z.; Morel, M.; Rudiuk, S.; Baigl, D., Modulation of the Coffee-Ring Effect in Particle/Surfactant Mixtures: the Importance of Particle–Interface Interactions. *Langmuir* **2015,** *31* (14), 4113-4120.
139. Still, T.; Yunker, P. J.; Yodh, A. G., Surfactant-induced Marangoni eddies alter the coffee-rings of evaporating colloidal drops. *Langmuir* **2012,** *28* (11), 4984-8.
140. Hu, H.; Larson, R. G., Analysis of the Effects of Marangoni Stresses on the Microflow in an Evaporating Sessile Droplet. *Langmuir* **2005,** *21* (3972-3980).
141. Hu, H.; Larson, R. G., Evaporation of a Sessile Droplet on a Substrate. *J Phys Chem B* **2002,** *106* (6), 1334-1344.
142. Ristenpart, W. D.; Kim, P. G.; Domingues, C.; Wan, J.; Stone, H. A., Influence of substrate conductivity on circulation reversal in evaporating drops. *Phys Rev Lett* **2007,** *99* (23), 234502.
143. Hertaeg, M. J.; Rees-Zimmerman, C.; Tabor, R. F.; Routh, A. F.; Garnier, G., Predicting coffee ring formation upon drying in droplets of particle suspensions. *J Colloid Interface Sci* **2021,** *591*, 52-57.
144. Gulka, C. P.; Swartz, J. D.; Trantum, J. R.; Davis, K. M.; Peak, C. M.; Denton, A. J.; Haselton, F. R.; Wright, D. W., Coffee Rings as Low-Resource Diagnostics: Detection of the Malaria BiomarkerPlasmodium falciparumHistidine-Rich Protein-II Using a Surface-Coupled Ring of Ni(II)NTA Gold-Plated Polystyrene Particles. *ACS Applied Materials & Interfaces* **2014,** *6* (9), 6257-6263.
145. Trantum, J. R.; Baglia, M. L.; Eagleton, Z. E.; Mernaugh, R. L.; Haselton, F. R., Biosensor design based on Marangoni flow in an evaporating drop. *Lab on a chip* **2014,** *14* (2), 315-24.
146. Trantum, J. R.; Wright, D. W.; Haselton, F. R., Biomarker-mediated disruption of coffee-ring formation as a low resource diagnostic indicator. *Langmuir* **2012,** *28* (4), 2187-93.
147. Deegan, R. D.; Bakajin, O.; Dupont, T. F.; Huber, G.; Nagel, S. R.; Witten, T. A., Capillary flow as the cause of ring stains from dried liquid drops. *Nature* **1997,** *389* (6653), 827-829.
148. Gulka, C. P.; Swartz, J. D.; Trantum, J. R.; Davis, K. M.; Peak, C. M.; Denton, A. J.; Haselton, F. R.; Wright, D. W., Coffee rings as low-resource diagnostics: detection of the malaria biomarker Plasmodium falciparum histidine-rich protein-II using a surface-coupled ring of Ni(II)NTA gold-plated polystyrene particles. *ACS Appl Mater Interfaces* **2014,** *6* (9), 6257-63.
149. Hu, H.; Larson, R. G., Marangoni Effect Reverses Coffee-Ring Depositions. *J Phys Chem B* **2006,** *110*, 7090-7094.
150. van Gaalen, R. T.; Diddens, C.; Wijshoff, H. M. A.; Kuerten, J. G. M., Marangoni circulation in evaporating droplets in the presence of soluble surfactants. *J Colloid Interface Sci* **2021,** *584*, 622-633.
151. Lumb, R.; Van Deun, A.; Bastian, I.; Fitz-Gerald, M., *Laboratory Diagnosis of Tuberculosis by Sputum Microscopy - The handbook, Global edition*. Global Laboratory Initiative: Adelaide, Australia, 2013.
152. Steingart, K. R.; Henry, M.; Ng, V.; Hopewell, P. C.; Ramsay, A.; Cunningham, J.; Urbanczik, R.; Perkins, M.; Aziz, M. A.; Pai, M., Fluorescence versus conventional sputum smear microscopy for tuberculosis: a systematic review. *Lancet Infect Dis* **2006,** *6* (9), 570-581.
153. Kinyoun, J. J., A Note on Uhlenhuths Method for Sputum Examination, For Tubercule Bacilli. *Am J Public Health* **1914,** *5* (9), 867-870.
154. Somoskovi, A.; Hotaling, J.; Fitzgerald, M.; O'Donnell, D.; Parsons, L.; Salfinger, M., Lessons From a Proficiency Testing Event for Acid-Fast Microscopy. *Chest* **2001,** *120* (1), 250-257.
155. Kurup, R.; Chester, K., Comparative evaluation of ziehl neelsen staining and knowledge, attitudes and practices of laboratory personnel in relation to ziehl nielsen. *West Indian Med J* **2014,** *63* (1), 34-9.

156. Sawadogo, T.; Savadogo, L.; Diande, S.; Ouedraogo, F.; Mourfou, A.; Gueye, A.; Sawadogo, I.; Nebié, B.; Sangare, L.; Ouattara, A., Comparaison des performances des colorations de Kinyoun et à l'auramine O, avec celle de Ziehl-Neelsen pour le diagnostic de la tuberculose au Centre national de lutte antituberculeuse du Burkina Faso [Comparison of Kinyoun, auramine O, and Ziehl-Neelsen staining for diagnosing tuberculosis at the National Tuberculosis Center in Burkina Faso]. *Med Sante Trop* **2012,** *22* (3), 302-306.
157. Van Deun, A.; Salim, A.; AUng, K.; Hossain, M. A.; Chambugonj, N.; Hye, M.; Kawria, A.; Declercq, E., Performance of variations of carbol fuschin staining of sputum smears for AFB under field conditions. *Int J Tuberc Lung Dis* **2005,** *9* (10), 1127-1133.
158. Khatun, Z.; Kamal, M.; Roy, C. K.; Sultana, T.; Rahman, M. Q.; Azad, M. B.; Ahmed, A. N., Usefulness of light emitting diode (LED) fluorescent microscopy as a tool for rapid and effective method for the diagnosis of pulmonary tuberculosis. *Bangladesh Med Res Counc Bull* **2011,** *37* (1), 7-10.
159. Gupta, S.; Shenoy, V.; Bairy, I.; Muralidharan, S., Comparison among three cold staining methods in the primary diagnosis of tuberculosis: a pilot study. *J Bras Pheumol* **2010,** *36* (5), 612-616.
160. Balakrishna, J.; Shahapur, P.; Chakradhar, P.; Hussein Saheb, S., Comparative Study of Different Staining Techniques - Ziehlneelsen Stain, Gabbet's Stain, Fluorochrome Stain for Detecting of Mycobacterium Tuberculosis in the Sputum. *J Pharm Sci & Res* **2013,** *5* (4), 89-92.
161. Manta, R.; Prabil, A.; Dalal, P., Comparison of staining techniques - Ziehl Neelsen stain, Gabbet's Stain, Fluorochrome stain for detection of mycobacterium tuberculosis in sputum. *Indian Journal of Microbiology Research* **2020,** *5* (1), 44-46.
162. Lahiri, K. K.; Chatterjee, S. K., A Simple Cold Staining Method for Acid Fast Bacilli. *Medical Journal Armed Forces India* **1994,** *50* (4), 256-258.
163. Hok, T., A Simple and Rapid Cold-Staining Method for Acid-Fast Bacteria. *Am Rev Respir Dise* **1962,** *85* (5), 753-754.
164. Shapiro, H. M.; Perlmutter, N. G., Killer applications: toward affordable rapid cell-based diagnostics for malaria and tuberculosis. *Cytometry B Clin Cytom* **2008,** *74 Suppl 1*, S152-64.
165. Truant, J.; Brett, W.; Thomas, W. J., Fluorescence Microscopy Of Tubercule Bacilli Stained with Auramine and Rhodamine. *Henry Ford Hosp Med Bull* **1962,** *10* (2), 287-296.
166. Hänscheid, T.; Ribeiro, C. M.; Shapiro, H. M.; Perlmutter, N. G., Fluorescence microscopy for tuberculosis diagnosis. *The Lancet Infectious Diseases* **2007,** *7* (4), 236-237.
167. Van Hung, N.; Sy, D. N.; Anthony, R. M.; Cobelens, F. G. J.; van Soolingen, D., Fluorescence microscopy for tuberculosis diagnosis. *The Lancet Infectious Diseases* **2007,** *7* (4), 238-239.
168. Richards, O., The Staining of Acid-Fast Tubercule Bacteria. *Science* **1941,** *93* (2408), 190.
169. Jarnagin, J. L.; Luchsinger, D. W., The use of fluorescein diacetate and ethidium bromide as a stain for evaluating viability of mycobacteria. *Stain Technol* **1980,** *55* (4), 253-8.
170. Schramm, B.; Hewison, C.; Bonte, L.; Jones, W.; Camelique, O.; Ruangweerayut, R.; Swaddiwudhipong, W.; Bonnet, M., Field evaluation of a simple fluorescence method for detection of viable Mycobacterium tuberculosis in sputum specimens during treatment follow-up. *J Clin Microbiol* **2012,** *50* (8), 2788-90.
171. Dezemon, Z.; Muvunyi, C. M.; Jacob, O., Staining techniques for detection of acid fast bacilli: what hope does fluorescein-diacetate (FDA) vitality staining technique represent for the monitoring of tuberculosis treatment in resource limited settings. *Trends in Bacteriology* **2014,** *1* (1).
172. Ryan, G. J.; Shapiro, H. M.; Lenaerts, A. J., Improving acid-fast fluorescent staining for the detection of mycobacteria using a new nucleic acid staining approach. *Tuberculosis* **2014,** *94* (5), 511-8.
173. Tuma, R.; Beaudet, M.; Jin, X.; Jones, L.; Cheung, C.; Yue, S.; Singer, V., Characterization of SYBR Gold Nucleic Acid Gel Stain: A Dye Optimized for Use with 300-nm Ultraviolet Transilluminators. *Anal Biochem* **1999,** *268* (2), 278-288.
174. Baliga, S.; Murphy, C.; Sharon, L.; Shenoy, S.; Biranthabail, D.; Weltman, H.; Miller, S.; Ramasamy, R.; Shah, J., Rapid method for detecting and differentiating Mycobacterium tuberculosis complex and non-tuberculous mycobacteria in sputum by fluorescence in situ hybridization with DNA probes. *Int J Infect Dis* **2018,** *75*, 1-7.
175. Shah, M.; Mishra, S.; Sakar, M.; Sudharshan, S., Automatic Detection and Classification of Tuberculosis Bacilli from Camera-enabled Smartphone Microscopic Images. *International Conference on Parallell, Distributed and Grid Computing* **2016,** *4*, 287-290.
176. St Amand, A. L.; Frank, D. N.; De Groote, M. A.; Basaraba, R. J.; Orme, I. M.; Pace, N. R., Use of specific rRNA oligonucleotide probes for microscopic detection of Mycobacterium tuberculosis in culture and tissue specimens. *J Clin Microbiol* **2005,** *43* (10), 5369-71.

177. Yuan, L.; Ke, Z.; Ma, J.; Li, Y., THe Fluorescence In Situ Hybridization for Diagnosis of Mycobacterium Tuberculosis Cmplex in Sputum Samples. *Ann Clin Lab Sci* **2015,** *45* (6), 631-638.
178. Lehtola, M. J.; Torvinen, E.; Miettinen, I. T.; Keevil, C. W., Fluorescence in situ hybridization using peptide nucleic acid probes for rapid detection of Mycobacterium avium subsp. avium and Mycobacterium avium subsp. paratuberculosis in potable-water biofilms. *Appl Environ Microbiol* **2006,** *72* (1), 848-53.
179. Stender, H.; Lund, K.; Petersen, K.; Rasmussen, O.; Hongmanee, P.; Miorner, H.; Godtfredsen, S., Fluorescence In Situ Hybridization Assay Using Peptide Nucleic Acid Probes for Differentiation between Tuberculous and Nontuberculous Mycobacterium Species in Smears of Mycbacterium Cultures. *J Clin Micro* **1999,** *37* (9), 2760-2765.
180. Kim, N.; Lee, S. H.; Yi, J.; Chang, C. L., Evaluation of dual-color fluorescence in situ hybridization with peptide nucleic acid probes for the detection of Mycobacterium tuberculosis and non-tuberculous mycobacteria in clinical specimens. *Ann Lab Med* **2015,** *35* (5), 500-5.
181. Shah, J.; Weltman, H.; Narciso, P.; Murphy, C.; Poruri, A.; Baliga, S.; Sharon, L.; York, M.; Cunningham, G.; Miller, S.; Caviedes, L.; Gilman, R.; Desmond, E.; Ramasamy, R., Dual color fluorescence in situ hybridization (FISH) assays for detecting Mycobacterium tuberculosis and Mycobacterium avium complexes and related pathogens in cultures. *PLoS One* **2017,** *12* (4), e0174989.
182. Kamariza, M.; Shieh, P.; Ealand, C. E.; Peters, J. S.; Chu, B.; Rodrigues-Rivera, F. P.; Sait, M. R. B.; Treuren, W. V.; Martinson, N.; Kalscheuer, R.; Kana, B. D.; Bertozzi, C. R., Rapid detection of Mycobacterium tuberculosis in sputum with a solvatochromic trehalose probe. *Sci Trans Med* **2018,** *10* (430), 1-12.
183. Hanscheid, T., The future looks bright: low-cost fluorescent microscopes for detection of Mycobacterium tuberculosis and Coccidiae. *Trans R Soc of Trop Med Hyg* **2008,** *102* (6), 520-1.
184. Van Deun, A.; Aung, K. J.; Khan, M. H.; de Jong, B. C.; Gumusboga, M.; Hossain, M. A., An operational study comparing microscopes and staining variations for tuberculosis LED FM. *Int J Tuberc Lung Dis* **2014,** *18* (8), 964-71.
185. Alfred, N.; Lovette, L.; Aliyu, G.; Olusegun, O.; Meshak, P.; Jilang, T.; Iwakun, M.; Nnamdi, E.; Olubunmi, O.; Dakum, P.; Abimiku, A., Optimising Mycobacterium tuberculosis detection in resource limited settings. *BMJ Open* **2014,** *4* (3), e004093.
186. PRIMO STAR ILED. https://www.finddx.org/pricing/primo-star-iled/ (accessed 2 February 2022).
187. ZEISS Primo Start iLED. https://www.zeiss.com/microscopy/us/products/light-microscopes/primo-star-iled.html - stop (accessed 2 February 2022).
188. CyScope Fluorescence Microscope In *Online*, partec, Ed. Munster, Germany, 2020.
189. Laboratory microscope/optical/fluorescence/binocular CyScope HP Sysmex Partec GmbH. https://healthmanagement.org/products/view/laboratory-microscope-optical-fluorescence-binocular-cyscope-r-hp-sysmex-partec-gmbh (accessed 2 February 2022).
190. Gwanzura, L.; Mayini, J.; Mabhanga, K.; Chipinduro, J.; Mashamba, K.; Mutenherwa, M.; Mutambu, S. L.; Mutsvangwa, J.; Mason, P. R., Evaluation of "Cyscope", a novel fluorescence-based microscopy technique for the detection of malaria. *J Infect Dev Ctries* **2012,** *6* (2), 212-5.
191. Lehman, L. G.; Ngapmen Yamadji, A. L.; Ngo Sack, F.; Bilong Bilong, C. F., The CyScope(R) fluorescence microscope, a reliable tool for tuberculosis diagnosis in resource-limited settings. *Am J Trop Med Hyg* **2010,** *83* (4), 906-8.
192. Tapley, A.; Switz, N.; Reber, C.; Davis, J. L.; Miller, C.; Matovu, J. B.; Worodria, W.; Huang, L.; Fletcher, D. A.; Cattamanchi, A., Mobile digital fluorescence microscopy for diagnosis of tuberculosis. *J Clin Microbiol* **2013,** *51* (6), 1774-8.
193. Lu, Q.; Liu, G.; Xiao, C.; Hu, C.; Zhang, S.; Xu, R. X.; Chu, K.; Xu, Q.; Smith, Z. J., A modular, open-source, slide-scanning microscope for diagnostic applications in resource-constrained settings. *PLoS One* **2018,** *13* (3), e0194063.
194. Cybulski, J. S.; Clements, J.; Prakash, M., Foldscope: origami-based paper microscope. *PLoS One* **2014,** *9* (6), e98781.
195. Kaur, T.; Dahiya, S.; Satija, S. H.; Nawal, S. J.; Kshetrimayum, N.; Ningthoujam, J.; Chahal, A. K.; Rao, A., Foldscope as a primary diagnostic tool for oral and urinary tract infections and its effectiveness in oral health education. *J Microsc* **2020,** *279* (1), 39-51.
196. Naqvi, A.; Manglik, N.; Dudrey, E.; Perry, C.; Mulla, Z. D.; Cervantes, J. L., Evaluating the performance of a low-cost mobile phone attachable microscope in cervical cytology. *BMC Womens Health* **2020,** *20* (1), 60.

197. Ephraim, R. K.; Duah, E.; Cybulski, J. S.; Prakash, M.; D'Ambrosio, M. V.; Fletcher, D. A.; Keiser, J.; Andrews, J. R.; Bogoch, II, Diagnosis of Schistosoma haematobium infection with a mobile phone-mounted Foldscope and a reversed-lens CellScope in Ghana. *Am J Trop Med Hyg* **2015,** *92* (6), 1253-6.
198. Breslauer, D. N.; Maamari, R. N.; Switz, N. A.; Lam, W. A.; Fletcher, D. A., Mobile phone based clinical microscopy for global health applications. *PLoS One* **2009,** *4* (7), e6320.
199. Skandarajah, A.; Reber, C. D.; Switz, N. A.; Fletcher, D. A., Quantitative Imaging with a Mobile Phone Microscope. *PLoS One* **2014,** *9* (5), e96906.
200. Vandeventer, P. E.; Lin, J. S.; Zwang, T. J.; Nadim, A.; Johal, M. S.; Niemz, A., Multiphasic DNA adsorption to silica surfaces under varying buffer, pH, and ionic strength conditions. *J Phys Chem B* **2012,** *116* (19), 5661-70.
201. Lee, S. B.; Shewale, J. G., DNA Extraction Methods in Forensic Analysis. In *Encyclopedia of Analytical Chemistry*, 2017; pp 1-18.
202. Mason, P.; Nielson, G.; Dempsey, C.; Barnes, A.; Cruickshank, The hydration structure of guanidinium and thiocyanate ions: Implications for protein stability in aqueous solution. *PNAS* **2003,** *100* (8), 4557-4561.
203. Bordelon, H.; Russ, P. K.; Wright, D. W.; Haselton, F. R., A magnetic bead-based method for concentrating DNA from human urine for downstream detection. *PLoS One* **2013,** *8* (7), e68369.
204. Chakravorty, S.; Simmons, A. M.; Rowneki, M.; Pamar, H.; Cao, Y.; Ryan, J.; Banada, P. P.; Deshpande, S.; Shenai, S.; Gall, A.; Glass, J.; Krieswirth, B.; Schumacher, S. G.; Nabeta, P.; Tukvadze, N.; Rodrigues, C.; Skrahina, A.; Tagliani, E.; Cirillo, D. M.; Davidow, A.; Dekinger, C. M.; Persing, D.; Kwiatkowski, R.; Jones, M.; Alland, D., The New Xpert MTB/RIF Ultra: Improving Detection of Mycobacterium tuberculosis and Resistance to Rifampin in an Assay Suitable for Point-of-Care Testing. *mBio* **2017,** *8* (4), e00812-17.
205. D'Amato, R. F.; Wallman, A. A.; Hochstein, L. H.; Colaninno, P. M.; Scardamaglia, M.; Ardila, E.; Ghouri, M.; Kim, K.; Patel, R. C.; Miller, A., Rapid Diagnosis of Pulmonary Tuberculosis by Using Roche AMPLICOR Mycobacterium tuberculosis PCR Test. *J Clin Micro* **1995,** *33* (7), 1832-1834.
206. Ozkutuk, A.; Kidar, S.; Ozden, S.; Esen, N., Evaluation of Cobas Amplicor MTB Test to detect Mycobacterium tuberculosis in pulmonary and extrapulmonary specimens. *New Microbiol* **2006,** *29* (4), 269-273.
207. Hillemann, D.; Rusch-Gerdes, S.; Richter, E., Evaluation of the GenoType MTBDRplus assay for rifampin and isoniazid susceptibility testing of Mycobacterium tuberculosis strains and clinical specimens. *J Clin Microbiol* **2007,** *45* (8), 2635-40.
208. Bordelon, H.; Adams, N. M.; Klemm, A. S.; Russ, P. K.; Williams, J. V.; Talbot, H. K.; Wright, D. W.; Haselton, F. R., Development of a low-resource RNA extraction cassette based on surface tension valves. *ACS Appl Mater Interfaces* **2011,** *3* (6), 2161-8.
209. Bitting, A. L.; Bordelon, H.; Baglia, M. L.; Davis, K. M.; Creecy, A. E.; Short, P. A.; Albert, L. E.; Karhade, A. V.; Wright, D. W.; Haselton, F. R.; Adams, N. M., Automated Device for Asynchronous Extraction of RNA, DNA, or Protein Biomarkers from Surrogate Patient Samples. *J Lab Autom* **2016,** *21* (6), 732-742.
210. Creecy, A.; Russ, P. K.; Solinas, F.; Wright, D. W.; Haselton, F. R., Tuberculosis Biomarker Extraction and Isothermal Amplification in an Integrated Diagnostic Device. *PLoS One* **2015,** *10* (7), 1-14.
211. Bordelon, H.; Ricks, K. M.; Pask, M. E.; Russ, P. K.; Solinas, F.; Baglia, M. L.; Short, P. A.; Nel, A.; Blackburn, J.; Dheda, K.; Zamudio, C.; Caceres, T.; Wright, D. W.; Haselton, F. R.; Pettit, A. C., Design and use of mouse control DNA for DNA biomarker extraction and PCR detection from urine: Application for transrenal Mycobacterium tuberculosis DNA detection. *J Microbiol Methods* **2017,** *136*, 65-70.
212. Schramm, B.; Nganaboy, R. C.; Uwiragiye, P.; Mukeba, D.; Abdoubara, A.; Abdou, I.; Nshimiymana, J. C.; Sounna, S.; Hiffler, L.; Flevaud, L.; Huerga, H., Potential value of urine lateral-flow lipoarabinomannan (LAM) test for diagnosing tuberculosis among severely acute malnourished children. *PLoS One* **2021,** *16* (5), e0250933.
213. Nicol, M. P.; Schumacher, S. G.; Workman, L.; Broger, T.; Baard, C.; Prins, M.; Bateman, L.; du Toit, E.; van Heerden, J.; Szekely, R.; Zar, H. J.; Denkinger, C. M., Accuracy of a Novel Urine Test, Fujifilm SILVAMP Tuberculosis Lipoarabinomannan, for the Diagnosis of Pulmonary Tuberculosis in Children. *Clin Infect Dis* **2021,** *72* (9), e280-e288.
214. Mullis, K., The Unusual Origin of the Polymerase Chain Reaction. *Sci Am* **1990,** *262* (4), 56-65.
215. Saiki, R.; Scharf, S.; Faloona, F.; Mullis, K.; Horn, G.; Erlich, H.; Arnheim, N., Enzymatic Amplification of B-Globin Genomic Sequences and Restriction Site Analysis for Diagnosis of Sickle Cell Anemia. *Science* **1985,** *230* (4732), 1350-1354.

216. Saito, M.; Kondo, A.; Kato, T.; Yamada, Y., Frequency-Volume Charts: Comparison of Frequency between Elderly and Adult Patients. *British Journal of Urology* **1993,** *72* (1), 38-41.
217. Adams, N. M.; Gabella, W. E.; Hardcastle, A. N.; Haselton, F. R., Adaptive PCR Based on Hybridization Sensing of Mirror-Image l-DNA. *Anal Chem* **2017,** *89* (1), 728-735.
218. Euliano, E. M.; Hardcastle, A. N.; Victoriano, C. M.; Gabella, W. E.; Haselton, F. R.; Adams, N. M., Multiplexed Adaptive RT-PCR Based on L-DNA Hybridization Monitoring for the Detection of Zika, Dengue, and Chikungunya RNA. *Sci Rep* **2019,** *9* (1), 11372.
219. Mishra, A. K.; Driessen, N. N.; Appelmelk, B. J.; Besra, G. S., Lipoarabinomannan and related glycoconjugates: structure, biogenesis and role inMycobacterium tuberculosisphysiology and host–pathogen interaction. *FEMS Microbiology Reviews* **2011,** *35* (6), 1126-1157.
220. Minion, J.; Leung, E.; Talbot, E.; Dheda, K.; Pai, M.; Menzies, D., Diagnosing tuberculosis with urine lipoarabinomannan: systematic review and meta-analysis. *Eur Respir J* **2011,** *38* (6), 1398-405.
221. Peter, J. G.; Theron, G.; van Zyl-Smit, R.; Haripersad, A.; Mottay, L.; Kraus, S.; Binder, A.; Meldau, R.; Hardy, A.; Dheda, K., Diagnostic accuracy of a urine lipoarabinomannan strip-test for TB detection in HIV-infected hospitalised patients. *Eur Respir J* **2012,** *40* (5), 1211-20.
222. Peter, J. G.; Zijenah, L. S.; Chanda, D.; Clowes, P.; Lesosky, M.; Gina, P.; Mehta, N.; Calligaro, G.; Lombard, C. J.; Kadzirange, G.; Bandason, T.; Chansa, A.; Liusha, N.; Mangu, C.; Mtafya, B.; Msila, H.; Rachow, A.; Hoelscher, M.; Mwaba, P.; Theron, G.; Dheda, K., Effect on mortality of point-of-care, urine-based lipoarabinomannan testing to guide tuberculosis treatment initiation in HIV-positive hospital inpatients: a pragmatic, parallel-group, multicountry, open-label, randomised controlled trial. *The Lancet* **2016,** *387* (10024), 1187-1197.
223. Lateral flow urine lipoarabinomannan assay (LF-LAM) for the diagnosis of active tuberculosis in people living with HIV. Policy update (2019). Organization, W. H., Ed. World Health Organization: Geneva, Switzerland, 2019.
224. Broger, T.; Sossen, B.; du Toit, E.; Kerkhoff, A. D.; Schutz, C.; Ivanova Reipold, E.; Ward, A.; Barr, D. A.; Macé, A.; Trollip, A.; Burton, R.; Ongarello, S.; Pinter, A.; Lowary, T. L.; Boehme, C.; Nicol, M. P.; Meintjes, G.; Denkinger, C. M., Novel lipoarabinomannan point-of-care tuberculosis test for people with HIV: a diagnostic accuracy study. *The Lancet Infectious Diseases* **2019,** *19* (8), 852-861.
225. Mitamura, K.; Shimizu, H.; Yamazaki, M.; Ichikawa, M.; Nagai, K.; Katada, J.; Wada, A.; Kawakami, C.; Sugaya, N., Clinical evaluation of highly sensitive silver amplification immunochromatography systems for rapid diagnosis of influenza. *J Virol Methods* **2013,** *194* (1-2), 123-8.
226. Sigal, G.; Pinter, A.; Lowary, T.; Kawasaki, M.; Li, A.; Mathew, A.; Tsionsky, M.; Zheng, R.; Plisova, T.; Shen, K.; Katsuragi, K.; Choudhary, A.; Honnen, W.; Nahid, P.; Denkinger, C.; Broger, T., A Novel Sensitive Immunoassay Targeting the 5-Methylthio-D-Xylofuranose-Lipoarabinomannan Epitope Meets the WHO's Performance Target for Tuberculosis Diagnosis. *J Clin Micro* **2018,** *56* (12), 1-17.
227. Kroidl, I.; Clowes, P.; Mwakyelu, J.; Maboko, L.; Kiangi, A.; Rachow, A.; Reither, K.; Jung, J.; Nsojo, A.; Saathoff, E.; Hoelscher, M., Reasons for false-positive lipoarabinomannan ELISA results in a Tanzanian population. *Scand J Infect Dis* **2014,** *46* (2), 144-8.
228. The WHO Standard Tuberculin Test. Sante, O. M. d. l., Ed. World Health Organization: 1963; pp 1-20.
229. Dacso, C., Chapter 47 - Skin Testing for Tuberculosis. In *Clinical Methods: The History, Physical, and Laboratory Examinations. 3rd edition.*, Walker, H.; Hall, W.; Hurst, J., Eds. Buttersworth: Boston, MA, 1990.
230. Rose, D.; Schechter, C.; Alder, J., Interpretation of the Tuberculin Skin Test. *J Gen Intern Med* **1995,** *10* (11), 635-642.
231. Campbell, J. R.; Krot, J.; Elwood, K.; Cook, V.; Marra, F., A systematic review on TST and IGRA tests used for diagnosis of LTBI in immigrants. *Mol Diagn Ther* **2015,** *19* (1), 9-24.
232. Slater, M. L.; Welland, G.; Pai, M.; Parsonnet, J.; Banaei, N., Challenges with QuantiFERON-TB Gold assay for large-scale, routine screening of U.S. healthcare workers. *Am J Respir Crit Care Med* **2013,** *188* (8), 1005-10.
233. Takasaki, J.; Manabe, T.; Morino, E.; Muto, Y.; Hashimoto, M.; Iikura, M.; Izumi, S.; Sugiyama, H.; Kudo, K., Sensitivity and specificity of QuantiFERON-TB Gold Plus compared with QuantiFERON-TB Gold In-Tube and T-SPOT.TB on active tuberculosis in Japan. *J Infect Chemother* **2018,** *24* (3), 188-192.
234. QuantiFERON-TB Gold (QFT) ELISA Package Insert. In www.QuantiFERON.com, Qiagen: 2016.
235. QuantiFERON-TB Gold Plus (QFT-Plus) Package Insert. In www.QuantiFERON.com, Qiagen, Ed. Germantown, MD, 2019; Vol. Rev. 6, pp 1-72.

236. Meier, T.; Eulenbruch, H. P.; Wrighton-Smith, P.; Enders, G.; Regnath, T., Sensitivity of a new commercial enzyme-linked immunospot assay (T SPOT-TB) for diagnosis of tuberculosis in clinical practice. *Eur J Clin Microbiol Infect Dis* **2005,** *24* (8), 529-36.
237. The T-SPOT.TB Test FAQ. https://www.oxforddiagnosticlaboratories.eu/resources/faqs/.
238. Pearlman, S. I.; Leelawong, M.; Richardson, K. A.; Adams, N. M.; Russ, P. K.; Pask, M. E.; Wolfe, A. E.; Wessely, C.; Haselton, F. R., Low Resource Nucleic Acid Extraction Method Enabled by High-Gradient Magnetic Separation. *ACS Appl Mater Interfaces* **2020,** *12* (11), 12457-12467.
239. *Global Tuberculosis Report 2018*; World Health Organization: Geneva, 2018.
240. Cambanis, A.; Ramsay, A.; Wirkom, V.; Tata, E.; Cuevas, L. E., Investing time in microscopy: an opportunity to optimise smear-based case detection of tuberculosis. *Int J Tuberc Lung Dis* **2007,** *11* (1), 40-45.
241. Green, C.; Hugett, J. F.; Talbot, E.; Mwaba, P.; Reither, K.; Zumla, A., I, Rapid diagnosis of tuberculosis through the detection of mycobacterial DNA in urine by nucleic acid amplification methods. *Lancet Infectious Disease* **2009,** *9*, 505-511.
242. Sur, K.; McFall, S. M.; Yeh, E. T.; Jangam, S. R.; Hayden, M. A.; Stroupe, S. D.; Kelso, D. M., Immiscible phase nucleic acid purification eliminates PCR inhibitors with a single pass of paramagnetic particles through a hydrophobic liquid. *The Journal of molecular diagnostics : JMD* **2010,** *12* (5), 620-8.
243. Aguilar-Arteaga, K.; Rodriguez, J. A.; Barrado, E., Magnetic solids in analytical chemistry: a review. *Anal Chim Acta* **2010,** *674* (2), 157-65.
244. Long, Z.; Shetty, A. M.; Solomon, M. J.; Larson, R. G., Fundamentals of magnet-actuated droplet manipulation on an open hydrophobic surface. *Lab on a chip* **2009,** *9* (11), 1567-75.
245. Berry, S. M.; Pezzi, H. M.; LaVanway, A. J.; Guckenberger, D. J.; Anderson, M. A.; Beebe, D. J., AirJump: Using Interfaces to Instantly Perform Simultaneous Extractions. *ACS Appl Mater Interfaces* **2016,** *8* (24), 15040-5.
246. Kolm, H. H.; Oberteuffer, J. A.; Kelland, D. R., High-gradient magnetic separation. *Scientific American* 1975, pp 45-54.
247. Oberteuffer, J. A., High Gradient Magnetic Separation. *IEEE Transactions on Magnetics* **1973,** *9* (3), 303-306.
248. Mitchell, R.; Bitton, G.; Oberteuffer, J. A., High Gradient Magnetic Filtration of Magnetic and Non-Magnetic Contaminants from Water. *Separ Purif Method* **1975,** *4* (2), 267-303.
249. Oberteuffer, J. A.; Wechsler, I.; Marston, P. G.; Mcnallan, M. J., High Gradient Magnetic Filtration of Steel Mill Process and Waste-Waters. *Ieee T Magn* **1975,** *11* (5), 1591-1593.
250. Gerber, R.; Birss, R. R., *High Gradient Magnetic Separation*. Research Studies Press: 1983.
251. Beall, S. G.; Cantera, J.; Diaz, M., H; Winchell, J. M.; Lillis, L.; White, H.; Kalnoky, M.; Gallarda, J.; Boyle, D. S., Diagnostic Performance and Workflow Assessment of Six Nucleic Acid Extraction Technologies for Suitability in Resource Limited Settings. *PLoS One* **2019,** *14* (4).
252. Sanders, N. N.; van Rompey, E.; de Smedt, S. C.; Demeester, J., Structural Alterations of Gene Complexes by Cystic Fibrosis. *Am J Respir Crit Care Med* **2001,** *164* (3), 486-493.
253. Ogusku, M. M.; Salem, J. I., Analysis of different primers used in the PCR method: diagnosis of tuberculosis in the state of Amazons, Brazil. *J. Bras. Pneumol.* **2004,** *30* (4), 433-439.
254. Ramakers, C.; Ruijter, J. M.; Deprez, R. H. L.; Moorman, A. F. M., Assumption-free analysis of quantitative real-time polymerase chain reaction (PCR) data. *Neuroscience Letters* **2003,** *339* (1), 62-66.
255. Ruijter, J. M.; Ramakers, C.; Hoogaars, W. M. H.; Karlen, Y.; Bakker, O.; van den Hoff, M. J. B.; Moorman, A. F. M., Amplification efficiency: linking baselike and bias in the analysis of quantitative PCR data. *Nucleic Acids Research* **2009,** *37* (6), e45-e45.
256. Farrell Jr., R. E., RNA Methodologies: Laboratory Guide for Isolation and Characterization. Fifth Edition ed.; Academic Press: 2017.
257. Schenck, J., The role of magnetic susceptibility in magnetic resonance imaging: MRI magnetic compatibility of the first and second kinds. *Medical Physics* **1996,** *23* (6), 815-850.
258. Cantera, J. L.; White, H.; Diaz, M. H.; Beall, S. G.; Winchell, J. M.; Lillis, L.; Kalnoky, M.; Gallarda, J.; Boyle, D. S., Assessment of eight nucleic acid amplification technologies for potential use to detect infectious agents in low-resource settings. *PLoS One* **2019,** *14* (4), e0215756.
259. Kishore, R.; Reef Hardy, W.; Anderson, V. J.; Sanchez, N. A.; Buoncristiani, M. R., Optimization of DNA extraction from low-yield and degraded samples using the BioRobot EZ1 and BioRobot M48. *J Forensic Sci* **2006,** *51* (5), 1055-61.

260. He, H.; Li, R.; Chen, Y.; Pan, P.; Tong, W.; Dong, X.; Chen, Y.; Yu, D., Integrated DNA and RNA extraction using magnetic beads from viral pathogens causing acute respiratory infections. *Sci Rep* **2017,** *7*, 45199.
261. Cook, L.; Starr, K.; Boonyaratanakornkit, J.; Hayden, R.; Sam, S. S.; Caliendo, A. M., Does Size Matter? Comparison of Extraction Yields for Different-Sized DNA Fragments by Seven Different Routine and Four New Circulating Cell-Free Extraction Methods. *J Clin Microbiol* **2018,** *56* (12).
262. Oreskovic, A.; Brault, N. D.; Panpradist, N.; Lai, J. J.; Lutz, B. R., Analytical Comparison of Methods for Extraction of Short Cell-Free DNA from Urine. *The Journal of molecular diagnostics : JMD* **2019,** *21* (6), 1067-1078.
263. Owen, C. S., High Gradient Magnetic Separation of Erythrocytes. *Biophysical Journal* **1978,** *22* (2), 171-178.
264. Dobby, G.; FInch, J. A., Capture of mineral particles in a high gradient magnetic field. *Powder Technology* **1977,** *17* (1), 73-82.
265. Gijs, M. A. M., Magnetic bead handling on-chip: new opportunities for analytical applications. *Microfluidics and Nanofluidics* **2004,** *1*, 22-40.
266. Gao, Y.; Beerens, J.; van Reenen, A.; Hulsen, M. A.; de Jong, A. M.; Prins, M. W.; den Toonder, J. M., Strong vortical flows generated by the collective motion of magnetic particle chains rotating in a fluid cell. *Lab on a chip* **2015,** *15* (1), 351-60.
267. Sato, M.; Kobayashi, T., A fundamental study of the flow past a cylinder using Abaqus/CFD. In *3DS SIMULIA Conference*, Providence, RI, 2012.
268. Oberteuffer, J. A., Magnetic Separation: A Review of Principles, Devices, and Applications. *IEEE Transactions on Magnetics* **1974,** *10* (2), 223-238.
269. Ferguson, T. M.; Weigel, K. M.; Lakey Becker, A.; Ontengco, D.; Narita, M.; Tolstorukov, I.; Doebler, R.; Cangelosi, G. A.; Niemz, A., Pilot study of a rapid and minimally instrumented sputum sample preparation method for molecular diagnosis of tuberculosis. *Sci Rep* **2016,** *6*, 19541.
270. Davis, K. M.; Gibson, L. E.; Haselton, F. R.; Wright, D. W., Simple sample processing enhances malaria rapid diagnostic test performance. *Analyst* **2014,** *139* (12), 3026-31.
271. Pai, M.; Clouse, K.; Blevins, M.; Lindegren, M. L.; Yotebieng, M.; Nguyen, D. T.; Omondi, A.; Michael, D.; Zannou, D. M.; Carriquiry, G.; Pettit, A., Low implementation of Xpert MTB/RIF among HIV/TB co-infected adults in the International epidemiologic Databases to Evaluate AIDS (IeDEA) program. *Plos One* **2017,** *12* (2).
272. Theron, G.; Zijenah, L.; Chanda, D.; Clowes, P.; Rachow, A.; Lesosky, M.; Bara, W.; Mungofa, S.; Pai, M.; Hoelscher, M.; Dowdy, D.; Pym, A.; Mwaba, P.; Mason, P.; Peter, J.; Dheda, K., Feasibility, accuracy, and clinical effect of point-of-care Xpert MTB/RIF testing for tuberculosis in primary-care settings in Africa: a multicentre, randomised, controlled trial. *Lancet* **2014,** *383* (9915), 424-435.
273. Cox, H.; Dickson-Hall, L.; Ndjeka, N.; Van't Hoog, A.; Grant, A.; Cobelens, F.; Stevens, W.; Nicol, M., Delays and loss to follow-up before treatment of drug-resistant tuberculosis following implementation of Xpert MTB/RIF in South Africa: A retrospective cohort study. *PLoS Med* **2017,** *14* (2), e1002238.
274. Magana Vergara, C.; Kallenberg, C. J. L.; Rogasch, M.; Hubner, C. G.; Song, Y. H., A versatile vector for mycobacterial protein production with a functional minimized acetamidase regulon. *Protein Sci* **2017,** *26* (11), 2302-2311.
275. Goude, R.; Parish, T., Chapter 13 - Electroporation of Mycobacteria. In *Mycobacteria Protocols*, 2 ed.; Parish, T.; Brown, A. C., Eds. Humana Press: Totowa, NJ, 2008; Vol. 465, pp 203-215.
276. Shea, T. M., Durable Hydrophobic Surface Coatings Using Silicone Resins. **2008,** *US7344783B2*.
277. Shea, T. M. Durable Hydrophobic Surface Coatings Using Silicone Resins. 2005.
278. Jamieson, D. T.; Irving, J. B., Thermal Conductivity of Silicone Oils of the Polymethylphenyl Siloxane Type. In *Thermal Conductivity 14*, 1 ed.; Klemens, P. G.; Chu, T. K., Eds. Springer, Boston, MA: 1976; pp 279-286.
279. Ishkhanov, A. M.; Nemzer, V. G.; Pugach, V. V.; Rastorguev, Y. L., Thermal Conductivity of Polymethylphenylsiloxanes at High Pressures. *J of Eng Phys* **1975,** *29*, 1547-1550.
280. Chemical, D., SYLGARD 184 Silicone Elastomer - Technical Data Sheet. The Dow Chemical Company: 2017; p 1.
281. DuPont, Teflon PTFE fluoropolymer resin - Properties Handbook. DuPont Fluoroproducts: 1996; p 23.
282. Touloukian, Y. S.; Powell, R. W.; Ho, C. Y.; Klemens, P. G., *Thermal Conductivity - Nonmetalic Solids*. Plenuum Publishing Corporation: New York, NY, 1970; Vol. 2, p 1302.

283. Thuau, D.; Koymen, I.; Cheung, R., A microstructure for thermal conductivity measurement of conductive thin films. *Microelectron Eng* **2011,** *88* (8), 2408-2412.
284. Huang, D.; Swanson, E. A.; Lin, C. P.; Schuman, J. S.; Stinson, W. G.; Chang, W.; Hee, M. R.; Flotte, T.; Gregory, K.; Puliafito, C. A., Optical coherence tomography. *Science* **1991,** *254* (5035), 1178-1181.
285. Chedore, P.; Th'ng, C.; Nolan, D. H.; Churchwell, G. M.; Sieffert, D. E.; Hale, Y. M.; Jamieson, F., Method for inactivating and fixing unstained smear preparations of mycobacterium tuberculosis for improved laboratory safety. *J Clin Microbiol* **2002,** *40* (11), 4077-80.
286. Schneider, C. A.; Rasband, W. S.; Eliceiri, K. W., NIH Image to ImageJ: 25 years of image analysis. *Nat Methods* **2012,** *9* (7), 671-5.
287. Hu, H.; Larson, R. G., Analysis of the Microfluidic Flow in an Evaporating Sessile Droplet. *Langmuir* **2005,** *21*, 3963-3971.
288. Barash, L. Y.; Bigioni, T. P.; Vinokur, V. M.; Shchur, L. N., Evaporation and fluid dynamics of a sessile drop of capillary size. *Phys Rev E Stat Nonlin Soft Matter Phys* **2009,** *79* (4), 1-16.
289. Brutin, D.; Sobac, B.; Loquet, B.; Sampol, J., Pattern formation in drying drops of blood. *Journal of Fluid Mechanics* **2010,** *667*, 85-95.
290. Rathaur, V. S.; Kumar, S.; Panigrahi, P. K.; Panda, S., Investigating the Effect of Antibody-Antigen Reactions on the Internal Convection in a Sessile Droplet via Microparticle Image Velocimetry and DLVO Analysis. *Langmuir* **2020,** *36* (30), 8826-8838.
291. Stetten, A. Z.; Iasella, S. V.; Corcoran, T. E.; Garoff, S.; Przybycien, T. M.; Tilton, R. D., Surfactant-induced Marangoni transport of lipids and therapeutics within the lung. *Curr Opin Colloid Interface Sci* **2018,** *36*, 58-69.
292. Yano, Y. F.; Ina, T.; Uruga, T., Understanding the Dynamics of a Lipid Monolayer on a Water Surface under a Marangoni Flow. *Colloids and Interfaces* **2021,** *5* (2).
293. Trantidou, T.; Elani, Y.; Parsons, E.; Ces, O., Hydrophilic surface modification of PDMS for droplet microfluidics using a simple, quick, and robust method via PVA deposition. *Microsyst* **2017,** *3* (1).
294. Spitze, L. A.; Richards, D. O., Surface Studies of Glass. Part I. Contact Angles. *J App Phys* **1947,** *18* (10), 904-911.
295. Sumner, A. L.; Menke, E. J.; Dubowski, Y.; Newberg, J. T.; Penner, R. M.; Hemminger, J. C.; Wingen, L. M.; Brauers, T.; Finlayson-Pitts, B. J., The nature of water on surfaces of laboratory systems and implications for heterogeneous chemistry in the troposphere. *Phys Chemi Chem Phys* **2004,** *6* (3), 604-613.
296. Schatz, M. F.; Neitzel, G. P., Experiments on Thermocapillary Instability. *Annu. Rev. Fluid. Mech.* **2001,** *33*, 93-127.
297. Hobby, G. L.; Holman, A. P.; Iseman, M. D.; Jones, J. M., Enumeration of tubercle bacilli in sputum of patients with pulmonary tuberculosis. *Antimicrob Agents Chemother* **1973,** *4* (2), 94-104.
298. Steingart, K. R.; Ng, V.; Henry, M.; Hopewell, P. C.; Ramsay, A.; Cunningham, J.; Urbanczik, R.; Perkins, M. D.; Aziz, M. A.; Pai, M., Sputum processing methods to improve the sensitivity of smear microscopy for tuberculosis: a systematic review. *Lancet Infect Dis* **2006,** *6* (10), 664-674.
299. Ghodbane, R.; Drancourt, M., Magnetic bead protocol for culturing Mycobacterium tuberculosis from sputum specimens. *J Clin Micro* **2013,** *51* (5), 1578-9.
300. Peterson, E. M.; Nakasone, A.; Platon-DeLeon, J. M.; Jang, Y.; de la Maza, L.; Desmond, E., Comparison of Direct and Concentrated Acid-Fast Smears to Identify Specimens Culture Positive for Mycobacterium spp. *J Clin Microbiol* **1999,** *37* (11), 3564-3568.
301. Albert, H.; Ademun, P. J.; Lukyamuzi, G.; Nyesiga, B.; Manabe, Y.; Joloba, M.; Wilson, S.; Perkins, M. D., Feasibility of magnetic bead technology for concentration of mycobacteria in sputum prior to fluorescence microscopy. *BMC Infect Dis* **2011,** *11* (1).
302. Wilson, S.; Lane, A.; Rosedale, R.; Stanley, C., Concentration of Mycobacterium tuberculosis from sputum using ligand-coated magnetic beads. *Int J Tuberc Lung Dis* **2010,** *14* (9), 1164-1168.
303. Sahile, H. A.; Rens, C.; Shapira, T.; Andersen, R. J.; Av-Gay, Y., DMN-Tre Labeling for Detection and High-Content Screening of Compounds against Intracellular Mycobacteria. *ACS Omega* **2020,** *5* (7), 3661-3669.
304. Jeon, K.; Koh, W.-J.; Kwon, O. J.; Suh, G. Y.; Kim, H.; Lee, N. Y.; Park, Y. K.; Bai, G. H., Recovery rate of NTM from AFB smear-positive sputum speciments at a medical centre in South Korea. *Int J Tuberc Lung Dis* **2005,** *9* (9), 1046-1051.
305. Yoon, S. H.; Lee, N. K.; Yim, J. J., Impact of sputum gross appearance and volume on smear positivity of pulmonary tuberculosis: a prospective cohort study. *BMC Infect Dis* **2012,** *12* (172), 1-8.

306. Salehi-Reyhani, A.; Sharma, S.; Burgin, E.; Barclay, M.; Cass, A.; Neil, M. A.; Ces, O.; Willison, K. R.; Klug, D. R.; Brown, A.; Novakova, M., Scaling advantages and constraints in miniaturized capture assays for single cell protein analysis. *Lab on a chip* **2013,** *13* (11), 2066-74.
307. Huerga, H.; Cossa, L.; Manhica, I.; Bastard, M.; Telnov, A.; Molfino, L.; Sanchez-Padilla, E., Systematic, Point-of-Care Urine Lipoarabinomannan (Alere TB-LAM) Assay for Diagnosing Tuberculosis in Severely Immunocompromised HIV-Positive Ambulatory Patients. *Am J Trop Med Hyg* **2020,** *102* (3), 562-566.
308. Khoo, K. H.; Tang, J. B.; Chatterjee, D., Variation in mannose-capped terminal arabinan motifs of lipoarabinomannans from clinical isolates of Mycobacterium tuberculosis and Mycobacterium avium complex. *J Biol Chem* **2001,** *276* (6), 3863-71.
309. Angala, S. K.; McNeil, M. R.; Shi, L.; Joe, M.; Pham, H.; Zuberogoitia, S.; Nigou, J.; Boot, C. M.; Lowary, T. L.; Gilleron, M.; Jackson, M., Biosynthesis of the Methylthioxylose Capping Motif of Lipoarabinomannan in Mycobacterium tuberculosis. *ACS Chem Biol* **2017,** *12* (3), 682-691.
310. Treumann, A.; Xidong, F.; McDonnell, L.; Derrick, P. J.; Ashcroft, A. E.; Chatterjee, D.; Homans, S. W., 5-methylthiopentose: a new substituent on lipoarabinomannan in Mycobacterium tuberculosis. *Journal of Molecular Biology* **2002,** *316* (1), 89-100.
311. DePas, W. H.; Bergkessel, M.; Newman, D. K., Aggregation of Nontuberculous Mycobacteria Is Regulated by Carbon-Nitrogen Balance. *Mol. Bio. Physio.* **2019,** *10* (4), e01715-19.
312. Kehr, J. C.; Zilliges, Y.; Springer, A.; Disney, M. D.; Ratner, D. D.; Bouchier, C.; Seeberger, P. H.; de Marsac, N. T.; Dittmann, E., A mannan binding lectin is involved in cell-cell attachment in a toxic strain of Microcystis aeruginosa. *Mol Microbiol* **2006,** *59* (3), 893-906.
313. Lysozyme (L7651) - Data Sheet. Sigma-Aldrich.
314. Smolelis, A. N.; Hartsell, S. E., Factors affecting the lytic activity of lysozyme. *J Bacteriol* **1952,** *63* (5), 665-674.
315. Sky-Peck, H. H.; Thuvasethakul, P., Human pancreatic alpha-amylase. II. Effects of pH, substrate and ions on the activity of the enzyme. *Ann Clin Lab Sci* **1977,** *7* (4), 310-317.
316. Chang, K. Y.; Carr, C. W., Studies on the structure and function of lysozyme. I. The effect of pH and cation concentration on lysozyme activity. *Biochim Biophis Acta* **1971,** *229*, 496-503.
317. Rigoldi, F.; Donini, S.; Redaelli, A.; Parisini, E.; Gautieri, A., Review: Engineering of thermostable enzymes for industrial applications. *APL Bioeng* **2018,** *2* (1), 011501.
318. Colla, L. M.; Ficanha, A. M. M.; Rizzardi, J.; Bertolin, T. E.; Reinehr, C. O.; Costa, J. A. V., Production and Characterization of Lipases by Two New Isolates ofAspergillusthrough Solid-State and Submerged Fermentation. *BioMed Research International* **2015,** *2015*, 1-9.
319. Sellak, H.; Franzini, J. H.; Pasquier, C., Mechanism of Lysozyme Inactivation and Degredation by Iron. *Arch Biochem Biophys* **1992,** *299* (1), 172-178.
320. Iwai, M.; Tsujisaka, Y.; Fukumoto, J., Studies on lipase. V. Effect of iron ions on the Aspergillus niger lipase. *J Gen App Microbiol* **1970,** *16*, 81-90.
321. Choudhary, A.; Patel, D.; Honnen, W.; Lai, Z.; Prattipati, R. S.; Zheng, R. B.; Hsueh, Y. C.; Gennaro, M. L.; Lardizabal, A.; Restrepo, B. I.; Garcia-Viveros, M.; Joe, M.; Bai, Y.; Shen, K.; Sahloul, K.; Spencer, J. S.; Chatterjee, D.; Broger, T.; Lowary, T. L.; Pinter, A., Characterization of the Antigenic Heterogeneity of Lipoarabinomannan, the Major Surface Glycolipid of Mycobacterium tuberculosis, and Complexity of Antibody Specificities toward This Antigen. *J Immunol* **2018,** *200* (9), 3053-3066.
322. Yan, Z. H.; Zhao, B.; Pang, Y.; Wang, X. J.; Yi, L.; Wang, H. L.; Yang, B.; Wei, P. J.; Jia, H. Y.; Li, S. P.; Zhao, Y. L.; Zhang, H. T., Generation of mycobacterial lipoarabinomannan-specific monoclonal antibodies and their ability to identify mycobacterium isolates. *J Microbiol Immunol Infect* **2021,** *54* (3), 437-446.
323. Ortalo-Magne, A.; Dupont, M.-A.; Lemassu, A.; Andersen, A. B.; Daffe, M., Molecular composition of the outmost capular material of the tubercle bacillus. *Microbiol* **1995,** *141* (7), 1609-1620.
324. Brausam, A.; Eigler, S.; Jux, N.; van Eldik, R., Mechanistic Investigations of the Reaction of an Iron(III) Octa-Anionic Porphyrin Complex with Hydrogen Peroxide and the Catalyzed Oxidation of Diammonium-2,2′-azinobis(3-ethylbenzothiazoline-6-sulfonate). *Inorganic Chemistry* **2009,** *48* (16), 7667-7678.
325. Kolloli, A.; Kumar, R.; Singh, P.; Narang, A.; Kaplan, G.; Sigal, A.; Subbian, S., Aggregation state of Mycobacterium tuberculosis impacts host immunity and augments pulmonary disease pathology. *Commun Biol* **2021,** *4* (1), 1256.
326. Pietersen, R. D.; du Preez, I.; Loots, D. T.; van Reenen, M.; Beukes, D.; Leisching, G.; Baker, B., Tween 80 induces a carbon flux rerouting in Mycobacterium tuberculosis. *J Microbiol Methods* **2020,** *170*, 105795.

327. Meyers, P. R.; Bourn, W. R.; Steyn, L. M.; van Helden, P. D.; Beyers, A. D.; Brown, G. D., Novel Method for Rapid Measurement of Growth of Mycobacteria in Detergent-Free Media. *J Clin Micro* **1988,** *39* (9), 2752-2754.
328. Anton, V.; Rouge, P.; Daffe, M., Identification of sugars involved in mycobacterial cell aggregation. *FEMS Microbiol Lett* **1996,** *144*, 167-170.
329. Lemassu, A.; Ortalo-Magne, A.; Bardou, F.; Silva, G.; Landeelle, M.-A.; Daffe, M., Extracellular and surface exposed polysaccharides of non-tuberculous mycobacteria. *Microbiol* **1996,** *143* (6), 1513-1520.
330. Ortalo-Magne, A.; Lemassu, A.; Laneelle, M. A.; Bardou, F.; Silve, G.; Gounon, P.; Marchal, G.; Daffe, M., Identification of the surface-exposed lipids on the cell envelopes of Mycobacterium tuberculosis and other mycobacterial species. *J Bacteriol* **1996,** *178* (2), 456-61.
331. Kalscheuer, R.; Palacios, A.; Anso, I.; Cifuente, J.; Anguita, J.; Jacobs, W. R., Jr.; Guerin, M. E.; Prados-Rosales, R., The Mycobacterium tuberculosis capsule: a cell structure with key implications in pathogenesis. *Biochem J* **2019,** *476* (14), 1995-2016.
332. Sani, M.; Houben, E. N.; Geurtsen, J.; Pierson, J.; de Punder, K.; van Zon, M.; Wever, B.; Piersma, S. R.; Jimenez, C. R.; Daffe, M.; Appelmelk, B. J.; Bitter, W.; van der Wel, N.; Peters, P. J., Direct visualization by cryo-EM of the mycobacterial capsular layer: a labile structure containing ESX-1-secreted proteins. *PLoS Pathog* **2010,** *6* (3), e1000794.
333. Nguyen, D. Q.; Duong, P. T.; Nguyen, H. M.; Nam, N. H.; Luong, N. H.; Pham, Y., New biological treatment targeting Mycobacterium tuberculosis in contaminated wastewater using lysing enzymes coupled to magnetic nanoparticles. *Green Processing and Synthesis* **2016,** *5* (5).
334. Dhiman, R. K.; Dinadayala, P.; Ryan, G. J.; Lenaerts, A. J.; Schenkel, A. R.; Crick, D. C., Lipoarabinomannan localization and abundance during growth of Mycobacterium smegmatis. *J Bacteriol* **2011,** *193* (20), 5802-9.
335. Prados-Rosales, R.; Carreño, L. J.; Weinrick, B.; Batista-Gonzalez, A.; Glatman-Freedman, A.; Xu, J.; Chan, J.; Jacobs, W. R.; Porcelli, S. A.; Casadevall, A., The Type of Growth Medium Affects the Presence of a Mycobacterial Capsule and Is Associated With Differences in Protective Efficacy of BCG Vaccination Against Mycobacterium tuberculosis. *Journal of Infectious Diseases* **2016,** *214* (3), 426-437.
336. Blanco, Y.; de Diego-Castilla, G.; Viúdez-Moreiras, D.; Cavalcante-Silva, E.; Rodríguez-Manfredi, J. A.; Davila, A. F.; McKay, C. P.; Parro, V., Effects of Gamma and Electron Radiation on the Structural Integrity of Organic Molecules and Macromolecular Biomarkers Measured by Microarray Immunoassays and Their Astrobiological Implications. *Astrobiology* **2018,** *18* (12), 1497-1516.
337. Nigou, J.; Gilleron, M.; Brando, T.; Puzo, G., Structural Analysis of Mycobacterial Lipoglycaons. *App Biochem Biotechnol* **2004,** *118*, 253-267.
338. Torrelles, J. B.; Khoo, K. H.; Sieling, P. A.; Modlin, R. L.; Zhang, N.; Marques, A. M.; Treumann, A.; Rithner, C. D.; Brennan, P. J.; Chatterjee, D., Truncated structural variants of lipoarabinomannan in Mycobacterium leprae and an ethambutol-resistant strain of Mycobacterium tuberculosis. *J Biol Chem* **2004,** *279* (39), 41227-39.
339. Karamat, A.; Ambreen, A.; Ishtiaq, A.; Tahseen, S.; Rahman, M. A.; Mustafa, T., Isolation of non-tuberculous mycobacteria among tuberculosis patients, a study from a tertiary care hospital in Lahore, Pakistan. *BMC Infect Dis* **2021,** *21* (1), 381.
340. Nyamogoba, H. D.; Mbuthia, G.; Mining, S.; Kikuvi, G.; Biegon, R.; Mpoke, S.; Menya, D.; Waiyaki, P. G., HIV co-infection with tuberculous and non-tuberculous mycobacteria in western Kenya: challenges in the diagnosis and management. *Afr Health Sci* **2012,** *12* (3), 305-11.
341. Zida, S.; Tarnagda, Z.; Kabore, A.; Zingue, D.; Hien, H.; Sanou, A.; Michel Gomgnimbou, K.; Nouctara, M.; Ouedraogo, M.; Ouedraogo, O.; Godreuil, S.; Meda, N., [Current status of atypical mycobacterial infections in Burkina Faso: results of a regional survey]. *Pan Afr Med J* **2014,** *17*, 188.
342. Akanbi, M. O.; Achenbach, C.; Taiwo, B.; Idoko, J.; Ani, A.; Isa, Y.; Agbaji, O.; Ukoli, C.; Akande, P.; Maiga, M.; Murphy, R. L., Evaluation of gene xpert for routine diagnosis of HIV-associated tuberculosis in Nigeria: A prospective cohort study. *BMC Pulm Med* **2017,** *17* (1), 87.
343. Shahzad-ul-Hussan, S.; Gustchina, E.; Ghirlando, R.; Clore, G. M.; Bewley, C. A., Solution structure of the monovalent lectin microvirin in complex with Man(alpha)(1-2)Man provides a basis for anti-HIV activity with low toxicity. *J Biol Chem* **2011,** *286* (23), 20788-96.
344. Huskens, D.; Ferir, G.; Vermeire, K.; Kehr, J. C.; Balzarini, J.; Dittmann, E.; Schols, D., Microvirin, a novel alpha(1,2)-mannose-specific lectin isolated from Microcystis aeruginosa, has anti-HIV-1 activity comparable with that of cyanovirin-N but a much higher safety profile. *J Biol Chem* **2010,** *285* (32), 24845-54.

345. Song, H.; Sandie, R.; Wang, Y.; Andrade-Navarro, M. A.; Niederweis, M., Identification of outer membrane proteins of Mycobacterium tuberculosis. *Tuberculosis* **2008,** *88* (6), 526-544.
346. Bae, W.; Yoon, T. Y.; Jeong, C., Direct evaluation of self-quenching behavior of fluorophores at high concentrations using an evanescent field. *PLoS One* **2021,** *16* (2), e0247326.
347. Ellman, G., Tissue Sulfhydryl Groups. *Arch Biochem Biophys* **1959,** *82* (1), 70-77.
348. Gasteiger, E.; Hoogland, C.; Gattiker, A.; S., D.; Wilkins, M. R.; Appel, R. D.; Bairoch, A., Protein Identification and Analysis Tools on the ExPASy Server. In *The Proteomic Protocols Handboo*, Walker, J., Ed. Humana Press: Totowa, New Jersey, 2005.
349. Shahid, M.; Qadir, A.; Yang, J.; Ahmad, I.; Zahid, H.; Mirza, S.; Windisch, M. P.; Shahzad-ul-Hussan, S., An Engineered Microvirin Variant with Identical Structural Domains Potently Inhibits Human Immunodeficiency Virus and Hepatitis C Virus Cellular Entry. *Viruses* **2020,** *12* (2).
350. Getz, E.; Xiao, M.; Chakrabarty, T.; Cooke, R.; Selvin, P., A Comparison between the Sulfhydryl Reductants Tris(2-carboxyethyl)phosphine and Dithiothreitol for Use in Protein Biochemistry. *Anal Biochem* **1999,** *273* (1), 73-80.
351. Bharti, S.; Maurya, R. K.; Venugopal, U.; Singh, R.; Akhtar, M. S.; Krishnan, M. Y., Rv1717 Is a Cell Wall - Associated beta-Galactosidase of Mycobacterium tuberculosis That Is Involved in Biofilm Dispersion. *Front Microbiol* **2020,** *11*, 611122.
352. Piddington, D.; Kashkouli, A.; Buchmeier, N., Growth of Mycobacterium tuberculosis in a Defined Medium Is Very Restructed by Acid pH and Mg2+ Levels. *Infect Immun* **2000,** *68* (8), 4518-4522.
353. Chapman, J. S.; Bernard, J. S., The tolerances of unclassified mycobacteria. *Am Rev Respir Dise* **1962,** *86* (4), 582-583.
354. Rao, M.; Streur, T.; Aldwell, F.; Cook, G., Intracellular pH regulation by Mycobacterium smegmatis and Mycobacterium bovis BCG. *Microbiol* **2001,** *147* (4), 1017-1024.
355. St-Pierre, C.; Ouellet, M.; Tremblay, M. J.; Sato, S., Galectin-1 and HIV-1 Infection. In *Glycobiology*, 2010; pp 267-294.
356. Miller, M. C.; Nesmelova, I. V.; Platt, D.; Klyosov, A.; Mayo, K. H., The carbohydrate-binding domain on galectin-1 is more extensive for a complex glycan than for simple saccharides: implications for galectin-glycan interactions at the cell surface. *Biochem J* **2009,** *421* (2), 211-21.
357. Blackburn, J.; Shoko, A., Protein Function Microarrays for Customized Systems-Oriented Proteome Analysis. In *Protein Microarrays Methods and Protocols*, Korf, U., Ed. Humana Press: New York, NY, 2011; Vol. 785, pp 305-330.
358. Zheng, J.; Li, L.; Tsao, H. K.; Sheng, Y. J.; Chen, S.; Jiang, S., Strong repulsive forces between protein and oligo (ethylene glycol) self-assembled monolayers: a molecular simulation study. *Biophys J* **2005,** *89* (1), 158-66.
359. Talbot, E.; Williams, D.; Frothingham, R., PCR Identification of Mycobacterium bovis BCG. *J Clin Micro* **1997,** *35* (3), 566-569.
360. Plikaytis, B.; Crawford, J.; Shinnick, T., IS1549 from Mycobacterium smegmatis Forms Long Direct Repeats upon Insertion. *J Bacteriol* **1998,** *180* (5), 1037-1043.
361. Torriani, A., Alkaline Phosphatase Subunits and Their Dimerization In Vitro. *J Bacteriol* **1968,** *96* (4), 1200-1207.
362. Rice, J. J.; Daugherty, P. S., Directed evolution of a biterminal bacterial display scaffold enhances the display of diverse peptides. *Protein Eng Des Sel* **2008,** *21* (7), 435-42.
363. Rice, J. J.; Schohn, A.; Bessette, P. H.; Boulware, K. T.; Daugherty, P. S., Bacterial display using circularly permuted outer membrane protein OmpX yields high affinity peptide ligands. *Protein Sci* **2006,** *15* (4), 825-36.
364. Suhoski, M. M.; Golovina, T. N.; Aqui, N. A.; Tai, V. C.; Varela-Rohena, A.; Milone, M. C.; Carroll, R. G.; Riley, J. L.; June, C. H., Engineering artificial antigen-presenting cells to express a diverse array of co-stimulatory molecules. *Mol Ther* **2007,** *15* (5), 981-8.
365. Dubos, R. J.; Dubos, J., *The white plague; tuberculosis, man and society*. 1st ed.; Little: Boston,, 1952; p viii, 277 p.
366. Vynnycky, E.; Fine, P. E., Interpreting the decline in tuberculosis: the role of secular trends in effective contact. *International journal of epidemiology* **1999,** *28* (2), 327-34.

APPENDIX A : CHAPTER 3 SUPPORTING INFORMATION

Supplementary Video Captions

Video A1. Paramagnetic bead separation from a flowing fluid stream using high-gradient magnetic separation. An external magnet is applied next to the ferromagnetic matrix to magnetize it. When the magnetic force is sufficiently great, the magnetic force draws beads to the surface of the wire, capturing them in the matrix. After all of the bead suspension has passed, all of the particles are retained in the ferromagnetic matrix, and no beads remain in the flow through.

Video A2. Paramagnetic bead separation from a flowing fluid stream using a stationary magnet. An external magnet is applied alongside the flowing fluid stream to separate particles from suspension. After all of the bead suspension has passed, only some of the beads are retained in the flow channel, and many still remain in the flow through. This is because the viscous drag forces applied by the liquid medium overcome the magnetic forces applied to the beads.

Supplementary Figures

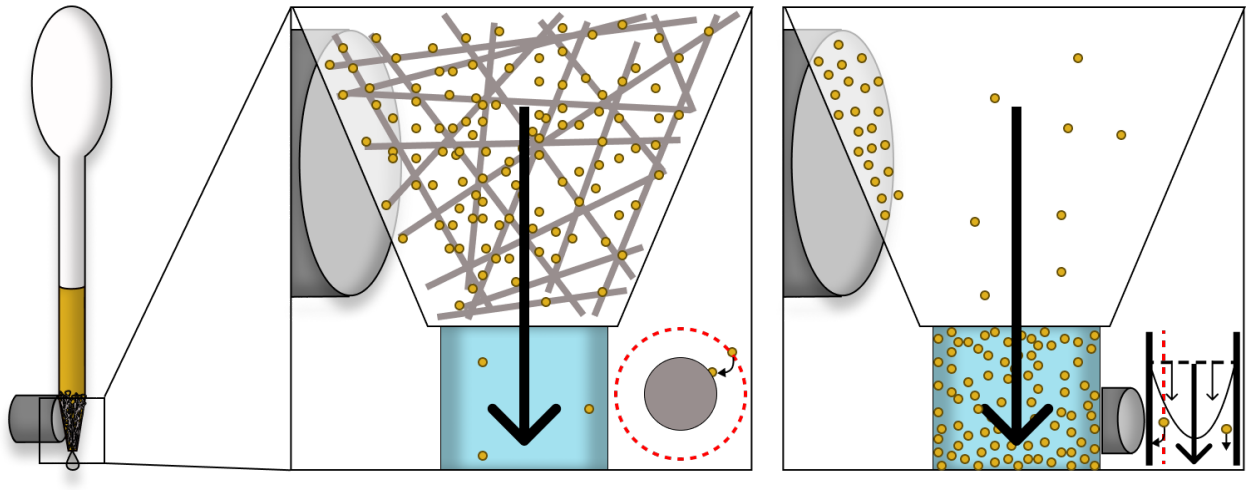

Figure A1. Overview of paramagnetic bead separation from a flowing fluid stream. Left panel: An external magnet is used to capture and contain magnetic beads in the ferromagnetic matrix (see **Video A1**). When the magnetic force is sufficiently great around a wire (red dashed line), the magnetic force draws beads to the surface, capturing them. Right Panel: Applying the magnetic field without the presence of the steel wool matrix results in significant loss of magnetic beads since the viscous drag forces applied by the liquid medium overcome the magnetic forces on the bead when the bead is sufficiently far away from the magnet (red dashed line) (see **Video A2**).

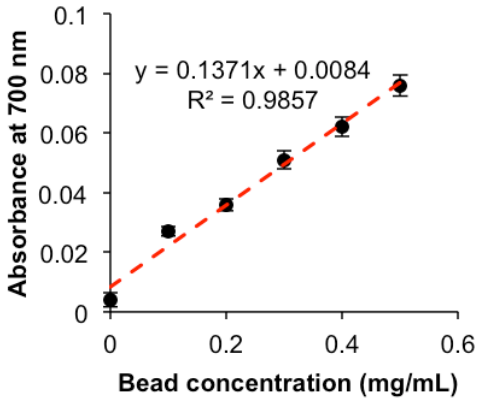

Figure A2. Nanodrop™ Spectrophotometer ND-1000 standard curve correlating absorbance at 700nm with known solution concentrations of MyOne™ Silane ™.

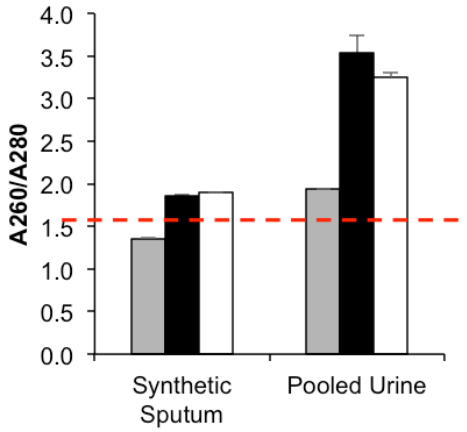

Figure A3. A260/A280 measurement for sample purity of DNA extracted sample. Samples with a value of 1.8 ± 0.1 (red dashed line) are considered to be pure and free from contaminating protein and salt that absorbs light at 280 nm. Values greater than 3.0 may indicate RNA contamination.[256] Gray bars = Raw sample; Black bars = HGMS-enabled extraction; White bars = Qiagen commercial extraction kits. (mean ± s.d.), $n \geq 3$.

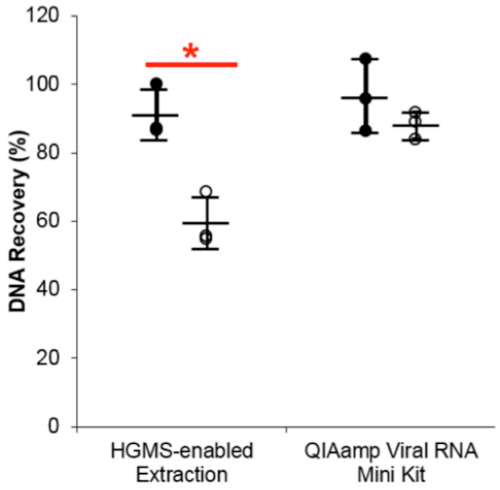

Figure A4. Extraction of IS*6110* DNA from urine is statistically improved using the HGMS-enabled extraction method, with the addition of 5.6 ug of carrier RNA to the binding mixture.[259] Black bars – with carrier RNA; Gray bars – without carrier RNA. (mean ± s.d., n ≥ 3). *Indicates statistical significance at $p < 0.05$.

APPENDIX B : CHAPTER 4 SUPPORTING INFORMATION

Supplementary Video Captions

Video B1. Sequential OCT images of evaporating 1 µL droplet containing 10^6 polystyrene particles/uL, which are 1 µm in diameter. A total of 800 repeated frames were taken at the same position for a total acquisition time of 36 s per measurement in order to monitor the changes in particle flow and the droplet evaporation. For each droplet, measurements were taken at two minute intervals beginning at one minute following droplet placement until complete evaporation.

Video B2. Sequential fluorescence microscopy images at 100x total magnification of evaporating 5 µL droplet containing 10^4 polystyrene particles/uL, which are 1 µm in diameter. A total of 40 frames at 100 ms exposure were taken at the same position near the solvent-substrate for a total acquisition time of 40 seconds per measurement in order to monitor the changes in particle flow and the droplet evaporation. In focus particles move inward along the substrate. Once particles reach the center of the droplet, they become out of focus, and begin moving in the opposite direction. This is consistent with the particles moving upward towards the top of the droplet, then moving outward along the outer surface of the droplet. Combined, the particle movement is consistent with the Marangoni flow pattern shown in **Figure 4.1**.

Supplementary Figures

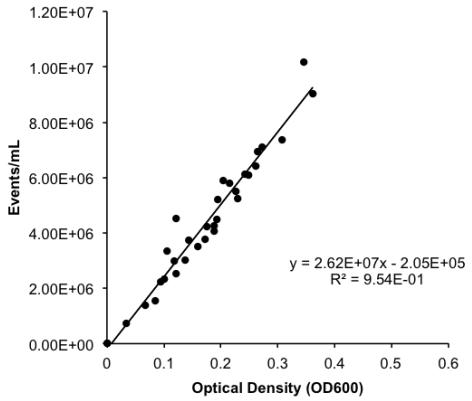

Figure B1. Flow cytometry curve correlating number of events counted against OD600 of *M. bovis* BCG bacteria.

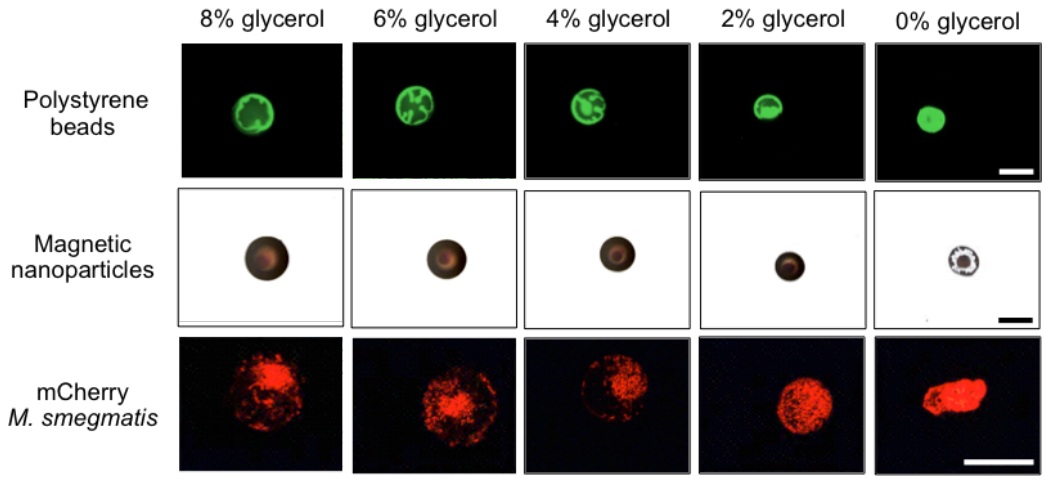

Figure B2. Removing glycerol from droplet solvent did not significantly change particle deposition location in droplets containing 1 µm polystyrene beads (top), 200 nm iron oxide magnetic nanoparticles (middle), or mCherry expressing *M. smegmatis* bacteria (bottom). Scale bars = 500 µm.

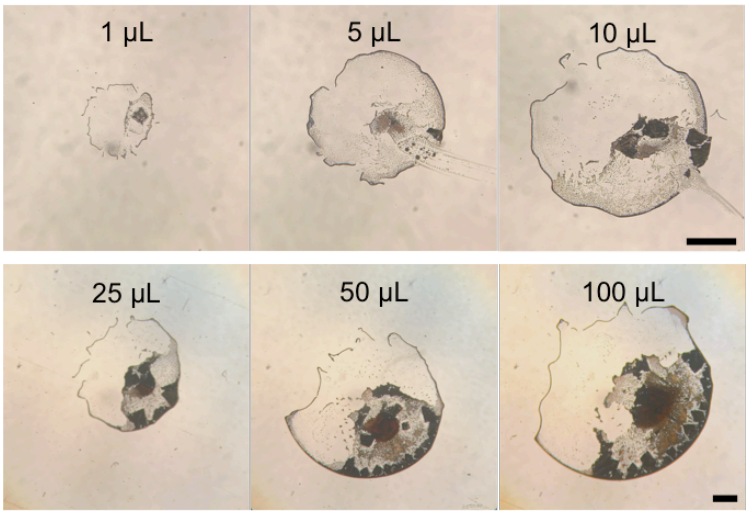

Figure B3. The size of the droplet did not impact the final deposition pattern of the droplet, up to a 100 µL volume. All droplets contained nanoparticles at a concentration of 0.2 mg/mL. Ambient temperature was 23°C. Images were taken on Nikon TE-200U with an iPhone XR and 10x smartphone camera adapter. The image temperature was adjusted for publication to reduce the orange hue of the image. Scale bars = 1 mm.

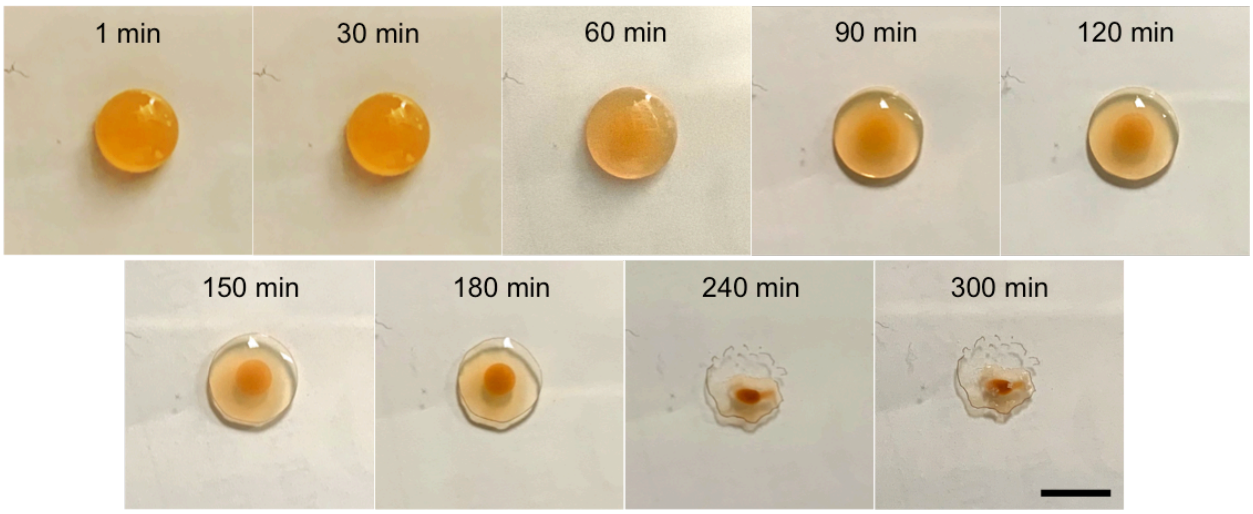

Figure B4. Time-lapse imaging of a 50 µL evaporating droplet shows the formation of the central deposition area as the droplet evaporated. Images were captured ever 30 min for the first three hours, and once an hour thereafter until evaporation was complete after five hours. Droplet contained nanoparticles at 0.2 mg/mL. Ambient temperature was 20°C. The shadows of the centrally concentrated nanoparticles and edges of the droplet observed are reflections off the backside of the glass slide. Images taken with an iPhone XR. Scale bar = 5 mm.

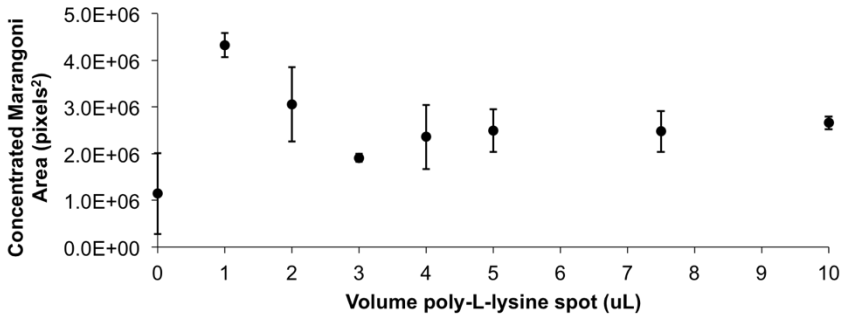

Figure B5. Effect of poly-L-lysine landing zone size on area of central Marangoni deposition area (mean ± s.d., $n \geq 6$).

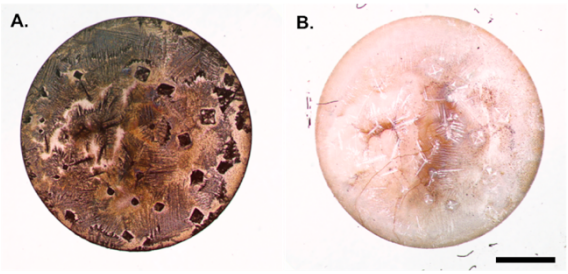

Figure B6. Drying of 50 μL droplet on plain glass did not result in characteristic Marangoni deposition pattern upon complete drying. **A.** Before rinsing off salt crystals. **B.** After rinsing off salt crystals. Droplet was imaged using Nikon TE 200-U using a Nikon DS-Ri1 camera at 10x total magnification since the entire droplet could not be imaged in a single field of view using optical setup on the Olympus CX23. To reduce the effects of uneven illumination using ImageJ,[286] nanoparticle droplets had a representative background image subtracted from the original deposition image. Scale bar = 1 mm.

APPENDIX C : CHAPTER 5 SUPPORTING INFORMATION

Supplementary Tables

Table C1. Measured Concentration of anti-LAM Antibodies from FIND.

Antibody clone	Measured total protein concentration (mg/mL)	Manufacturer Reported Concentration (mg/mL)
FDX01	8.94	No data‡‡‡
A194	5.95	4
BJ-03	6.94	4.7-5.6[3]
BJ-76	6.31	5.1-5.8[3]

Supplementary Figures

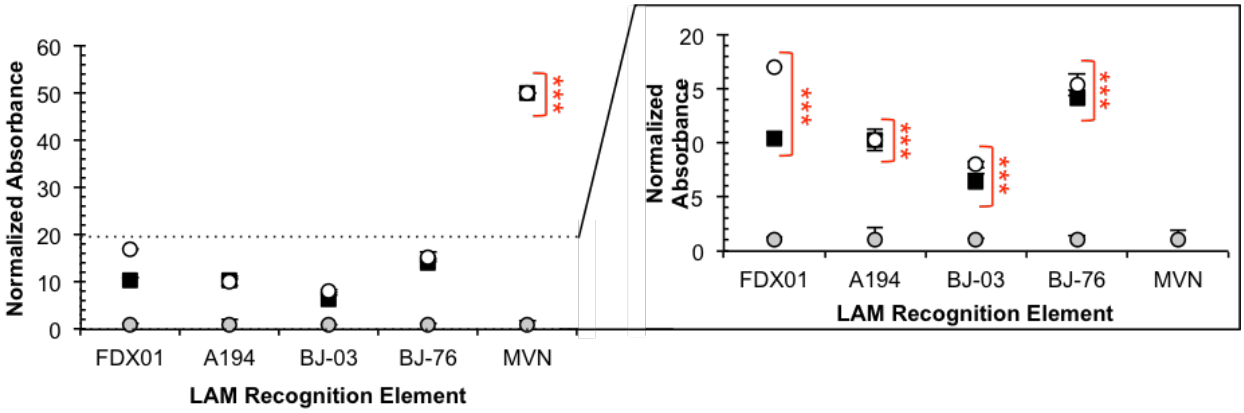

Figure C1. Inclusion of 0.02 mM $FeSO_4$ and 0.05 mM $FeSO_4$ in staining buffer statistically increases signal compared to an untreated control for all LAM recognition elements. Impact of FeSO4 concentration on each LAM recognition element (left), with adjusted Y-axis in cutout (right). Gray circle = No treatment. Black square = 0.02 mM $FeSO_4$. White circle = 0.05 mM $FeSO_4$. n = 3. (mean ± SEM). ***Indicates statistical significance at $p < 0.0005$.

‡‡‡ *Because of instances where exact concentrations of antibody were not provided from the manufacturer, for all antibodies, the total protein concentration was assumed to be the antibody concentration measured on a Nanodrop™ Spectrophotometer ND-1000 for all experiments.*

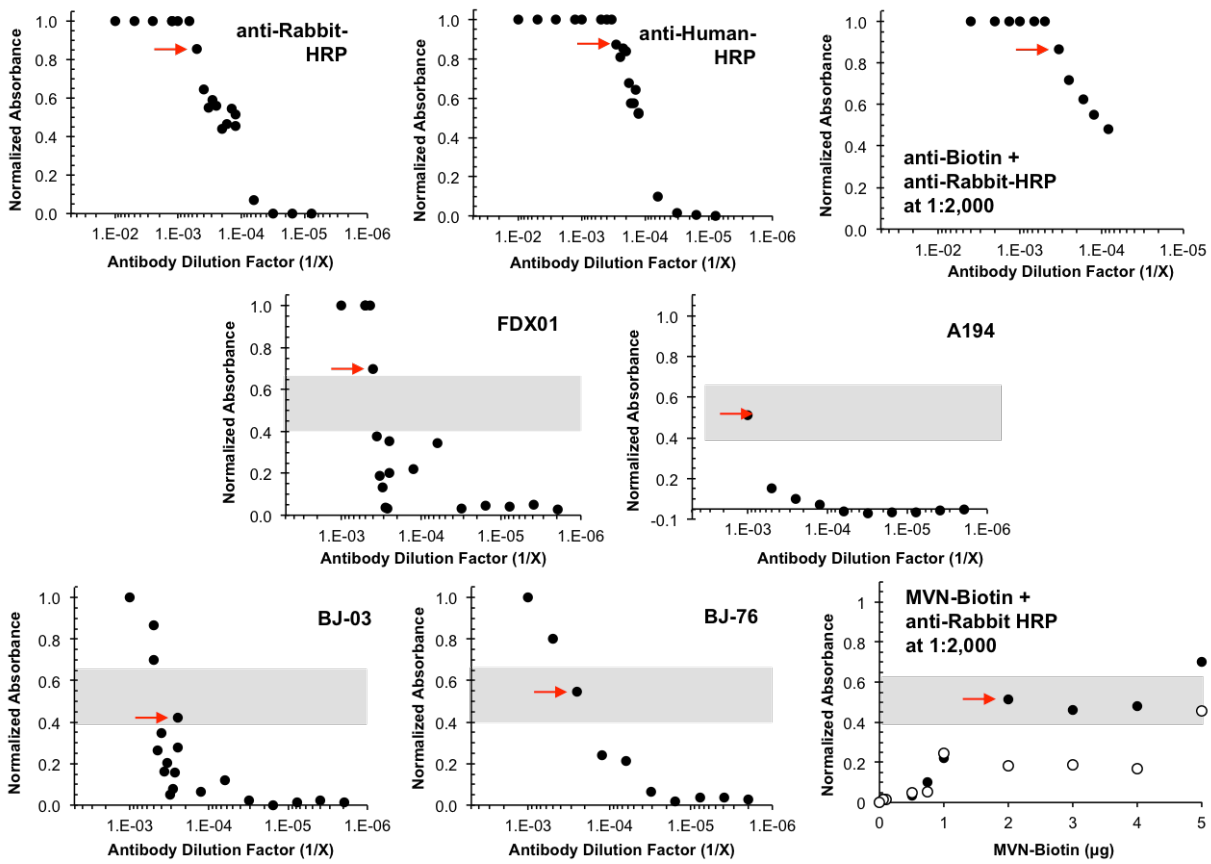

Figure C2. Antibody titration curves and selected working concentration. Name of plot indicates the antibody titrated. For MVN-Biotin, dilutions of anti-Biotin used were: 1:1,000 (black circle) or 1:3,000 (white circle) with anti-Rabbit HRP at 1:2,000. The selected antibody titrations used are indicated with a rightward-facing red arrow. The desired detection absorbance for combined primary and secondary antibodies is indicated by a gray bar, and was selected to be in the middle readable range of the plate reader. For MVN-Biotin, due to the low binding observed for the given quantity of MVN, two dilutions of MVN were used to determine the concentration of MVN for experimentation. Though it was higher than the originally selected 1:3,000 dilution, a 1:1,000 dilution of anti-Biotin was selected because it reduced the amount of MVN required for the desired absorbance by over half.

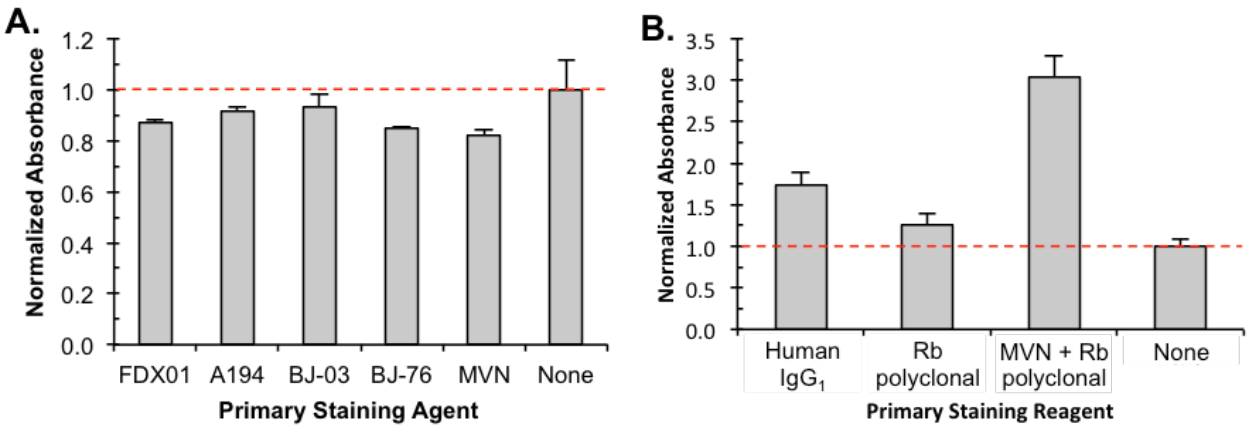

Figure C3. Normalized absorbance values for isotype controls with secondary-only background subtracted. **A.** LAM recognition elements stained with goat anti-Mouse HRP at 1:2,000 in place of goat anti-Rabbit (Rb) HRP or goat anti-Human HRP. **B.** Replacement of human or rabbit LAM recognition elements with Human IgG1 or rabbit IgG polyclonal antibody at a 1:1,000 dilution. Values were normalized to the average background absorbance for the secondary-only control for each condition, labeled as "None." Values greater than the unstained sample (red dashed line) indicate nonspecific background staining from the isotype antibodies. Isotype controls were used for background staining subtraction, unless the secondary-only control had a higher background, as was seen with in some samples treated with $FeSO_4$ for enzyme inactivation.

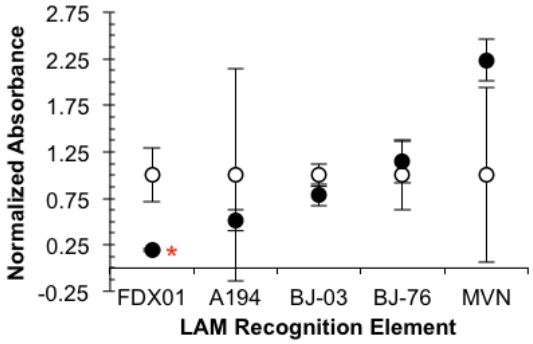

Figure C4. On single cells that were initially recovered from cultures without any mechanical dissociation (unprocessed control), needle aspiration generally does not significantly impact the accessibility of LAM on the surface of *M.tb*. Statistical significance for FDX01 borders on statistical significance ($p = 0.046$). White circle = No treatment. Black circle = Needle aspiration. n = 3. (mean ± SEM). *Indicates statistical significance at $p < 0.05$.

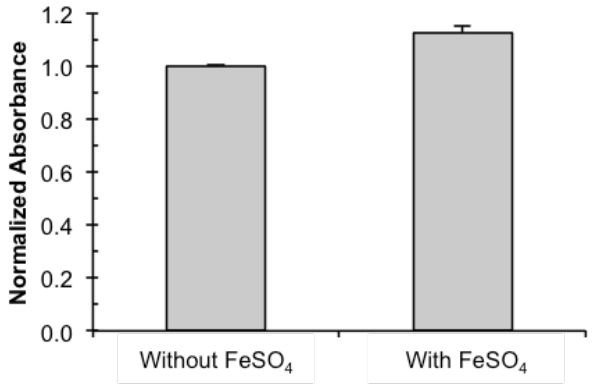

Figure C5. Iron(II) sulfate hepatahydrate ($FeSO_4 \bullet 7H_2O$) suspended in ABTS and H_2O_2 at a concentration of 0.05mM did not significantly oxidize ABTS after 30 min, as measured using absorbance.

APPENDIX D : CHAPTER 6 SUPPORTING INFORMATION

Supplementary Tables

Table D1. Collection Parameters for Capture of BCG, *M. smeg*, and *E. coli* on MVN-beads.

Parameter ($PnN)	Stain ($PnS)	Range ($PnR)	Bits ($PnB)	Decades ($PnE)	Gain ($PnG)	Voltage ($PnV)
Time		64	32	0,0	1.0	
FSC-A		262144	32	0,0	1.0	243
FSC-H		262144	32	0,0	1.0	243
FSC-W		262144	32	0,0	1.0	243
SSC-A		262144	32	0,0	1.0	401
SSC-H		262144	32	0,0	1.0	401
SSC-W		262144	32	0,0	1.0	401
APC-A	AF405	262144	32	0,0	1.0	665
Pacific Blue-A	mCherry	262144	32	0,0	1.0	606
PE-TexasRed-A	GFP	262144	32	0,0	1.0	644
FITC-A	DyLight® 650	262144	32	0,0	1.0	684
Comp-APC-A		262144	32	0,0	1.0	
Comp-Pacific Blue-A		262144	32	0,0	1.0	
Comp-PE-TexasRed-A		262144	32	0,0	1.0	
Comp-FITC-A		262144	32	0,0	1.0	

Table D2. Compensation Matrix for Capture of BCG, *M. smeg*, and *E. coli* on MVN-beads.

	APC-A	Pacific Blue-A	PE-TexasRed-A	FITC-A
APC-A	100	3.1899	9.62	23.7305
Pacific Blue-A	4.0412	100	4.2532	0.6009
PE-TexasRed-A	1.4284	0	100	0
FITC-A	0	0	0	100

Table D3. Collection Parameters for Capture of BCG on MVN and Galectin-1 Surface-Functionalized Beads.

Parameter ($PnN)	Stain ($PnS)	Range ($PnR)	Bits ($PnB)	Decades ($PnE)	Gain ($PnG)	Voltage ($PnV)
Time		128	32	0,0	1.0	
FSC-A		262144	32	0,0	1.0	223
FSC-H		262144	32	0,0	1.0	223
FSC-W		262144	32	0,0	1.0	223
SSC-A		262144	32	0,0	1.0	361
SSC-H		262144	32	0,0	1.0	361
SSC-W		262144	32	0,0	1.0	361
FITC-A	GFP	262144	32	0,0	1.0	493
APC-A	DyLight® 650	262144	32	0,0	1.0	655
Pacific Blue-A	AF405	262144	32	0,0	1.0	429
Comp-FITC-A		262144	32	0,0	1.0	
Comp-APC-A		262144	32	0,0	1.0	
Comp-Pacific Blue-A		262144	32	0,0	1.0	

Table D4. Compensation Matrix for Capture of BCG on MVN and Galectin-1 Functionalized Beads.

	FITC-A	APC-A	Pacific Blue-A
FITC-A	100	0.1572	0.3498
APC-A	9.3913	100	1.3552
Pacific Blue-A	0	8.294	100

Supplementary Figures

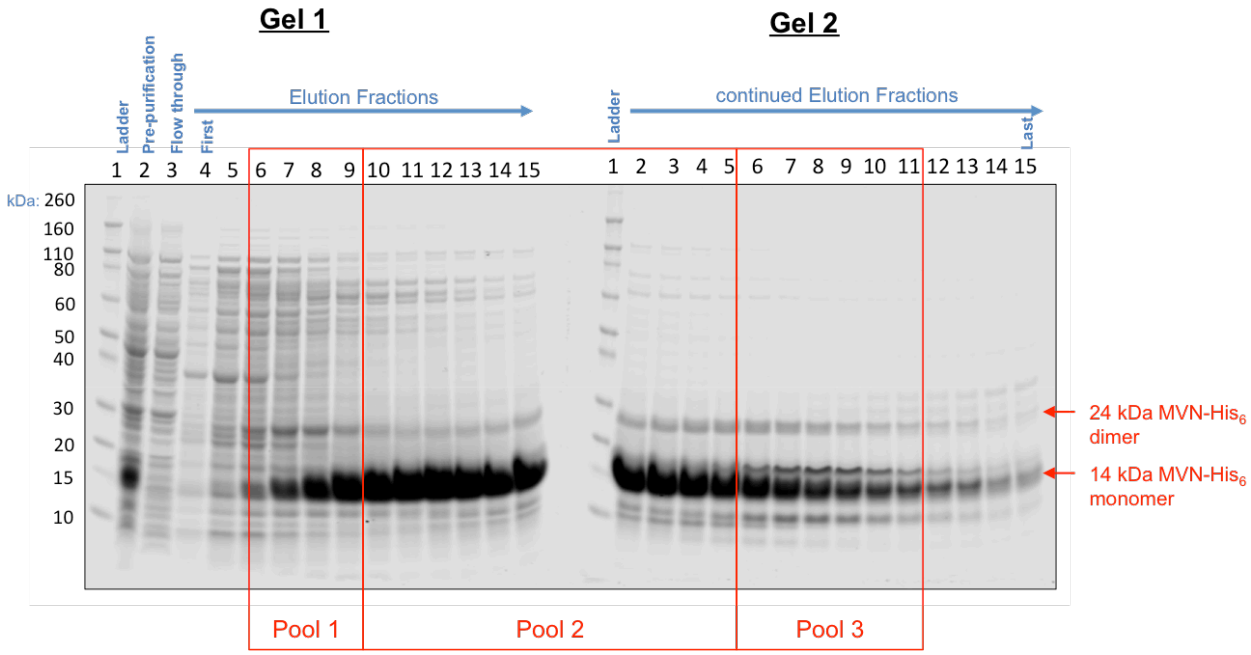

Figure D1. Coomassie blue staining depicting final IMAC-purified fractions containing MVN-His_6 under reducing conditions. A total of 10 µL from each 2 mL fraction was loaded into the gel. For the "Pre-purification" and "Flow through," 10 µL from the ~150 mL volume were loaded onto the gel. The pooled 2 mL fractions are indicated.

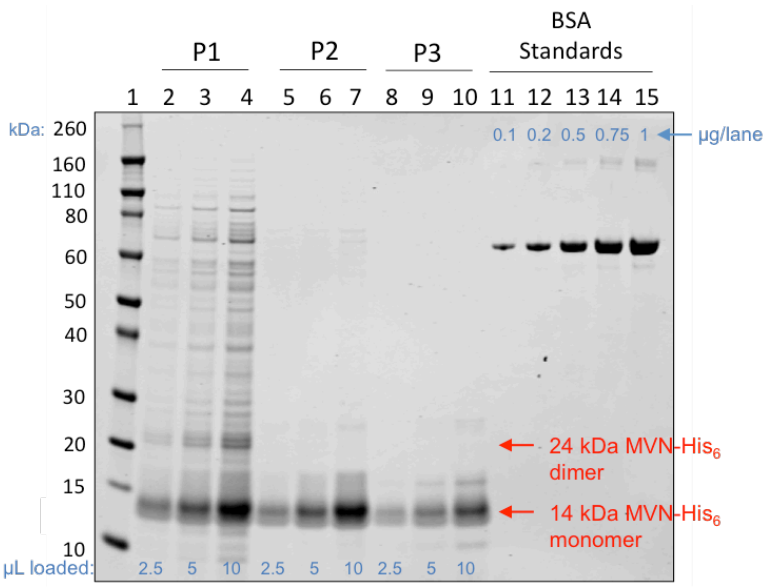

Figure D2. Coomassie blue staining depicting final IMAC-purified and pooled fractions of MVN-His_6. The volume of Pool 1 and Pool 3 loaded onto the gel were 10-fold dilutions of the final purified products. Pool 2 was a 20-fold dilution of the final purified products.

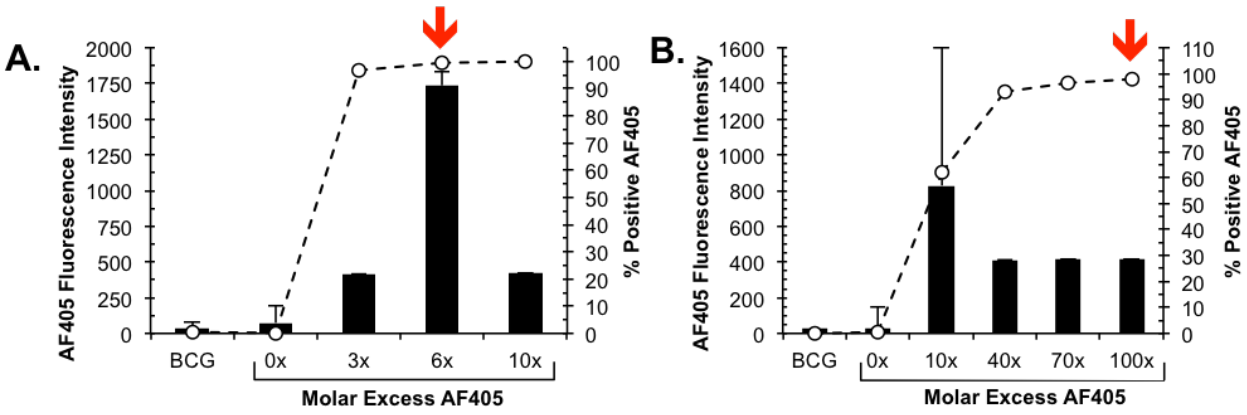

Figure D3. Titration of NHS-AF405 onto naked streptavidin beads compared to autofluorescence in cultured *M. bovis* BCG. **A.** Dynabeads™ 1 µm. **B.** SuperMag 200 nm Beads. Red arrows indicate the selected streptavidin molar excess of AF405 used to label MVN beads during downstream development. The reduction in fluorescence intensity above 6x excess for Dynabeads™ and 10x excess for SuperMag beads is likely due to self-quenching. Black bar – AF405 fluorescence intensity. (- -O- -) – % beads positive for AF405. n = 1. (GMean ± rSD).

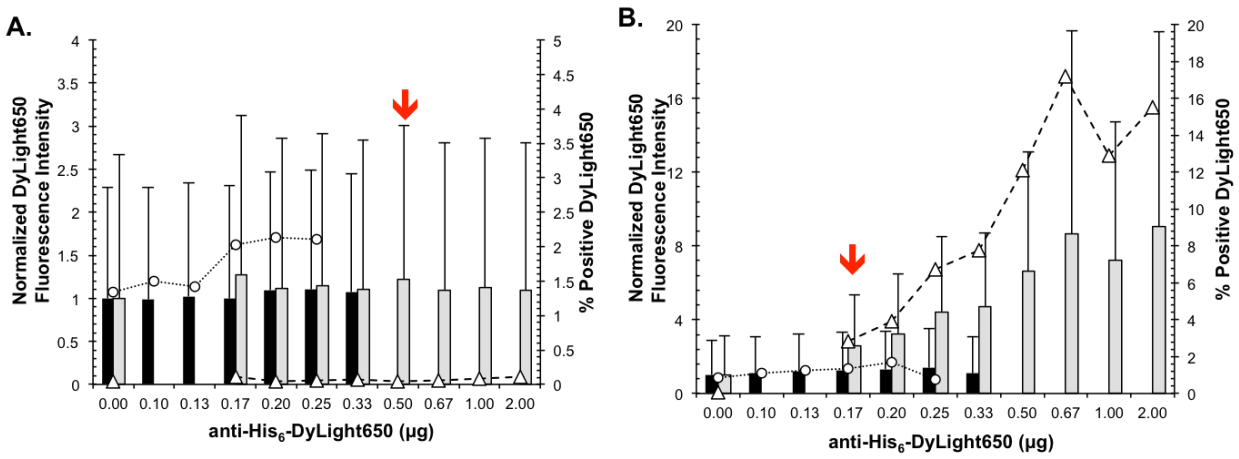

Figure D4. Titrations of anti-His_6-DyLight® 650 onto naked streptavidin beads through measurement of signal noise from nonspecific binding. **A.** For, Dynabeads™ 1 µm, the low background signal across all conditions demonstrated minimal nonspecific binding of the antibody to the beads. For simplicity, 0.5 µg (1:1,000, red arrow) was chosen for downstream detection of MVN loading. **B.** SuperMag 200 nm Beads displayed a greater amount of nonspecific binding to the antibody, and therefore 0.17 µg (1:3,000, red arrow) of antibody was selected for downstream analysis. Bar graph = Normalized DyLight fluorescence intensity for Dilution Series 1 (black) and Dilution Series 2 (gray). Line graph = % beads positive for DyLight® 650 for Dilution Series 1 (···O···) and Dilution Series 2 (- -Δ- -). n = 1. (GMean ± rSD).

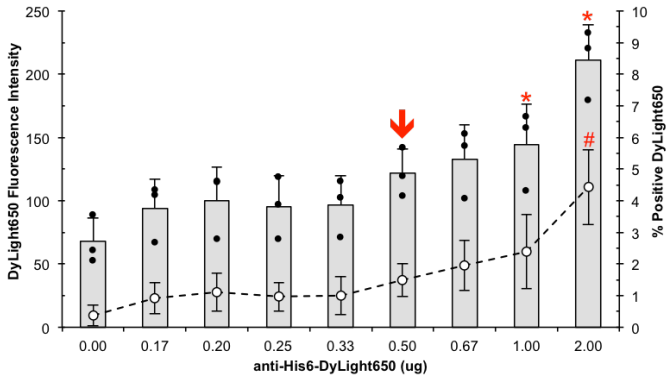

Figure D5. Titration of anti-His_6-DyLight® 650 onto BCG cells by measuring signal noise from nonspecific binding. Samples containing 1 µg (1:500) and 2 µg (1:250) of antibody displayed a statistically increased fluorescence intensity compared to the background, and the % of cells positive for DyLight® 650 statistically increased. However, some false staining was observed on the flow cytometry plots containing 0.67 µg (1:750) of anti-His_6-DyLight® 650, so 0.5 µg (1:1000) was selected for downstream analyses (red arrow). Gray bar – DyLight® 650 fluorescence intensity. • – Individual population GMean for DyLight® 650 fluorescence intensity. (- -O- -) – % positive for DyLight® 650. n = 3. (mean ± s.d.). (*, #) Indicate statistical significance at $p < 0.05$.

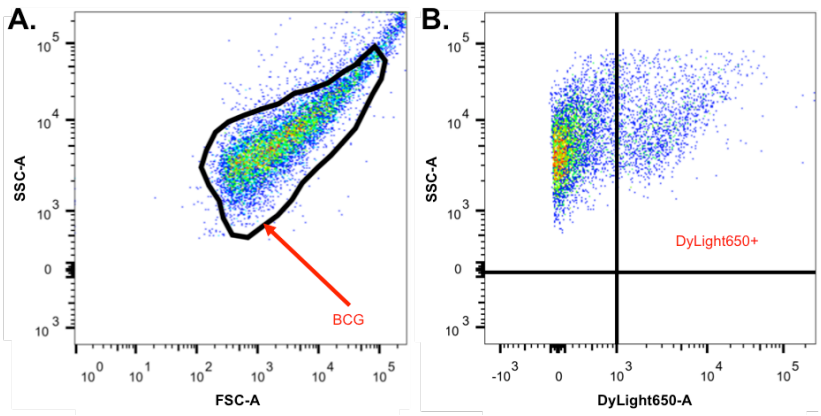

Figure D6. Visual depiction of gating strategy for analysis of fluorescence intensity levels for anti-His_6-650 loading to bacteria or beads. **A.** BCG population gate. Apply statistics (e.g., geometric mean, standard deviation, median) to this gate. **B.** To determine the number of cells positive for the detection fluorophore, the cell population was further gated based on fluorophore intensity.

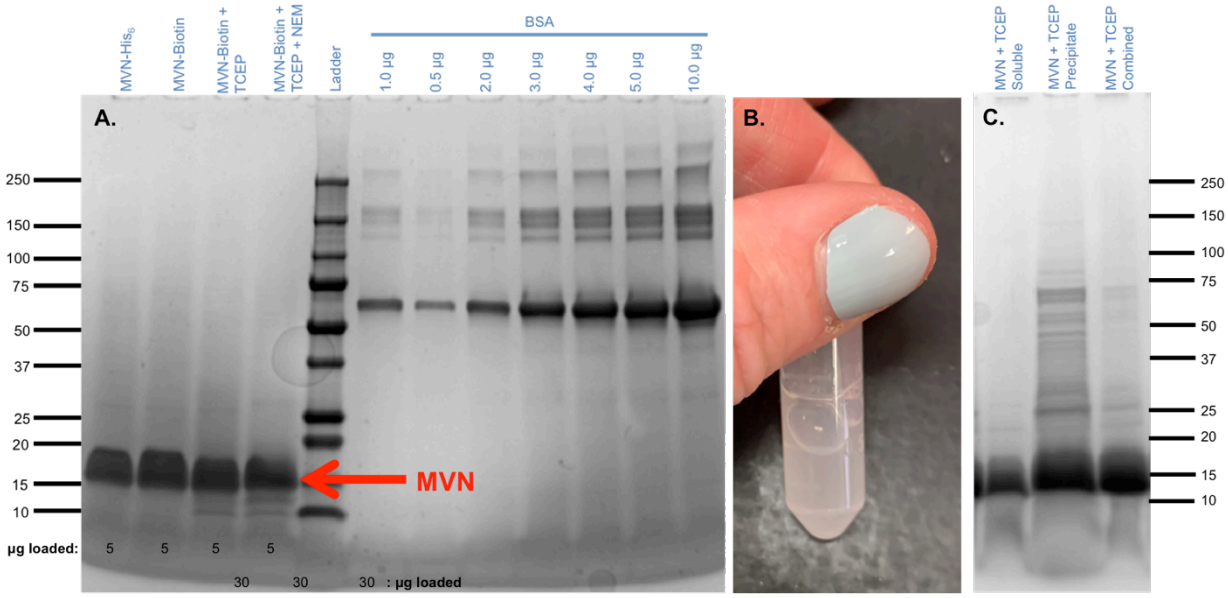

Figure D7. SDS-PAGE analysis of reduced and alkylated MVN-Biotin fractions collected during each process step. **A.** A total of 5 µg of MVN was reserved and loaded into each well after each chemical modification step. **B.** Protein precipitation was observed following TCEP addition. **C.** In a previous initial test of TCEP reduction, the precipitated protein was separated from the soluble fraction using centrifugation, and 30 µg were analyzed, indicating the presence of MVN in both the soluble and insoluble fraction. As a result, for the experiments displayed in **A.**, the soluble and insoluble fractions were not separated and dialyzed and treated with NEM.

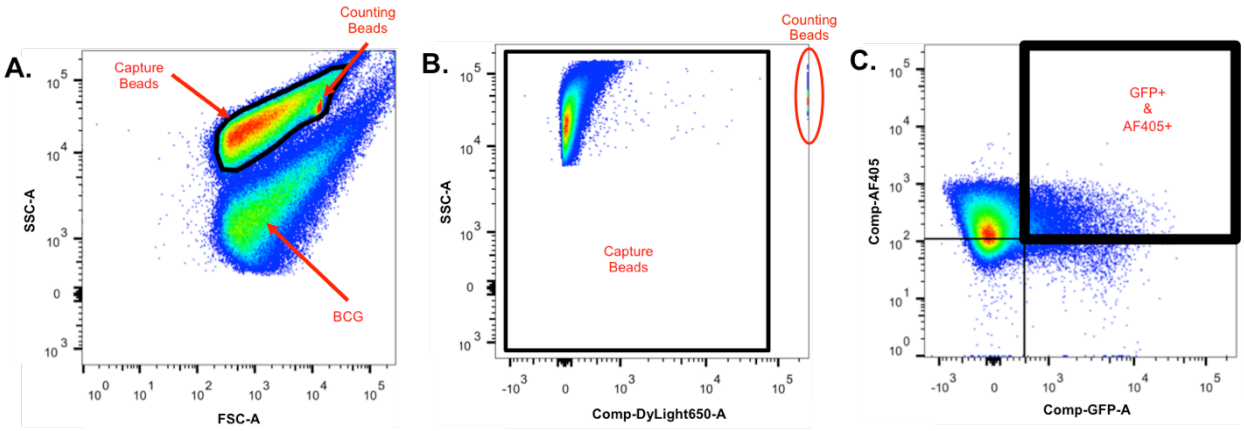

Figure D8. Visual depiction of gating strategy for analysis of bacteria and bead interactions. **A.** When BCG binds to capture beads with a higher granularity, they take on that quality and will appear along with the beads. Conservatively gate the bead population to avoid accidental overlap of BCG cells. **B.** If Counting Beads were included in the sample for quantification, they would overlap with the capture bead size and granularity gate. Their insanely high fluorescence across multiple channels allows them to be easily excluded. **C.** When beads bind to bacteria, they take on their GFP-fluorescence in addition to being AF405-positive. The black box defines this double fluorophore positive gate on the plot.

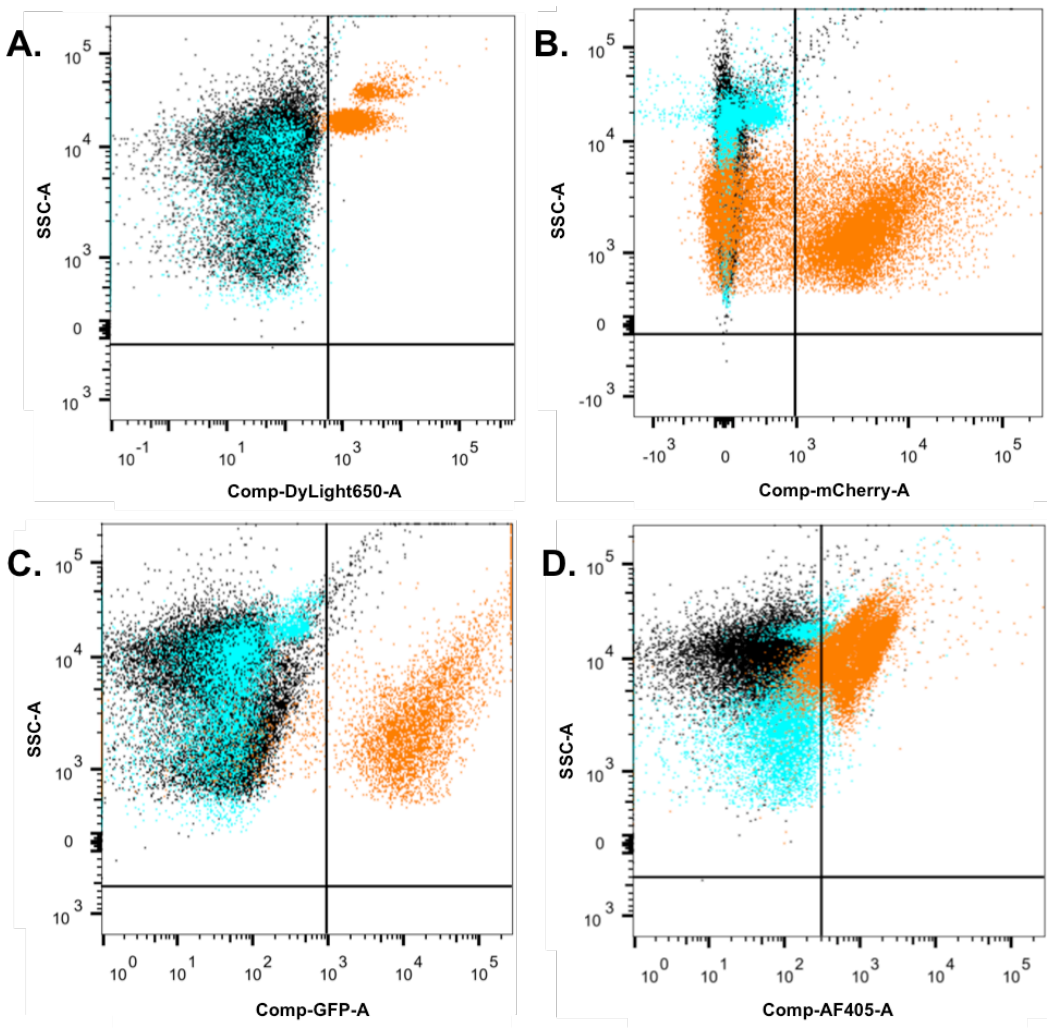

Figure D9. Controls and intensity gating for each compensated fluorescent channel. **A.** anti-His_6-DyLight® 650. **B.** mCherry *M. smegmatis* and mCherry *E. coli*. **C.** GFP BCG. **D.** AF405 magnetic capture beads. The location where the black vertical line intersects the x-axis is the defined cutoff for fluorophore positivity. Compensation was performed at the time of data collection using the FACSDiva™ software. Black population − Unstained bacteria and beads. Blue population – FMO control. Orange population – Positive control.

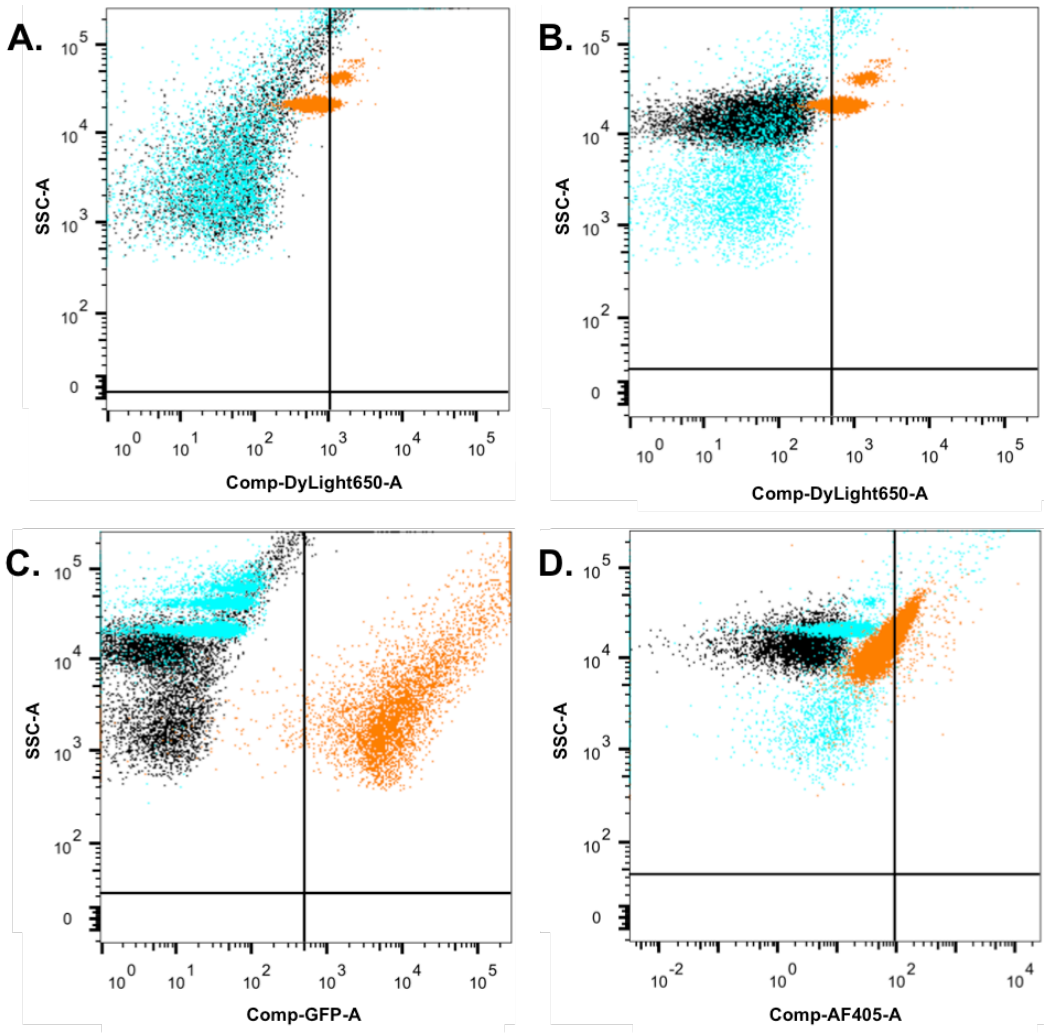

Figure D10. Controls and intensity gating for each compensated fluorescent channel for MVN-Galectin-1 capture experiments. **A.** anti-His_6-DyLight® 650; gate for cell populations. **B.** anti-His_6-DyLight® 650; gate for bead populations. **C.** GFP BCG. **D.** AF405 magnetic capture beads. The location where the black vertical line intersects the X-axis is the defined cutoff for fluorophore positivity. Compensation was performed at the time of data collection using the FACSDiva™ software. Black population − Unstained bacteria and beads. Blue population – FMO control. Orange population – Positive control.

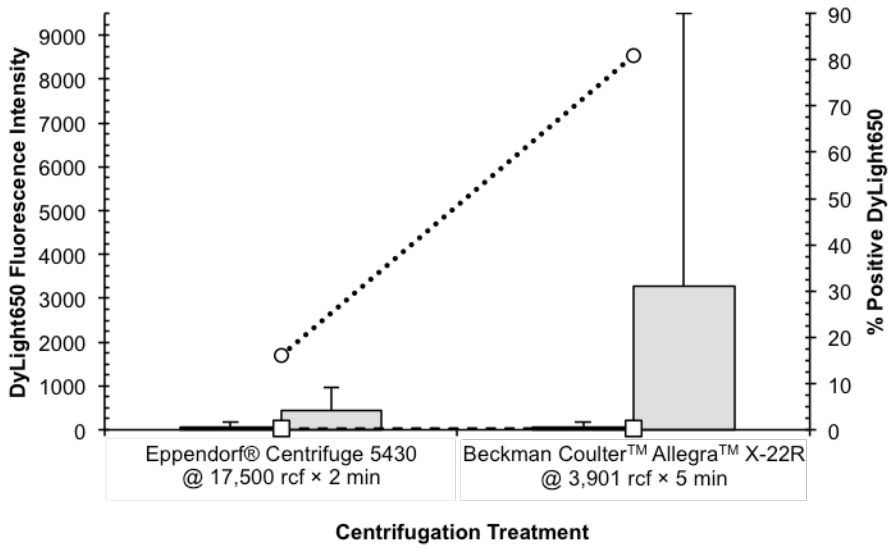

Figure D11. The centrifugation conditions used during MVN and antibody staining changed the surface accessibility of ManLAM available for MVN binding. Cells stained with 0 µg (black bars; DyLight® 650 Fluorescence Intensity) or 15 µg of MVN-Biotin (gray bars; DyLight® 650 Fluorescence Intensity) and a 1:250 dilution (2 µg) of anti-His_6-650. (− −□− −) − % Positive DyLight® 650 for cells stained with 0 µg MVN. (••O••)− % Positive for DyLight® 650 for cell stained with 15 µg MVN. n = 1. (GMean ± rSD).

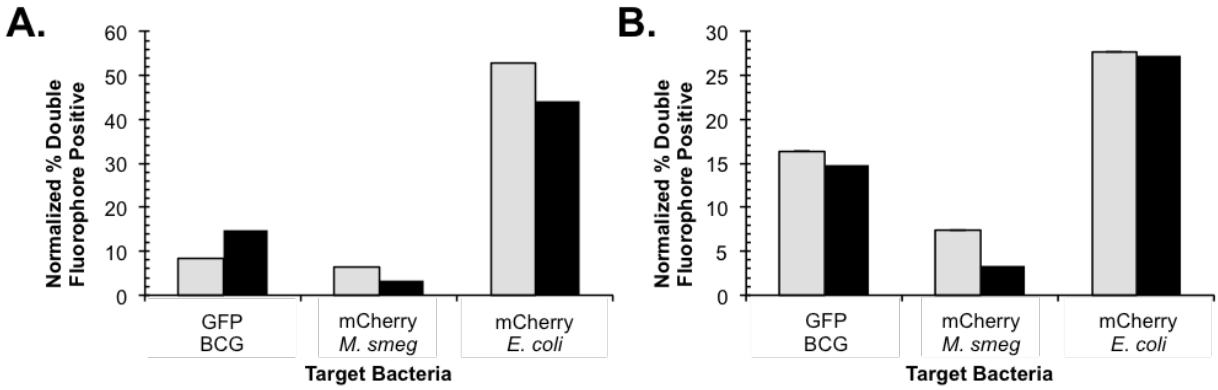

Figure D12. Capture of GFP BCG, mCherry *M. smeg*, and mCherry *E. coli* each bacteria on AF405 Dynabeads™ 1 µm (**A.**) and AF405 SuperMag 200 nm beads (**B.**) surface-loaded with D-Biotin (gray bars) or MVN-Biotin (black bars). Because the number of bacterial cells between each species was different, the reported values cannot be cross-examined between species. However, these values demonstrate nonspecific binding onto both the naked beads for all species and nonspecific binding of *M. smeg* and *E. coli* onto the MVN-functionalized beads. n = 1.

APPENDIX E : CHAPTER 5 COMPANION EXPERIMENTS

The experiments outlined here were performed as part of the studies discussed in Chapter 5, but did not fit into the story told. However, these results will also interest researchers looking to develop LAM-based diagnostics or trying to understand or characterize the *M.tb* cell surface.

Materials and Methods

Bioconjugation of candidate antibodies and MVN for binding kinetic experiments.

Anti-LAM antibodies A194, FDX01, BJ-03, BJ-76, BTM-1, and BTM-8 were generously gifted by Foundation for Innovative and New Diagnostics (FIND). A194,[226, 321] BJ-03 and BJ-76,[322] have previously been described in the literature. Measured primary antibody concentrations, LAM recognition element titrations, and the target structural motifs of each LAM recognition element can be found in **Table E1**, **Figure C2**, and **Figure 5.1**, respectively. All antibodies were diluted to a concentration of 2 mg/mL in 1x PBS (137 mM NaCl, 2.7 mM KCl, 10 mM Na_2HPO_4, 1.8 mM KH_2PO_4, pH = 7.4), and reacted with 20x molar equivalents of EZ-Link™ NHS-PEG_{12}-Biotin (ThermoFisher, A35389) for one hour at room temperature on a lab rotisserie. Unreacted NHS-PEG_{12}-Biotin was removed using Zeba™ Spin Desalting Columns, 7K MWCO (ThermoFisher, 89882). The concentration of the conjugated antibodies was determined using absorbance at 280 nm on a Nanodrop™ Spectrophotometer ND-1000. The same protocol was used to conjugate the 14 kDa and 24 kDa fragments of MVN at their measured stock concentration, except that unreacted NHS-PEG_{12}-Biotin was removed using dialysis with Slide-A-Lyzer™ Dialysis Cassettes, 2K MWCO, 3 mL (ThermoFisher, 66203). This reduced protein loss of the dilute SEC-purified MVN fractions. We have seen protein losses up to 50% with Zeba™ Columns.

Screening of candidate antibodies and MVN for LAM specificity using biolayer interferometry.

Mycobacterium tuberculosis, H37Rv, Purified Lipoarabinomannan (NR-14848) and *Mycobacterium smegmatis*, Purified Lipoarabinomannan (NR-14849) were obtained from the Biodefense and Emerging Infections Research Resources Repository (BEI Resources, Manassas, VA), NIAID, NIH. The binding affinity of LAM recognition elements was screened against LAM from *M.tb* H37Rv (ManLAM) and *M. smegmatis* (PILAM) using a

ForteBio Octet RED96 based on the methods by van der Horst *et al.*[86] Dip and Read Streptavidin Biosensors (ForteBio, 18-5019) were used in the binding experiments for all samples. All experiments were performed in 1x PBS + 0.02% Tween-20 + 0.1% Bovine Serum Albumin (BSA; MilliporeSigma, A7030). After a 10 min delay for sensor tip rehydration, as recommended by the manufacturer, the biosensor tips were moved into a well of PBS-T-BSA for a 300 s equilibration step. After, the biotinylated antibodies or MVN were loaded onto the biosensor tip by introducing them to a well containing 0.5 µg/mL of the LAM recognition element for 400 s. The loaded biosensors were transferred into wells containing PBS-T-BSA for a 60 s baseline step, then transferred into wells containing 2-fold serially diluted ManLAM or PILAM for 400 s. After this association, the biosensors were transferred back into the buffer-only sample well for 900 s to measure dissociation between LAM and the loaded antibody/MVN. A global 1:1 fit model calculated the binding kinetic and equilibrium constants (k_{on}, k_{off}, and K_D). Ideally, the manufacturer recommends that the serial dilutions start at a concentration 10x higher than the calculated K_d, and the lowest concentration was at least 2x lower than the calculated K_d. However, these concentration ranges were not achieved for all LAM recognition elements. Serial dilutions of ManLAM and PILAM started at 1,000 nM for the anti-LAM antibodies and 20 nM for MVN. The values reported here should be used to refine the range of serial dilutions and improve the reported value's accuracy.

Table E1. Measured Concentration of anti-LAM Antibodies from FIND.

Antibody clone	Measured total protein concentration (mg/mL)	Manufacturer Reported Concentration (mg/mL)
FDX01	8.94	No data[§§§]
A194	5.95	4
BJ-03	6.94	4.7-5.6[3]
BJ-76	6.31	5.1-5.8[3]
FIND28	2.23	2
BTM-1	6.37	4.8-8.1[3]
BTM-8	6.23	5.2-9.8[3]

[§§§] *Because of instances where exact concentrations of antibody were not provided from the manufacturer, for all antibodies, the total protein concentration was assumed to be the antibody concentration measured on a Nanodrop™ Spectrophotometer ND-1000 for all experiments.*

Expression and purification of 14 kDa and 24 kDa microvirin-N (MVN) monomer and dimer.

MVN was expressed and purified using immobilized metal affinity chromatography (IMAC) and further refined using size exclusion chromatography (SEC). This was performed to help elucidate the binding behavior of MVN to *M.tb*. The MVN that was isolated using combined His-tag purification and SEC is referenced using the molecular weight of the recovered lectin in each fraction. The "14 kDa MVN" is the primary species expressed and isolated, and it is approximately the same size as endogenous MVN. The "24 kDa MVN" is a dimer of MVN,[312, 344] and is expressed in minor amounts compared to 14 kDa MVN.

Plasmid information.

The microvirin-N (MVN) DNA sequence was previously cloned into the pET15b vector, resulting in the expression of an N-terminally His-tagged MVN protein. Dr. Carole Bewley generously gifted the cloned pET15b-MVN plasmid (Laboratory of Bioorganic Chemistry, NIDDK, National Institutes of Health).[343] Cloning methods inserting the MVN into the pET-15b vector are described by Kehr *et al.*[312]

Expression of MVN.

According to manufacturer's instructions, a total of 20 ng pET15b-MVN plasmid was transformed into One-ShotTM BL21 (DE3) pLysS E. coli (Invitrogen, C606010). Transformed bacteria were plated at colony-forming density on 1.5% agar plates containing Lysogeny Broth with 100 µg/mL ampicillin and 34 µg/mL chloramphenicol (LB + AmpCam), then incubated overnight at 37°C. No colonies grew for cells transfected with water in place of the MVN plasmid.

A 20 mL LB + AmpCam overnight starter culture was inoculated with one colony and cultured at 37°C with shaking at 200 rpm for 18 h. The following day, four 1 L baffled flasks, each containing 300 mL Terrific Broth (1.2% w/v tryptone, 2.4% w/v yeast extract, 0.4% v/v glycerol, 17 mM KH_2PO_4, 72 mM K_2HPO_4), were each inoculated with 3 mL of the overnight starter culture. The 300 mL cultures were incubated at 37°C with shaking at 160 rpm for 3 h, until the OD600 reached 0.5 – 0.8. Isopropyl β-D-1-thiogalactopyranoside (IPTG; RPI Corp., I56000) was added at a final concentration of 1 mM to each culture to induce MVN expression and the cultures were incubated for an additional 3 hours at 37°C with shaking at 160 rpm to complete the protein expression. Cultures were collected into 4 pre-weighed centrifuge tubes and pelleted at 4,200 x rcf, 4°C, for 15 min. The supernatant was discarded, the pellet weights were recorded, and the pellets were frozen at −20°C until further processing.

Bacterial lysis.

For each gram of pellet to be lysed, 4 mL of Bacterial Protein Extraction Reagent (ThermoFisher 78243) was added. The pellet was vortexed, then sonicated in 5 x 20 s pulses on ice, with rest times of 1 min each. For each original gram of pellet, 0.75 µL of Benzonase® Nuclease (SigmaAldrich, E1014-5KU) was then added. The tube was swirled and inverted to mix and incubated at room temperature for 15 min. Lysates were clarified by centrifuging them at 4,300 x rcf at 4°C for 25 min. The supernatant was removed and placed into a clean tube and diluted to a final volume of 50 mL in water supplemented with a final concentration of 25 mM Tris (pH = 7.6), 500 mM NaCl, and 10 mM imidazole. The final lysate was filtered through a 0.45 µm filter for additional clarification.

IMAC and SEC purification.

All protein purification was carried out using BioRad's Biologic Duoflow Fast Protein Liquid Chromatography system. A 5 mL HiTrap™ TALON (Cobalt Manganese Acetate) crude column (Cytiva Life Sciences, 28953767) was equilibrated at 5 mL/min with 10 column volumes (CV) equilibration buffer (25 mM Tris (pH 7.6), 500 mM NaCl, 10 mM imidazole). The 50 mL bacterial lysate, containing an equivalent of 2.5 g pelleted bacteria and prepared in the method described above, was loaded onto the column at 3 mL/min. The column was washed with 8 CV of equilibration buffer at 5 mL/min, and the protein was eluted in a single-step elution, at 4 mL/min, with 40 mL elution buffer (25 mM Tris (pH = 7.6), 500 mM NaCl, and 500 mM imidazole). Elution fractions of 3.5 mL were collected and analyzed by SDS-PAGE (12% gel) for the presence of the 14 and 24 kDa MVN monomer and dimer, respectively. The fractions with the highest protein content were pooled and concentrated to a volume of 1.5 mL, using Amicon Ultra-15 Centrifugal Filter Units with a 3000 MWCO (EMD Millipore, UFC900324).

Purified, concentrated MVN was separated into 14 kDa and 24 kDa-enriched fractions using a size-exclusion chromatography via a 16/60 Sephacryl™ S-200 High-Resolution Column (Cytiva Life Sciences, 17116601). The column was equilibrated at 0.5 mL/min with 1.5 CV Equilibration Buffer of "high salt" PBS (10 mM Na_2HPO_4, 1.8 mM KH_2PO_4, 2.7 mM KCl, and 150 mM NaCl). A volume of 1.5 mL of the concentrated MVN sample was injected via static loop, and the sample was separated on the column with continual application of 2 CV equilibration buffer at 0.5 mL/min. Elution fractions of 0.8 mL were collected, and real-time UV monitoring measuring absorbance at 220 nm revealed a broad peak in the 10-30 kDa region (**Figure E1A**). SDS-PAGE analyzed fractions from this region to determine which fractions contained the 14 kDa fragment and the 24 kDa fragment. The two fragments could not be completely separated from each other, but pools could be generated for

enriching each fragment (**Figure E1B**). Once the pools were created, they were again concentrated with Amicon Ultra-15 3000 MWCO units and then filtered through a 0.22 µm filter (**Figure E2**). Aliquots of purified MVN were stored at −80°C until use.

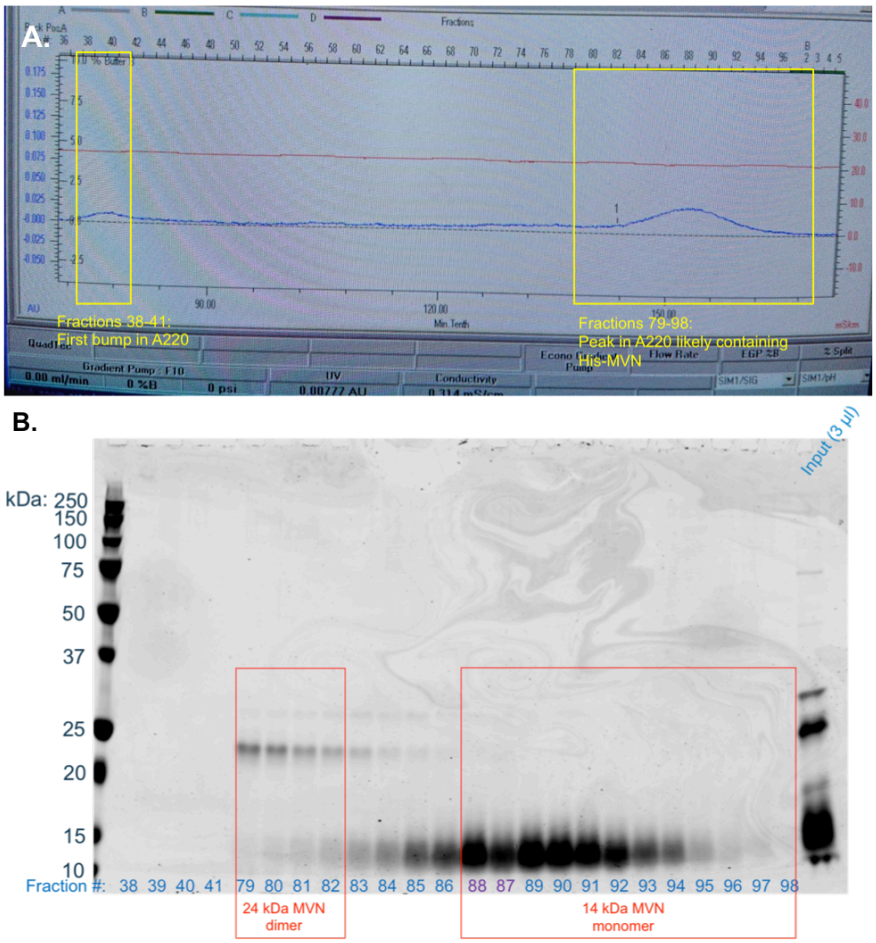

Figure E1. Analysis of SEC fractions for 14 kDa and 24 kDa MVN monomer and dimer. A. Real-time monitoring of protein content in SEC fractions using absorbance at 220 nm. B. Colloidal blue staining depicting SEC fractions with increased A220 measurements. A volume of 11 µL of each 0.8 mL fraction were loaded and separated using SDS-PAGE under reducing conditions. Fractions for the 14 kDa MVN monomer and 24 kDa dimer were pooled as indicated.

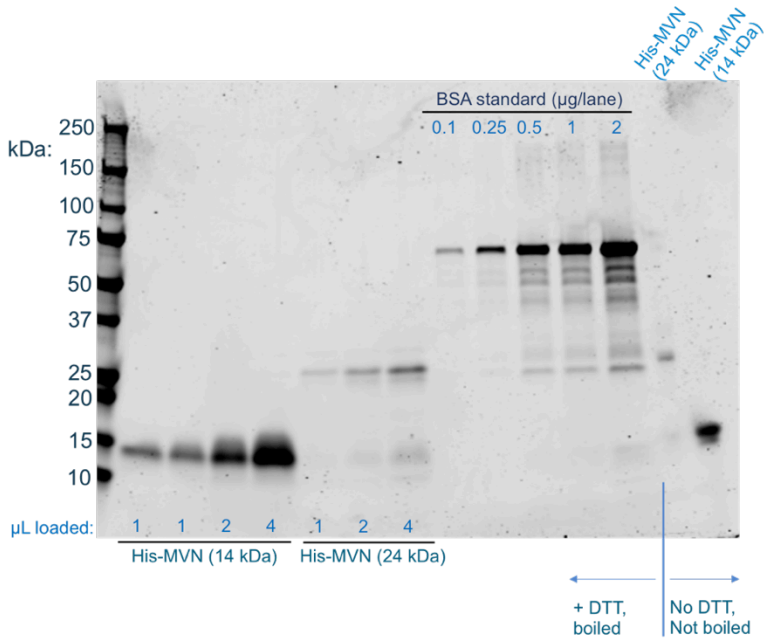

Figure E2. Colloidal blue staining depicting final SEC-purified fractions containing 14 kDa MVN monomer and 24 kDa MVN dimer. The 14 kDa monomer is the primarily expressed protein, with some 24 kDa dimer also recovered. Pseudo-native samples (right two lanes) containing SDS but no disulfide bond reducing agent dithiothreitol (DTT) were included for both fractions alongside SDS and DTT-reduced samples used for quantification.

Results

Biolayer interferometry.

We have identified several candidate antibodies and novel cyanobacterial lectin microvirin-N[86] as possible LAM detection molecules, which could be used for TB diagnosis and discernment between MTBC and NTM infections. Therefore, using biolayer interferometry, we characterized the binding of these LAM recognition elements to both ManLAM, the mannose-capped LAM found in MTBC species, and PILAM, the phosphoinositol capped LAM found in fast-growing mycobacterial species commonly associated with difficult to diagnose NTM infections. The binding affinity of the LAM recognition elements was measured by the dissociation constant (K_D) using biolayer interferometry. The results are summarized in **Table E2**.

The results in **Table E2** are expected given the known binding targets of each detection molecule (shown in **Figure 5.1**). Because the structure of LAM is conserved across all mycobacterial species, antibodies designed to bind the conserved terminal end of the arabinose-backbone of LAM just before the carbohydrate capping motif,

FIND28, FDX01, and A194, all exhibit binding to both ManLAM and PILAM. FIND28 and FDX01 bind different structural variations of the arabinose backbone than A194, as shown in **Figure 5.1**.

Table E2. K_d of LAM Regognition Elements for ManLAM and PILAM.

LAM-recognition element	K_d ManLAM (M)	K_d PILAM (M)
BJ-03	$1.2\times10^{-10} \pm 1.7\times10^{-11}$	N.B.[****]
BJ-76	$4\times10^{-8} \pm 4.2\times10^{-10}$	N.B.[****]
BTM-1	$6.8\times10^{-10} \pm 8.0\times10^{-11}$	N.B.[****]
BTM-8	$<1.0\times10^{-12} \pm 8.2\times10^{-11}$	N.B.[****]
FIND28	$1.3\times10^{-8} \pm 1.4\times10^{-10}$	$1.4\times10^{-8} \pm 1.4\times10^{-10}$
FDX01	$<1.0\times10^{-12} \pm 1.5\times10^{-11}$	$<1.0\times10^{-12} \pm 7.6\times10^{-12}$
A194	$1.8\times10^{-8} \pm 3.0\times10^{-10}$	$1.4\times10^{-9} \pm 2.4\times10^{-11}$
MVN-Biotin	$<1.0\times10^{-12} \pm 3.9\times10^{-10}$	N.B.[****]

Since the difference in LAM structure between species is exclusively in the terminal carbohydrate-capping motif, it is logical that the antigen recognition elements known to bind mannose structures bind ManLAM but not PILAM. However, these elements bind different types of mannose caps, and this difference is essential for understanding changes in surface expression levels. Both types of mannose caps found on LAM can be mono-, di-, or tri-mannosyl caps, with di-mannosyl caps most common.[308] These mannosyl residues connect through α-(1,2)-glycosidic linkages. MVN is known to bind this glycosidic linkage specifically and was previously shown to bind ManLAM but not PILAM,[86] for which our reported K_d values are consistent. BJ-03 binds standard mannose caps containing two sugars. The reported K_D for BJ-03 and BJ-76 are consistent with values previously reported in the literature.[322] It is important to note that the K_d for BJ-76 in the literature was reported as "undetectable" under the reported test conditions, which, based on the value reported here, did not use a high enough concentration of ManLAM to accurately detect and quantify binding between BJ-76 and ManLAM, based on the manufacturer's recommended concentration range for the given K_d.

Based on the results given in **Table E2**, a single antibody was selected for each target structure where applicable. FDX01, A194, BJ-03, and BJ-76 were selected and used to assess dissociation methods on LAM surface accessibility. BJ-76 was chosen over BTM-1 and BTM-8 because it produced a higher signal during antibody titrations than the quantity applied during titrations. FDX01 was chosen over FIND28 because as of the time this manuscript was written, there was only literature publically available characterizing FIND28.[86, 226] We did not find

[****] *N.B. – No binding observed.*

any reports discussing the use of FDX01, and we thought the added information this report could provide about FDX01 would be beneficial to other researchers.

Investigation of MVN signal and impact on LAM detection.

Throughout the studies performed in Chapter 5, we used MVN, a novel lectin known to bind the Man*p*-(1→2)-α-D-Man*p* linkages found in the mannosyl caps on ManLAM.[86] However, the high quantity of MVN needed for detection (2 µg), and the difference in signal trends from BJ-03 and BJ-76 led us to investigate further MVN and its potential use as a LAM recognition element in whole-cell binding assays. As shown in (**Figure E3**), the purified primary 14 kDa MVN fragment throughout the previously discussed experiments resulted in statistically less detection signal than background for almost all processing methods. Given that MVN has such a high affinity for ManLAM (**Table E2**), we hypothesized MVN does not bind well in practical experimental conditions. As previously theorized, the mannosyl caps on MVN may be broken or damaged by applying shear forces, eliminating the α-(1,2)-glycosidic linkages MVN binds.

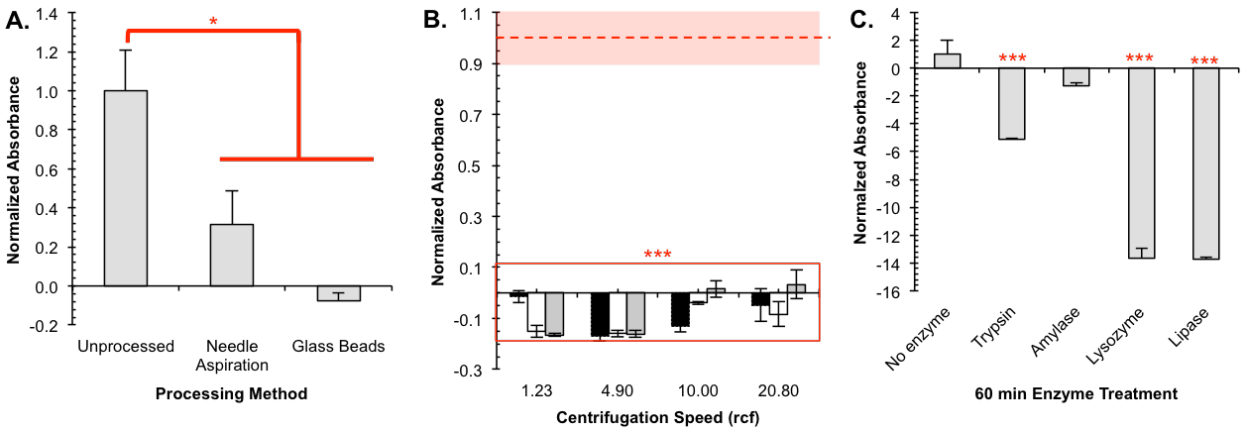

Figure E3. Binding of the 14 kDa monomer of MVN is significantly impacted by mechanical and enzymatic processing. **A.** 14kDa MVN binding to *M.tb* is statistically reduced with both mechanical processing methods. **B.** Regardless of centrifugation speed or repetition, MVN binding is significantly reduced. The red dashed line indicates the normalized mean absorbance for the unprocessed control; the pink shaded box the graphs are superimposed over indicates the ± SEM. Black bar = 1x centrifugation. White bar = 3x centrifugation. Gray bar = 5x centrifugation. n = 3. (mean ± SEM). **C.** 14 kDa MVN binding is significantly reduced for all enzymatic treatments methods, except for amylase digestion. *Indicates statistical significance at $p < 0.05$. ***Indicates statistical significance at $p < 0.0005$.

However, native MVN is monovalent and only has a single mannose-binding pocket for ManLAM. This makes it structurally unique from similar lectins, usually with two binding domains.[349] Therefore, it is possible that a single 14 kDa fragment cannot remain bound to the surface, resulting in a drastically reduced signal when there are modest fluctuations in LAM accessibility. If this were the case, binding could be improved through dimerization. MVN spontaneously dimerizes in small amounts relative to the amount monomer MVN, so we hypothesized that the signal from MVN binding would increase if cells were probed with the 24 kDa fragment, relative to the 14 kDa fragment or sample containing standard proportions of 14 kDa and 24 kDa. As shown in **Figure E4**, while there is no statistical difference between the three groups, there is an increase in signal when treated with 2 μg of 24 kDa MVN by an average of 40-fold compared to the mixture. When a t-test was performed between the 14 kDa and 24 kDa fragments, there was still no statistical difference between the two groups because of the wide variability in the 24 kDa treated samples; a higher n-value is needed for all conditions to determine if these relative differences are practically significant.

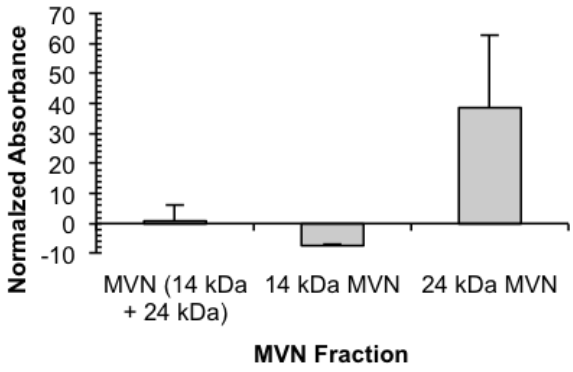

Figure E4. The binding of the minority 24 kDa dimer of MVN produced a higher signal than the 14 kDa fragment or a mixture of the two, though the difference between the three groups was not statistically significant. n = 3. (mean ± SEM).

Acknowledgments and Funding

The authors thank Dr. Megan van der Horst for instruction on using the biolayer interferometer and for assistance characterizing MVN. We also thank Dr. Raymond L. Mernaugh for insightful discussions. The authors thank Dr. Carole Bewley, Dr. Megan van der Horst, BEI Resources, and FIND for the reagents gifted for use in this

report. The authors thank the Vanderbilt Antibody and Protein Resource Core expressed MVN gifted by Dr. van der Horst.

This work was funded in part by the US National Institutes of Health Grant No. R01-AI135937.